Functional and structural substrates of increased dosage of *Grik4* gene elucidated using multi-modal MRI

Doctoral Thesis presented by

Amr Fawzy Kamel Eed

- 2020 -

Thesis Director

Juan Lerma Gómez

PhD Program in Neuroscience

Instituto de Neurociencias – UMH-CSIC

INSTITUTO DE NEUROCIENCIAS

1999 - 2019 AÑOS

INSTITUTO DE NEUROCIENCIAS

EXCELENCIA SEVERO OCHOA

Sant Joan d'Alacant, April 2021

To whom it may concern,

The doctoral thesis entitled "**Functional and structural substrates of increased dosage of *Grik4* gene elucidated using multi-modal MRI**" has been developed by myself, **Amr Fawzy Kamel Eed**. This thesis is presented in a conventional format. It is based on experimental studies undertaken at the Neuroscience Institute of Alicante during the PhD program in neuroscience of the Miguel Hernández University.

Yours sincerely,

Amr Fawzy Kamel Eed

INSTITUTO DE NEUROCIENCIAS

1999 - 2019 AÑOS
INSTITUTO DE NEUROCIENCIAS

EXCELENCIA SEVERO OCHOA

Sant Joan d'Alacant, April 2021

To whom it may concern,

The doctoral thesis entitled "**Functional and structural substrates of increased dosage of Grik4 gene elucidated using multi-modal MRI**" has been developed by myself, **Amr Fawzy Kamel Eed**. This thesis includes the following publication(s), of which I am the first author. I declare that the publication has not been used and will not be used in any other thesis in agreement with my thesis director **Juan Lerma Gómez**:

Eed, A., A. Cerdán Cerdá, J. Lerma and S. De Santis (2020). "Diffusion-weighted MRI in neurodegenerative and psychiatric animal models: Experimental strategies and main outcomes." Journal of Neuroscience Methods **343**: 108814.

Yours sincerely,

Doctorando

Prof./ Juan Lerma Gómez

INSTITUTO DE NEUROCIENCIAS

1999 - 2019 20 AÑOS
INSTITUTO DE NEUROCIENCIAS

EXCELENCIA SEVERO OCHOA

Sant Joan d'Alacant, 10 de abril 2021

D. **Juan Lerma Gómez**, Profesor de Investigación del Consejo Superior de Investigaciones Científicas,

AUTORIZO la presentación de la Tesis Doctoral titulada "**Functional and structural substrates of increased dosage of Grik4 gene elucidated using multi-modal MRI**" y realizada por D. **Amr Fawzy Kamel Eed**, bajo mi inmediata dirección y supervisión como director de su Tesis Doctoral en el Instituto de Neurociencias (UMH-CSIC) y que presenta para la obtención del grado de Doctor por la Universidad Miguel Hernández.

Y para que conste, a los efectos oportunos, firmo el presente certificado.

Prof./ Juan Lerma Gómez

Sant Joan d'Alacant, 10 de abril 2021

Dña. **Elvira De la Peña García**, Profesora titular de la Universidad Miguel Hernández (UMH) y Coordinadora del programa de doctorado en Neurociencias del Instituto de Neurociencias de Alicante, centro mixto de la Universidad Miguel Hernández (UMH) y de la Agencia Estatal Consejo Superior de Investigaciones Científicas (CSIC).

CERTIFICA:

Que la Tesis Doctoral titulada "**Functional and structural substrates of increased dosage of Grik4 gene elucidated using multi-modal MRI**" ha sido realizada por D. **Amr Fawzy Kamel Eed**, bajo la dirección de D. **Juan Lerma Gómez** como director, y doy mi conformidad para que sea presentada a la Comisión de Doctorado de la Universidad Miguel Hernández.

Y para que conste, a los efectos oportunos, firmo el presente certificado.

Fdo. Elvira De la Peña García

Coordinadora Programa de Doctorado en Neurociencias

E-mail:
elvirap@umh.es
www.in.umh.es

Tel: +34965919540
Fax: +34965919549

Av. Ramón y Cajal s/n
CAMPUS DE SANT JOAN
03550 SANT JOAN D'ALACANT
ESPAÑA

Acknowledgment

First and foremost, I would like to express my utmost gratitude to my supervisor, Prof. Juan Lerma for his help, support, and for allowing me to develop such a project defying the long-held tradition of working in electrophysiology in the lab. He granted me all the autonomy I needed to bring this project to fruition.

I have to thank Prof. Santiago Canals and his lab, especially, Dr. Silvia De Santis for their help and their insights that guided me through the toughest patches of the work. They have provided me with a much-needed place to channel my questions and my doubts and I cannot thank them enough for that.

Even though my work parted ways with the main theme of the lab, I still had a wonderful relationship with everyone there (hopefully, not because of that). Despite my miserable failure to learn electrophysiology, I have been always grateful to Dr. Ana Valero and her patience in teaching me. I always considered her as a friend, to whom I can confine my secrets, more than a superior.

Communicating with people from outside the lab and other groups have been always challenging to me. I could not have done a lot of the work without Dr. Isabel Aller holding my hands and introducing me to people. I cannot overstate what I have learned from her in getting things done at the institute.

I would also like to thank my wonderful desk companion, Monica for her tolerance of my quarks and my excessive movements. I could not have never asked for a better companion.

A special thanks to my friend and colleague, Kat, without whom I would never have managed to find a way through the jungle of papers I had to do to get the degree (Kat knows better).

I consider myself truly blessed by all the people I got to meet in and outside the lab. I would like to say thanks to all of them, my dear friend Álvaro, Valeria, Sergio, Vineet, Javi (my window neighbor and my gym pal), Kat (again), Kevin, Selim, Lucía, Salma, Ana, Laura, Robertos (yes, plural; there are many of them), Michael, Deli, and Khalid.

Last but not least, I would like to thank our MRI technician, Luis Tuset for all the work he has done and the long hours he spent working on improving the quality of the images. I do not think he would have worked with such devotion had the work been his.

Finally, I hope that the people I have crossed paths with would remember me with more than “the guy who used to sleep in seminars”.

Amr,
Sant Joan d’Alacant, 26th,
April, 2021.

Work communications:

- **Eed, A**. et al., (2017, September). Brain resting activity in an animal model of autism. A functional magnetic resonance study. Presented at Sociedad Española de Neurociencia (SENC), Alicante, 2017.
- **Eed, A**. et al., (2018, July). Functional and structural abnormalities in an animal model of autism determined by multimodal MRI. Presented at Federation of European Neuroscience Societies forum (FENS), Berlin, 2018.
- **Eed, A**. et al., (2019, June). Disruption of Functional and Structural Networks in An Animal Model of Autism Determined by Multimodal MRI. Will be presented at Organization for Human Brain Mapping meeting (OHBM), Rome, 2019.
- **Eed, A**., A. Cerdán Cerdá, J. Lerma and S. De Santis (2020). "Diffusion weighted MRI in neurodegenerative and psychiatric animal models: Experimental strategies and main outcomes." Journal of Neuroscience Methods 343: 108814.

LIST OF ABBREVIATIONS

6CP	6th cerebellar lobule

A

Acb	accumbens nucleus
ACC	anterior cingulate cortex
AD	axial diffusivity
ADC	apparent diffusion coefficient
AFD	apparent fiber density
AHP	anterior hypothalamic nucleus
AK	axial kurtosis
AMBMC	Australian mouse brain mapping consortium
Amg	Amygdala
Au/TeA	auditory/temporal association cortex
AWF	axonal water fraction

B

BOLD	blood-oxygenation-level dependent

C

CA1	cornu ammonis-1
CA3	cornu ammonis-3
CBF	cerebral blood flow
CBV	cerebral blood volume
cc	corpus callosum
CF	carbon fiber
CFE	connectivity-based fixel enhancement
Cg	cingulate cortex
CHARMED	The composite hindered and restricted models of diffusion
Cpu	caudate putamen
CSD	constrained spherical deconvolution
CSF	cerebrospinal fluid

D

DEC	directionally-encoded color map
DEC FA	directionally-encoded color fractional anisotropy
Δ	diffusion time
δ	gradient duration
DEn	dorsal endopiriform nucleus
DG	dentate gyrus
DM	dorsomedial hypothalamic nucleus
DMN	default mode network
dmPFC	dorsomedial prefrontal cortex
dMRI	diffusion MRI
dof	degrees of freedom
DR	Dual Regression
DS	down syndrome

DTI	diffusion tensor imaging
DWI	diffusion weighted image

E

ec	external capsule
ECOG	electrocorticography
EEG	electroencephalography
ENIGMA	enhancing neuroimaging genetics through meta-analysis
EPI	echo-planar imaging
EPM	elevated plus maze

F

FA	fractional anisotropy
FBA	fixel-based analysis
FC	fiber cross-section
FD	fiber density
FDC	combined measure of fiber density and cross-section
fi	fimbria
FICVF	intra-cellular volume fraction (neurite density)
fMRI	functional MRI
FMRP	fragile X mental retardation protein
FOD	fiber orientation distribution
FOV	field of view
FR	restricted fraction
FWER	family-wise error rate
FWHM	full-width at half maximum
FXS	fragile X syndrome

G

GE-EPI	gradient-echo echo-planar imaging
Gi	gigantocellular reticular nucleus
Glu	Glutamate
Gly	Glycine
GM	gray matter
GRFT	Gaussian Random Field Theory

H

Hb	hemoglobin
hpc	hippocampus
HRF	hemodynamic response function

I

IAD	intra-axonal diffusivity
ic	internal capsule
ICA	independent component analysis
IL	infralimbic cortex
IL	infralimbic cortex

K

KA	kurtosis anisotropy

L

Lat	lateral cerebellar nucleus
LH	lateral hypothalamic area
Lo	lateral orbital cortex
LS	lateral septal nucleus
LS	lateral septal nucleus

M

M1	1º motor cortex
M2	2º motor cortex
MBP	myelin basic protein
MD	mean diffusivity
Med	medial cerebellar nucleus
MEG	magnetoencephalography
MK	mean kurtosis
MO	medial orbital cortex
MS	matrix size
msmt-CSD	Multi-shell, multi-tissue CSD

N

NBR	negative BOLD response
NODDI	neurite orientation dispersion and density imaging

O

OB	olfactory bulb
ODI	orientation dispersion index
OF	open field
OFC	orbitofrontal cortex

P

PCC	posterior cingulate cortex
PCP	phencyclidine
PCR	polymerase chain reaction
PGSE	pulsed gradient spin echo sequence
PPC	posterior parietal cortex

R

R	right side
RARE	rapid acquisition with relaxation enhancement
RD	radial diffusivity
RK	radial kurtosis
RMS	root mean square
ROIs	regions of interest
RS	retrosplnial cortex;
RS/PCC	restrosplenial/posterior cingulate cortex
RSFC	resting-state functional connectivity
rsfMRI	resting-state fMRI

RSNs	resting-state networks

S

S	septum
S1	1º somatosensory cortex
SC	superior colliculus
SE-EPI	spin-echo echo-planar imaging
SEM	standard error of the mean
SNX27	sorting nexin 27
SyN	symmetrical normalization

T

TBSS	tract-based spatial statistics
TE	echo time
TFCE	threshold-free cluster enhancement
TG	transgenic
TMBTA	Turone mouse brain template and at-las
tort	tortuosity
TR	repetition time

V

V1	1º visual cortex
V2	2º visual cortex
VBA	voxel-based analysis
VBM	voxel-based morphometry
vmPFC	ventromedial prefrontal cortex

W

wks	weeks
WM	white matter
WT	wild-type

ABSTRACT

Grik4 is the gene responsible for encoding the high-affinity GluK4 subunit of the kainate receptors. Increased dosage of this subunit in the forebrain was linked to an increased level of anxiety, lack of social communication, and depression. On the synaptic level, abnormal synaptic transmission was also reported. The manifestations of this abnormal expression have not been investigated at the circuit level, nor the correlations between those circuits and the abnormal patterns of the behavior previously reported. In this line of work, we aspired to use different non-invasive magnetic resonance imaging (MRI) modalities to elucidate any disturbance that might stem from the increased dosage of *Grik4* and how those changes might explain the abnormal behaviors. MRI offers a non-invasive way to look into the intact brain *in vivo*. Resting-state functional MRI casts light on how the brain function at rest on the network level and has the capability to detect any anomalies that might occur within or between those networks. On the microstructural level, the diffusion MRI is concerned with the underlying features of the tissues, using the diffusion of water molecules as a proxy for that end. Moving more macroscopically, using structural scans, voxel-based morphometry can detect subtle differences in the morphology of the different brain structures. We recorded videos of our animals performing two tasks that have long been linked to anxiety, the open field and the plus-maze tests before acquiring structural and functional scans. Lastly, we recorded blood-oxygenation-level dependent (BOLD) signals in a different set of animals during electrical stimulation of specific white matter tracts in order to investigate how neuronal activity propagates.

Our analysis showed a vast spectrum of changes in the transgenic group relative to the animals in the control group. On the resting-state networks level, we observed an increase in the within-network strength spanning different structures such as the hippocampus, some regions of the cortex, and the hypothalamus. The increased internal coherence or strength in the networks contrasted with a significant reduction in between-networks connectivity for some regions such as parts of the cortex and the hypothalamus, suggesting long-range network decorrelation. Supporting this idea, major white matter (WM) tracts, such as the corpus callosum and the hippocampal commissure, suffered from substantial changes compatible with an important reduction in myelination and/or a decrease in the mean axonal diameter. Macrostructurally speaking, the overexpression of GluK4 subunit had a bimodal effect, with expansion in some cortical areas in the transgenic animals

accompanied by a shrinkage in the subcortical regions. Upon stimulating the brain with an electrical current, we noticed a difference in activity propagation between the two hemispheres. In transgenic animals, the evoked activity remained more confined to the stimulated hemisphere, again consistent with an impaired long-range connectivity. The structural changes both, at the micro and macro level, were in tight correlation with different aspects of the behavior including markers of anxiety such as the time spent in the open arms vs the closed arms in the plus-maze test and the time spent in the center vs the corners in the open field test. Our findings reveal how the disruption of kainate receptors, or more globally the glutamate receptors, and the abnormal synaptic transmission can translate into brain-wide changes in connectivity and alter the functional equilibrium between macro-and mesoscopic networks. The postsynaptic enhancement previously reported in the transgenic animals was here reflected in the BOLD signal and measured as an increase in the within-network strength. Importantly, the correlations between the structural changes and the behavior help to put the developmental changes and their behavioral ramifications into context.

RESUMEN

Grik4 es el gen responsable de codificar la subunidad GluK4 de alta afinidad de los receptores de kainato. El aumento de la dosis de esta subunidad en el prosencéfalo se relacionó con un mayor nivel de ansiedad, falta de comunicación social y depresión. A nivel sináptico, también se informó una transmisión sináptica anormal. Las manifestaciones de esta expresión anormal no se han investigado a nivel de circuito, ni las correlaciones entre esos circuitos y los patrones anormales de la conducta previamente informada. En esta línea de trabajo, aspiramos a utilizar diferentes modalidades de imágenes por resonancia magnética (MRI) no invasivas para dilucidar cualquier alteración que pudiera derivarse del aumento de la dosis de *Grik4* y cómo esos cambios podrían explicar los comportamientos anormales. La resonancia magnética ofrece una forma no invasiva de observar el cerebro intacto in vivo. La resonancia magnética funcional en estado de reposo arroja luz sobre cómo funciona el cerebro en reposo en el nivel de la red y tiene la capacidad de detectar cualquier anomalía que pueda ocurrir dentro o entre esas redes. En el nivel microestructural, la resonancia magnética de difusión se ocupa de las características subyacentes de los tejidos utilizando la difusión de moléculas de agua como un proxy para ese fin. Moviéndose más macroscópicamente, utilizando escaneos estructurales, la

morfometría basada en vóxeles puede detectar diferencias sutiles en la morfología de las diferentes estructuras cerebrales. Grabamos videos de nuestros animales realizando dos tareas que durante mucho tiempo se han relacionado con la ansiedad, el campo abierto y las pruebas de laberinto positivo antes de adquirir escaneos estructurales y funcionales. Por último, registramos señales dependientes del nivel de oxigenación de la sangre (BOLD) en un grupo diferente de animales durante la estimulación eléctrica de tractos específicos de materia blanca para investigar cómo se propaga la actividad neuronal. Nuestro análisis mostró un amplio espectro de cambios en el grupo transgénico en relación con los animales en el grupo de control. En el nivel de las redes de estado de reposo, observamos un aumento en la fuerza dentro de la red que abarca diferentes estructuras como el hipocampo, algunas regiones de la corteza y el hipotálamo. La mayor coherencia interna o fuerza en las redes contrastó con una reducción significativa en la conectividad entre redes para algunas regiones como partes de la corteza y el hipotálamo, lo que sugiere una descorrelación de redes de largo alcance. Apoyando esta idea, los grandes tractos de materia blanca (WM), como el cuerpo calloso y la comisura del hipocampo, sufrieron cambios sustanciales compatibles con una importante reducción de la mielinización y / o una disminución del diámetro axonal medio. Macroestructuralmente hablando, la sobreexpresión de la subunidad GluK4 tuvo un efecto bimodal, con expansión en algunas áreas corticales en los animales transgénicos acompañada de una contracción en las regiones subcorticales. Al estimular el cerebro con una corriente eléctrica, notamos una diferencia en la propagación de la actividad entre las dos hemiesferas. En los animales transgénicos, la actividad evocada permaneció más confinada al hemisferio estimulado, de nuevo consistente con una conectividad de largo alcance deteriorada. Los cambios estructurales, tanto a nivel micro como macro, estaban en estrecha correlación con diferentes aspectos de la conducta, incluidos marcadores de ansiedad como el tiempo pasado con los brazos abiertos frente a los brazos cerrados en la prueba del laberinto positivo y el tiempo pasado en el centro vs las esquinas en la prueba de campo abierto. Nuestros hallazgos revelan cómo la interrupción de los receptores de kainato, o más globalmente los receptores de glutamato, y la transmisión sináptica anormal pueden traducirse en cambios de conectividad en todo el cerebro y alterar el equilibrio funcional entre las redes macro y mesoscópicas. La mejora postsináptica informada anteriormente en los animales transgénicos se reflejó aquí en la señal BOLD y se midió como un aumento en la fuerza dentro de la red. Es importante destacar que las correlaciones entre los cambios estructurales y el

comportamiento ayudan a contextualizar los cambios en el desarrollo y sus ramificaciones conductuales.

I. INTRODUCTION

Probably nothing has intrigued humanity for the last few centuries more than how the brain works. How is it possible that such a small organ defines who we are and how we behave and interact with the outside world. However, the journey to understand the brain has taken many turns and has run through numerous obstacles. The first mention of the brain can be traced back to Ancient Egypt, where the infamous Edwin Smith Surgical Papyrus was scripted approximately 1700 B.C. In a particularly interested case of a patient with a fractured skull, the papyrus described what appeared to be the folding of the cortex as a reminiscent of the "corrugations which form on molten copper" and the brain as an organ was referred to as the "marrow of the skull" (Breasted 2013). The notion that the brain is the organ of mind as opposed to the heart came much later as one of the many contributions of the famed Golden Age of the Greek culture. Thanks to Hippocrates and his followers, the brain was finally brought into light as the major controlling center of the body (Finger 2004). Even though they did not know how it works, they still contemplated the brain as responsible for all the functions and emotions that a human might do or experience.

A shred of more solid evidence regarding brain functions started arising from studying cases of brain damage in the nineteenth century. Classical examples are the contributions by Paul Broca and Carl Wernicke, who stumbled across cases of patients with an apparent inability to speak or comprehend the language, while maintaining the cognitive and mental functions intact. The autopsy of those patients led to the description of the brain areas involved in speech generation and language comprehension. Those areas were named Broca's and Wernicke's areas in their honor (Berker et al., 1986).

The introduction of microscopes and advancements in staining and preparing specimens pushed the boundaries of all the biology-related sciences. By the mid of the nineteenth century, the cell theory, that all living tissues are forming from cells arranged as a net, was already in place as a piece of common knowledge. Using only a microscope and endless passion and tenacity, Ramón y Cajal dedicated his life to studying the anatomy of the nervous system. Cajal's observations led him to believe that the nerve cells were the building blocks of the nervous system and can be regarded as independent units, but unlike other tissues, they were not arranged in as a web or reticulum. These ideas compose the essence of what we now know as the "neuron doctrine" (Ramón y Cajal 1909). Establishing the neuron as the computational units of the brain can be regarded as a major

step in the quest of understanding how the brain operates. The next step was to understand how these units talk to each other.

1. Neural transmission

Our understanding of how neurons communicate among themselves has gone through dramatic changes over the years. It was believed until the late 1890s that neurons are connected through an intact physical connection and impulses from one nerve cell to another is transferred by means of physical continuity. Thanks to the work of Ramón y Cajal and others (Ramón y Cajal 1909), we now know that tiny gaps are separating those neurons. It was not until 1899 that this was changed when C. S. Sherrington declared that neurons are "anatomically discontinuous, physiologically continuous" and he continued to say, "a feature of the concatenation of neurons more probably explicative of modification and delay of nerve impulses is the synapse" and the term "synapse" was born (Davenport 1991). The discovery of adrenaline by the end of the nineteenth century paved the way for the development of our understanding of how nerve cells might communicate with each other through chemical transmission. The tremendous work of pioneers like Oliver, Shäfer (Oliver and Schäfer 1895), Langley (Langley 1901), Elliot (Elliott 1905), and Loewi Loewi 1935 helped to establish the role of neurotransmitters and receptors in the process of conveying impulses between neurons. An average neuron can form and receive up to several thousand of these connections (Mack et al., 2013).

Although in some special cases, the direct connection between two adjacent cells might be found, where the cytoplasm of two cells is attached via channels called gap junction, chemical synapses are the place where the sheer majority of communication between neurons takes place through the release of the neurotransmitters as mentioned earlier. Chemical transmission undergoes numerous steps from the synthesis and storage of neurotransmitters in the presynaptic vesicles to unloading in the synaptic cleft when a stimulation arrives at the presynaptic neuron. Upon the release of neurotransmitters in the synapses, they bind to specific receptors, those receptors are responsible for decoding the chemical message conveyed by neurotransmitters into an electric response that propagates to following neurons (Fig. 1).

Within the brain and the spinal cord, two main effects ensue from the fast-synaptic transmission: excitation and inhibition with Glutamate being the predominant excitatory neurotransmitter and γ-aminobutyric acid (GABA) the main inhibitory neurotransmitter.

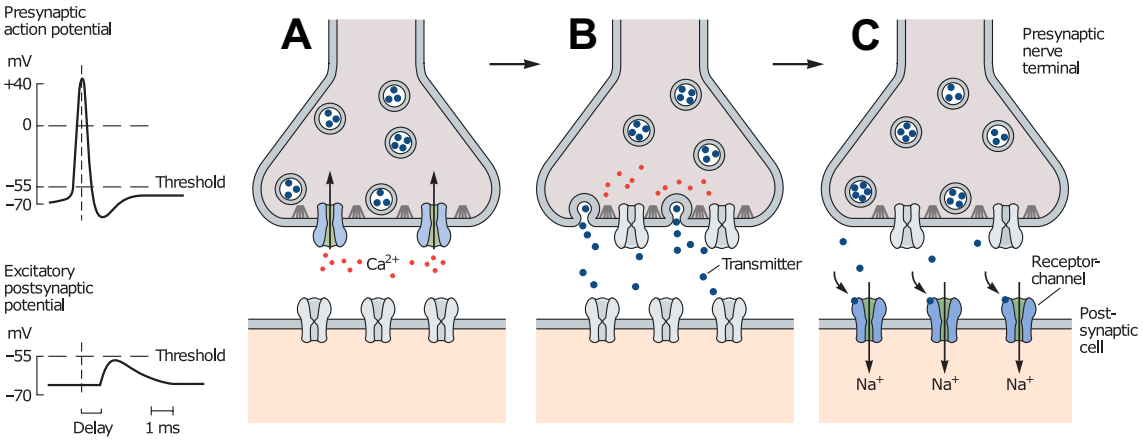

Fig. 1 | Chemical synaptic transmission. (A) The arrival of the action potential at the presynaptic nerve terminal causing the opening of the voltage-gated Ca^{2+} channels. **(B)** The neurotransmitter vesicles fuse with the presynaptic cell membrane unloading the neurotransmitters into the synaptic cleft. **(C)** The released neurotransmitters bind to the receptors on the postsynaptic membrane causing the propagation of the action potential to the postsynaptic nerve terminal (Kandel et al., 2013).

1.1. Glutamate receptors

Glutamate interacts with two broad types of receptors, ionotropic (neurotransmitter gated ion channels) and metabotropic receptors (Fig. 2). Ionotropic receptors are permeable to cations such as sodium ions (Na^+) which leads depolarization and hence to direct excitation. On the other hand, activation of GABA receptors prompts the influx of anions like chloride ions (Cl^-), hyperpolarizing the neuron cell membrane, i.e., moving the membrane potential away from the firing threshold (Traynelis et al., 2010, Brady et al., 2012).

1.1.1. Ionotropic receptors

As indicated, Glutamate receptors fall into one of two major categories, ionotropic Glutamate receptors (iGluRs) which essentially are postsynaptic channels allowing cations influx upon Glutamate binding and are responsible for the fast and brief synaptic actions and metabotropic Glutamate receptors (mGluRs) that activate an intracellular cascade after being activated with Glutamate and lead to a slower but longer-lasting effects compared to the other type (Mack et al., 2013).

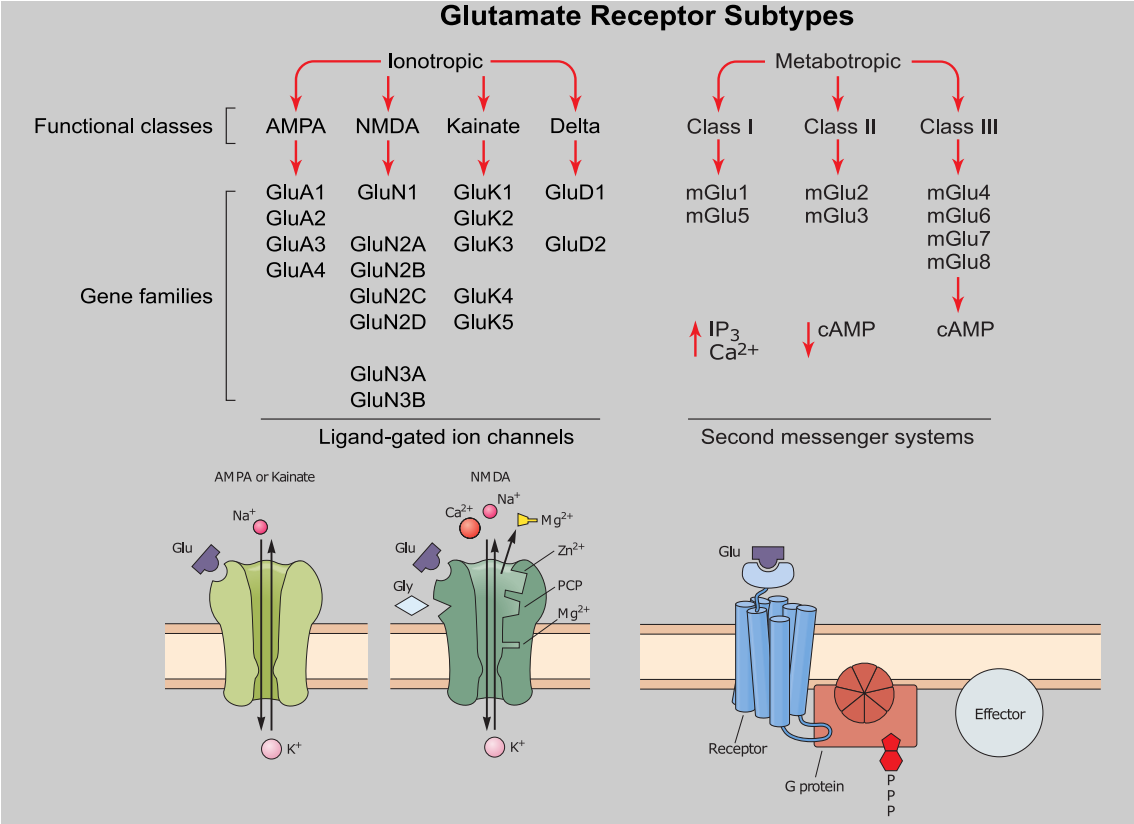

Fig. 2 | Glutamate receptors subtypes and their signaling mechanisms. The two main Glutamate receptor families consist of the ionotropic family and the metabotropic family. Each family has multiple members that function a little bit differently from the other members, however, the members of each family share a similar signaling mechanisms (adapted from Hassel and Dingledine 2012, Kandel et al., 2013). **Abbreviations:** PCP, phencyclidine; Glu, Glutamate; Gly, Glycine.

The iGluRs assemble into four big families of receptors encoded by a sum of 18 genes. Those families are α-amino-3-hydroxy-5-methyl-4-isoxazolepropionic acid (AMPA), N-methyl-D-aspartate (NMDA), kainate (KA), and delta receptors. Sometimes AMPA receptors and kainate receptors are referred to as the non-NMDA receptors. AMPA and NMDA receptors are the major players behind postsynaptic excitatory currents, while KA receptors can be found pre and postsynaptically. Delta receptors are still poorly understood with their functions remain enigmatic due to their inability to gate an ion channel following Glutamate binding which renders them electrically silent (Valbuena and Lerma 2016).

1.1.1.1. AMPA receptors (AMPARs)

AMPARs currents have an extraordinary fast kinetics peak at a sub-millisecond level making these receptors primed for fast depolarization and propagation of impulses to the postsynaptic neurons. Four distinct genes (*Gria1–Gria4*) encode for the four subunits

(GluA1-4) that constitute the AMPARs (Fig. 2). AMPARs subunits can assemble to form tetramers of homo- or heteromers structure with the heterotetramers type being the preponderant in the brain (Jonas and Burnashev 1995).

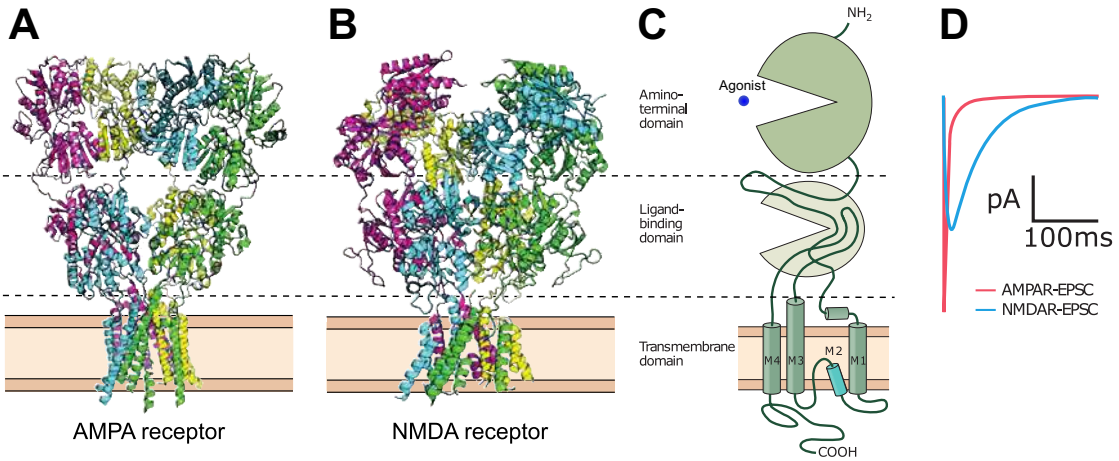

Fig. 3 | Molecular structure of ionotropic Glutamate receptors. (A) Crystal structure of a GluA2 AMPA receptor consisting of four GluA2 subunits (tetrameric receptor). **(B)** Crystal structure of GluN1a/GluN2B NMDA receptor. **(C)** Schematic representation of an ionotropic Glutamate receptor showing the domains that form the receptor. **(D)** Stereotypical excitatory postsynaptic current showing the difference in kinetics between the AMPA and NMDA receptors response (adapted from Kandel et al., 2013, Iacobucci and Popescu 2017).

Each of the aforementioned subunits can be divided into four well-defined domains: an extracellular N-terminal domain (NTD; also known as the amino-terminal domain or ATD), a ligand-binding domain (LBD), transmembrane domain (TMD) forming the ion channel embedded in the membrane, and a C-terminal domain (CTD) in the cytoplasm (Fig. 3C). The TMD consists of three transmembrane α-helices designated as (M1, M3, M4), the M2 forms a loop between M1 and M3 helices (Greger et al., 2017). All the subunits in the different classes of iGluRs share this modular structure (Fig. 3A). The receptor as a whole has an extracellular region (ECR) occupying the vast majority of the receptor (Fig. 3A), and a highly flexible structure of an intertwined dimer of dimers (Sobolevsky et al., 2009).

The subunit assembly of AMPARs crucially determines the properties of the receptor such as ion conductance, trafficking, and calcium permeability (Erreger et al., 2004). Most of these properties are governed by the presence or absence of the GluA2 subunit. The post-transcriptional modifications of mRNA of this unit lead to the replacement of the negatively charged glutamine amino acid with a positively charged amino acid, R607, changing the ion channel conductance and leaving the receptor impermeable to Ca^{2+} with

a linear or an outwardly rectifying current-voltage relationship. This particular site is dubbed “Q/R” site (Q for glutamine and R for arginine).

AMPARs have fast kinetics and a small single-channel conductance (Fig. 3D), and they tend to get inactivated and desensitized rapidly upon exposure to agonists like Glutamate or AMPA with a low affinity to natural agonists such as L-Glutamate (Dingledine et al., 1999). A typical AMPAR would have a brief response to Glutamate causing an opening of the pores of the channels permeable to Na^+ and K^+ ions (Fig. 2). This response rises and decays rapidly within a small window of 1-2 ms as determined by its subunit composition and the density of the receptor, in addition to the time course of the neurotransmitter release and uptake. The AMPAR-mediated excitatory postsynaptic potential (EPSP) is large, with a fast rise and decay, and can trigger an action potential within a rapid time course (Geiger et al., 1997).

AMPARs can be found widely expressed throughout the brain in neurons and glia alike. They are also expressed in a wide variety of neurons in the peripheral nervous system and even in some nonneuronal cell types (Wisden and Seeburg 1993, Belachew and Gallo 2004). Within the adult brain, especially in the pyramidal cells of the hippocampus and the cerebral neocortex, GluA1 and GluA2 receptors comprise the vast majority of AMPARs, with a minor existence of GluA3/GluA4 receptors (Lu et al., 2009). Structures like the cerebellum, the retina, and the reticular thalamic nucleus display a different pattern with GluA4 receptors being highly enriched as GluA2/GluA4 heteromers (Keinanen et al., 1990, Gallo et al., 1992).

Changes in the strength of the connections between nerve cells is widely accepted to underpin the mechanism by which memories are encoded and learning is happening. Among the multiple models of such synaptic plasticity, long-term potentiation (LTP) and long-term depression (LTD) are the most studied (Martin et al., 2000). The complicity of AMPARs changes in the expression and the maintenance of such forms has long been implicated. A staggering volume of literature suggests a critical role for AMPARs phosphorylation in different forms of synaptic plasticity and memory retention.

Phosphorylation of GluA1 subunit seems to be necessary for signaling mechanisms involved in LTP. Various studies have proven a critical role for this phosphorylation through knock-in studies and inhibition or deletion of protein kinases implicated in the

phosphorylation process. Phosphorylation of GluA1 seems necessary in AMPARs upregulation and delivery of the receptors from extrasynaptic locations to the synapse during LTP. Absent this role, in most cases, this form of potentiation was greatly diminished or was absent altogether. Through different mechanisms, studies have shown also that LTD emanates from the rapid removal of synaptic AMPARs through a pathway involving endocytosis and entailing various steps of dephosphorylation and phosphorylation of AMPAR subunits (Shepherd and Huganir 2007).

1.1.1.2. NMDA receptors (NMDARs)

NMDRs represent the second major class of iGluRs and can be distinguished from the rest of iGluRs by several unique features. Analogous to the rest of iGluRs, NMDARs exist in heterotetramers (Fig. 3B). Unlike AMPARs, NMDARs tetramers are made of seven possible subunits, GluN1 encoded by a single *GRIN1* gene, four *GRIN2* genes that encode GluN2A-D, and two *GRIN3* genes encoding GluN3A-B (Fig. 2). GluN1 subunit is encoded by a single gene, but, due to alternative splicing, can exist in eight different isoforms dubbed GluN1-1a-4a and GluN1-1b-4b. The assembly of the receptor forms a central ion channel pore that is permeable to Ca^{2+} as well as to Na^{+} and K^{+} and subject voltage-dependent blockade by extracellular Mg^{2+} (Fig. 2). In a striking breach of the iGluRs norm, NMDARs require two agonists for the ion channel to be activated (Fig. 2). Besides Glutamate, the receptor requires a second agonist which can be either glycine or D-serine (Lerma et al., 1990). The Glutamate remains the de facto controller of the channel activation since the glycine or D-serine exist in surplus in the extracellular space. Utilizing glycine or D-serine as a coagonist greatly depends on the brain region as well as on the receptor subcellular localization. Some reports suggested the D-serine to be the coagonist at synapses with the glycine role confined to the extrasynaptic locations. The necessity of a second agonist offers an extra layer of regulation for the receptors function as the changes in the surrounding levels of the coagonist can modulate the synaptic activation (Paoletti et al., 2013, Hansen et al., 2018).

The release of Glutamate in the brain synapses activates excitatory postsynaptic currents (EPSCs) and the time course of these currents can be broken into two components: a fast component with rapid rise and decay mediated by AMPARs and another slower component with slow rise and decay mediated by the NMDARs (Fig. 3D) (Hestrin et al., 1990, Sah et al., 1990, Trussell et al., 1993, Geiger et al., 1997). In resting condition, NMDARs

are typically occluded by Mg^{2+}, but upon the release of Glutamate into the synaptic cleft, the rapid activation of AMPA/KA receptors leads to depolarization of the cell membrane relieving the blockade of the NMDARs ion channel (Mayer et al., 1984, Nowak et al., 1984). The prolonged activation of NMDARs is proposed to be the result of a higher affinity of those receptors to Glutamate which leads to slower dissociation from the receptor (Lester et al., 1990, Lester and Jahr 1992).

Owing to the relatively big number of subunits, NMDARs exist in many different forms of subunit assembly and, as with AMPARs, these forms affect the functions and the properties of the receptor. Attributing certain functions or defining special properties to each form of the receptors remain an active area of research since studying each kind in isolation proved to be a daunting task (Hatton and Paoletti 2005, Hansen et al., 2014).

As briefed in the AMPARs, the modular structure of the iGluRs subunits is highly conserved. Each subunit consists of four distinct domains: a large extracellular ATD or NTD, a bi-lobed LBD, ion channel-forming TMD, and an intracellular CTD (Fig. 3B, C). Three helices form the TMD (M1, M2, and M4) and a membrane re-entrant loop (M2) connecting M1 and M3. The ATD exists in a clamshell-like structure and harbors an extra binding site for multiple substances acting as allosteric modulators such as zinc ions and polyamines. The LBD is composed of two polypeptide chain segments, namely S1 and S2 forming a kidney-shaped formation serves as a binding site for glycine or D-serine in the case of GluN1 or GluN3 and for Glutamate in GluN2 subunits. The amino acid residue sitting at the tip of the M2 reentrant loop of the TMD (Q/R/N site; N for asparagine) determines Ca^{2+} permeability and Mg^{2+} block (Hansen et al., 2017).

NMDARs act as the trigger of LTP or LTD as a function of their voltage-dependent Mg^{2+} block. Following the depolarization of the cell membrane and the relief of the Mg^{2+}, the influx of Ca^{2+} activates various kinases that initiate various pathways end up with the incorporation of more synaptic AMPARs in the case of LTP or their retrieval from their synaptic sites (Lau and Zukin 2007).

1.1.1.3. Kainate receptors (KARs)

The third class of iGluRs is the KARs, characterized by their high affinity to kainate, a derivative of the seaweed known as “kaininso”. The history of KARs from their isolation for the first time to the investigation and characterization of their properties and functions

highlights an important chapter of iGluRs knowledge due to their peculiar roles in regulating neuronal networks.

The characterization of KARs proved over the years to be elusive and far from easy, as most of the pharmacological agents lack specificity and can act on both AMPARs and KARs. The existence of pure functional KARs has long been questioned and often they were pooled together under the name of non-NMDA receptors along with AMPARs.

The cloning of the first KARs subunits in the early 1990s paved the way to the subsequent revolution in describing and studying these receptors. GluK1 subunit was first cloned in 1990 (Bettler et al., 1990) and not so long after, the same group successfully cloned two other subunits that were later designated as GluK2 and GluK3 (Bettler et al., 1990, Egebjerg et al., 1991). Receptors with high affinity to kainate were described in dorsal root ganglion cells of the peripheral nervous system, albeit they were also sensitive to AMPA (Huettner 1990).

The first evidence of specific KARs within the brain that were responsive to kainate, but not to AMPA came in 1993. In their seminal article, Lerma et al. described for the first time, in dissociated hippocampal cultures, neurons that were selectively sensitive to kainate and not AMPA and with molecular properties akin of receptors composed of homomeric of GluK2 early described (Lerma et al., 1993). The development of compounds able to block AMPARs responses while savoring KARs' such as GYKI 53655 made it possible to isolate currents ensuing from KARs (Paternain et al., 1995, Contractor et al., 2011).

KARs form, like the rest of iGluRs, tetrameric receptors made from five unique subunits: GluK1, GluK2, GluK3, GluK4, and GluK5. GluK1-3 subunits can form homomeric or heteromeric receptors, whereas GluK4-5 are only capable of forming heteromeric channels with a partner of GluK1-3. GluK4-5 receptors have a higher affinity to kainate more than GluK1-3 receptors (for a review, see Lerma et al., 2001).

KARs subunits share the common modular structure of iGluRs subunits with a large extracellular NTD, TMD forming the ion gating channel and composed of four domains (M1, M2, and M3) and a hydrophobic M2 loop, CTD intracellularly, and an LBD made of two modular lobes: D1 and D2 (Fig. 3C) (Lerma 2003).

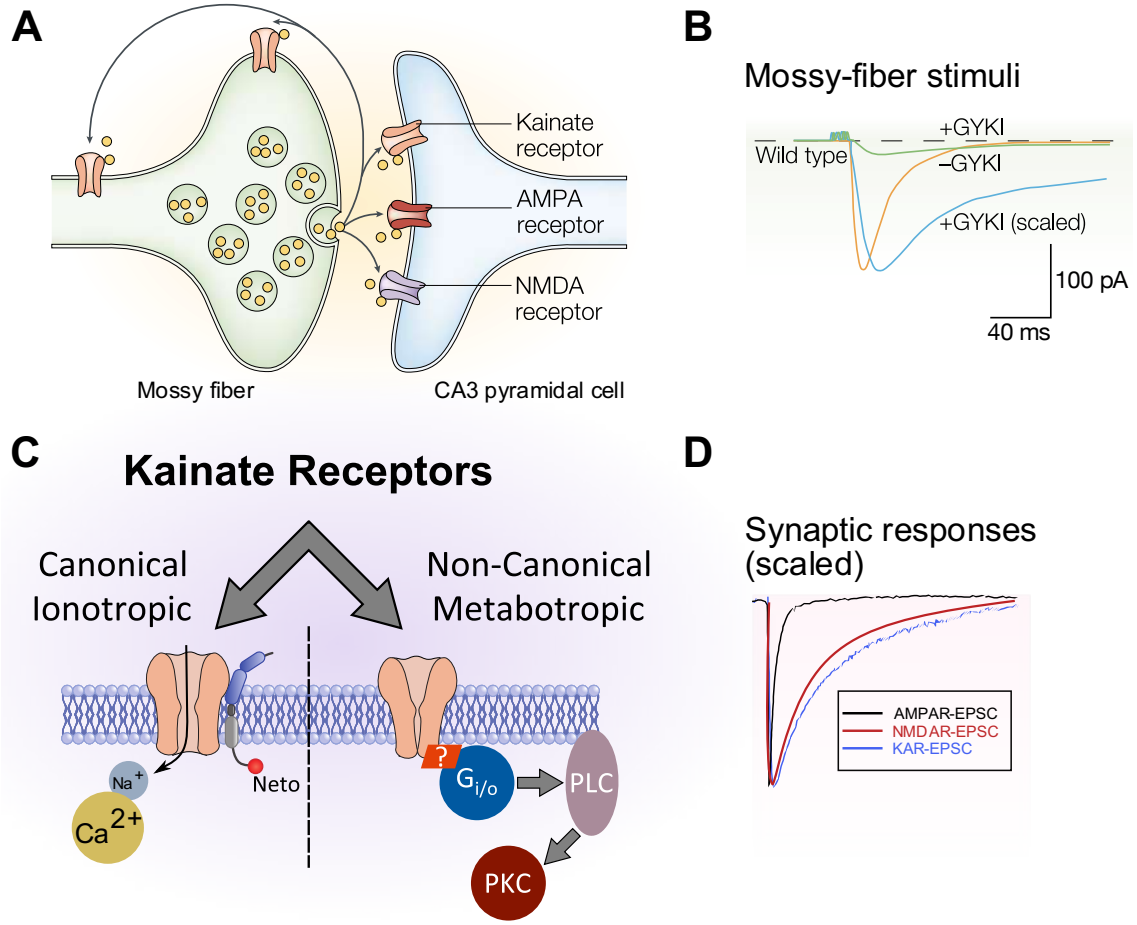

Fig. 4 | KARs and their signaling pathways. (A) Glutamate receptors arrangement in the connection between the Mossy fibers and the pyramidal cells of the CA3 region showing the presynaptic locations of the KARs. **(B)** Stimulating Mossy fibers with short impulses train in the presence and absence of AMPAR antagonist (GYKI 53655). **(C)** The canonical and the non-canonical signaling pathways of the KARs. **(D)** EPSCs of the three Glutamate receptors showing the difference in kinetics (adapted from Lerma 2003, 2011, Lerma and Marques 2013).

Description of the distribution of KARs subunits within the different brain's compartments lag behind since the detection methods available such as specific antibodies against the different subunits, are still limited. The introduction of some specific antisera made it possible to define some charts depicting the expression of these subunits, but most of this knowledge relies on in situ hybridization data. GluK1 subunit is mainly expressed in the interneurons of the hippocampus and the cortex as well as in Purkinje cells and sensory neurons, whilst GluK2 exists in preponderance in the principal cells of the cerebellum and the hippocampus. GluK3 subunit is expressed poorly and is restricted to layer IV of the neocortex and the dentate gyrus (DG) of the hippocampus. GluK4 has a wide distribution in the hippocampus Cornus Ammonis 3 (CA3) and DG as well as in the neocortex, and the Purkinje cells. GluK5 is profusely expressed throughout the brain (Lerma and Marques 2013).

The isolation of pure kainate receptors cast a question of whether KARs are involved in postsynaptic activation. The introduction of selective antagonists to AMPARs like GYKI 53655 made it possible to examine such an intriguing postulation (Fig. 4B). Early studies failed to record EPSC due to KARs in the presence of NMDARs and AMPARs blockers (Lerma 1997), however, subsequent research presented evidence of a role of KARs in synaptic transmission. Repetitive stimulation of the connections between the granule cells and the CA3 pyramidal cells, named the mossy fibers, in the presence of AMPARs and NMDARs blockers elicited a small current with slow rise and decay time akin to that of NMDARs (Fig. 4D); this current was abolished upon the introduction of the antagonist CNQX (Castillo et al., 1997, Vignes and Collingridge 1997). The slow kinetics of the EPSCs mediated by KARs stirred up a controversy as this kinetics cannot be explained by the properties and affinity of the recombinant receptors which these receptors share with the fast-kinetics AMPARs (Lerma 1997).

The mystery was solved by the discovery of two auxiliary proteins Neto1 and Neto2 that interact with KARs (Fig. 4C) (Zhang et al., 2009). Straub et al. reported that upon the coexpression of Neto1 with GluK2 receptors in recombinant systems, the KARs displayed slower kinetics that was faster earlier in these systems which suggests a role for Neto proteins in receptors' affinity. He further showed that knockout mice that lack Neto1 KAR synaptic component has fast kinetics similar to those of AMPARs (Lerma 2011, Straub et al., 2011).

Another interesting aspect of the KARs is their ability to act through two distinct pathways: a canonical traditional one through ligand gating and another non-canonical way via a metabotropic mechanism involving second messengers (Fig. 3C). KARs have an abundant localization presynaptically in both excitatory and inhibitory terminals (Fig. 4A) modulating the release modulating neurotransmitters release and controlling cells excitability (Valbuena and Lerma 2016).

In excitatory synapses, presynaptic KARs modulate the release of Glutamate either enhancing or inhibiting it in a bidirectional manner. In synapses such as mossy fibers to CA3, nanomolar concentrations of kainate elicit facilitation in Glutamate release, while higher concentrations lead to a decrease in Glutamate release (Lerma 2003). Dependence of such action on presynaptic rather than synaptic KARs was demonstrated by showing that these effects remained intact after destruction of the postsynaptic CA3 pyramidal

cells while they were abrogated upon the destruction of the afferent mossy fibers (Represa et al., 1987).

Perhaps the first postulation of the involvement of KARs in decreasing inhibition in the hippocampus came in 1981 by Sloviter and Damiano when they investigated the epileptogenic effect of kainic acid (Sloviter and Damiano 1981). The complicity of KARs and not AMPARs in the inhibition decrease came much later by studies demonstrating that KARs indeed can inhibit GABA release at inhibitory synapses in rat hippocampus manifested as a decrease in evoked inhibitory postsynaptic current (IPSC) (Rodríguez-Moreno et al., 1997, Vignes et al., 1998). This inhibition is likely due to a metabotropic process and independent of ion channel current as it was sensitive to disruption of the G protein signal transduction pathway using Pertussis toxin (Rodriguez-Moreno and Lerma 1998). Changes in properties such as an increase in synaptic transmission failure and decrease in miniature IPSCs frequency prompted the idea that these effects are mediated by presynaptic KARs (Clarke et al., 1997, Rodríguez-Moreno et al., 1997)

On the other hand, other studies reported facilitation, rather than inhibition, of GABA release. Cossart et al reported an increase in miniature IPSCs and a reduction in neurotransmission failures upon application of exogenous kainate or Glutamate at CA1 interneurons inhibitory synapses which the authors attributed to presynaptic KARs through an ionotropic pathway (Cossart et al., 2001). These findings and others ignited a controversy about the role of KARs in the modulation of GABA release and the involvement of presynaptic receptors in such bidirectional modulation. One way to reconcile this paradox was the conjecture that the two effects can be dissociated and ascribed to two different populations of KARs with two disparate pharmacological profiles and signaling pathways with the metabotropic pathway mediate the inhibition and the facilitation mediated by the ionotropic pathway (Valbuena et al., 2019).

KARs metabotropic signaling pathway is not limited to the presynaptic receptors as it has been also described in a subset of postsynaptic receptors. It is well established that KARs in CA1 interneurons and CA3 pyramidal neurons mediate postsynaptic currents, however, in the Schaffer collateral-CA1 pyramidal cells, KARs elicit no ionotropic participation to synaptic responses (Bureau et al., 1999). It has been very speculative until Melyan and team provided a different insight; they demonstrated that these receptors are not functionless, instead they exert their action through a metabotropic pathway (Melyan et al.,

2002). These receptors are reported to cause a long-lasting inhibition of the slow afterhyperpolarization current (I_{sAHP}), which in turn causes an increase in neuronal excitability (Melyan et al., 2002). Interestingly, the same metabotropic effect was also described in CA3 pyramidal neurons, where KARs activation inhibits slow (I_{sAHP}) and medium (I_{mAHP}) afterhyperpolarization currents alike (Fisahn 2005); indicating that both signaling modes can coexist at the same synapses (for a review on metabotropic signaling in KARs, see Rodrigues and Lerma 2012, Valbuena and Lerma 2016).

From these shreds of evidence and more, we can safely conclude that KARs are controlling both the excitability and inhibition of neurons throughout the different brain regions using disparate signaling mechanisms bestowing a capability to regulate and control the neuronal circuits and further the brain functions upon the KARs.

Neuronal growth and maturation during development is another critical process where KARs significantly contribute. Tashiro and others investigated the participation of KARs in the regulation of axonal filopodial motility from the mossy fibers of the hippocampus (Tashiro et al., 2003). The results showed that, once again, KARs bidirectionally regulate filopodial motility where it gets enhanced in younger slices and inhibited in mature ones in a concentration-dependent manner. The authors proposed a two-step model of synaptogenesis, whereby in early stages of development the rapid dilution of Glutamate due to the large extracellular space limits the amount of neurotransmitter available for KARs which by their turn promote the filopodial motility to find its synaptic targets. Conversely, KARs stimulation inhibits such motility once these contacts are already there in later stages of development where the extracellular space is much limited allowing for a high concentration of Glutamate to reach the receptors. Intriguingly, the motility enhancement was putatively dependent on voltage-gated Ca^{2+} channels, whilst a PTx-sensitive G-protein downstream mechanism seemed to be responsible for the inhibition, which prompted the authors to attribute these different processes to two different populations of KARs with different affinities and downstream pathways (Tashiro et al., 2003, Valbuena and Lerma 2016).

Another study investigated the implications of KARs in neurite outgrowth. Marques et al. showed that in dorsal root ganglion neurons (DRG), KARs bidirectionally modify neurite outgrowth. Low concentration of the agonist elicited an enhancement in neurite outgrowth accompanied by a maturation delay, whilst high doses, akin to filopodial

motility, leads to a restricted neuronal outgrowth with stimulation to the maturation of neurons (Marques et al., 2013). It appears in the case of neurite growth, unlike filopodial motility regulation, that a canonical pathway is implicated in the restriction of neuronal outgrowth, while a non-canonical mechanism incorporating CRMP2 protein is liable to the other effect (Marques et al., 2013).

These studies paint quite a picture of a critical role played by KARs during development involving two different scenarios: in an actively developing brain, high-affinity KARs will respond to the low amount of endogenous Glutamate available and promote filopodial motility and neurite outgrowth while putting a cap on neuronal maturation. Once these developing neurons find their targets and establish their connections, low-affinity KARs would come into play limiting the motility and suppressing neurite outgrowth while promoting neurons maturation.

KARs have also been linked to many disorders such as schizophrenia, bipolar disorder, and autism, but the heterogeneous build of these disorders and the likely involvement of many several genes cast a lot of adversaries on a role played by KARs. Some studies reported a change to KAR subunits expression in schizophrenia (Benes et al., 2001, Scarr et al., 2005), while others failed to detect any change (Dracheva et al., 2008). The pitfall of these studies is using mRNA as a proxy for protein expression, which is not always the case; the development of more specific antibodies against KAR subunits can further confirm or refute these findings (Lerma and Marques 2013).

Paddock et al. examined the correlation between a myriad of genetic markers and response to treatment in number of patients diagnosed with major depressive disorder; they reported a new marker in the gene of *GRIK4* that were more abundant in the cases that showed better response to treatment more than the cases that did not, hinting at a role played by KARs in modulating response to certain kinds of depression treatments (Paddock et al., 2007). *GRIK3*, as well, has been linked to major depressive disorder and schizophrenia (see Lerma and Marques 2013 for a review and the references within).

Mice studies lent very useful insights. Genetic ablation of *Grik4* gene in mice gave rise to animals that performed better in tests assessing anxiety and depression-like behavior while manifesting hyperactivity and other hallmarks of schizophrenia and bipolar disorder (Catches et al., 2012, Lowry et al., 2013). These studies imply a protective role for

the lack of *Grik4* gene. However, human studies seem to defy these findings. Pickard et al. identified the disruption of *GRIK4* gene as a risk factor for schizophrenia and learning disability in the Scottish population (Pickard et al., 2006). In a case-control study, the same group reported that a variant within *GRIK4* gene was negatively associated with the risk of developing bipolar disorder (Pickard et al., 2008). An increase in *GRIK4* mRNA (Pickard et al., 2008) and protein (Knight et al., 2012) abundance granting a protective effect against bipolar disorder through increasing GluK4 subunit affluence. Using functional magnetic resonance imaging (fMRI), Whalley and team demonstrated that the same *GRIK4* variant modifies hippocampal function (Whalley et al., 2009). In two healthy groups, there was an increase in the left hippocampal activity during face processing task in the group carrying the protective haplotype which might indicate that the protective role played by *GRIK4* is exerted through modulation of the activity of the hippocampus (Whalley et al., 2009).

This contradiction between mice and human studies might be reconciled by considering the problem of interpreting the readouts of the behavior results rather than a problem of contradictory results. Indeed, in his study, Lowry reported that the knockout animals were suffering from learning and memory deficits (Lowry et al., 2013). On the other hand, some of the behavior tests such as the forced swimming test can be interpreted as a readout of depressive-like behavior rather than a sign of mania Lerma and Marques 2013.

In a genome-wide study, as discussed thoroughly below, Griswold et al. identified several copy number variants (CNVs) in a number of genes that might be implicated in the etiology of ASD (Griswold et al., 2012). Among these genes were *GRIK2* and *GRIK4*, the genes encoding for the subunits GluK2 and GluK4, respectively; *GRIK4* was found to be duplicated *de novo* (Griswold et al., 2012). Recent findings from animal studies lent support to the engagement of duplicated *GRIK4* in ASD.

1.1.1.4. Delta receptors

The fourth and last flavor of iGluRs is the δ receptors (GluDs). They were first discovered by homology screening in the early 1990s and were considered as part of iGluRs superfamily on the basis of the amino acid sequence similarity to other members of iGluRs despite their inability to bind to Glutamate (Yamazaki et al., 1992, Araki et al., 1993, Lomeli et al., 1993). GluDs share the same characteristic modular structure of iGluRs

(Fig. 3C). *GRID1* and *GRID2* genes encode for the two subunits that constitute GluDs, namely GluD1 and GluD2 and they are thought to exist as homomers *in vivo* (Gereau and Swanson 2008). On the account of the lack of known endogenous ligands, GluDs have long been dubbed as "orphan receptors" (Lomeli et al., 1993). The status-quo has since been challenged as two endogenous ligands for GluD2 have been reported; D-serine was found to be able to bind to the LBD of GluD2 in the cerebellum (Kakegawa et al., 2011) and Cbln1 protein to the ATD (Matsuda et al., 2010, Uemura et al., 2010). Endogenous ligands for GluD1 receptors are yet to be discovered, however, D-serine and various members of the Cbln family proteins have been reported to bind to GluD1 receptors *in vitro* (Matsuda et al., 2010, Yasumura et al., 2012). Metabotropic receptors

Until the mid of 1980s, the general consensus in the scientific community was that the actions of Glutamate within the brain are only mediated by means of ligand-gated ion channels. However, this consensus was dramatically changed on the account of the characterization of multiple Glutamate receptors that exert their actions through a second messenger system pathway which later came to be identified as mGluRs (Conn and Pin 1997).

The mGluRs are the second superfamily of Glutamate receptors (Fig. 2). This family of receptors belongs to the most abundant type of receptors in the animal genome, the membrane-bound G-protein-coupled receptors (GPCRs) and more specifically to family C of GPCRs. Unlike ion-gated channels, GPCRs work through a second messenger cascade. Activation of GPCRs upon ligand binding leads to a conformational change that activates the attached G protein which initiates various effects within the cell, modulating many targets such as enzymes or ion channels. GPCRs can be activated not only by neurotransmitters but also are responsive to photons and a multitude of small peptides. Like the rest of GPCRs, mGluRs consist of seven transmembrane domains and an intracellular C-terminal domain. Members of family C of GPCRs are characterized by the presence of an exceptionally large extracellular N-terminal domain harboring the ligand-binding site of the receptor (Fig. 2) (Pin et al., 2003).

Eight types of mGluRs have been identified so far (Fig. 2) with different expression profiles throughout the brain in neuronal cells and glia alike. Based on sequence homology, mGluRs can be broken down into three groups. Group I consists of mGluRs 1 and 5 and predominantly expressed in postsynaptic sites where they tend to modulate neuronal excitability through activation of various ion channels. Conversely, Group II consists of 2

and 3 and Group III of 4,6,7, and 8 and they both mostly localized presynaptically playing an inhibitory role on the release of Glutamate and GABA (Niswender and Conn 2010).

Thanks to genetically modified mice, we now know a plethora of information about the putative functions of mGluRs. Knocking out various types of mGluRs leads to animals suffering from different patterns of anomalies such as abnormal synaptic plasticity, gait problems, learning and memory deficits, anxiety, and depression to name a few (for a review, see Niswender and Conn 2010 and the references therein).

1.2. Glutamate receptors dysfunction

Owing to the critical role GluRs play in the CNS as the major excitatory neurotransmitter, aberrations in the function or development of the glutamatergic synapses can lead to dire consequences cognitively and intellectually (Volk et al., 2015).

A faulty synaptic function has been described in nearly all classes of intellectual disability. In Down Syndrome (DS) for instance, a key regulator of AMAPRs and NMDARs function and expression goes by the name sorting nexin 27 (SNX27) is significantly reduced (Wang et al., 2013, Hussain et al., 2014). Interestingly, mice lacking SNX27 showed diminished glutamatergic synaptic transmission along with total loss of LTP mediated by NMDARs (Wang et al., 2013). The mice which had SNX27 protein level restored exhibited normal synaptic function coupled with normal cognitive functions (Wang et al., 2013). Likewise, in Rett syndrome where the animals that recapitulate the disorder show a diminished glutamatergic synaptic transmission (Dani et al., 2005).

Aside from proteins that affect glutamatergic synaptic function, various mutations in iGluRs subunits have been extensively studied. GluA3 is the most commonly mutated subunit in intellectual disability with mutations in other subunits such as GluA2, Gluk1-4, GluN1, and GluN2A-B have been also described (see Soto et al., 2014 for a detailed review). Despite the lack of direct involvement of mutations in GluRs, the fragile X mental retardation protein (FMRP), the lack of which is responsible for fragile X syndrome (FXS), interact with various synaptic proteins including GluA1 and GluA2 (Volk et al., 2015). Another apparent synaptic dysfunction in the most common inherited form of intellectual disability is the disruption of mGluRs-dependent plasticity as revealed by animal studies (Moretto et al., 2018).

The implication of faulty glutamatergic pathways in schizophrenia has been always challenging to establish. The psychotic symptoms that ensue from the administration of NMDARs antagonists such as ketamine and phencyclidine gave some merit to a model of Glutamate hypofunction in schizophrenia (reviewed in Tsai and Coyle 2002). It is quite undebatable that schizophrenia is a complex disorder with the complicity of multiple gene mutations rendering pinpointing a single gene or a group of genes as a key risk unfeasible. Genome-wide association studies (GWAS) shed some light on multiple Glutamate subunits genes that associated with schizophrenia such as *GRIN2A* and *GRIA1* (Schizophrenia Working Group of the Psychiatric Genomics 2014).

The case with ASD, as detailed below, is quite similar to schizophrenia in terms of the involvement of multiple risk genes. The time window when the symptoms of ASD start to show early in childhood coincides with the period of active synapses formation and maturation (Volk et al., 2015). The majority of genetic cases of ASD can be attributed to mutations in gene families such as *SHANK*, *NLGN*, and *NRXN* (Chaste and Leboyer 2012). These families encode for multiple proteins at the heart of glutamatergic synapses regulation and maturation both pre and postsynaptically (Moretto et al., 2018). Indeed, postmortem studies and ASD animal models confirmed abnormal synaptic density and trafficking (Volk et al., 2015). Disruptions in NMDARs subunits, particularly in GluN2A-B have a prominent role in ASD risk as they can lead to hyperactivation of NMDARs disturbing the delicate balance of excitation/inhibition within the brain circuitry (Burnashev and Szepetowski 2015).

2. Autism Spectrum Disorder (ASD)

Autism spectrum disorder (ASD) is a neurodevelopmental disorder spanning a myriad group of heterogeneous disorders that vary etiologically and clinically with early onset of symptoms, typically in the first two years of life (Health 2018). According to the world health organization (WHO), ASD affects 1 in 160 children globally with more prevalence in boys than girls (Fombonne 2001, Elsabbagh et al., 2012). Recent epidemiologic studies have witnessed a surge in the number of autism cases, which might not reflect an “autism epidemic” as much it reflects an increase of consciousness among professionals as well as among the public of the disease and a widening in the diagnostic criteria (Fombonne 2001, Gernsbacher et al., 2005).

ASD was first described in 1943 by the American psychiatrist, L. Kanner as "a new form of emotional disorder" (Kanner 1943). The illness was simultaneously described by H. Asperger and was referred to as Asperger's syndrome (Asperger 1944).

2.1. Presentation and symptoms

Autism symptoms can be fully described on the basis of three main behavioral symptoms: diminished social interactions, problems in communication with others, and pervasiveness of repetitive behaviors and restricted interests (Miles 2011). These symptoms comprise the constellation of the diagnosis of autism as per the fifth edition of the *diagnostic and statistical manual of mental disorders* (*DSM-V*), the American psychiatric association's guide used to diagnose individuals with mental disorders. The new edition of the DSM guide expanded to include Asperger's syndrome and pervasive development disorder (PDD) under the wider umbrella of ASD. However, different individuals with ASD can have different presentations and different comorbidities and these presentations are amenable to change over the course of life (Werner and Dawson 2005). Such heterogeneity poses a difficulty in terms of diagnosis and treatment of autism.

2.2. Risk factors

Environmental causes have long been considered to be the major culprit behind ASD cases. This perception was not negated until the 1980s when twin studies compared the concurrence of autism in identical and fraternal twins and concluded that there is a major genetic component to autism and it is over 90% heritable (Monaco and Bailey 2001).

Since then, a substantial number of genes have been identified and linked to ASD susceptibility. Genetic causes of autism can be broadly categorized into chromosomal aberrations, single-gene mutations, and CNVs which constitute the majority of the genetic abnormalities pertaining to ASD (Miles 2011). Due to underpowered studies and failure of replication, only two genome-wide chromosomal abnormalities can be considered a risk factor for ASD; one on chromosome 7q35 (Abrahams and Geschwind 2008) and the other on 20p13 (Werling et al., 2014).

CNV is a variation in the chromosomal structure of more than 1K nucleotides. This variation can be common (exists in more than 1% of the population) or rare (in less than 1% of the population), de novo (appears in offspring, but does not exist in parents) or

transmitted (passed from parents to children). A plethora of CNVs risk factors for ASD has been identified including variants at chromosomal regions 1q21, 7q11.23, 15q11-13, 16p11.2, and 22q11.2 (for a review, see Geschwind and State 2015). Albeit considered as risk factors for ASD, these CNVs are considered as risk factors for a number of neurodevelopmental disorders as well including schizophrenia and bipolar disorder to name a few (Malhotra and Sebat 2012).

GWAS studies enabled the identification of multiple genes associated with the development of ASD. *ANK2*, *ARID1B*, *CACNA2D3*, *FOXP1*, *GRIN2B*, and *SCN2A* are examples of such genes with *de novo* mutations (Iossifov et al., 2014). These genes are mainly involved in synaptic transmission and development, action potentials propagation, and chromatin remodeling, especially in the neural cells in the brain (De Rubeis et al., 2014). Of particular interest are genes taking part in the function of glutamatergic synapses. *SHANK* genes family, for example, encodes for multiple scaffolding post-synaptic proteins (Grabrucker et al., 2011). A recent meta-analysis showed that mutations in *SHANK* genes were present in 1% of the cases diagnosed with ASD, with *SHANK3* mutations to be the most prevalent in most cases of ASD and different degrees of mental disability (Leblond et al., 2014). Other genes encode for some of the Glutamate receptor subunits such as *GRID1*, *GRIK2*, and *GRIK4* were also linked to increasing the risk of ASD (Griswold et al., 2012).

Despite the high heritability index, the environmental factors still come into play as a risk factor in developing ASD. Different factors such as activation of the immune system of the pregnant mother due to an infection (Smith et al., 2007), neonatal exposure to neurotoxins (Berman et al., 2007b), or oxidative stress (James et al., 2009) were deeply investigated. Albeit done mostly in mice, these studies shed some light on what might contribute to the development of neurodevelopmental disorders such as ASD.

A recent study conducted on subjects from five different countries and included a little more than two million subjects tried to elucidate the contribution of multiple genetic and non-genetic factors in the development of ASD (Bai et al., 2019). The study unequivocally reported the genetic factors to be the major risk with a huge leap in developing ASD and non-shared environmental factors such as cesarean delivery to come second with a little evidence for a contribution of maternal or shared environmental factors (Bai et al., 2019).

2.3. ASD animal models

Over the years, mouse (*Mus musculus*) emerged as the animal of choice as a model for various diseases through genetic manipulation; stemming from the relative ease of handling and breeding. Genetic manipulation can come in two distinct flavors, disrupting a gene of interest rendering it inoperative (gene knock-out) or the introduction of a desirable mutation or sequence in a particular gene of interest (gene knock-in) (Schroeder et al., 2017). Numerous mice models of ASD were designed over the years by inducing mutations in candidate genes identified in individuals diagnosed with ASD (see above). These models paved the ground for studying the disorder in-depth and enabled testing new treatments.

Trying to model autistic behavioral phenotypes in animal models proved to be a daunting task, owing to the heterogeneity and the variability of these phenotypes and being uniquely human as mentioned previously. On account of the work of several behavioral neuroscientists, we now have a multitude of paradigms examining different aspects of mouse social and communication deficits aiming to mimic those diagnostic hallmarks of humans (Silverman et al., 2010b).

An animal model of autism must satisfy a few criteria to serve as an effective model. These criteria can be summarized into three major points: face validity (replicating symptoms of individuals diagnosed with ASD), construct validity (suffering from the same molecular and anatomical abnormalities as the human subjects), and predictive validity (exhibiting similar outcomes to treatment strategies in terms of symptoms and progression of the ailment) (Crawley 2008).

Different tests are designed to examine different facets of animal behavior. Anxiety and anxiety-like behaviors can be explored using elevated plus-maze (EPM) and light-dark exploration. Tests like Y-maze and open field (OF) tests are designed to assess exploratory behaviors of the animals as well as their locomotion. Motor coordination and locomotion can be further assessed using the rotarod paradigm. Other tests, like the three-chambered social test, try to probe the sociability of the animal, one of the salient impairments in ASD, by introducing a familiar or a novel animal and examine how the already-introduced animal will react (for a review, see Silverman et al., 2010b).

BTBR T/+ *tf/J* (BTBR) inbred strain was reported to lack communication between the two brain hemispheres as a result of corpus callosum absence. Moreover, it suffers from an abnormal reduction in the hippocampal commissure (Wahlsten et al., 2003). Based on behavioral phenotyping, BTBR strain serves as an excellent model of autism; as it displays a myriad of social and communication abnormalities. In particular, diminished social interaction reciprocity as demonstrated by the three-chambered test (Moy et al., 2007, Yang et al., 2007, McFarlane et al., 2008), impaired communication that can be deduced from the unusual ultrasonic vocalization pattern in those animals (Scattoni et al., 2008, Wöhr et al., 2011), and abundance of repetitive behavior manifested from repetitive self-grooming (Yang et al., 2007, McFarlane et al., 2008, Silverman et al., 2010a) recapitulating face validity of the diagnostic features of ASD.

Another promising model is the *Shank3* mutant mice. As mentioned previously, *SHANK and SHANK3* mutations specifically have a high prevalence in ASD cases. Disruption of the *Shank3* gene in mice (knocking-out) led to autistic-like behavior in those animals manifested as abrasions of social interaction and affluence of repetitive behavior such as compulsive self-grooming that might prompt skin lesions (Peça et al., 2011, Wang et al., 2016). Abnormal ultrasonic vocalizations were also observed in *Shank3* mutant mice hinting at atypical communication (Bozdagi et al., 2010, Wang et al., 2016). Wang et al. reported anxiety-like behaviors in those animals demonstrated as reduced locomotion and period spent in the center in the OF paradigm and delayed entrance to the lighted chamber associated with fewer transitions between the light-dark chambers (Wang et al., 2016).

Another prominent example of aberrations in genes implicated in ASD in humans translating into an ASD model in mice in the GluK4^{over} animals. Transgenic animals overexpressing *Grik4* in the forebrain exhibited an aberrant synaptic transmission in addition to a number of behavioral abnormalities such as social impairments and anxiety recapitulating the hallmarks of ASD in humans, prompting to use these animals as a model of ASD (Aller et al., 2015, Arora et al., 2018).

Given the huge evolutionary gulf between humans and rodents, mice models might not be the optimum candidates to recapitulate the intricateness that is the human behavior and higher cognitive functions (Berry-Kravis et al., 2016). A number of non-human primate models have emerged recently modeling different neurodevelopmental disorders aspiring to better describe these disorders (Katsnelson 2018). Interestingly, monkey-models have

also come into play with *SHANK3* as a model of autism. A *SHANK3*-mutant macaque, engineered using CRISPR-Cas9 technology, displayed a wide range of behavioral abnormalities reminiscent of those formerly observed in *Shank3* mutant mice like impaired social interaction, vocalization scarcity, repetitive behavior preponderance, mobility reduction, and abnormal sleeping patterns (Zhou et al., 2019).

3. Magnetic resonance imaging (MRI)

Backed by multiple Nobel prizes and a promise of a sneak peek inside the intact brain, MRI revolutionized not only neuroscience and brain research but also multiple branches of medicine. The idea of nuclear magnetic resonance (NMR), the concept behind all forms of MRI, has developed slowly over the first half of the last century and benefited from the contributions of numerous brilliant scientists such as Pauli, Rabi, Purcell, Bloch, and many more. The concept of resonance, simply put, means that if the spinning frequency (resonant frequency) of the atomic nuclei could be matched by a frequency from an outside magnetic field, the atomic nuclei will absorb energy from the field and move a higher energy level (Fig. 5). The energy emitted as the nuclei go back to their original state forms the basis of the MRI signal (see Huettel et al., 2014). This signal starts off strong and decays over time and how fast this decaying time is, depends on many factors and can vary between tissues and conditions. Of particular interest, is the T_2 and the T_2* times. Measuring these quantities in different conditions and in different tissue types is what is usually described as a contrast, e.g., T_2 or T_2* contrast.

The field of chemistry was the first profiter of the new technique. NMR proved to be an invaluable resource in chemical analyses and understanding the chemical composition of different samples. Probably ensuing from this huge success in chemical analysis, NMR was not deployed in medicine or biology until much later.

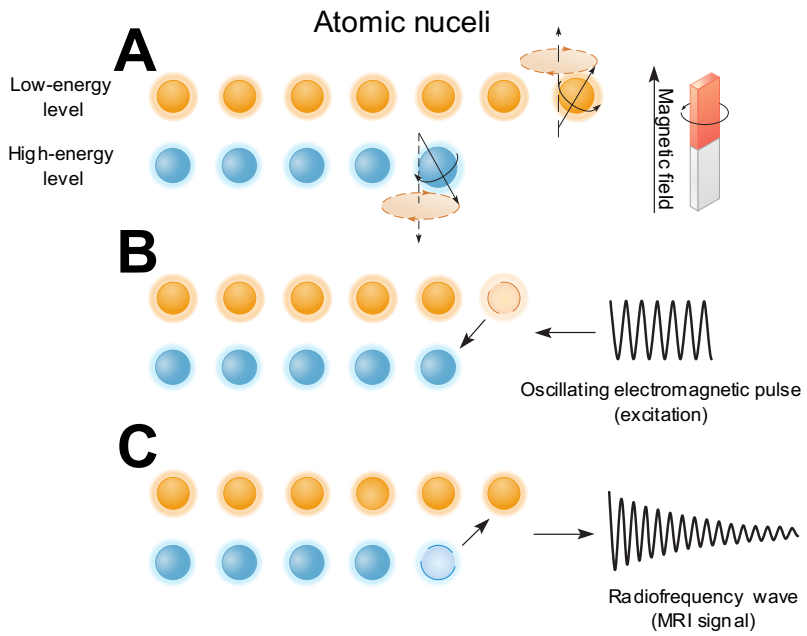

Fig. 5 | Demonstration of the resonance phenomenon. **(A)** Atomic nuclei align themselves in the direction of the constant magnetic field with more atoms occupying low-energy state. **(B)** Upon introducing the electromagnetic pulse oscillating as the same frequency as the spining atoms (resonant frequency), some atoms move to a high-energy level. **(C)** Once the excitation pulse stops, atoms go back to the low-energy level releasing radio-frequency wave (MRI signal) that can be detected (adapted from Huettel et al., 2014).

3.1. Functional magnetic resonance imaging (fMRI)

As already established, until the end of the 20th century the only available way to peek into the human brain's functions was through lucky coincidences as was the case with Broca and Wernicke. The circumstances of Broca, Wernicke, and many others of naturally occurring lesions or injuries contributed dramatically to our knowledge about the inner organization of the brain and its functions. However, these circumstances were far from being the norm and upon the unlikely happening of such coincidences, the damage is usually widespread, far from localized, and altogether hard to interpret.

This limited situation shifted dramatically after the introduction of MRI and further the development of fMRI which gave, in a uniquely elegant way, a mean by which we can look into the brain in action. An appreciation of where the MRI technique and its various modalities stand among other common neuroscience techniques in terms of both the spatial and temporal resolution can be perceived from figure 6.

3.1.1. Origin of the signal

The blood-oxygenation-level dependent (BOLD) contrast forms the basis of most of the functional imaging of the brain while at rest or engaged in a task. It is basically the MRI signal is sensitive to the amount of oxygen in the blood. The magnetic properties of hemoglobin and its variation based on its bounding to oxygen has long been known.

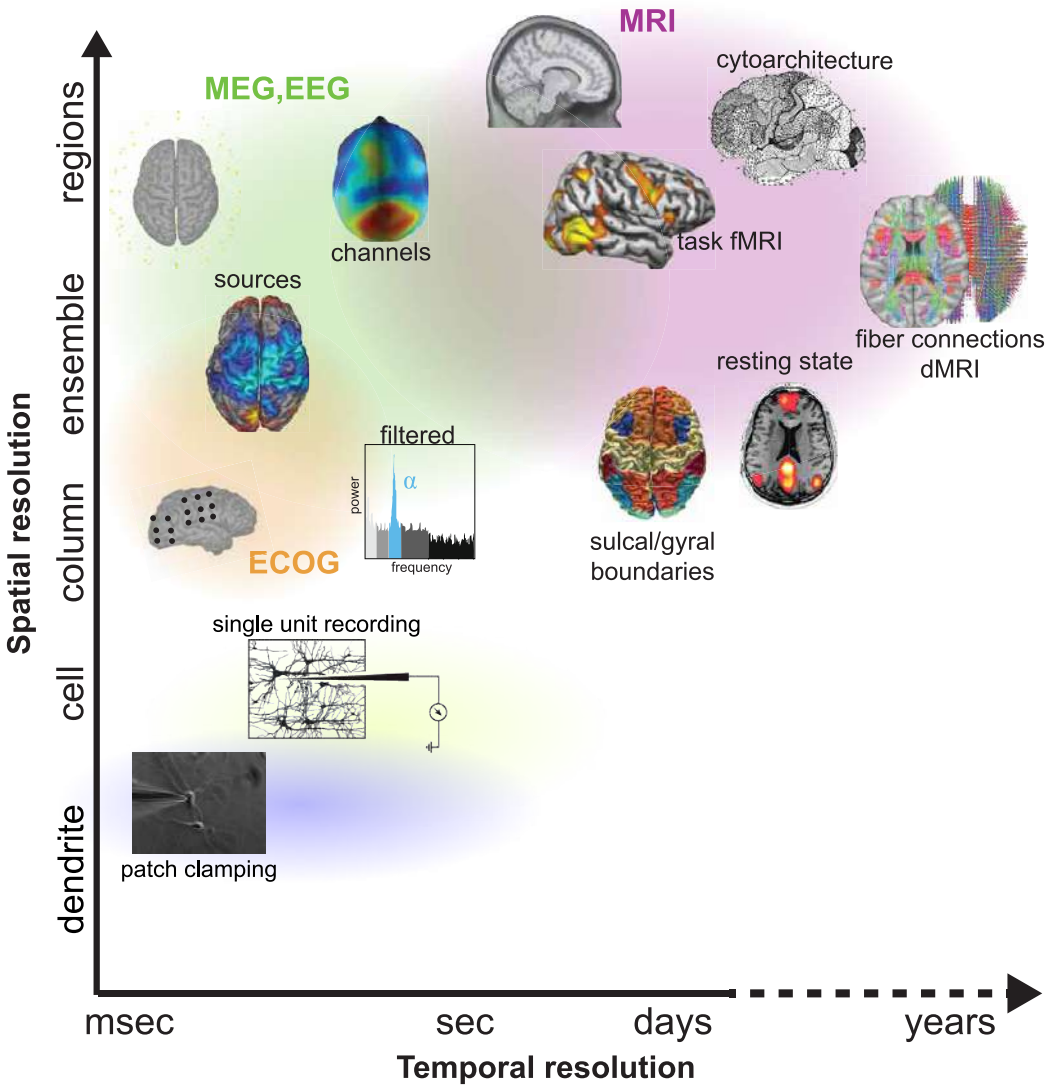

Fig. 6 | Spatial and temporal resolution of different neuroscience techniques. The MRI techniques in general offer a unique spatial and temporal resolution compared to the rest of the tool frequently used to investigate the brain (adapted from Garcia et al., 2018). **Abbreviations:** dMRI, diffusion MRI; ECOG, electrocorticography; EEG, electroencephalography; fMRI, functional MRI; MEG, magnetoencephalography.

The Nobel laureate Pauling and his student Coryell published in 1936 a phenomenal study reporting oxygenated hemoglobin (Hb) to be diamagnetic, i.e., lacking a magnetic moment, while deoxygenated hemoglobin (dHb) was reported to be paramagnetic displaying a considerable magnetic moment with difference of about 20% of their magnetic susceptibility (Pauling and Coryell 1936). These paramagnetic properties were postulated to affect and distort the surrounding magnetic field causing the protons to precess at slightly different frequencies. Thanks to the work of Thulborn and others in the early 1980s, we now know that, indeed, deoxygenated blood leads to a faster decay of the transversal decay of the MRI signal and this decay is more evident the stronger the magnetic field

(Thulborn et al., 1982, Thulborn 2012). These results established, at least in part, that blood oxygenation level could be measured by means of MRI.

Searching for a signal correlates of the physiological conditions in the brain, Seiji Ogawa stumbled across a very intriguing finding (Fig. 7A). He noticed, upon acquiring T_2* contrast (which is particularly sensitive to the protons inhomogeneities), the presence of dark lines in the images of a dead rodent that were never reported before. These lines would disappear when the animal was breathing pure oxygen and started to be apparent once the animal was chocking (Fig. 7A). He speculated, bearing Thulborn earlier work in mind, that these lines were due to magnetic susceptibility around blood vessels due to the paramagnetic properties of the dHb (Ogawa et al., 1990b). Ogawa coined the term BOLD contrast reflecting the fact this contrast was dependent on dHB content of the blood and proposed it as a rival for positron emission tomography (PET) to study brain activity (Ogawa et al., 1990a). He speculated that this contrast is determined by the participation of two factors: the supply through blood flow to the tissue and the demand of oxygen by the tissue as it extracts it from the blood (Ogawa et al., 1990a, Ogawa 2012, Thulborn 2012).

At this point of history, it was known, as a courtesy of the early work of Roy and Sherrington (Roy and Sherrington 1890) and the later meticulous work of Fox and Raichle using PET (Fox and Raichle 1986) that stimulating the brain with an activity leads to an increase in the blood flow. While the cerebral blood flow (CBF) is coupled with a regional increase in the metabolic rate of glucose, it does not show the same rate of coupling with oxygen metabolic rate ($CMRO_2$) (Fox and Raichle 1986, Fox 2012). Ogawa interpreted these findings as a regional activation in the brain would lead to an elevation in the venous blood oxygenation which would lead to a change in magnetic susceptibility due to the paramagnetic dHb prompting to use the BOLD contrast to “map human mental operations” (Fig. 7B) (Ogawa et al., 1992).

Hemodynamic response (HDR) describes the changes in blood oxygenation triggered by neuronal activity that eventually lead to changes in the MR signal that can be captured by the BOLD contrast (Fig. 7C, D).

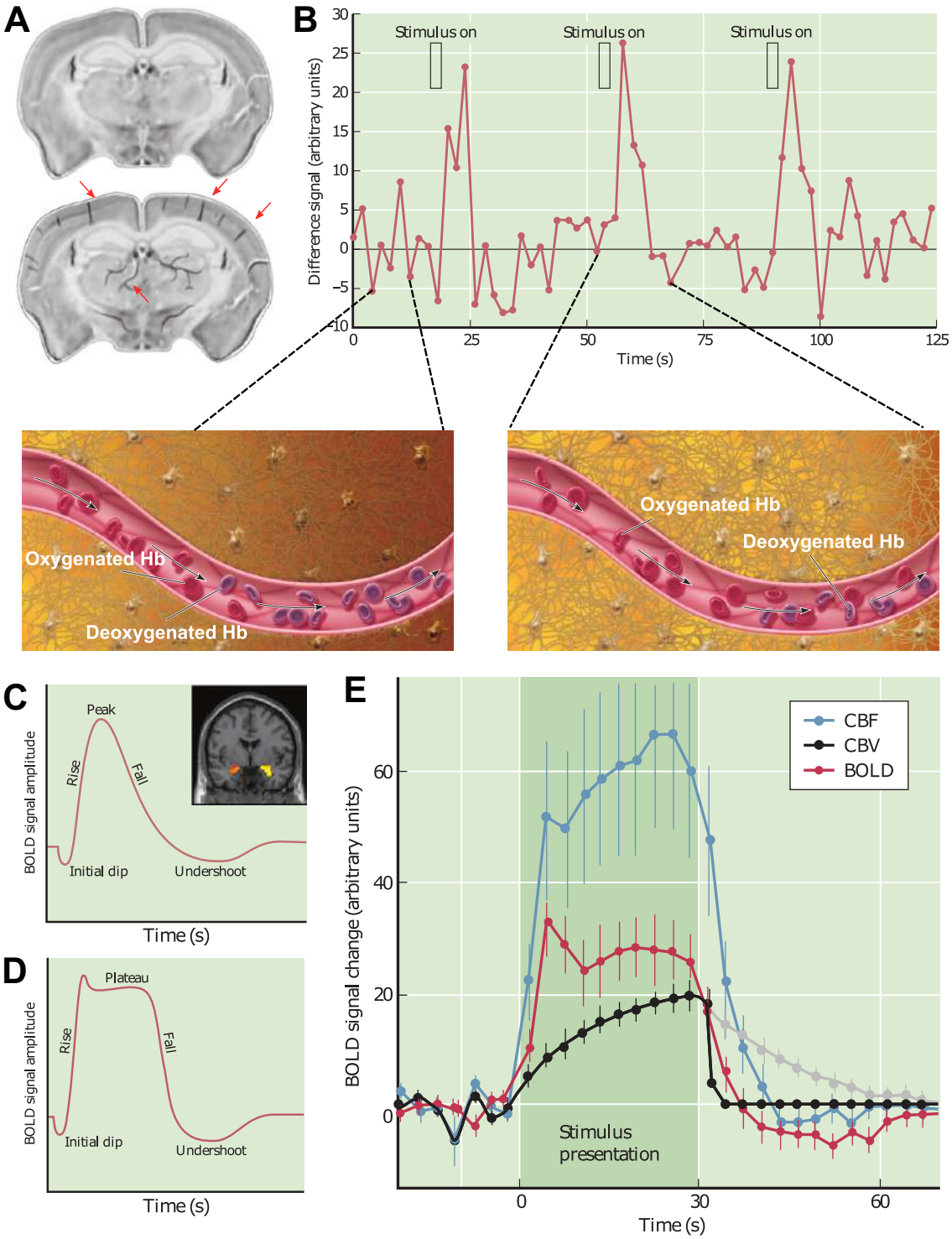

Fig. 7 | Origin the BOLD signal and the hemodynamic response function. (A) Ogawa's observed that dead or asphyxiated rats showed black lines (red arrows) that disappeared upon breathing oxygen. **(B)** BOLD response changes and the accompanying changes in venous blood composition from rest (more deoxygenate Hb) to activity (more oxygenated hemoglobin). **(C, D)** Hemodynamic response function upon stimulation **(C)** and extended stimulation **(D)** and an example of activated brain. **(E)** Comparison of the relative changes in BOLD signal (in red) compared to the cerebral blood volume (in black) and flow (in blue) (adapted from Huettel et al., 2014). **Abbreviations:** BOLD, blood oxygen level-dependent; CBF, cerebral blood flow; CBV, cerebral blood volume; Hb, hemoglobin.

The waveform description of such an event is usually referred to as the hemodynamic response function (HRF). HRF can vary significantly between different brain regions (Handwerker et al., 2004) and from an individual to another (D'Esposito et al., 1999, D'Esposito et al., 2003), however, it is usually described by the canonical double gamma function. This waveform captures the intricate interplay of the CBF, the CBV, and the blood oxygenation in generating the BOLD signal (Fig. 7E).

Following a stimulus, the neurons usually respond in a brief time window of tens of millisecond (Fig. 7B-D), while the HDR is not evident until 1 or 2 seconds later prompting to describe HDR as a sluggish response that lags the events that trigger it (Buxton et al., 1998). Canonically, such a response can be broken down into phases. The response usually starts with an initial dip for 1 to 2 s allegedly due to accumulation of dHb following as the active neurons are extracting oxygen which leads to accumulation of dHb and loss of MR signal prior to the overflow of fresh blood (Fig. 7C) (Buxton et al., 1998). Following this brief dip around 2s after the initial stimulus, the signal starts to increase over the baseline and reaching its maximum value 5 s after the stimulus in what is called the peak. This increase in the signal after the initial dip is corresponding to the increase in the CBF and the CBV providing necessary oxygen to the active zone and washing the dHb and increasing the MR signal as it does so (Fig. 7B, E). This excess or "generous" delivery of oxygen has been speculated as a safety mechanism preventing the neurons from going through hypoxia (Leithner et al., 2009, Leithner and Royl 2014). The signal starts to drop again following the abolishment of the stimulus to a below-baseline level for an extended period of time before it goes back to the pre-stimulus level (Buxton et al., 1998). The post-stimulus undershoot can persist up to 20 s after the stimulus and can be attributed to a myriad of biophysical and metabolic factors.

3.1.2. Neural correlates of task-based fMRI

How these vascular events are correlated with the underlying neuronal activity is known as neurovascular coupling. Neurovascular coupling stands as one of the most significant areas of dispute as it fundamentally affects how we can interpret the fMRI results. The exact nature of the neuronal firing and changes in blood oxygenation is still largely a poorly understood question with no simple answer. However, assembling pointers from different reports that tried to tackle this fundamental issue can paint us a picture or at least a general idea of who those phenomena are correlated. In their tour de force 2001 article,

Logothetis and colleagues investigate the relationship between neural firing and the BOLD signal (Logothetis et al., 2001). They simultaneously recorded single-, multi-unit activity, and local field potential (LFP) along with BOLD fMRI in the visual cortex of anesthetized monkeys (Logothetis et al., 2001). Among these measures, LFP responses were found to provide the best estimate of the BOLD signal; these results prompted the authors to conclude that the BOLD signal unequivocally reflects the underlying neural responses triggered by a stimulus (but see Sirotin and Das 2009, Logothetis 2010) and that the signal reflects incoming input to the active areas and local processing within these areas instead of output spiking activity (Logothetis et al., 2001, Logothetis 2008).

Using the rat cerebellum as a model, Lauritzen and his group conducted a number of thorough studies aiming to elucidate how CBF and $CMRO_2$ correlate with the underlying synaptic activity (for a review, see Lauritzen et al., 2012). They indicated that the hemodynamic signal is context-dependent as it tends to be capricious and more than often unpredictable, for instance in the cerebellum, activation of the Purkinje cell or the inhibitory neurons can lead to a positive BOLD response that might be interpreted as excitation or inhibition (Lauritzen et al., 2012). They also reported different control mechanisms for the CBF and the $CMRO_2$ following a stimulus; the hemodynamic signal can largely be explained by the rise in Ca^{2+} level in neurons and supporting astrocytes, whilst they found that the turnover of ATP better explains the increase in oxygen metabolism (Lauritzen 2005, Lauritzen et al., 2012). Accordingly, the hemodynamic response cannot tell us exactly what is going on the synaptic level, additionally, the dichotomy in the control mechanisms between the CBF and $CMRO_2$ can explain the uncoupling between both of them as previously indicated. Collectively, from all these reports we can safely assume that the BOLD signal nonlinearly captures a certain aspect of synaptic activity and information processing that happen on this level.

3.1.3. Task-based fMRI in ASD

The inherent flexibility of task-based fMRI invigorated the effort to use it as an auxiliary tool in clinical investigation. Based on the task assigned to the subject in question, task-based fMRI can hack into different networks and catch them in action. ASD is an epitome of the abnormalities that task-based fMRI might help in elucidating its etiology and the pathways involved. Based on the symptoms of the patient, an experiment can be designed to investigate a certain system or a network in the brain, especially those responsible for

emotional processing in what is usually referred to as "the social brain" such as the medial prefrontal cortex and the amygdala. Face processing task was the most common paradigm used to investigate ASD as faces represent the most typical social cue. Exposing to faces in neurotypical subjects would elicit activation in various brain areas including the fusiform gyrus, the amygdala, the orbitofrontal cortex, and the superior temporal sulcus (Kanwisher et al., 1997, Grill-Spector et al., 2004). The majority of studies reported a significant hypoactivation in the fusiform gyrus in ASD subjects compared to controls (see for example, Pierce et al., 2001, Pelphrey et al., 2007, Humphreys et al., 2008, Corbett et al., 2009, Hall et al., 2010), while other studies reported normal fusiform gyrus activation in ASD participants (Pierce et al., 2004, Pierce and Redcay 2008, Sterling et al., 2008). The uniqueness of nearly every subject with ASD and the complexity of fMRI, its design, and interpreting the results must be always considered.

3.2. Resting-state fMRI

Up until now, we have discussed the most common type of fMRI, which is often referred to as the task-based fMRI where the subject is sitting inside the scanner and is exposed to a certain stimulus like a visual stimulus or asked to engage in a certain task such as tapping the finger according to a specific paradigm aiming to understand the localization of different functions in the brain. The second flavor of fMRI is the resting-state fMRI (rsfMRI) where the main goal is to understand the coarse network structure of the brain and how these networks communicate with each other.

It has long been appreciated that the brain is never actually at "rest", instead, it is never idle as the brain has to be working constantly to keep the body functions regardless of the observable behavior. The rest in the resting-state is an operational definition where the subject is experiencing a constant condition rather than exposed to a certain stimulus or a behavioral task. The first characterization of resting-state fluctuations came in 1994 by Bharat Biswal in the Medical College of Wisconsin when he noticed a persistent source of noise in his BOLD fMRI data after filtering the respiration and heart rate signal out (for a brief history see, Lowe and Medicine 2010, Biswal 2012). Interestingly, those low-frequency noise signals were showing a pattern of temporal correlation between the left and right sensorimotor cortices (Biswal 2012). He later conducted a more-thorough study using 11 subjects performing motor tasks alternating with periods of no task where the subjects were instructed to try to abstain from particular thoughts or cognitive tasks

(Biswal et al., 1995). Using a low-pass filter with 0.08Hz as a frequency cut-off, Biswal found a strong temporal correlation between the areas of the motor cortex that were active during the motor task in the data of no task (Biswal et al., 1995). This phenomenon of low-frequency spontaneous oscillations was dubbed as resting-state and the temporal correlations were designated to be resting-state functional connectivity (RSFC) (Biswal et al., 1995, Biswal 2012). Those observed correlations were replicated many times by the same group as well as other investigators, albeit with different conditions and analysis methods (Biswal et al., 1997a, Biswal et al., 1997b, Lowe et al., 1998, Xiong et al., 1999, Arfanakis et al., 2000, Li et al., 2000, Lowe et al., 2000, Stein et al., 2000). These connectivity patterns were shown to be highly conserved in other species, for instance Vincent el al. showed patterns of functional connectivity in the brains of anesthetized monkeys (Vincent et al., 2007) and Pawela et al. demonstrated the same in rodents (Pawela et al., 2008).

3.2.1. Resting-state networks (RSNs)

A group of interconnected brain regions is usually referred to as a network and in case the fluctuations of these regions during rest are showing correlations these regions are commonly called an RSN (Fig. 8). In their pursuit to define a “baseline” brain activity level, Raichle et al., using a big pile of human PET data, defined multiple brain regions that exhibited a decrease from the baseline activity in a task-independent manner (Raichle et al., 2001). Based on these findings, the authors posited a default state or mode that the brain exists in absent an attention-taxing task (Raichle et al., 2001). These results were in resemblance to an earlier study done by Binder and team, where the same regions of the brain were more active during rest than during a task, albeit the study was done using rsfMRI (Binder et al., 1999). The pivotal article by Greicius and others demonstrated that most of these regions referred to by the previous studies were in fact correlated during rest (Greicius et al., 2003). Moreover, the study emphasized that these correlations still hold during passive sensory tasks such as visual stimulation (Greicius et al., 2003).

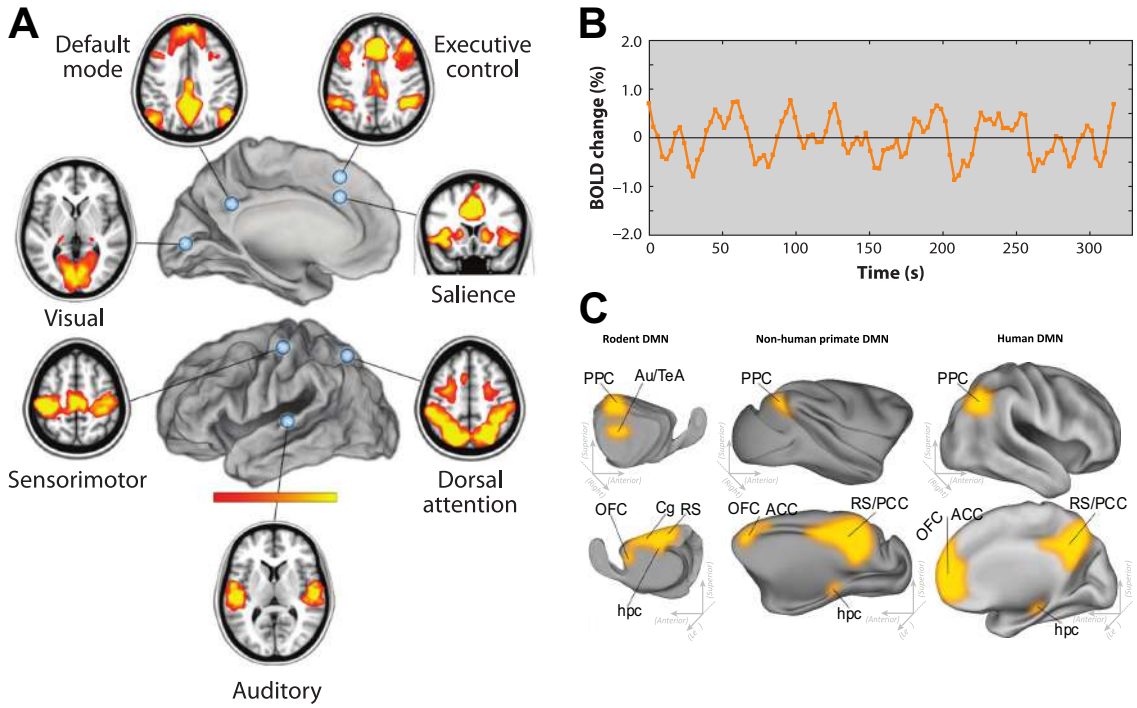

Fig. 8 | Resting-state networks and time-series. (A) Most common resting-state networks displaying functional connectivity patterns. **(B)** Typical time-series averaged over a resting-state network. **(C)** Default mode network in different species overlaid on the brain surface (adapted from Smucny et al., 2014, Raichle 2015). **Abbreviations:** ACC, anterior cingulate cortex; Au/TeA, auditory/temporal association cortex; Cg, cingulate cortex; DMN, default mode network; hpc, hippocampus; OFC, orbitofrontal cortex; PCC, posterior cingulate cortex; PPC, posterior parietal cortex; RS, retrosplenial cortex; RS/PCC, restrosplenial/posterior cingulate cortex.

In the modern literature, the default mode network (DMN) is mostly defined as three major brain areas: the ventromedial prefrontal cortex (vmPFC), the dorsomedial prefrontal cortex (dmPFC), and the posterior cingulate cortex (PCC) and the precuneus plus the lateral parietal cortex (Raichle 2015) which is in great resemblance to studies we have discussed above (Fig. 8C). The robustness of the DMN across studies during consciousness or sedation (Greicius et al., 2008) gave it huge validation and acceptance in the community and spurred the interest to further investigate its functions. Animal studies have further lent validation to the existence of DMN (Fig. 8C) by showing that the network is highly conserved among species such as monkeys (Vincent et al., 2007), cats (Popa et al., 2009), rats (Lu et al., 2012), and mice (Stafford et al., 2014) with a little differences (for a review about DMN, see Buckner et al., 2008, Buckner 2012, Raichle 2015, Buckner and DiNicola 2019).

Interesting as it is, the DMN is not a unique case as more RSNs were identified spanning different cortical and subcortical areas of the gray matter (GM) within the brain. Using a blind source separation method like the independent component analysis (ICA)

(Beckmann and Smith 2004), many statistically independent neural networks with spatio-temporal correlations were isolated such as executive control network, the visual network, the salience network, the sensorimotor network, the dorsal attention network, and the auditory network (Fig. 8A) (Beckmann et al., 2005, De Luca et al., 2006). Interestingly, these RSNs mirrored with a high similarity the networks that get activated during different tasks implying that these networks are always active (Smith et al., 2009).

3.2.2. Neural origin of resting state fMRI

The neural origins of these oscillations are still enigmatic and a hot topic of debate and ongoing research. Nonetheless, a few remarkable efforts are worth mentioning. In the quest to establish blood-related origin to these oscillations, one of Biswal's first experiments demonstrated the temporal correlations and the magnitude of the oscillations were diminished upon exposing a subject to 5% CO_2, which affects CBF and oxygen concentration, and were restored after switching back to normal air-breathing akin to Ogawa's early results of the BOLD signal discussed above Biswal et al., 1997a. Taking advantage of the then-newly introduced arterial spin technique (ASL), Biswal showed that temporal correlations between the two sensorimotor cortices were existent in ASL data as well, albeit to a lower extent, substantiating a direct relationship between these oscillations and the blood flow at least partially (Biswal et al., 1997b).

Aside from the landmark results from Logothetis et al. earlier study discussed previously, which plausibly hold true for spontaneous fluctuations as well, a few groups tried to concomitantly use electroencephalography (EEG) and fMRI to record activity from human subjects during rest (Laufs et al., 2003, Mantini et al., 2007, Scheeringa et al., 2012). EEG measures both the excitatory and the inhibitory potentials of the pyramidal cells perpendicular to the surface of the cortex through the electrical activity that reaches the scalp. These studies reported an association between the activity within some of the RSNs and certain bands of broad EEG frequency spectra indicating that the electrical activity fluctuation in the power of higher frequency might be the electrophysiological correlate of the low-frequency oscillations of the rsfMRI (for a review, see Fox and Raichle 2007, Laufs 2008, Scholvinck et al., 2013, Keilholz 2014). In a recent report, Lake and group managed to record resting-state spontaneous fluctuations along with Ca^{2+} signal from excitatory neurons (Lake et al., 2020). Interestingly enough, they reported that Ca^{2+} signal accounts for at least 30% of the variance of the BOLD resting-state fluctuations.

Furthermore, brain parcellations based on the Ca^{2+} signal was substantially similar to those based on the resting-state signal (Lake et al., 2020). From these studies we can safely conclude that the BOLD spontaneous fluctuations are indeed reflecting brain activity. Which aspect of the brain activity those fluctuations represent exactly remains an open question.

3.2.3. Using fMRI in animal models

The extraordinary success of fMRI in humans spurred the interest to extend it to animals, hoping to take advantage of the advanced genetic manipulation techniques and the feasibility of doing more invasive work and back translate this work to humans (Pan et al., 2015). Animals use has a long history in investigating the mechanisms and neural origins of the neurovascular coupling of the BOLD signal (reviewed in Martin 2014). A big chunk of our knowledge pertaining to the nature and origin of the fMRI signal came from earlier studies in animals (Logothetis et al., 2001, Goense et al., 2012). The dichotomy between how positive and negative BOLD responses emerge were predominantly elucidated through studies done in monkeys (Goense et al., 2012), rats (Rancillac et al., 2006, Devor et al., 2007, Kocharyan et al., 2007, Devor et al., 2008, Enager et al., 2009, Shih et al., 2013), and mice (Huang et al., 1996, Sharp et al., 2015 (reviewed inMartin 2014).

Due to apparent challenges, using task-based fMRI with animals, especially rats and mice, a different paradigm is taking place. Exposing the animal to a sensory stimulus such as electrical stimulation to the paws (Hyder et al., 1994, Ogawa et al., 2000, Van Camp et al., 2005, Devor et al., 2008, Jeffrey-Gauthier et al., 2013), stimulation of the whiskers (Yang et al., 1996, Lu et al., 2004, Chen et al., 2020), flashing lights into the eyes (Van Camp et al., 2006, Niranjan et al., 2016), apply odors (Schafer et al., 2005, Schafer et al., 2006, Reed et al., 2013, Chen et al., 2020), or a sound (Blazquez Freches et al., 2018, Chen et al., 2020). Another popular approach is directly stimulating the desired structure by means of electrical stimulation or through optogenetics tools. Brain stimulation by directly applying an electrical current through MR-compatible electrodes gained substantial popularity in recent years due to its ability to reach deep brain structures that cannot be engaged via simple sensory paradigms. This approach considerably pushed our understanding of circuit connectivity between different brain areas by observing how the signal transferred following applying the stimulation. Using tungsten custom-built electrode, Van Den Berge and co-authors were able to map the connectivity of the striatal output

(Van Den Berge et al., 2017). A remarkable study came from Canals et al. where they, using glass-coated iridium electrodes to stimulate the performant pathway, provided the first evidence ever of LTP using fMRI (Canals et al., 2009). Other studies also successfully used other types of material to craft MR-compatible electrodes such as carbon fiber (Moreno et al., 2016).

Following the optogenetics revolution over the last years (Deisseroth 2011), concomitant use of fMRI combined with optogenetics modulation started to be a mainstream trend in the current literature. In their tour de force article, Lee and team demonstrated for the first time that light stimulation of excitatory neurons infected with channelrhodopsin 2 was, in fact, capable of eliciting a positive BOLD response (Lee et al., 2010).

Drug research benefited tremendously from applying fMRI in animals. By comparing the patterns of brain activity before and after administration of a certain drug, researchers can gather important insights about the effectiveness of the substance in question (Jonckers et al., 2013, Jonckers et al., 2015). Pain and analgesia research particularly has flourished on the awake of animals fMRI due to the widespread of animal models of pain and the feasibility to test how analgesics can alter the pain perception in the brain (see, Borsook and Becerra 2011).

The rsfMRI research in animals got its fair share of attention as well. As we briefed earlier, the DMN was demonstrated to be conserved across different animal species including monkeys (Vincent et al., 2007), rats (Lu et al., 2012), and mice (Stafford et al., 2014). Another interesting aspect of rsfMRI research in animals and specifically in mice is using RSFC to study the different disease models aiming to extract endophenotypes that might be translated back to humans with these conditions. This approach has been successfully employed with models of Alzheimer's disease (Shah et al., 2013, Grandjean et al., 2014b, Zerbi et al., 2014), ASD (Dodero et al., 2013, Squillace et al., 2014, Sforazzini et al., 2016, Liska et al., 2017, Michetti et al., 2017, Bertero et al., 2018, Pagani et al., 2019), and schizophrenia (Errico et al., 2015) (for a review, see Pan et al., 2015, Gozzi and Schwarz 2016).

In summary, fMRI (both the task-based and the resting-state) is an interesting tool for it provides a spectacular insight into the intrinsic activity of the brain and has the potential to make it as an objective diagnostic tool and a clinical biomarker for plenty of brain

disorders, ASD included. However, various hurdles need to be overcome and numerous limitations need to be addressed. Starting from defining minimum requirements for acquisition as it has a profound impact on the results. Despite the reasonable statistical robustness and the consistency of the spatial components, determining the appropriate number of components to which the signal can be decomposed into is far from resolved conflicting (in case of the rsfMRI), the problem is even more extensive when trying to reach a conclusion about a single subject as, to date, there is no standard spatial template of networks to which new subjects can be compared. Because of these issues and more, the analysis pipelines need to be standardized and fully described. On a separate note, if fMRI were to make it into the clinic, the internal physiological mechanism that leads to these oscillations needs to be vividly understood.

3.3. Diffusion MRI (dMRI)

The notion that MRI can be used to give insights about diffusion in tissues on a molecular level is quite old and can be dated back to the 1980s (Le Bihan and Breton 1985, Merboldt et al., 1985, Taylor and Bushell 1985, Le Bihan et al., 1986). Albeit theoretically feasible, the technical difficulties impeded the development of the technique until much later years that witnessed the introduction of higher field strengths (Basser et al., 1994).

The interest in diffusion as a phenomenon can be traced back to Robert Brown when he noticed in 1826 that pollen grains in a water suspension were moving in what seemed to be a random kind of motion (Brown 1828). Being a botanist, he first attributed that kind of "peculiar" motion to biological underpinnings, however, he observed the same pattern in different inanimate and inorganic substances which urged him to refute the biological conjecture (Brown 1828). We now know that the molecules and atoms of substances are in constant motion, colliding with each other, and transfer energy among themselves. Having weaker bonds, molecules of liquids and gases can move more freely than those in the solid-state which can explain why a drop of ink will spread in a glass of water. The mathematical foundations of diffusion were later laid down courtesy of the work done by early prominent scientists such as Adolf Fick (Fick 1855) and much later by Albert Einstein (Einstein 1905, 1956).

3.3.1. The origin of diffusion and how signal is generated

The diffusion of water molecules inside living tissues is the main concern of dMRI (Fig. 9A). Absent obstacles, water molecules will move freely in all directions obstructed only by other molecules. This kind of diffusion is usually called isotropic diffusion (Fig. 9B) and it leads to a Gaussian distribution of particle displacements with a zero mean. A zero mean does not imply lack of displacement, but rather indicates that a molecule is highly likely to circle back to its initial position (Rowe et al., 2016). The deviation from this Gaussian displacement can give us pointers about the geometric characters of the underlying tissue. Isotropic or free diffusion exists only in finite compartments in the brain such as ventricles where the cerebrospinal fluid (CSF) molecules exhibit free diffusion (Fig. 9B). If, on the other hand, those water molecules impeded by a barrier or an obstacle, the diffusion will be restricted or hindered (Fig. 9A). The restricted diffusion depicts a situation where the water molecules are restricted within a barrier that prevents the motion in a particular direction beyond a certain threshold. These conditions can be met in the presence of a barrier such as the cell membrane where the water molecules are trapped intracellularly and can freely move only along the main direction of the cell, but not perpendicular to that direction (Rowe et al., 2016). The extracellular water molecules in the interstitial spaces between cells are subjected to a slightly different regime where they are impeded by obstacles albeit not confined to a certain space as in restricted diffusion. This causes the diffusion to be reduced in certain directions in an obstacle-dependent manner. As opposed to isotropic diffusion when the water molecules are moving along the main axis of a confined compartment such as inside a cell or a cylinder, this kind of directionally dependent diffusion is commonly referred to as “anisotropic diffusion” (Fig. 9B) (Jones 2010, Van Hecke et al., 2015).

3.3.2. Diffusion tensor imaging (DTI)

The tensor model was introduced in 1994 by Peter Basser and team in 1994 and is considered as the most popular model of diffusion (Basser et al., 1994). Despite its simplicity, the tensor model has reasonable acquisition requirements that make it an attractive choice and further outs it on track for adoption in clinical research (Mori and Zhang 2006).

For freely diffusing water molecules such as those in the CSF or in a glass of water where the diffusivity does not depend on the orientation of the tissue, the self-diffusion

coefficient D of water in each 3D cube (voxel) of the brain can simply be calculated using only one diffusion-weighted image (DWI) and one b_0 image (an image with no diffusion) by simply applying the infamous Stejskal-Tanner equation (Stejskal and Tanner 1965).

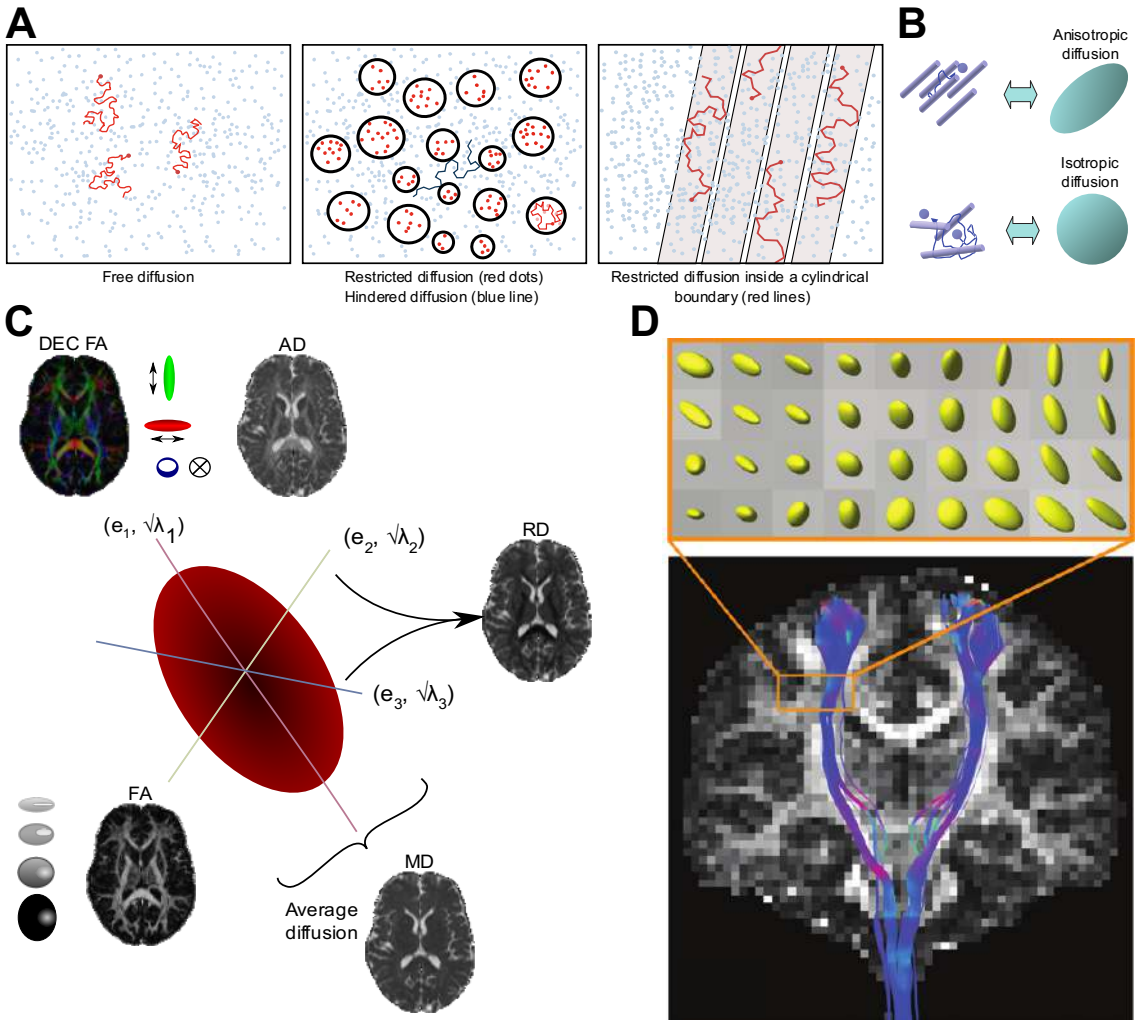

Fig. 9 | Diffusion and diffusion tensor imaging. (A) Different types of diffusion water molecules encounter with different barriers. **(B)** Difference between anisotropic (parallel to the axon) and isotropic diffusion (in all directions). **(C)** Geometric representation of the diffusion tensor as an ellipsoid and its main eigen vectors (e) and values (λ) and the different maps calculated from them. **(D)** Demonstration of fiber tractography and the corresponding shapes of the diffusion ellipsoid (adapted from Mori and Tournier 2013, Van Hecke et al., 2015). **Abbreviations:** AD, axial diffusivity; DEC FA, directionally-encoded color fractional anisotropy; FA, fractional anisotropy; MD, mean diffusivity; RD, radial diffusivity.

While this approximation holds for freely diffusing molecules or along a single axis, in the case of hindered or restricted diffusion in tissues such as the WM, the situation is quite different. Due to the presence of multiple biological obstacles such as proteins and membranes (Fig. 9A), the diffusion tends to be restricted or hindered. In such cases, the diffusion can no longer be fully described by a single coefficient, instead, the apparent diffusion coefficient (ADC) is calculated across multiple since the diffusion in those

circumstances is often anisotropic and depends on the measurement direction (Mori and Tournier 2013).

This anisotropic diffusion will be modeled as an ellipsoid (Fig. 9C) and a tensor D is used to represent such ellipsoid mathematically (Kingsley 2006). The tensor is 3 x 3 symmetric matrix with 6 unique elements, the diagonal elements (D_{xx}, D_{yy}, D_{zz}) represent the ADC across $x, y,$ and z directions and the off-diagonal (D_{xy}, D_{xz}, D_{yz}) elements represent the covariance between pairs of axes (Basser et al., 1994).

3.3.2.1. DTI parametric maps

Using the three eigenvalues we can extract multiple quantitative measurements that can give us insights about some of the microstructural features of the underlying tissue (Fig. 9C). Measures such as mean diffusivity (MD), fractional anisotropy (FA), axial diffusivity (AD), and radial diffusivity (RD) are the forerunners for most used in the literature that employ DTI to study brain structures or abnormalities (Basser 1995). ThMD and the FA are typically reported in most studies. They are not opposite values; however, MD is a measure of the overall diffusivity within each voxel and tends to be higher in regions where the isotropic diffusion is prevalent such as the ventricles (Le Bihan and Johansen-Berg 2012). On the other hand, FA reports the fraction of diffusion that is anisotropic and regions with white matter fibers such as the corpus callosum tend to display bigger FA values (Le Bihan and Johansen-Berg 2012).

Interestingly, combining a directionally-encoded color map of the principal eigenvector with the FA map (DEC FA map) following the same color code can be a very informative and fast way to evaluate the quality of the DTI dataset by simply investigating the main tracts and their directions as encoded by colors (Fig. 9C) (Pajevic and Pierpaoli 1999).

3.3.2.2. Tractography

One more intriguing aspect of using DTI is that we can use the orientation information given by the main eigenvector to reconstruct streamlines representing the WM tracts (Conturo et al., 1999, Jones et al., 1999, Mori et al., 1999, Basser et al., 2000, Lazar et al., 2003, Tournier et al., 2011). The process, famously known as tractography (Fig. 9D), typically starts from a seed point usually defined as a certain voxel in an area of particular interest by building a streamline along the diffusion orientation from both ends (Chung

et al., 2011). The streamline gets updated step by step along the orientation of the principal eigenvector and gets terminated once it reaches a voxel with low anisotropy as represented by a low FA value (Fig. 9D) (Tournier et al., 2011). Different algorithms with various degrees of complexity and different acquisition requirements exist, nonetheless capturing the exact anatomy of the brain using tractography still is a formidable task (Curran et al., 2016). Histological studies of postmortem studies in humans (Stieltjes et al., 2001, Catani et al., 2002) and tracer studies in animals (Parker et al., 2002, Dauguet et al., 2007, Delettre et al., 2019) have shown that tractography can generate tracts that accurately match the underlying anatomy at least in the most prominent tracts (reviewed in Jbabdi and Johansen-Berg 2011).

3.3.2.3. Limitations

Despite its ability to accurately capture some of the innate features of the underlying tissues, the tensor model, like any other model, suffers from a number of limitations. While these shortcomings do not limit the use of the model itself, caution in interpreting the results and using these results to guide further investigation must be deployed (Jones et al., 2013).

The complexity of the brain casts a tremendous challenge for attempts to model any aspect of its processing mathematically. Modeling diffusion using the tensor model, or any other model is no exception as they assume a simpler version of diffusion within the brain that rarely captures the real thing. A case in point is that the tensor model assumes a Gaussian diffusion which appears to be far-fetched even in the coherently oriented main tracts of the white matter due to the presence of many biological barriers. Assuming Gaussian diffusion inherently means that any restricted diffusion will be translated into hindered diffusion (Curran et al., 2016). Moving further from the main tracts such as the corpus callosum where the fibers run mono-directionally, it is hard to encounter fibers running coherently along a single direction as the tensor model assumes. The more realistic situation is that multiple fibers with different and sometimes opposing directions run in each voxel. Another critical drawback in the tensor model is pertaining to the exchange between compartments where the model assumes none. The exchange between intra and extracellular compartments is a continuously occurring phenomenon and water molecules cross the barrier between intra and extracellular compartments constantly leading to

variations in temperature (Jones et al., 2013, Mori and Tournier 2013, Van Hecke et al., 2015).

3.3.3. Other diffusion models

The simplicity of the tensor model and the reasonable acquisition time made it an enticing choice for the sheer majority of dMRI studies. However, other models have also been developed over the years trying to tackle the shortcomings of the tensor model and provide richer information about the brain tissues. Diffusion kurtosis imaging is one of these techniques (Jensen et al., 2005, Lu et al., 2006). While DTI is concerned with modeling the hindered Gaussian diffusion, DKI aims at modeling the deviation from Gaussianity, hence it tries to model the restricted diffusion in the intracellular compartments (Jensen et al., 2005, Lu et al., 2006).

A different kind of models are those try to fit a multi-compartment biophysical model to the diffusion data and try to separate the signal contributions of the intra and extracellular compartments (reviewed in Alexander et al., 2019). The composite hindered and restricted models of diffusion (CHARMED) in its simplest form models the intracellular compartment as impermeable parallel cylinders and the extracellular compartment as a diffusion tensor (Assaf et al., 2004, Assaf and Basser 2005). Other multi-compartment models such as the neurite orientation dispersion and density imaging (NODDI) model the diffusion signal as three compartments namely, the intra and extracellular compartments, and the CSF (Zhang et al., 2012). These correspond to the three distinct types of diffusion observed in the brain: the restricted, the hindered, and the free diffusion. One spectacular feature of the NODDI model is that it models the intracellular diffusion as sticks with zero diameters (Zhang et al., 2012). These models yield many parameter maps that extend far beyond the typical MD and FA maps we get from the tensor model. Some of these measures can be considered as proxies to things such as axon diameter and neurite density.

One major drawback of these advanced models beside the inherent simplicity is that they usually require more demanding data acquisition protocols such as requiring multi-shell acquisition with multiple b-values. These steep acquisition requirements usually translate into longer acquisition time limiting their clinical potential and bound them to preclinical research and animal studies (Alexander et al., 2019).

Another recent advancement in the field of dMRI is extracting metrics from the different fiber populations. This can be considered as moving a few steps further than what the common tractography achieves. By estimating the orientation distributions of the different fiber populations (FODs) withing each voxel (in what came to be known as fixels (Raffelt et al., 2015)), numerous metrics can be calculated. One prominent example of those approaches is the fixel-based analysis (FBA), where we can calculate metrics reflecting the morphological changes in each fiber population within each voxel. Metrics such as fiber density (FD), fiber cross-section (FC), and the combined measure of both (FDC) are all common output to such analysis (Fig. 10). The FD carries information about the intra-axonal volume and the FC is pertaining to the corss-section of those bundles, while the combined measure (the FDC) returns what can be considered as the closest measure to what volume-based morphometry (see below) usually reports (reviewed in Dhollander 2020).

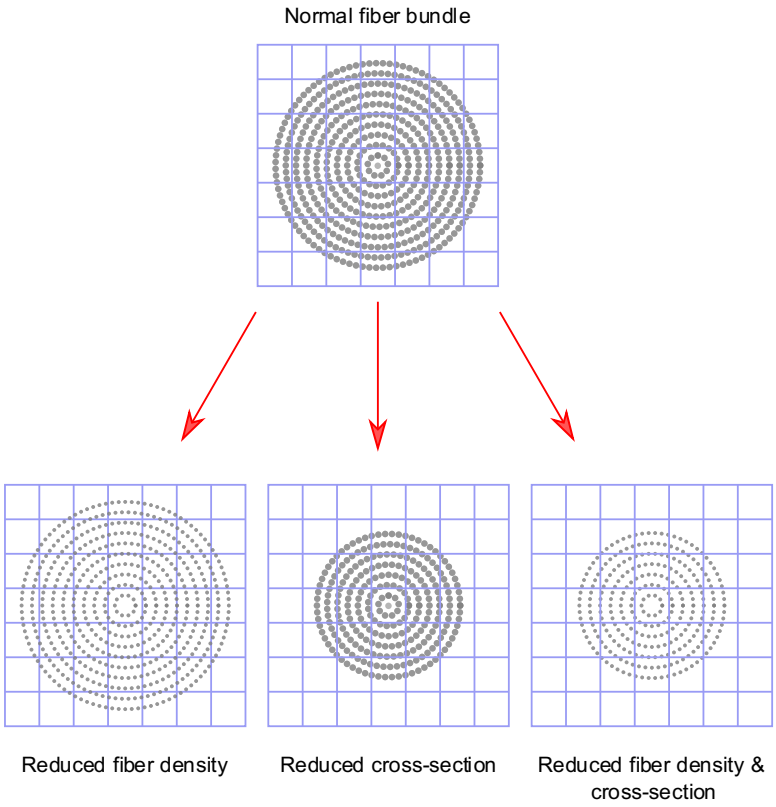

Fig. 10 | Schematic visualization of a horizontal section of a fiber bundle. The changes in the morphology of the bundle can be a red-uction in density, cross-section, or both (adapted from Raffelt et al., 2017).

3.3.4. Clinical applications of dMRI

Given the rich information, dMRI can convey about the microstructure of the brain WM, introducing dMRI to the clinic has been for a long-sought-after goal. DMRI and at the heart of it, DTI has been used in numerous studies to study not only brain abnormalities

and dysfunctions, but also to investigate the plasticity of the brain and in planning surgical procedures by means of tractography (Van Hecke et al., 2015).

DTI has been used extensively in a multitude of psychiatric and neurodevelopmental disorders for instance schizophrenia (Ellison-Wright and Bullmore 2009, Kyriakopoulos and Frangou 2009, Fornito et al., 2012), major depressive disorder , bipolar disorder (Vederine et al., 2011, Emsell et al., 2013a, Emsell et al., 2013b, Emsell et al., 2014, Sarrazin et al., 2014), obsessive-compulsive disorder (Liao et al., 2013), attention deficit hyperactivity disorder (Peterson et al., 2011, van Ewijk et al., 2012), and alcohol use disorder (De Santis et al., 2019). Other studies have focused on demonstrating structural changes following learning using DTI as a way of demonstrating brain plasticity (Blumenfeld-Katzir et al., 2011, Hofstetter et al., 2013). Another promising area of dMRI is aiding in neurosurgical planning. Tractography has been successfully employed in several studies where it was used to delineate important white matter tracts that should be preserved during tumor resection surgeries (Berman et al., 2007a, Kamada et al., 2009, Ohue et al., 2011, Costabile et al., 2019).

The relatively-easy use of dMRI has spurred the interest in the venue of animal models as well, where it is employed alone or along with more-invasive techniques to investigate models of different disorders. Studies in animal models of neurodevelopmental and psychiatric disorders have yielded astounding findings. The DTI and rarely more advanced models have been used to investigate disorders such as Alzheimer's disease (Vanhoutte et al., 2013), Parkinson's disease (Cong et al., 2016), multiple sclerosis (Crombe et al., 2018), Huntington's disease (Xiang et al., 2011), ASD (Ellegood et al., 2011), Alcoholism (De Santis et al., 2019), and schizophrenia (Wu et al., 2016). Deploying dMRI in animal models is still at its infancy but taking big leaps by the day (reviewed in Eed et al., 2020).

3.4. Voxel-based morphometry (VBM)

Human brains share a common global structure, however subtle anatomical differences can still be detected between different populations such as the morphological differences between males and females (Ruigrok et al., 2014). Some ailments have the potential to alter the cortical or the subcortical structures within the brain, changes such as atrophy that can be elucidated in group-level comparison with healthy subjects.

VBM is an unbiased automated technique aiming at detecting those subtle regional changes in the entire brain structure (Wright et al., 1995, Ashburner and Friston 2000, 2001). The technique typically uses anatomical images and it works by bringing all the subjects involved in a given study to the same anatomical space, segment the brain into GM, WM, and CSF , and then uses some parameters extracted from the transformations used in moving each single subject to get a voxel-by-voxel estimation of the volumetric differences between the groups incorporated in the study (Ashburner and Friston 2000, Good et al., 2001). The accuracy and the pragmatic nature of the technique in addition to the safe and non-invasive nature of MRI played a major role in furthering its popularity and adoption in numerous studies (Mechelli et al., 2005, Whitwell 2009).

Well-documented alterations that ensue from the normal aging process (Good et al., 2001) or conditions such as Alzheimer's disease (Karas et al., 2004) and Parkinson's disease (Price et al., 2004) were the prime candidates for investigation using the new technique. Another interesting application of VBM was testing whether learning can lead to tangible structural changes in the brain. A fascinating study was conducted by Maguire and others where they demonstrated that posterior hippocampi in London taxi drivers were significantly bigger than control subjects with this increase in size positively correlated with the years spent as a driver elucidating how spatial learning can lead to structural changes in the gray matter (Maguire et al., 2000).

Comparing the findings of visual and manual inspection to those from VBM showed great correspondence corroborating and validating the technique (Good et al., 2002, Giuliani et al., 2005, Davies et al., 2009, Pergher et al., 2019).

VBM has been for long an important tool in the arsenal of searching for the structural correlates of ASD and other disorders. The vast majority of the literature suggests morphological alterations in tissue structures of ASD subjects, however, the direction of these changes is highly debatable (Chen et al., 2011). One important issue to take into consideration when attempting to interpret these findings is the age group under investigation as studies have compared different age groups from infancy to adolescence all the way to adulthood. By assembling all these findings together, we can deduce that ASD subjects undergo abnormal trajectory of development with cortical and subcortical structures expand early in development and later this development get stalled or the other way around with multiple interaction from other factors such as gender as demonstrated by multiple

meta-analyses (Chen et al., 2011, Via et al., 2011, Haar et al., 2016, Carlisi et al., 2017, van Rooij et al., 2018, Bedford et al., 2019).

4. Aim of the thesis project

The project at hand aimed mainly at exploring the changes that the overexpression of the GluK4 subunit (Aller et al., 2015, Arora et al., 2018) can induce beyond the synaptic and molecular levels. MRI techniques were perfectly suitable to tackle this task. By using the proper modality, different aspects of the brain and brain circuits can be investigated. We employed structural and functional MRI for that end. Moreover, we set out to explore how changes unraveled with MRI, if any, can explain or relate to the behavioral abnormalities.

The specific aims of the work were:

1) To investigate how GluK4 overexpression can change the communication within and between the resting-state networks of the brain.

2) To investigate the effects of GluK4 overexpression on the microstructure of the white matter (WM) fibers.

3) To investigate changes in the volumes of the different brain regions in response to the overexpression induced by the *Grik4* gene.

4) To establish the relationship between the parameters extracted from the MRI analyses and the behavioral metrics extracted from the behavioral tasks.

5) To investigate how the hippocampal neurons respond to electrical stimulation with different frequencies.

6) To investigate how morphological and microstructural changes can affect signal transfer between the brain hemispheres in the transgenic and in the control groups.

II. METHODS

1. Animals

All experimental procedures used in this work have been conducted according to the Spanish and European Union regulations (2010/63/EU) and have been approved by the bioethical committees of the Instituto de Neurociencias de Alicante and the Consejo Superior de Investigaciones Científicas. Mice were group-housed in ventilated cages and maintained in a standard pathogen-free environment with *ad libitum* access to food and water and the cages were weekly changed. The temperature was maintained at 23 °C and humidity at (40-60%) on a 12h light/dark cycle.

Two groups, each consisting of 34 male mice aging between 8-12 weeks were used in all the experiments (Fig. 11). The genotype of the animals in all the experiments was unknown to the experimenter during the acquisition and the initial stages of the data analysis. We used the first group to perform the behavioral tasks and later to acquire the rsfMRI, dMRI, and 3D images (Fig. 12). The second group was further split into two groups; one subgroup was used in the perforant pathway stimulation experiments and the other one in the CA3 experiments.

1.1. Genotyping

DNA extracted from tail samples was used to assess the *Grik4* recombination of wild-type (WT) and GluK4^{over} animals (as described in Aller et al., 2015) using a polymerase chain reaction (PCR) consisting of the following thermal cycle: 3 minutes at 94 °C; 30 seconds at 94 °C, 30 seconds at 62 °C, and 30 seconds at 72 °C repeated for 35 consecutive cycles terminated by 8 minutes at 72 °C.

2. Behavioral tests

Open field (OF) and elevated plus maze (EPM) tests were performed on the first group (34 male mice consisting of 17 GluK4$^{+/+}$ wild-type control and 17 Gluk4^{over} animals).

The OF tests were run by placing each individual mouse in a square arena (50 × 50 cm) illuminated by light bulbs with an intensity of 30 lux for 30 min. The setup for the EPM tests was a cross-shaped metal structure featuring one pair of arms enclosed by 30 cm walls and another pair of open arms, illuminated from the top by a white neon lamp. Each arm was 50 cm tall and 10 cm wide and the experimenter would place the animal in the

10 × 10 cm square that separates the four arms for 10 min. SMART video tracking (Harvard Apparatus) system was used to record the videos of the animals while performing the tests and, for videos of more than one animal, FFmpeg was used to separate them into individual videos with only one animal per video. DeepLabCut (Mathis et al., 2018) was used offline for pose estimation and tracking the animals' movements in each frame. We used 20 frames and 10,000 iterations (20 frames and 50,000 in case of EPM videos) to train the neural networks to detect the lower part of the animal's body. Using the body's *x* and *y* coordinates, we calculated different behavioral metrics such as the distance traveled, the velocity, the time spent in each compartment, and the ratio between time spent in the different compartments as well as maps representing animal's trajectories. The code used for the analysis is available (git repository: https://github.com/amrka/Behavior_OF_EPM/tree/master).

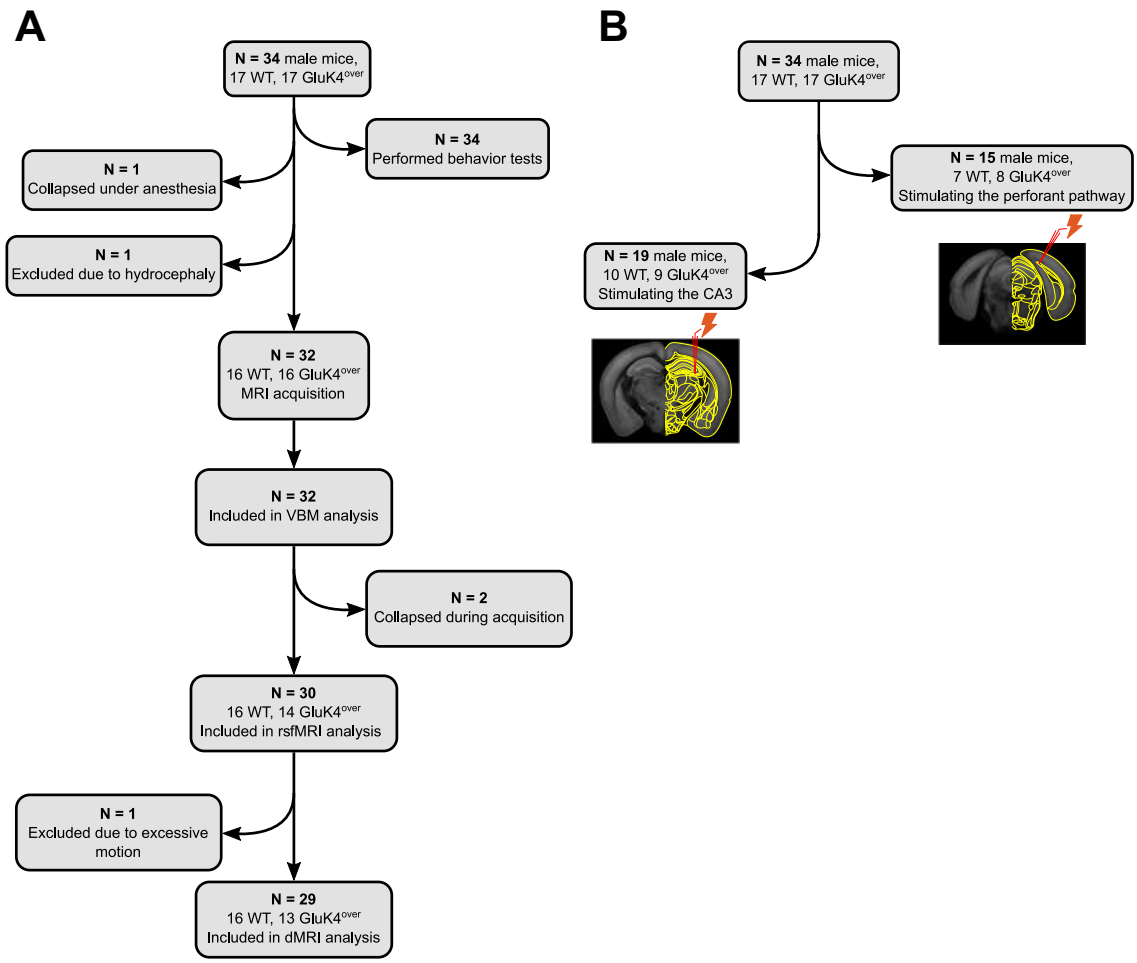

Fig. 11 | Number of animals used in the current project. Two groups (each of 34 mice) were used, split equally between the two genotypes. **(A)** The group of animals used in the behavioral, rsfMRI, dMRI, and VBM experiments. **(B)** The group of animals used for brain stimulation experiments; one subgroup was used to stimulate the perforant pathway and the other one was used to stimulate the CA3 region of the hippocampus. **Abbreviations:** dMRI, diffusion MRI; rsfMRI, resting-state fMRI; VBM, voxel-based morphometry; WT, wild-type.

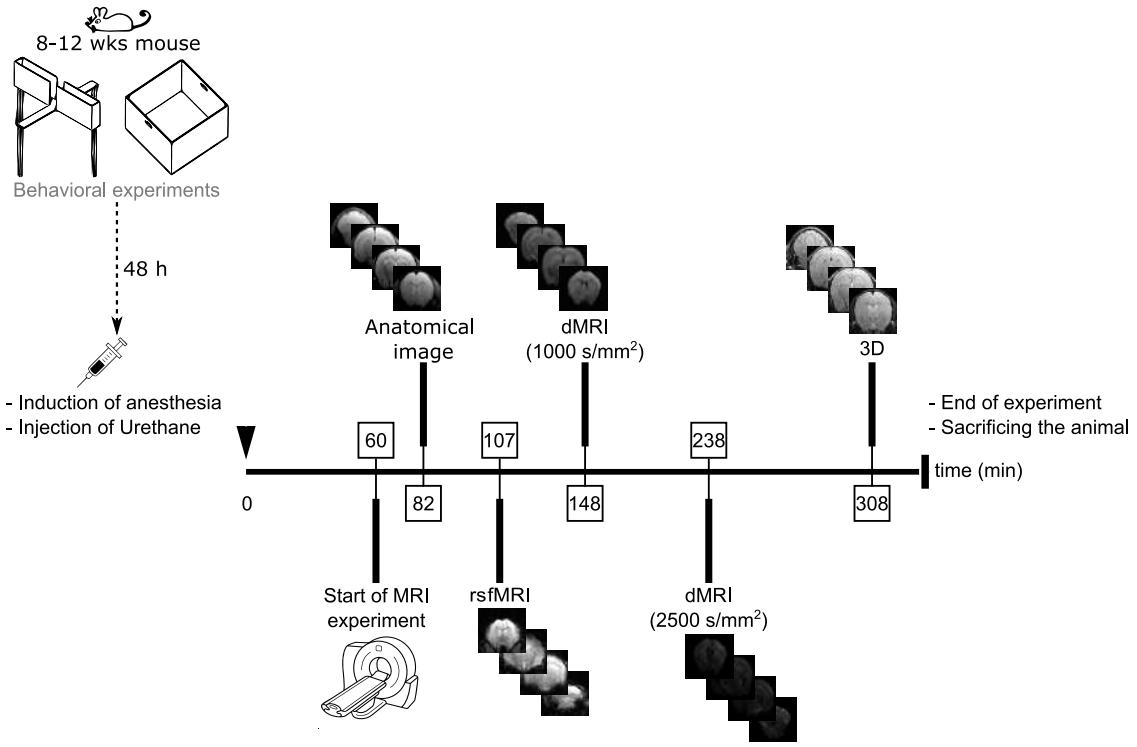

Fig. 12 | Schematic overview of the experimental design. We typically use adult mice aging between 8-12 weeks. The animal would go first through a battery of behavioral tests consists of an open field and an elevated plus-maze test. At least 48 h after performing the behavioral tasks, we inject our anesthetic (urethane) and fix the animal inside the MRI machine. The MRI sequence consists of three modules: resting-state fMRI (along with an anatomical image in the same space), diffusion MRI (2 shells of 1000 s/mm^2 and 2500 s/mm^2), and a 3D volumetric image. The timeline represents the amount of time (in min) that every module consumes. The figure represents a typical acquisition; however, the order of the acquisition might change on occasions, especially, when waiting for the animal's temperature to stabilize. **Abbreviations:** dMRI, diffusion MRI; rsfMRI, resting-state fMRI; wks, weeks.

3. Brain MRI

Animals were anesthetized with 1.2-1.4 g/kg intraperitoneal injection of urethane (U2500, Sigma-Aldrich) divided into two-three doses until the animal losses withdrawal reflexes. The crystals were dissolved in sterile 0.9% normal saline solution warmed to room temperature and mixed until complete dissolution. The solution is usually prepared in bulk and stored at -20 °C in small 2 ml Eppendorf tubes for later use. Urethane was chosen as it is a stable, long-lasting anesthetic and it has a minimal effect on the fMRI signal (Grandjean et al., 2014a, Schlegel et al., 2015). The animal would then be brought down to the MRI facility where its head was fixed to a custom-built holder with MRI-compatible bite and ear bars. The animal was constantly supplied with O_2 through a face-mask. The body temperature was monitored through an anal probe and maintained at 37 ± 0.5 °C by the means of a heating blanket. All the experiments were carried out using a horizontal 7 T MRI scanner with a 30 cm diameter bore (Biospec 70/30, Bruker Medical,

Ettlingen, Germany). All scans were acquired at least 48h after the behavioral experiments.

An additional animal was scanned with agarose gel on the right side of the head to clearly identify the right side from the left side of the brain during data processing due to its magnetic susceptibility and distinctive look in the MRI scans.

3.1. Acquisition protocols

3.1.1. Resting-state fMRI

T_2* images were acquired in 16 coronal slices using a gradient-echo echo-planar imaging (GE-EPI) sequence covering the whole brain with the following parameters: repetition time (TR) of 2000 ms, echo time (TE) of 15 ms, field of view (FOV) of 25 × 25 mm^2, matrix size (MS) of 100 × 100, and slice thickness of 0.8 mm to produce a voxel size of 0.25 × 0.25 × 0.8 mm^3. A total of 750 volumes were acquired consecutively for 25 minutes (Fig. 12). An additional T_2-w anatomical image was acquired in the same space using a rapid acquisition with relaxation enhancement (RARE) sequence with the following parameters: TR of 2500 ms, TE of 14 ms, 6 averages, FOV of 25 × 25 mm^2, MS of 200 × 200, a slice thickness of 0.8 mm to yield a voxel size of 0.125 × 0.125 × 0.8 mm^3. These kinds of acquisitions lasted 22 minutes and 45 seconds.

3.1.2. Diffusion MRI

DWIs were acquired using a 2-shell spin-echo EPI (SE-EPI) sequence across 19 contiguous coronal slices with no gaps to cover the whole brain. The following parameters were employed: TR = 9500 ms, TE = 25.8 ms, diffusion time (Δ) = 15 ms, gradient duration (δ) = 3 ms, flip angle = 90°, number of averages = 6, FOV = 20 × 20 mm^2, MS = 100 × 100, and slice thickness = 0.8 mm to produce a voxel size of 0.2 × 0.2 × 0.8 mm^3. The first shell consisted of 20 noncollinear unique gradient directions with a b-value of 1000 s/mm^2 in addition to 2 images without diffusion gradients (2 b0 images) that mounted to 41 minutes and 48 seconds of acquisition time (Fig. 12). Another 45 unique directions were acquired with a b-value of 2500 s/mm^2 along with 4 b0 images and acquisition time of 1 hour, 33 minutes, and 6 seconds as the second shell.

3.1.3. 3D structural images

Scans of 3D volumetric images were acquired with a RARE sequence with the following parameters: TR = 1000 ms, TE = 46.8 ms, number of averages = 4, FOV = 17 × 11 × 8 mm^3, MS = 170 × 110 × 80, and an isotropic voxel resolution of 0.1 mm^3. The acquisition took 1 hour, 10 minutes, and 24 seconds (Fig. 12).

3.2. Data processing

The analysis was done using multiple tools from FSL 5.0.11 (Jenkinson et al., 2012) (www.fmrib.ox.ac.uk/fsl), SPM (Friston et al., 1994) (www.fil.ion.ucl.ac.uk/spm), AFNI (Cox 1996) (afni.nimh.nih.gov/afni), ANTs (Avants et al., 2011) (http://stnava.github.io/ANTs/), MRtrix3 (Tournier et al., 2019) (https://www.mrtrix.org/), ExploreDTI (Leemans et al., 2009) (https://www.exploredti.com/), Dipy (Garyfallidis et al., 2014) (https://dipy.org/), MDT Python toolbox (Harms et al., 2017) (https://github.com/robbert-harms/MDT), and ITKSnap (Yushkevich et al., 2006) (http://www. itksnap.org/). All the processing workflows were implemented using the Nipype Python library (Gorgolewski et al., 2011) (https://nipype.readthedocs.io/).

The analysis was run on a computer cluster server (Trueno cluster, operated by Comunidad de Cálculo Científico del CSIC, Madrid) running CentOs Linux 7.

Raw data from all modules was converted from Bruker's data format (2dseq) to Nifti format using `pvcpnv.pl` script (https://github.com/matthew-brett/pvconv) then the voxel size was augmented by a factor of 10 to match the human brain's dimension making the usage of the various software feasible.

3.2.1. Resting-state fMRI (git repository: https://github.com/amrka/RS_fMRI_Mice)

The skull tissue was manually removed from the anatomical images using ITKSnap (Yushkevich et al., 2006). The brain-extracted images were then corrected for bias field using the `N4BiasFieldCorrection` ANTs command. The resulting images were then used to create a study based anatomical template using `buildtemplateparallel.sh`. Correction for head motion was done using rigid-body registration of 6 degrees of freedom (dof) to the middle volume using `MCFLIRT` (Jenkinson et al., 2002).

Removing the skull from around the EPI scans was technically challenging. We used one EPI volume from each subject to create an EPI template and the skull was removed manually from this template. The middle volume of each subject was then moved to this template using rigid registration and the back-transformed image was then binarized and used to remove the skull from the motion-corrected images. The images were then blurred to increase the SNR using an in-plane FWHM kernel of 4 × 4 mm as implemented in AFNI's `3dBlurToFWHM` function. Different kernel sizes were tried (such as 3 × 3 mm and 5 × 5 mm), however, we found that 4 × 4 gives the middle ground and the desired level of smoothing with a reasonable ability to distinguish the anatomical features. In order to unify the mean signal level between animals, we normalized the global signal using the following equation:

$$4D\ images * \frac{(1000)}{median\ intensity\ of\ presmoothed\ iamges}$$

High-pass filtering using a cutoff 100 sec was then performed to remove the low-frequency noise and to keep the signal associated with resting-state networks (> 0.01 Hz). To get rid of the noise artifacts that were not filtered out in the high-pass filtering step, the within-subject independent component analysis (ICA) as implemented in FSL's MELODIC was used (Beckmann and Smith 2004). The signal was decomposed into 15, 20, and 25 components to check which number of dimensions capture the resting-state network better. We finally chose the 20 dimensions as we observed that the networks were better reserved and less fragmented using this number of dimensions. The components were then classified as signal or noise manually based on the guidelines outlined by (Zerbi et al., 2015, Griffanti et al., 2017). Briefly, for a component to be considered as a signal it needs to overlap with a known GM structure, to have a smooth time-series, and to have a low-frequency power spectrum. The signal corresponding to the components classified as noise was then regressed out of the functional data.

The middle volume of 4D data that was extracted earlier (see above) was co-registered to the bias-field corrected anatomical images using 6 dof of linear rigid-body transformations (`FLIRT`). The anatomical images were non-linearly registered to the study based anatomical template using ANTs (Fig. 13).

The transformations from the native space to the anatomical space and from the anatomical space to the template space were combined and the filtered functional data of each subject was transformed to the anatomical template to allow combining all the subjects together.

To perform a group-level analysis, the preprocessed 4D images of all subjects were concatenated and group ICA analysis was run using MELODIC. The concatenated data was decomposed into 10, 15, 20, 25, 30, 40, and 50 dimensions. The 20 dimensions decomposition gave the best representation of the resting-state networks (Zerbi et al., 2015). We excluded 3 components that did not overlap with any known network and the rest 17 components were used in further analysis. We then ran the Dual Regression (DR) and used the 2nd stage maps in assessing the within-component connectivity (Nickerson et al., 2017). To assess between-component connectivity strengths, FSLNets was used; normalized full correlation, inverse covariance partial correlation, and partial correlation regularized with Ridge regression (rho = 0.1) between components were calculated (see Smith et al., 2011 for details). The different networks were hierarchically clustered to reveal the internal organization of the networks based on their full correlations and using Ward's clustering method (Thirion et al., 2014).

N.B. all the subject-level operations were done in the EPI's native space and the group-level operations were performed in the space of the anatomical template. Transformations into the high-resolution space was done only for visualization purposes.

3.2.2. Diffusion MRI (git repository: https://github.com/amrka/Diffusion_MRI_Analysis)

The skull was removed from the 1st shell (1000 s/mm^2) by manually drawing a mask around the b0 image of each subject using ITKSnap software (Yushkevich et al., 2006). The data was corrected for Eddy current and motion distortions using `eddy_correct` (FSL) with the first b0 image as a reference and 12 dof (Fig. 14). The diffusion tensor was then fit to each voxel using weighted least squares algorithm as implemented in `dtifit` (FSL). We used the FA maps of all the animals to create a study-based template using `buildtemplateparallel.sh` script (ANTs).

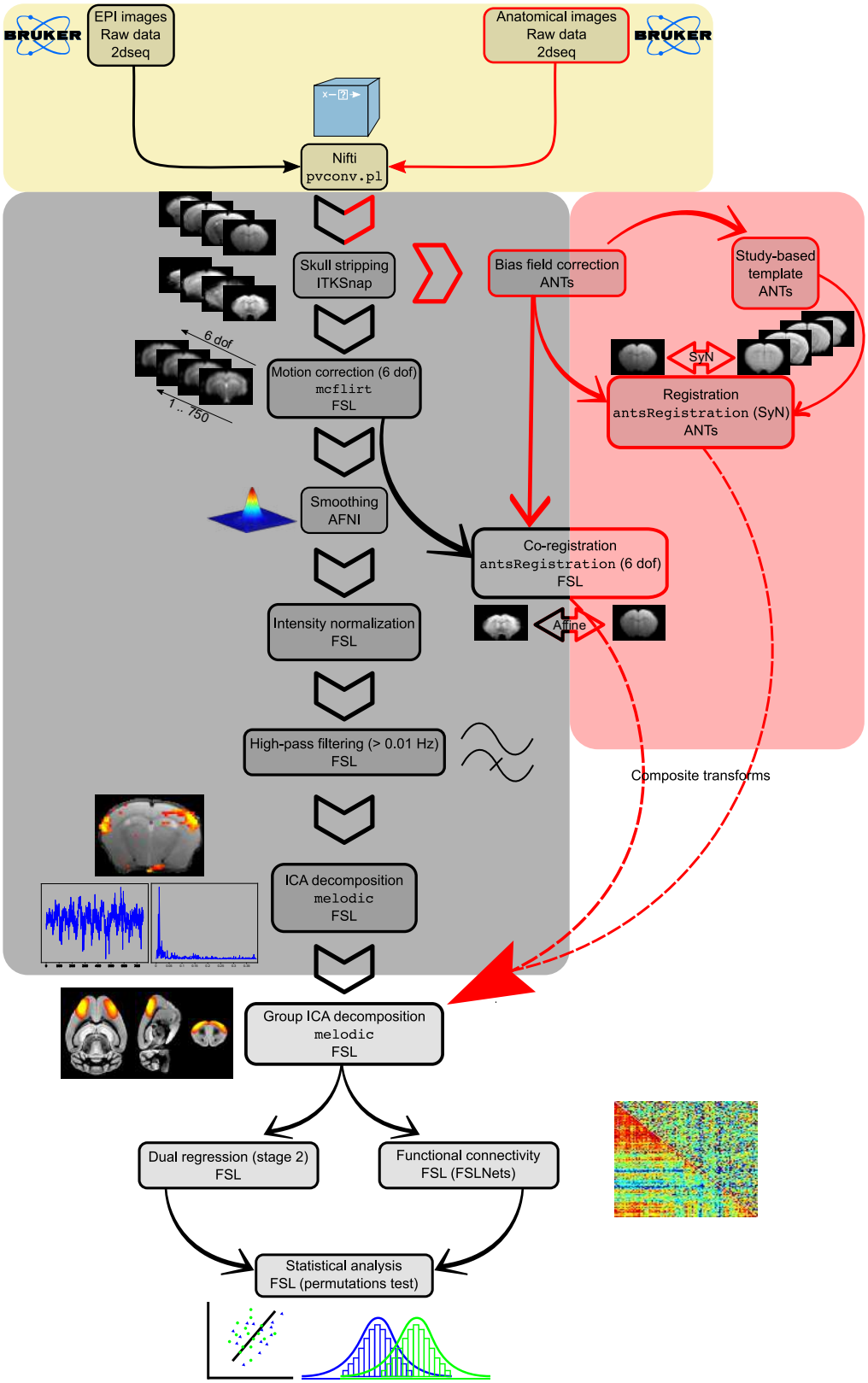

Fig. 13 | Processing of the resting states fMRI data. The pipeline used to process the rsfMRI images with the major steps and packages used. The raw data was transformed from Bruker's format (2dseq) to the more-useful Nifti format. EPI and anatomical images were processed separately and combined in later in the co-registration step. The light-yellow box highlights the initial conversion of the raw data. The light-red and gray boxes delineate the processing steps for the anatomical and the functional scans. **Abbreviations:** dof, degrees of freedom; EPI, echo-planar imaging; ICA, independent component analysis; SyN, symmetrical normalization (non-linear).

The skull was removed from the 2nd shell (2500 s/mm^2) using the same mask previously drawn. The Nifti data from both shells (b = 1000 s/mm^2, b = 2500 s/mm^2) were then combined and corrected for Eddy current distortions using `eddy_correct` (FSL) (Fig. 14). We then proceeded to fit various multi-compartment models to this data as detailed below.

3.2.2.1. Kurtosis

The linear REKINDLE algorithm (Tax et al., 2015) as implemented in ExploreDTI and the RESTORE nonlinear algorithm (Chang et al., 2005) as implemented in dipy were used to estimate the kurtosis tensor voxel-wise in each subject. The kurtosis tensor was later used to calculate a number of parametric maps: FA, MD, AD, RD, kurtosis anisotropy (KA), mean kurtosis (MK), axial kurtosis (AK), radial kurtosis (RK), axonal water fraction (AWF), and tortuosity (tort).

3.2.2.2. NODDI

The NODDI multicompartment model was fit to the data using the NODDI Matlab Toolbox (https://www.nitrc.org/projects/noddi_toolbox). The Gauss-Newton nonlinear algorithm was used for optimization. The orientation dispersion index (ODI) and the neurite density or the intracellular volume fraction (FICVF) were obtained from fitting the model to the data. An ODI study-based template was built as previously using `buildtemplateparallel.sh` instead of using the aforementioned FA study-template on the account of failed attempts of reregistering ODI maps to that template.

3.2.2.3. CHARMED

The MDT python toolbox was used to fit the CHARMED model to the data. The restricted compartment was modeled as two cylinders using the Levenberg-Marquardt as an optimization algorithm. The following maps were calculated from the model: the FA, MD, AD, RD, the restricted fraction (FR), and the intra-axonal diffusivity (IAD).

3.2.2.4. Tract-based spatial statistics (TBSS)

TBSS is a fully-automated voxel-wise whole-brain analysis method that was developed as a mean to address the shortcomings of the VBM-style analysis where registration

misalignments and the unresolved issue of the smoothing kernel size are a common concern (Smith et al., 2006).

Due to some technical challenges imposed by the nature of the mice data, the standard TBSS pipeline could not be followed faithfully (Fig. 14). Our modified pipeline was composed of: (1) the erosion step was emitted as it led to the removal of viable brain tissues. (2) we used the study-based template mentioned earlier as a target for registration. Due to the poor performance of the FSL's native non-linear registration algorithm (FNIRT) on mice data and the proven superiority of the ANTs-SyN registration algorithm (Klein et al., 2009), the latter algorithm was used to non-linearly register the individual FA map to the study based template; (3) a mean image was created from all the registered FA images and this mean image was used to create the WM skeleton; (4) heeding the FSL's developers' recommendation, a threshold of 0.2 was used to create the mean skeleton mask onto which all the FA maps were projected. As for the non-FA maps such as MD, AD, and RD, the transformations from the FA maps to the template were used to move these maps to respective template space. The same FA skeleton mask was again used to project the individual maps. All the different maps generated from fitting (the diffusion tensor, kurtosis tensor, NODDI, and CHARMED) went through the same modified TBSS pipeline.

3.2.2.5. Fixel-based analysis

The processing pipeline was constructed using MRtrix3 version 0.3.91, following the instructions outlined in the software's documentation (https://mrtrix.readthedocs.io; Raffelt et al., 2017). The multi-shell augmented, brain-extracted Nifti images were denoised using `dwidenoise` command and then corrected for Eddy current and motion distortions using FSL's `eddy_correct` as mentioned previously. The response functions for the WM, GM, and CSF were determined using `dwi2repsonse` command employing "dhollander" algorithm. Tissue-specific average response functions were calculated from all subjects using `average_response` command. The individual preprocessed images along with their masks were upsampled to an isotropic resolution of 2 mm^3 (0.2 mm^3 without augmentation). To estimate the WM fiber orientation distribution (FOD) from the average response functions, constrained spherical deconvolution (CSD) was used by invoking the `dwi2fod` command with the multi-shell, multi-tissue CSD (msmt-CSD) algorithm as an argument. A joint bias field correction and global intensity normalization

were then run for each individual FOD with `mtnormalize` command and these FODs were later used to create a population template to which all the individual's FOD was registered (`mrregister`). The brain mask for each subject was brought to the FOD population template and the intersection of those masks was designated as the population template mask; this step is necessary to ensure that any later operation is performed in voxels that contain data from all subjects. A fixel mask for the ODF template was created using `fod2fixel` and a peak value of 0.06; this mask determines the fixels where the statistical analysis will be conducted later and the threshold was chosen based on visual assessment to avoid including gray matter tissues in the analysis and limit our operations to the WM fibers only. However, choosing a higher value such as 0.1, 0.2, or 0.3 removed some of the crossing fibers in some of the WM tracts along with the GM, hence we decided to settle with a rather lower value in spite including some GM tissues in our analysis. The subjects' FODs were then brought to the FOD template space using the transformations calculated previously in the registration step and once in template space, they were segmented using the command `fod2fixel` one more time to identify the fixels apparent fiber density (AFD) or fiber density (FD) for short in each voxel. The fixels of each subject were reoriented using the affine transformations from earlier registration and then matched across subjects and each one of them and the template. This was achieved using the commands `fixelreorient` and `fixelcorrespondence`, respectively. The fixel-based metrics fiber cross-section (FC) and its log (as per MRtrix3 documentation, ensures a Gaussian distribution) were calculated along with the combined measure of fiber density and cross-section (FDC), the output of multiplying the FD and FC in each subject. FBA uses connectivity-based fixel enhancement (CFE) (Raffelt et al., 2017) as an alternative to the FSL's threshold-free cluster enhancement (TFCE) for statistical inference by using the probabilistic global tractography connectivity information. In order to achieve that, we ran a whole-brain global tractography on the population FOD template using `tckgen` with an angle of 215°, a maximum length of 250, a minimum length of 10, a power of 1, and 2 million streamlines produced. In order to reduce the bias in the whole-brain tractogram, `tcksift` command was employed and 200 thousand streamlines that resulted from the operation were used in the subsequent statistical analysis.

3.2.2.6. Tractography and fiber tracts analysis:

ExploreDTI was used to perform a whole-brain deterministic tractography for the multi-shell data using an FA threshold of 0.2, a maximum angle deviation of 30°, step size of 0.1, and a seeding of 2 mm. To extract the corpus callosum (cc) fibers, we used one AND mask and one NOT mask. Briefly, to avoid drawing these masks separately, we used the FA study-based template to draw a cc mask and we used the inverse of the previously-calculated transformations to put this mask in each subject's space and this mask was designated as the AND mask. To prevent the software from including other undesired tracts, we used the rest of the brain as the NOT mask and back-transformed them individually. The resulting cc tracts were checked visually to make sure the desired outcome was obtained. Segmenting the cc tracts to different parts such as the genu, internal capsule, and external capsule was technically challenging, hence we decided to isolate the cc tracts as a single unit. Following the isolation of those tracts, Multiple metrics such as the average tract length. The average values from previous analyses such as FA, MD, ODI, FR, …. were also calculated across the cc tracts.

3.2.3. 3D structural images (https://github.com/amrka/VBM_Mice)

The raw images were converted to Nifti format and the voxel sizes were augmented. Images were corrected for bias field using ANTs. The bias-field corrected images were fed into `buildtemplateparallel.sh` to create a 3D study-based template. Manual segmentation (ITKSnap) was used to remove the skull from the template. The skull-striped template was used then to remove the skull from the individual subjects with `antsBrainExtraction.sh` script.

To avoid creating inaccurate, manually-drawn GM, WM, and CSF priors, we registered our study-based template to the high resolution, Turone mouse brain template and atlas (TMBTA) (Barrière et al., 2020, https://www.nitrc.org/projects /tmbta_2019) using ANTs non-linear registration. We brought the probabilistic GM, WM, and CSF maps to our in-house template using the inverse transformations. Those priors were used for initialization in `Atropos` in segmenting the individual images into the 3 probabilistic maps (Fig. 15).

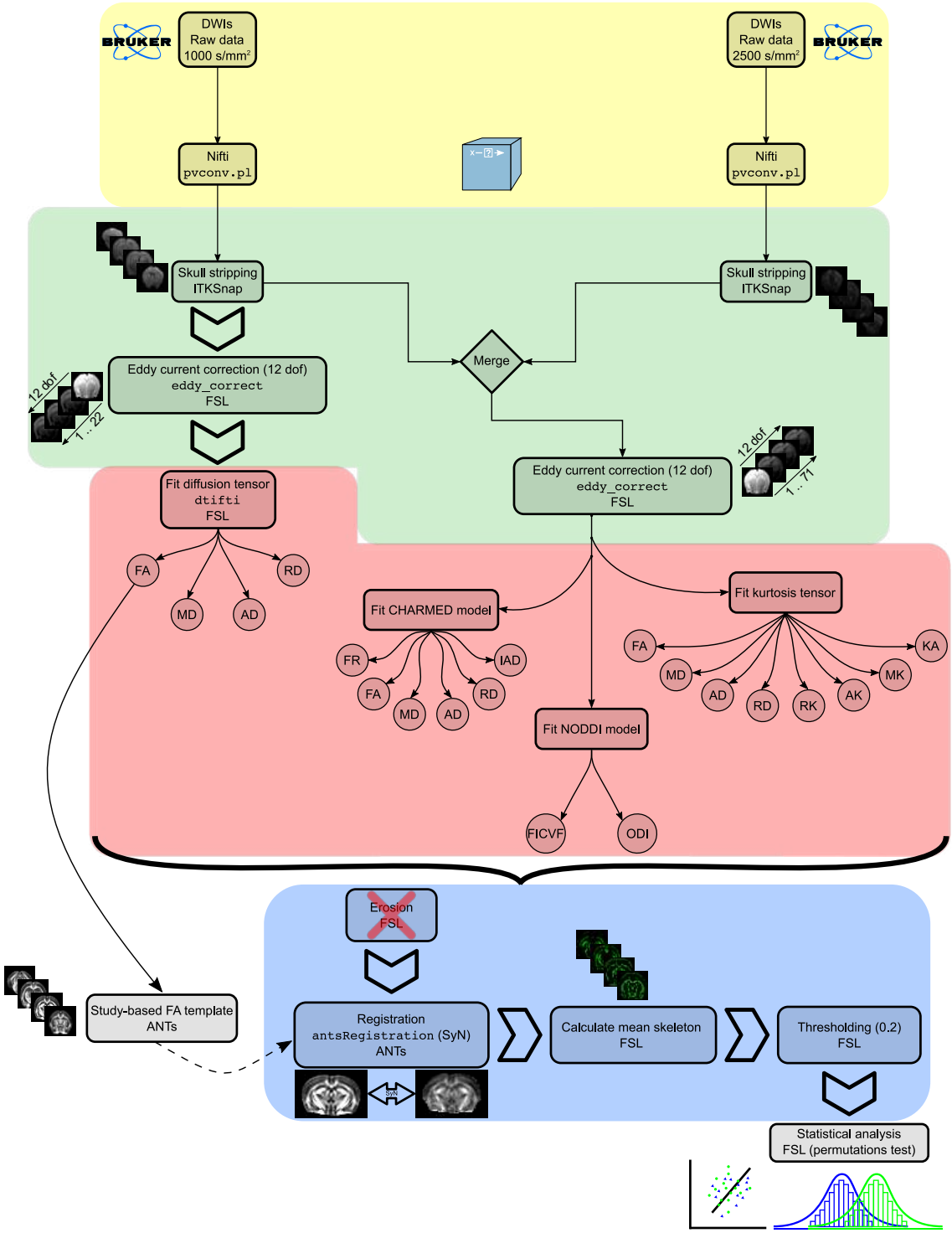

Fig. 14 | Processing of the two shells of the diffusion MRI data. The light-yellow box indicates the initial phase of converting the raw data, the light green one highlights the preprocessing phases, fitting the different models' stage is highlighted in light red. The modified TBSS pipeline in enclosed in light blue with a red cross mark highlighting the step in the original pipeline that was removed in our analysis. **Abbreviations:** AD, axial diffusivity; AK, axial kurtosis; CHARMED, The composite hindered and restricted models of diffusion; dof, degrees of freedom; DWIs, diffusion-weighted images; FA, fractional anisotropy; FICVF, intracellular volume fraction (neurite density); FR, restricted fraction; IAD, intra-axonal diffusivity; KA, kurtosis anisotropy; MD, mean diffusivity; MK, mean kurtosis; NODDI, neurite orientation dispersion and density imaging; ODI, orientation dispersion index; RD, radial diffusivity; RK, radial kurtosis; SyN, symmetrical normalization (non-linear).

The GM maps were modulated by multiplying them by the Jacobian determinants calculated from the registration non-linear warp field only. The modulation is a necessary step to compensate for shrinkage and expansion that might happen during the registration step (Ashburner and Friston 2000). The modulated GM images were then smoothed with an isotropic kernel of 3 mm^3.

Region of interests (ROIs) analysis was done using the structural atlas of the TMBTA template. The labels were back-registered to the native space of each subject and the number of voxels within each ROI was calculated using ANTs' `LabelGeometryMeasures` and used later for statistical analysis (Fig. 15). The volume in mm^3 was calculated for each ROI as the number of voxels * voxel size (0.1 × 0.1 × 0.1).

3.3. Statistical analysis

Of the 34 mice performed the behavioral tasks, 1 animal collapsed upon injecting with urethane and before the MRI acquisition session. Another animal displayed a hydrocephalic brain and was excluded from the analysis. Due to excessive motion that could not be corrected, an extra animal was excluded from the dMRI data processing and subsequent statistical analysis. Two mice collapsed during the acquisition session and their rsfMRI and dMRI scans were not considered (Fig. 11). This finally mounted to the inclusion of the data from 30 animals in the rsfMRI analysis (16 WT, 14 $Gluk4^{over}$), 29 mice in the dMRI analysis (16 WT, 13 $Gluk4^{over}$), and 32 in the 3D images analysis (16 WT, 16 $Gluk4^{over}$).

We generated design matrices to assess the genotype effect between the two groups. Voxel-wise statistical analyses for the 2^{nd} stage maps of the DR, FSLNets, TBSS, and VBM were done using the nonparametric permutations test as implemented in FSL's `palm` (Winkler et al., 2016). The analyses were done using 10,000 permutations (5,000 for DR), TFCE-enhancement, and family-wise error rate (FWER) correction for multiple comparisons. DR results were further corrected across modalities (considering different ICA components as modalities). *P* values < 0.05 were deemed significant. Fixel-wise FD, log (FC), and FDC statistical inferences were done using 10,000 permutations as well with CFE enhancement and FWER correction for multiple comparisons (`fixelcfestats`).

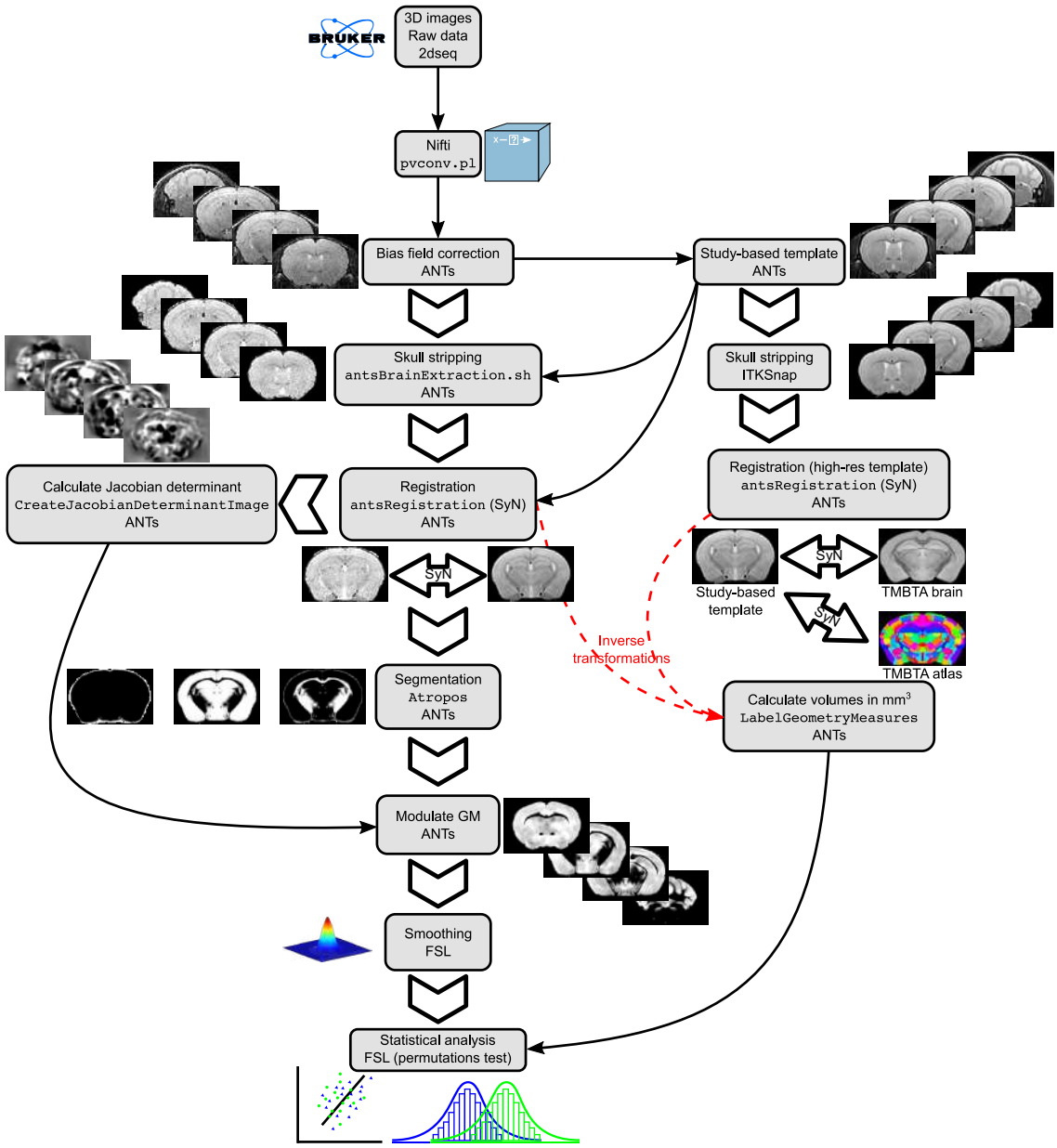

Fig. 15 | Processing of the structural 3D images. The figure represents the major steps used in the voxel-based morphometry analysis. After converting the raw data into Nifti and removing the skull, the study-based template was registered to the TMBTA high-resolution template and the template's priors were brought to the study-template space to be used in individual subject's segmentation. The gray matters were modulated by the Jacobian determinants calculated from the warp field of the non-linear transformations. **Abbreviations:** GM, gray matter; SyN, symmetrical normalization (non-linear); TMBTA, the Turone mouse brain template and atlas.

Voxel-wise Pearson correlation coefficients between DR, skeletonized dMRI, and modulated GM maps and the different parameters extracted from behavioral videos. The between-networks connectivity correlation with the behavioral parameters were also assessed in the same manner. To calculate how significant the coefficients are, we performed a one-sample t-test using 10,000 permutations (5,000 for DR maps), TFCE enhancement, and FWER correction for multiple comparisons.

For visualization purposes, the anatomical and the 3D study-based templates were both registered to a down-sampled version (0.03 mm^3) of the Australian mouse brain mapping consortium (AMBMC) and the transformations were used to bring the statistical maps to the AMBMC space (http://www. imaging.org.au/AMBMC). Statistical maps resulted from the dMRI analyses were displayed on the FOD template. Statistical maps with significant values were displayed as 1- *P* values (hence the higher, the more significant).

To compare the average values calculated from the cc fiber tracts in dMRI maps, multiple independent t-tests were done using the nonparametric permutation test and 10,000 permutations. Values below *P* value of 0.05 were considered significant. Raincloud plots (Allen et al., 2019) were used to display the data.

In the case of 3D images, we performed a whole-brain ROI analysis using TMBTA atlas regions. We used 10,000 permutations and FWER corrected the results for multiple comparisons across the whole brain regions.

4. Stimulation experiments

4.1. Animals

A separate batch of 34 animals was used for the stimulation experiments (Fig. 11). For the perforant pathway stimulation experiments, 7 wild-type males and 8 GluK4^{over} males; for the CA3 stimulation, 10 wild-type males and 9 GluK4^{over} males were used. Two experiments were done featuring applying intracerebral electrical microstimulation to the perforant pathway and to the CA3 region of the hippocampus. T_2* images were recorded during electrical stimulation applied using MRI-compatible carbon-fiber glass electrodes.

4.2. Fabrication of the electrodes

Electrical current was applied using bipolar carbon-fiber glass electrodes (Shyu et al., 2004, Moreno et al., 2016, Perez-Cervera et al., 2018). Carbon-fiber threads (Goodfellow Cambridge Limited, England) of 7 μm diameter were bundled together and carefully inserted into both sides of a theta-shaped glass capillary (World Precision Instruments). Each pipette is pulled to produce a tip diameter of 200 μm and a resistance of 40–65 kΩ (Fig. 16D) depending on the structure to which electrical stimulation is going to be applied. Regular copper wire is then attached to the carbon fibers of both sides using

conducting silver epoxy resin (RS Components, Spain). The attachment points are then isolated with a clear nonconducting epoxy resin. The tip of the electrode is then bent by heating to produce a right angle with the electrode's body. The electrodes were inserted using a stereotaxic frame into the desired structure and fixed to the skull with dental cement. Toothpaste was used to cover the exposed part of the skull in order to minimize the signal loss due to magnetic susceptibility. The electrodes were positioned in the perforant pathway at 4.2 mm anterior-posteriorly, 15 mm medio-laterally from Bregma, and 1.2 mm vertically from the skull surface (Fig. 16A). To target the CA3 region, the electrodes were placed at 1.9 mm anterior-posteriorly, 16 medio-laterally from Bregma, and 115 vertically from the skull surface (Fig. 16B). Experiments were performed using urethane anesthesia (see above). The places of the electrodes in both experiments were confirmed by the presence of the electrode's artifact in the anatomical image acquired along with the functional scans.

4.3. Stimulation protocols

Multiple stimulation protocols were used in stimulating both structures. Each protocol consists of different stimulation (5, 10, 20, 40 Hz) frequency of 800 μAmp and 4s of stimulation. For each frequency, 3 consecutive runs of 150 volumes of fMRI each were acquired such that every 30s there is a 4s electrical stimulus mounting up to 10 trains of stimulation per run starting with the lowest frequency (Fig. 16). An anatomical image was acquired for each animal before collecting the functional scans. The electrical stimulations were applied through the carbon-fiber electrodes using a constant current source and a pulse generator (STG2004, Multichannel Systems, Reutlingen, Germany). The fMRI and the anatomical images were acquired using the same parameters employed in acquiring the resting-state and their anatomical images (see above).

4.4. Processing and statistical analysis (git repository: https://github.com/amrka/stimulation_perforant_pathway, *_CA3)

The same preprocessing pipeline that we used for preprocessing the rsfMRI data and the anatomical images were deployed with the stimulation scans. A minor distinction was the omission of the ICA cleaning step (Fig. 13). The statistical analysis was done on three-levels. The stimulation boxcar was convolved with the traditional double-gamma hemodynamic response function (HRF) to produce the predicted response (the regressor). The

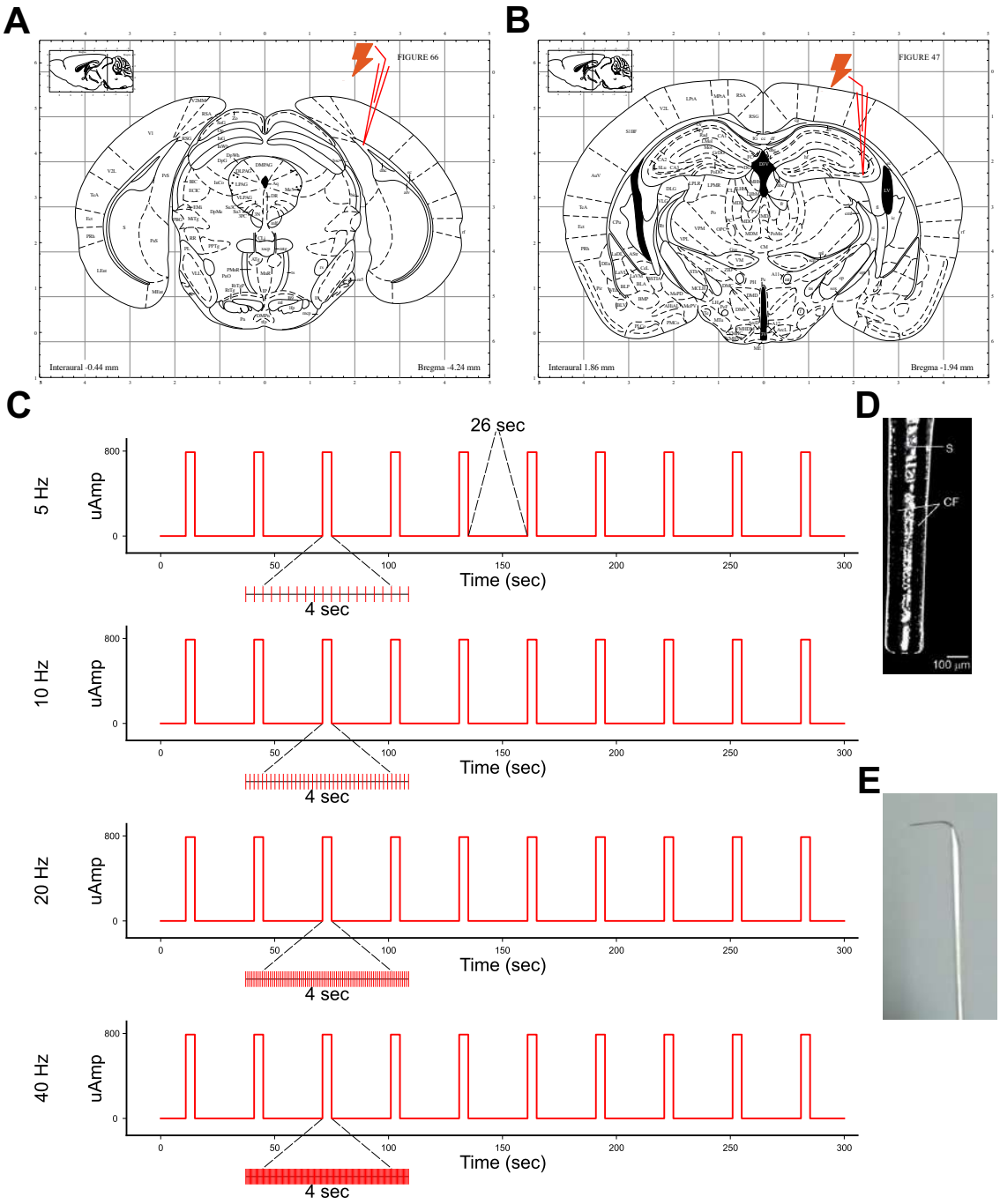

Fig. 16 | Experimental design of the stimulation experiments. (A, B) show the place of the stimulation electrode in the stereotaxic coordinates of Paxinos and Franklin (Paxinos and Franklin 2004); (**A)** in the perforant pathway at 4.2 mm posterior to the Bregma, (**B)** in the CA3 region of the hippocampus at 1.9 mm posterior to the Bregma. (**C)** Shows the stimulation protocol with the different frequencies used (5, 10, 20, and 40 Hz). Each stimulation cycle consists of 4 sec of stimulation and 26 of rest for a total of 10 cycles (300 sec) per run. (**D)** Micrograph of most anterior part (the tip) of the bipolar glass electrode showing the two threads of carbon fiber separated by borosilicate glass septum (adapted from Moreno et al., 2016). **(E)** A picture of upper part of the glass electrode. **Abbreviations,** CF, carbon fiber; S, septum.

high-pass filtered functional time-series of each frequency were then fit to the regressor in a voxel-wise manner using `film_gls` (FSL). An experiment would be deemed successful and later incorporated in higher levels of analysis if there is an activation in any

frequency. For this lower level of analysis, Z (Gaussianised T) statistic images were clustered using a threshold of $Z > 2.3$ and a cluster significance threshold of $p < .05$ corrected for the whole brain using Gaussian random fields theory (GRFT). In the second-level of analysis, the three runs of each frequency were mixed for each subject using a fixed-effects model and using a cluster threshold > 2.3 and significance level < 0.05 corrected for the whole brain using GRFT (`flameo`). The third-level or group-level analysis comprised of a mixed-effect model (`flameo`) with a cluster threshold > 3.1 (following the recommendations of Eklund et al., 2016) and a significance level < 0.05 with GRFT correction for the whole-brain analysis. Two one-sample t-tests were performed to test the positive and negative activation of each group and two two-sample t-tests were performed to compare the two groups. We used the same study-based template previously constructed as a target for group comparisons and the same template was registered to the AMBMC model for better visualization.

The percentage change in the BOLD signal was calculated in each animal using a hippocampus mask extracted from the TMBTA atlas and registered back to each subject's space. The signal was scaled by the regressor height and divided by the mean signal. The average signal in the hippocampus across all sessions was averaged across all animals in each group. The final signal was smoothed using a sliding window of the size of 5.

III. RESULTS

1. Animals description

Two groups of animals performed the OF and EPM behavior tasks and were later scanned using MRI. The first group consisted of 17 wild-type animals, the second group consisted of 17 previously generated (Aller et al., 2015, Arora et al., 2018) Grik4^{over} transgenic animals. Those animals overexpress *Grik4*, the gene responsible for encoding the KA high-affinity subunit, GluK4. The majority of this overexpression happens in the fore-brain regions leading to multiple synaptic anomalies (Aller et al., 2015). The animals were between. 10-12 weeks at the time of performing the behavioral tasks with no signif-icant weight difference between the two groups. Of the 34 animals that performed the OF and EPM tests, 3 animals died as a result of the anesthesia, one animal was excluded on the account of having a hydrocephalic brain, and another animal's scans were removed due to excessive head motion during DWIs acquisition that could not be rectified. This brought the final tally of the animals' data that was analyzed to (32 animals in case of VBM analysis, 30 for rsfMRI analysis, and 29 in dMRI analysis).

1.1. Tracking and pose estimation

In order to investigate how different behavioral phenotypes are correlated with the MRI data, we started by allowing the animals to perform two standard behavioral tasks, namely the OF and the EPM tasks. We collected footages of each animal performing 30 mins of OF and 10 mins of EPM and used DeepLabCut (Mathis et al., 2018) to track the animals and later we used this tracking information to extract plenty of information such as the animal's speed, the average distance traveled, and preferences in terms of corners to name a few. Even though we used rather mild parameters to perform the training of the neural nets (30 frames and 50,000 iterations in case of the OF task and 20 frames and only 10,000 iterations for the EPM task), the tracking was quite seamless (Fig. 17). The neural nets were able to identify the animals even in situations (e.g. around the corners) where only parts of the animal are visible. This tracking was also uninterrupted by the mild shadow that can be cast by the edges of the box in case of the arena in the OF task or the reflections of the animal on the smooth, polished surface of the closed arm internal walls in the EPM device. Compared to our previous experiences with tracking software that uses segmen-tation algorithms, using DeepLabcut seems to be superior in almost every way posing only the challenge of the steep computational resources that sometimes might be required.

We designed an in-house algorithm to extract the metrics from the *x* and *y* coordinates in each frame that resulted from performing the tracking. Our code is completely data-driven and does not require any extra input from the user rather than the tracked element's coordinates (Fig. 17). For example, in the OF arena, the code will automatically divide the arena into four corners and a middle sector and separate the frames that belong to each sector (Fig. 17B). Similarly, the code will separate the EPM arena into two closed arms, a center, and two open arms (Fig. 17D).

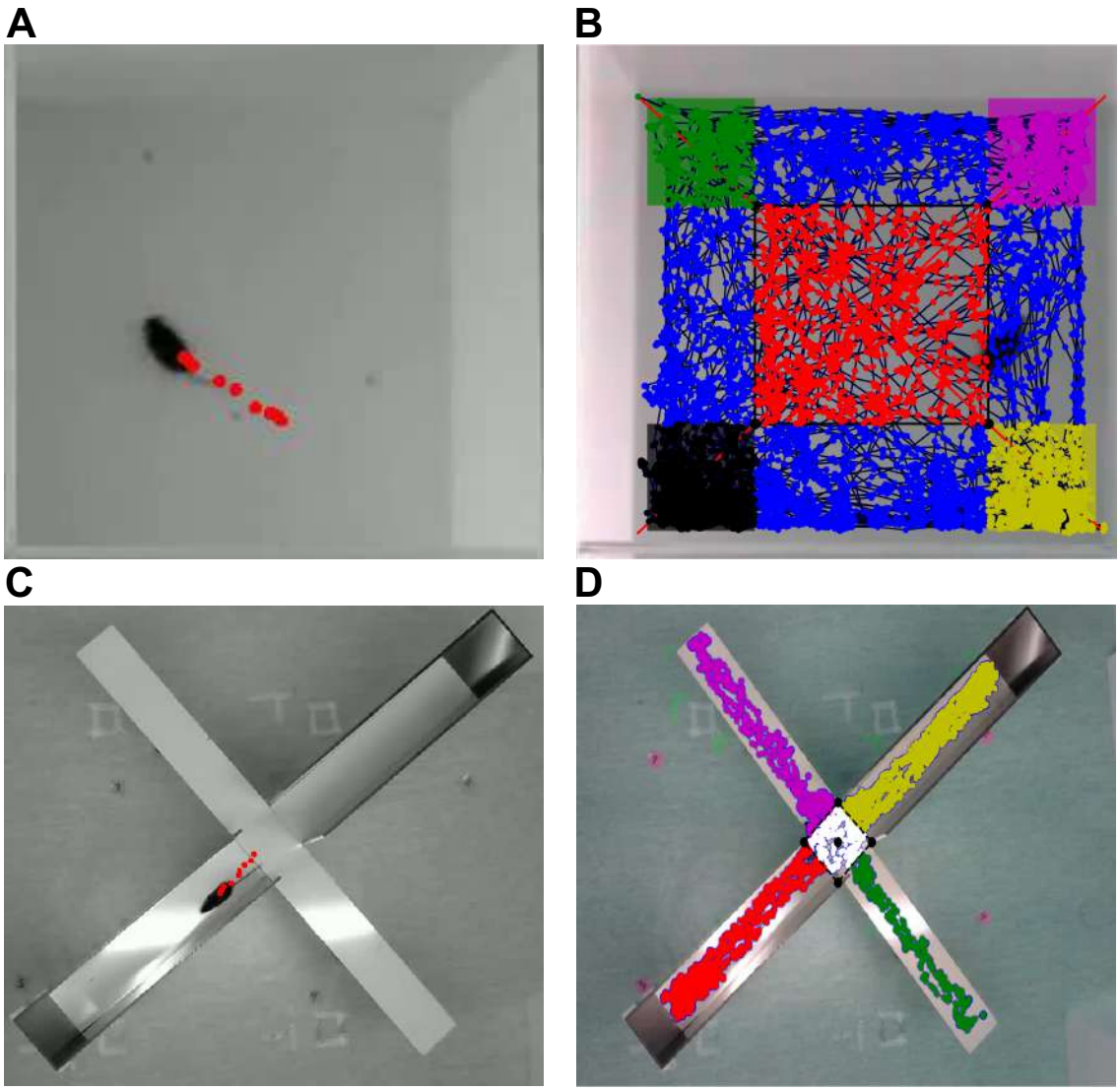

Fig. 17 | Animals tracking and different compartments segmentation using DeepLabCut. (A, C) Example of an animal tracked during an open field **(A)** and an EPM **(C)** tasks showing trail points of the animal's position in red during 10 consecutive frames. **(B)** Data-driven segmentation of the OF arena into four corners and center. **(D)** Data-driven segmentation of the EPM into two open and two closed arms. The videos were converted into grayscale to accentuate the trail points. **Abbreviations:** EPM, elevated plus maze; OF, open field.

For comparison, we also performed the tracking with commercial software and compared the output from our code to our design. We found the results to be quite similar giving an extra edge to depending on open-source tools rather than commercial ones.

1.2. Animals performance in behavioral tasks

The earlier work from our lab (Aller et al., 2015) demonstrated, using a wider battery of behavior tasks, that GluK4^{over} animals suffer from a severe form of anxiety and lack of motivation for social interaction reflected by their poor performance in OF, EPM, dark-light box, and three-chambered tests. Despite the lack of such extensive battery of tasks, our results from OF and EPM demonstrated similar results. While wild-type animals seem to be eager to explore the whole arena in the OF test (Fig. 18A), the GluK4^{over} mice limited themselves to the corners with obvious avoidance of the center region of the arena (Fig. 18B). This can be seen from trajectories of the animals as well as from the density maps that show where the animals prefer to spend their time.

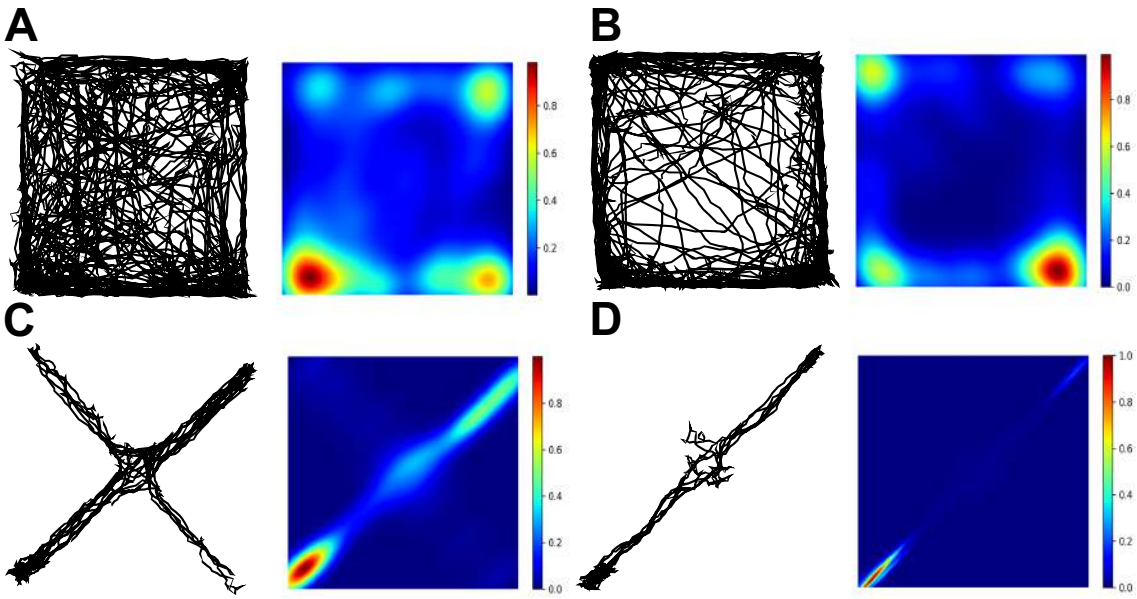

Fig. 18 | Transgenic animals overexpressing *Grik4* elicit manifestations of anxiety. The figure shows the trajectory and density maps of representative animals during performing an OF **(A, B)** or an EPM task **(C, D)**. WT animals **(A, C)** explore more and spend more time in the center area. On the other hand, transgenic animals **(C, D)** prefer to stay localized in the corners or the close arms and trying to avoid the center regions. **Abbreviations:** EPM, elevated plus maze; OF, open field; WT, wild-type.

The results of the EPM task cemented these observations, where the wild-type animals would explore both pairs of arms (albeit not equally) and visit the center area more often (Fig. 18C) than a transgenic animal would do (Fig. 18D). Both OF and EPM tests have

been long used (Lalonde and Strazielle 2008) to assess anxiety and related abnormalities in mice. As we demonstrated previously (Aller et al., 2015) this pattern of behavior cannot be attributed to motor deficiency, since the animals perform motor tasks indifferently from their WT counterparts.

2. MRI acquisition and techniques

While the previous work from our lab investigated the effect of overexpressing *Grik4* gene on the neurons of the hippocampus and the amygdala on the synaptic level (Aller et al., 2015, Arora et al., 2018), we tried in this body of work to unfold the effects of this overexpression on the circuit level as well as on the microstructural level employing MRI as our technique of choice. we acquired three different modalities, namely, rsfMRI with their anatomical images, multishell dMRI, and 3D images. The whole acquisition time, along with positioning the animal inside the machine, took an average of five hours. Using urethane as the anesthetic agent provided the long-term stability needed for such an extended acquisition.

2.1. Image quality enhancement

The small size of the mouse brain poses a lot of challenges related to the SNR. To overcome these challenges, we used a phased array coil with full-brain coverage and filled the ear canals of each animal with toothpaste to decrease the magnetic susceptibility that results from air pockets inside the ear canals (Fig. 19B). This magnetic susceptibility is of particular interest to tissues adjacent to ear canals such as the amygdala. Using these additions, we were able to collect high-quality images with reasonable SNR.

The second challenge was to accurately determine the right from the left side of the brain. The raw data as generated by the machine is usually unusable. Only by converting it to a more standard format (e.g. Nifti), it can be used. However, different software uses different conventions (anatomical vs. radiological) to define the right and left sides. While these conventions might be appropriate in human subjects, it is quite irrelevant when it comes to mice. To avoid all confusion resulted from this discrepancy, we imaged one animal with agarose gel positioned on the right side of the head (Fig. 19A). This animal was processed with the rest of the animals to guarantee that we correctly identify the sides of the brain at any phase of the analysis.

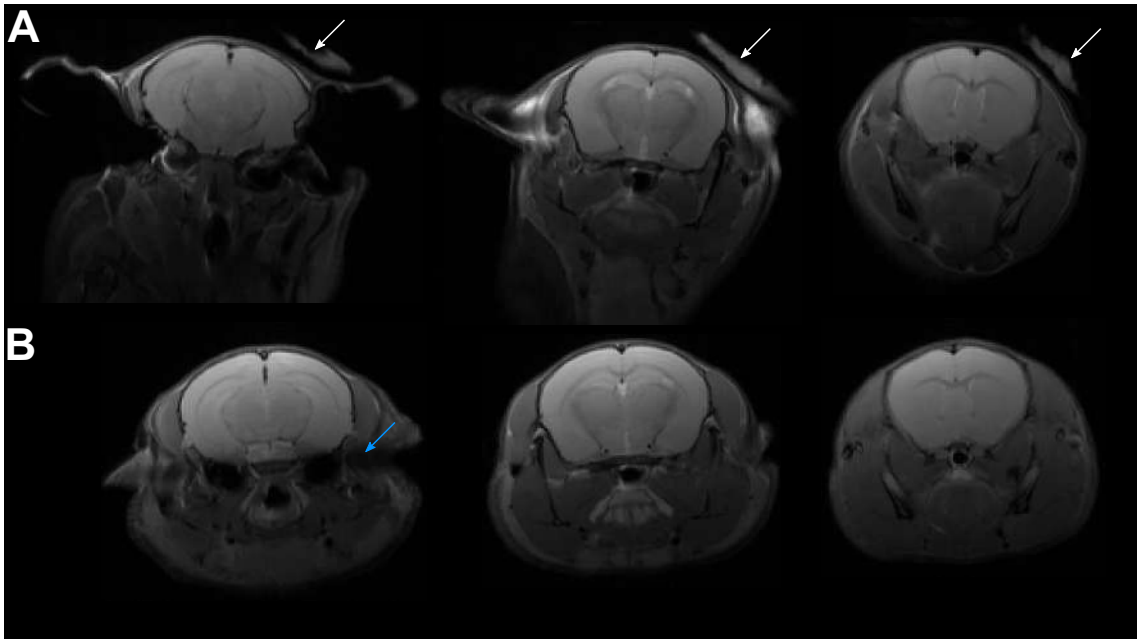

Fig. 19 | Agarose gel used to clearly demark the right side of the brain. Putting agarose gel on the right side of the head indicates the right side. **(A)** Shows an image acquired with agarose gel put on the right side of the animal's head and **(B)** Shows the same planes in a different animal acquired without using the agarose gel. The little white arrows pointing at the agarose gray patches and the small azure arrow indicates the place of the toothpaste in the ear canal.

2.2. Resting-state fMRI and functional connectivity

We used rsfMRI to assess how the different brain networks interact and how this interaction might change between and within those networks upon the overexpression of the KAR high-affinity subunit GluK4. RsfMRI has long been used to investigate abnormality in multiple psychological conditions in both humans and animals.

2.2.1. Raw data

We acquired 750 EPI volumes per animal and an anatomical scan in the same anatomical space (Fig. 20B). As we were trying to maintain a TR of 2 sec with a reasonable in-plane resolution, we could not perform an isotropic acquisition. However, with an in-plane resolution of 0.25×0.25 mm^2 and a slice thickness of 0.8 mm we were able to get a high SNR in reasonable acquisition time. Keeping the functional acquisition time to a minimum was a particularly important concern as, due to the anesthesia and the long experiments, the animal might start to lose temperature or even collapse. Along with the EPI volumes, we acquired an additional anatomical image to co-register the EPI volumes to (Fig. 20A).

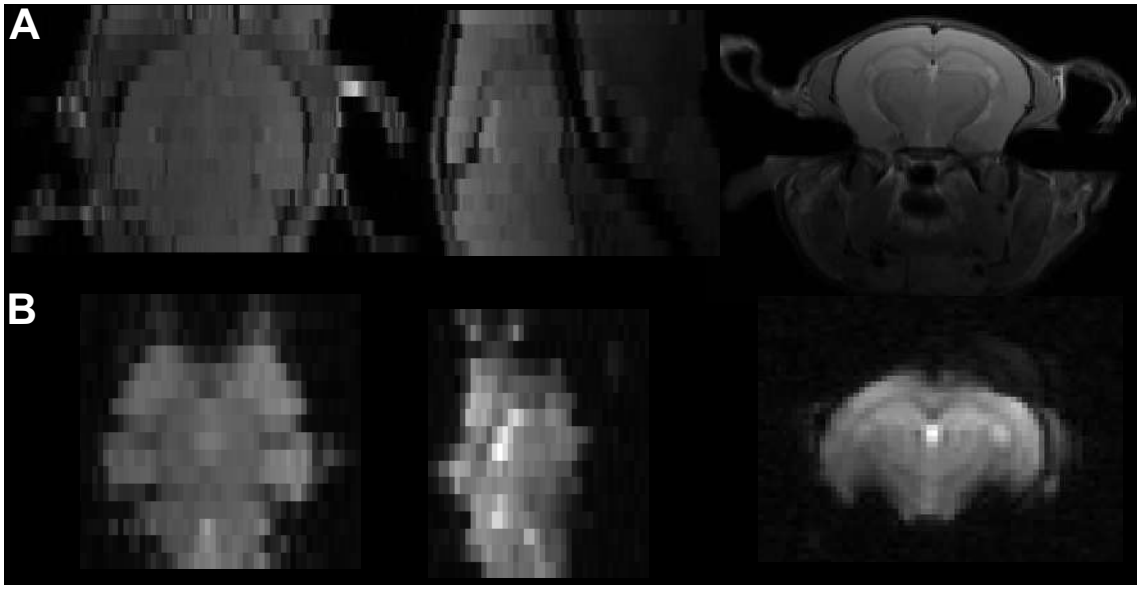

Fig. 20 | Ortho view of raw anatomical and EPI scans acquired in the same anatomical space. **(A)**an anatomical image from a representative subject. **(B)** functional scans acquired using GE-EPI protocol in the same space as the anatomical image from the same subject. **Abbreviations:** EPI, echo-planar imaging; rsfMRI, resting-state functional MRI.

2.2.2. Single-subjects ICA components classification

We started our rsfMRI analysis by an initial phase of preprocessing included multiple steps (see Methods section and Fig. 13) such as motion correction, smoothing, and high-pass filtering. We decomposed the preprocessed 4D data of each subject into 20 independent components (networks) using ICA. For each subject, we classified the components manually into signal or noise depending on the location of the peak of the signal, its time-series, and the power spectrum (Zerbi et al., 2015, Griffanti et al., 2017). The motion plots of each subject were also examined to see if any sudden jumps coincide with irregularities in the time-series of the ICA components (Fig. 21A). Figure 21 gives examples of components that were classified as noise (Fig. 21A, B) or as a signal (Fig. 21C, D). Noise components usually have the signal peak lies either outside the known gray matter structures, close to a major vasculature, or in the CSF (Fig. 21B). Looking at the time-series for sudden jumps can also be a major indicative (Fig. 21A). RsfMRI fluctuations usually occupy the lower segment of the frequency spectrum (0.1–0.3 Hz); components with power spectra in the higher frequencies or extended over multiple segments are usually classified as noise (Fig. 21A). Adversely, components with fluctuations of neural origin have power spectra predominately localized in the lower-frequency band (Fig. 21C, D).

2.2.3. Group ICA components

The noise components were regressed out of each subject and the filtered data from all subjects was concatenated and decomposed using probabilistic ICA into 20 networks. We visually identified 17 of those components as relevant RSNs with neurobiological origin (Fig. 22) and 3 components as noise (Fig. 23). We were able to identify multiple networks overlapping with known anatomical regions and agree with networks previously reported (Nasrallah et al., 2014, Zerbi et al., 2015, Grandjean et al., 2020). The identified networks can be globally divided into cortical networks, sub-cortical networks, and cerebellar networks (Fig. 22). The cortical networks span the olfactory bulbs and parts of the cortex such as the somatosensory cortex, the motor cortex, the visual cortex, and the cingulate cortex. Structures such as the hippocampus, the amygdala, the thalamus, and the striatum were considered to be sub-cortical networks. We recognized three different networks as part of the cerebellar nuclei including the 6th cerebellar lobule, the lateral and medial cerebellar nucleus, and the gigantocellular reticular nucleus. Noise components, on the other hand, were the components lying in the ventricles (Fig. 23B), the WM (Fig. 23C), or showing the ringing effect that characterizes components resulting from motion artifacts (Fig. 23A).

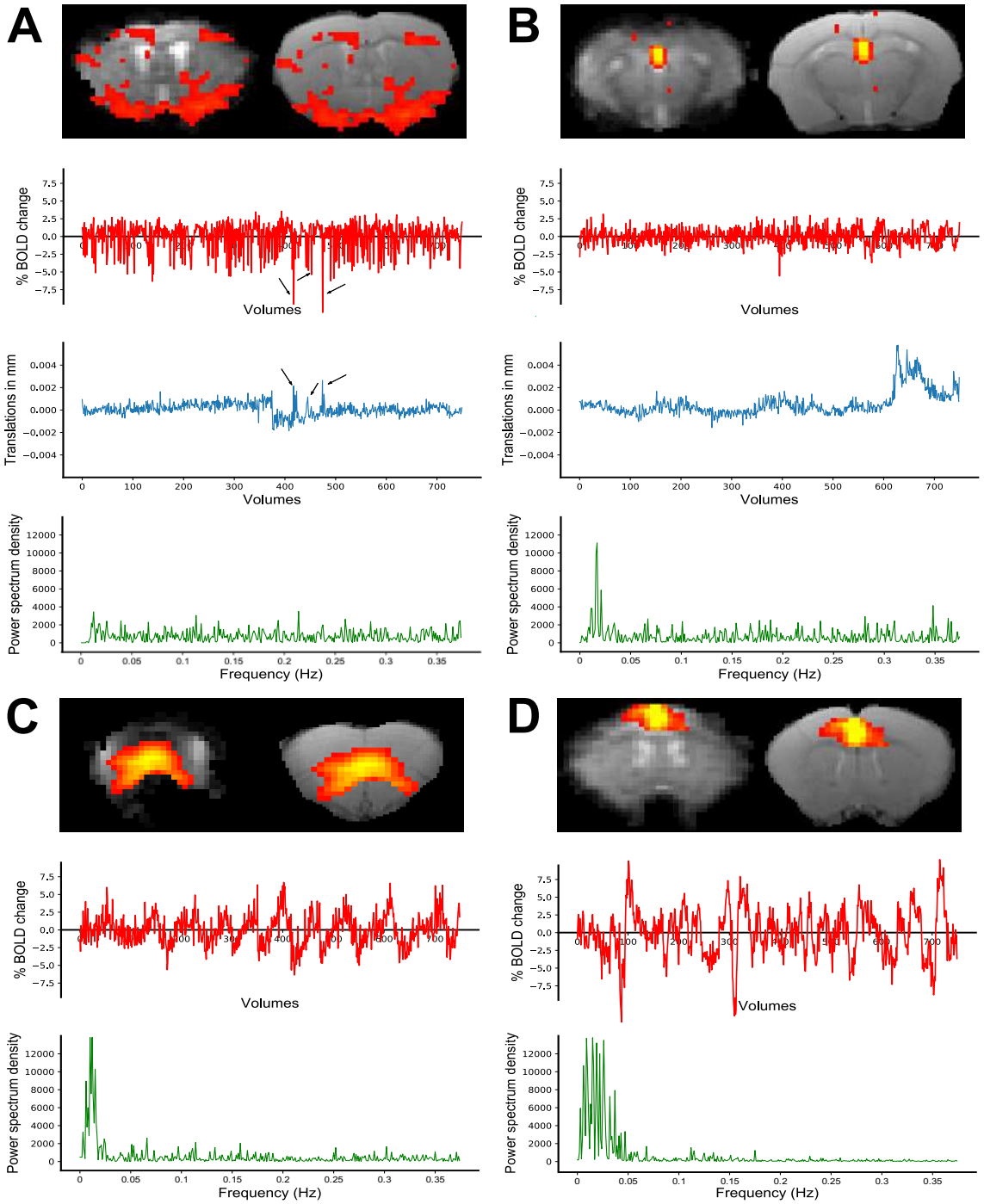

Fig. 21 | Manual classification of ICA components into signal and noise using the signal spatial location, BOLD time-series, and power spectrum. (A, B) Examples of components classified as noise. **(C, D)** Examples of components classified as a signal. **(A)** Notice the sudden jumps in the time-series indicated by the small black arrows and their correspondence with jumps in the volumes across the *x*-axis indicating that the component is a motion artifact. The power spectrum is showing fluctuations across all frequency bands. **(B)** Another noise component with fluctuations frequencies in the right place of the power spectrum and no major jumps in the time-series, however, it is overlapping with a major ventricle. **(C, D)** Components with smooth time-series, fluctuations in the lower frequency band, and overlapping with known gray matter structures, thus both were classified as signals. Each component is showed overlaid on an EPI volume and the corresponding anatomical plane. **Abbreviations:** BOLD: blood-oxygenation-level dependent; EPI, echo-planar imaging; ICA, independent component analysis.

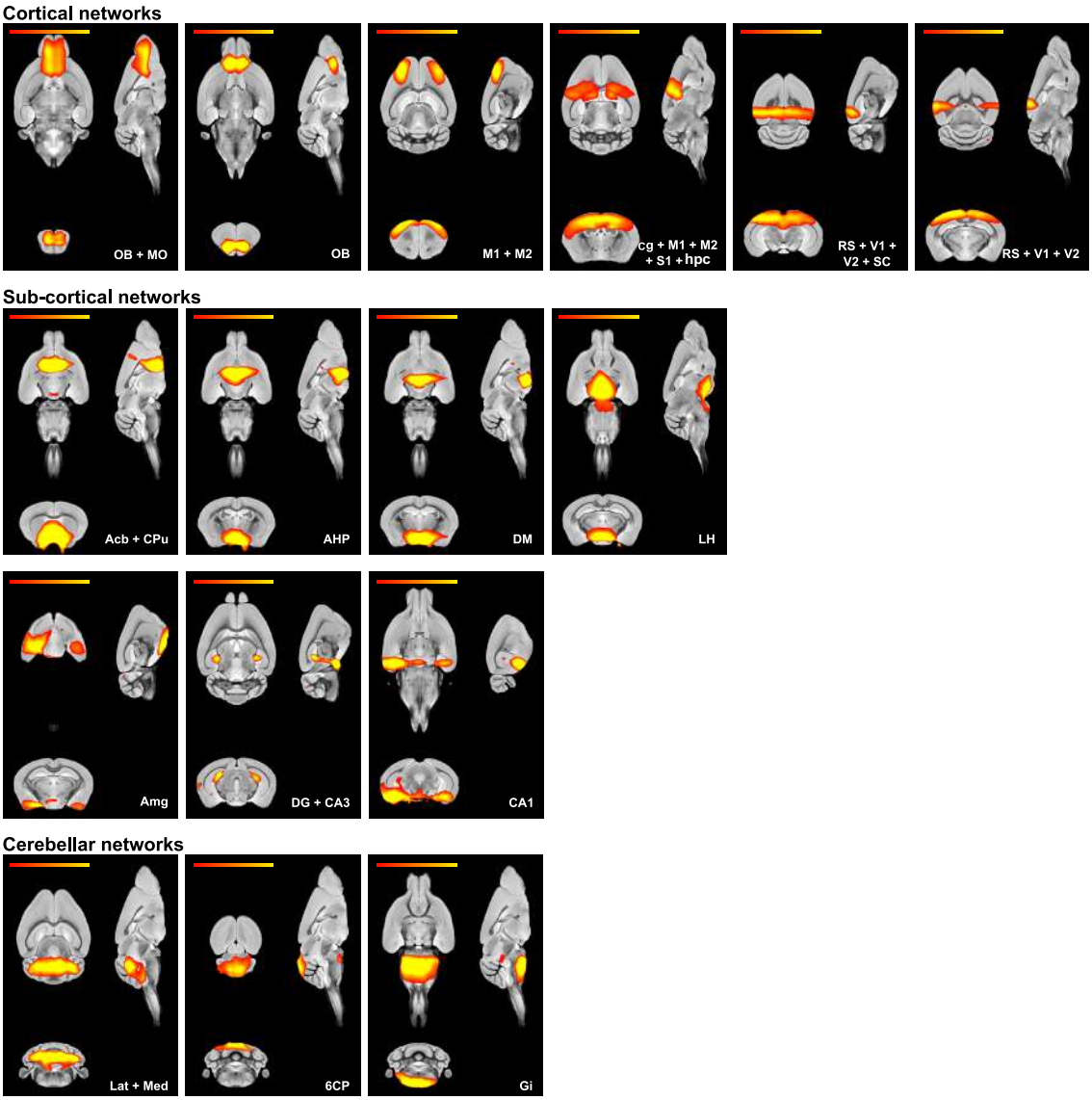

Fig. 22 | RSNs identified by ICA. We used probabilistic ICA on the concatenated prefiltered group data from all subjects (30 mice) to identify different RSNs. We identified networks in the cerebral cortex, the thalamus, the hippocampus, the amygdala, the striatum, and the cerebellum. All components showed significant overlap with known anatomical structures and were labeled based on Paxinos' mouse brain atlas (Paxinos and Franklin 2004). The images are shown in anatomical view overlaid on AMBMC high-resolution template and the networks are scaled in pseudo-*z*-scores, i.e., how many standard deviations away from the background noise. **Abbreviations:** 6CP, 6th cerebellar lobule; Acb, accumbens nucleus; AHP, anterior hypothalamic nucleus; AMBMC, Australian mouse brain mapping consortium; Amg, Amygdala; CA1, cornu ammonis-1; CA3, cornu ammonis-3; Cg, cingulate cortex; Cpu, caudate putamen; DG, dentate gyrus; DM, dorsomedial hypothalamic nucleus; ICA, independent component analysis; Gi, gigantocellular reticular nucleus; hpc, hippocampus; Lat, lateral cerebellar nucleus; LH, lateral hypothalamic area; M1, 1º motor cortex; M2, 2º motor cortex; Med, medial cerebellar nucleus; MO, medial orbital cortex; OB, olfactory bulb; RS, retrosplenial cortex; RSNs, resting-state networks; S1, 1º somatosensory cortex; SC, superior colliculus; V1, 1º visual cortex; V2, 2º visual cortex.

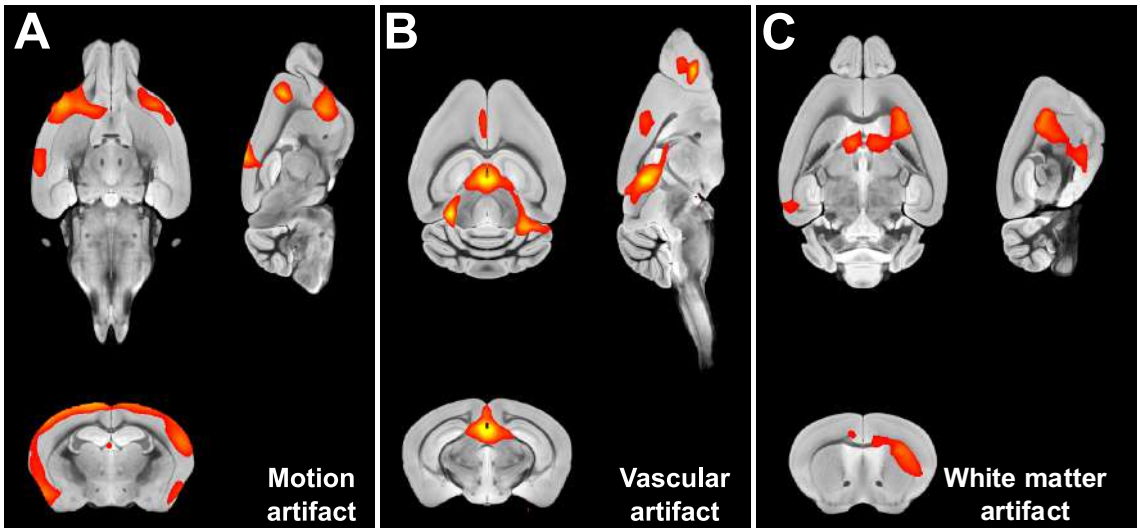

Fig. 23 | Group-components classified as noise using probabilistic group ICA. (A) A component showing the ringing effect on the periphery of the brain indicating a motion artifact. **(B)** A component with its peak in the ventricle. **(C)** A component lying in the white matter. The images are shown in anatomical view overlaid on AMBMC high-resolution template. **Abbreviations:** AMBMC, Australian mouse brain mapping consortium; ICA, independent component analysis.

2.2.4. DMN network

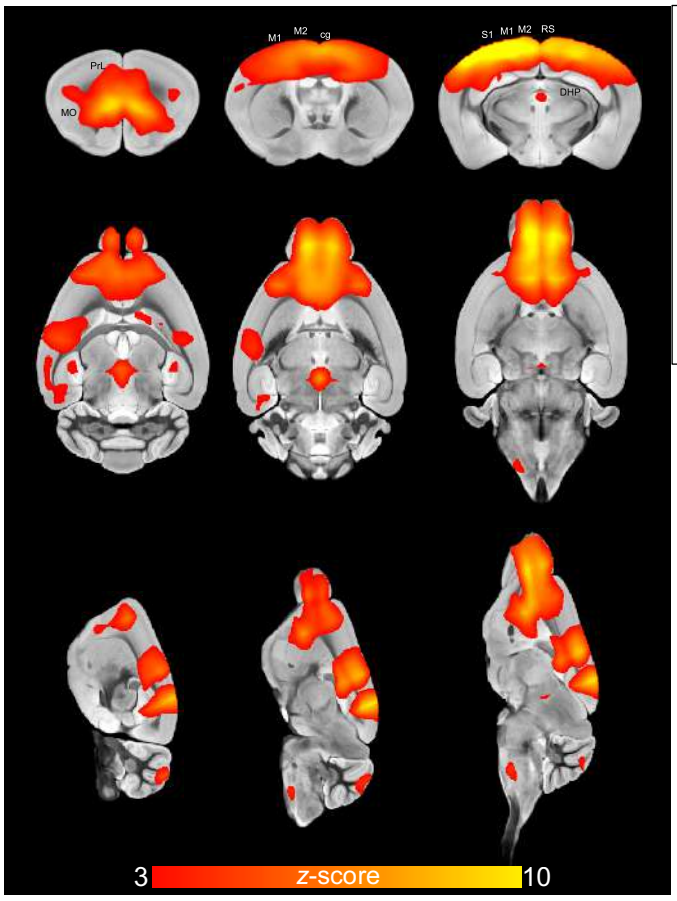

Fig. 24 | Default mode network identified from multiple ICA components. From the group-ICA analysis, we identified multiple components with anatomical structures similar to those recognized to be the default-mode network. The images are shown in anatomical view overlayed on AMBMC high-resolution template and the network is thresholded pseudo in *z*-score. **Abbreviations:** cg, cingulum; DHP, dorsal hippocampus; M1, 1º motor cortex; M2, 2º motor cortex; MO, medial orbital cortex; PrL, prelimbic cortex; RS, retrosplenial cortex; S1, 1º somatosensory cortex.

2.2.5. Between components analysis

We assessed the correlation between the different RSNs using FSLNets. After regressing out the components previously dubbed as noise, the rest of the components from both groups were used as nodes for the subsequent network analysis. We calculated the edge strength between each pair of the components (Fig. 25) using three correlation measures. The normalized full correlation coefficient (Fig. 25A), unregularized partial correlation (Fig. 25B), and partial correlation regularized with Ridge regression (L2-norm) and a rho value of 0.1 (Fig. 25C) were all employed for this purpose (see Smith et al., 2011 for more details about computing these coefficients). Using the full correlation edge strengths, we performed a hierarchical clustering of the different nodes (Fig. 26A, B) to depict how the networks are organized inside the mice brains. Next, we examined how the interaction strengths in the three measures are altered in GluK4^{over} animals with respect to the control group (Fig. 26C, D).

The mean interaction strengths did not differ much among the three measures used as evident from the color maps in Fig. 25. The highest interaction strengths were observed between the anterior and dorsomedial hypothalamus, the caudate putamen and the anterior hypothalamus, anterior and posterior parts of the olfactory bulb, and the dorsal hippocampus and the 6th cerebellar lobule. Strong anticorrelations were also observed between the amygdala and lateral hypothalamus, the posterior olfactory bulb and parts of the cortex (including the cingulate cortex, 1º, 2º motor cortices, and the somatosensory cortex), 6th cerebellar lobule and the same parts of the cortex, and the gigantocellular reticular nucleus and the network consists of the retrosplenial cortex, the 1º, and 2º visual cortices.

The hierarchical clustering algorithm was able to separate the RSNs into three big clusters (Fig. 26A, B) that were further differentiated into much finer clusters. Interestingly, components of the DMN (the cingulate cortex, the motor cortices, and the dorsal hippocampus) were grouped together as part of the middle cluster. Other clusters consisted of structures with high interaction strengths as detailed previously.

The interaction strengths were also assessed between the two genotypes. The two groups seemed to display similar interaction strengths irrespective of the measure investigated. The interaction strength between two particular nodes (namely, the motor cortex and

lateral hypothalamus) showed a significant difference that survived the FWER multiple-comparison correction ($P = 0.01$) in cases of the partial correlation (Fig. 26C). The difference between the two nodes was quite similar in the case of the regularized correlation coefficient, however, it did not reach statistical significance ($P = 0.062$) after FWER correction (Fig. 26D). Upon further inspection, we deduced that the difference is not due to a change in the interaction strength, but rather due to shifting from the positive correlation in the case of GluK4$^{+/+}$ (Fig. 26C) to negative correlation in the case of GluK4^{over} (Fig. 26D). Such a shift can have important implications for the effect of Glutamate on functional connectivity.

Partial correlation is considered to be superior to normal correlation when the goal is to assess the direct connection between two nodes. However, caution should always be practiced in interpreting the meaning of such correlations as it depends on many factors such as the number of nodes in the analysis and the number of volumes acquired in the dataset.

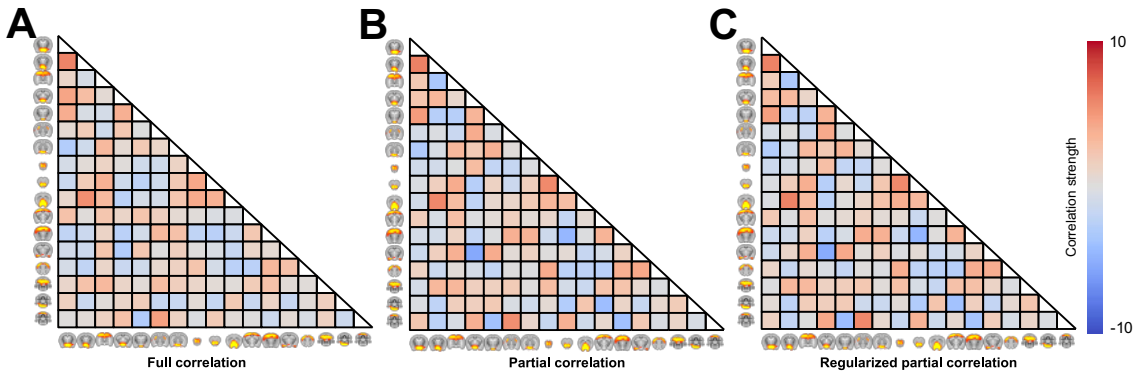

Fig. 25 | Between-RSNs group average: (A) full correlation, (B) partial correlation, and (C) regularized partial correlation showing similar connectivity patterns. The values were calculated by performing a one-sample t-test on the full correlation **(A)**, the partial correlation **(B)**, and regularized partial correlation **(C)** coefficients between the RSNs resulted from the ICA analysis from both groups. The results are shown in *z*-score calculated from t-stats. **Abbreviations:** ICA, independent component analysis; RSNs, resting-state networks.

2.2.6. Within-components analysis

In order to investigate the genotype effects of the extra copy of the *Grik4* gene on the RSNs previously identified, we used Dual Regression to perform RSNs voxel-wise comparison between the two genotypes. The results were enhanced using TFCE and corrected for multiple comparisons using FWER correction and the results were further corrected networks. The voxel-wise analysis unearthed a strong unidirectional genotypic effect on the functional coactivation of multiple networks (Fig. 27) in favor of the GluK4^{over} animals.

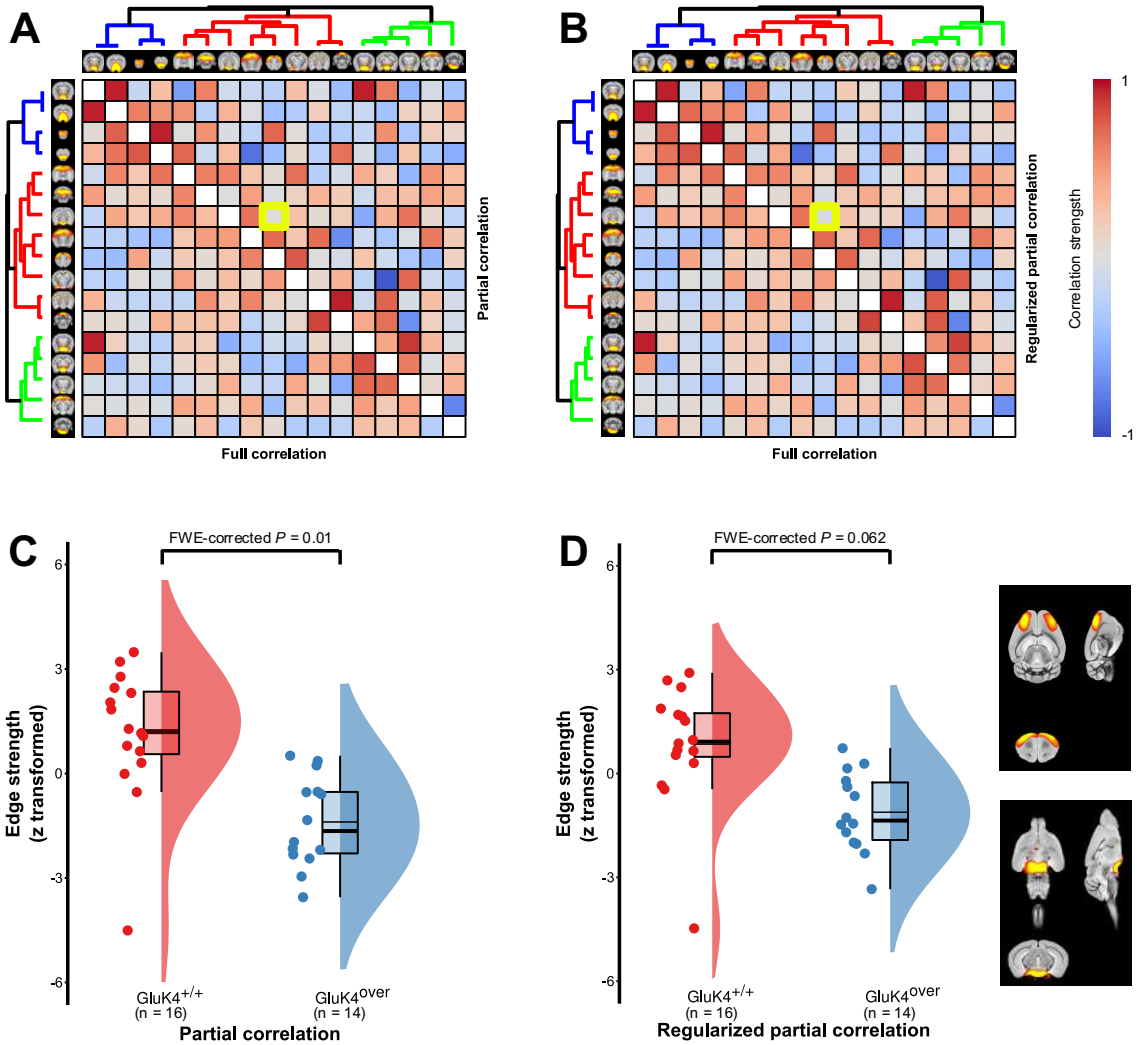

Fig. 26 | Hierarchical clustering of the 17 RSNs calculated from the group-ICA analysis based on their full correlations. (A) Shows the hierarchy, the full correlation (below diagonal), and the partial correlation (above diagonal) between the RSNs extracted from all subjects. **(B)** Shows the hierarchy, the full correlation (below diagonal), and the regularized partial correlation (above diagonal) between the RSNs extracted from all subjects. The significant differences between the two genotypes in correlation strength are highlighted by a yellow box and showed below each matrix. **(C)** Raincloud plots of the difference in partial correlation strength and **(D)** regularized partial correlation strength between the motor cortex network and the lateral hypothalamus. **Abbreviations:** ICA, independent component analysis; RSNs, resting-state networks.

The cerebellar networks are showing a stronger connection with the hippocampus especially the dorsal part as well as an increase in the within-network connection (Fig. 27A). A similar increase in the within-network connection is also observed in the hippocampus (Fig. 27B), regions of the cortex spanning the retrosplenial and visual cortices (Fig. 27C), and in the lateral hypothalamic network (Fig. 27E). The network consists of the olfactory bulb and the medial orbital cortex shows an increase in the functional connection with parts of the cortex such as the somatosensory cortex (Fig. 27F). All the changes in the intra-components functional connectivity appear to follow the same direction, where it

increases in the transgenic group with respect to the wild-type animals. On the other hand, we failed to see any brain regions where the GluK4^{over} showed a decrease in the intra-network functional synchronization relative to the GluK4$^{+/+}$ animals.

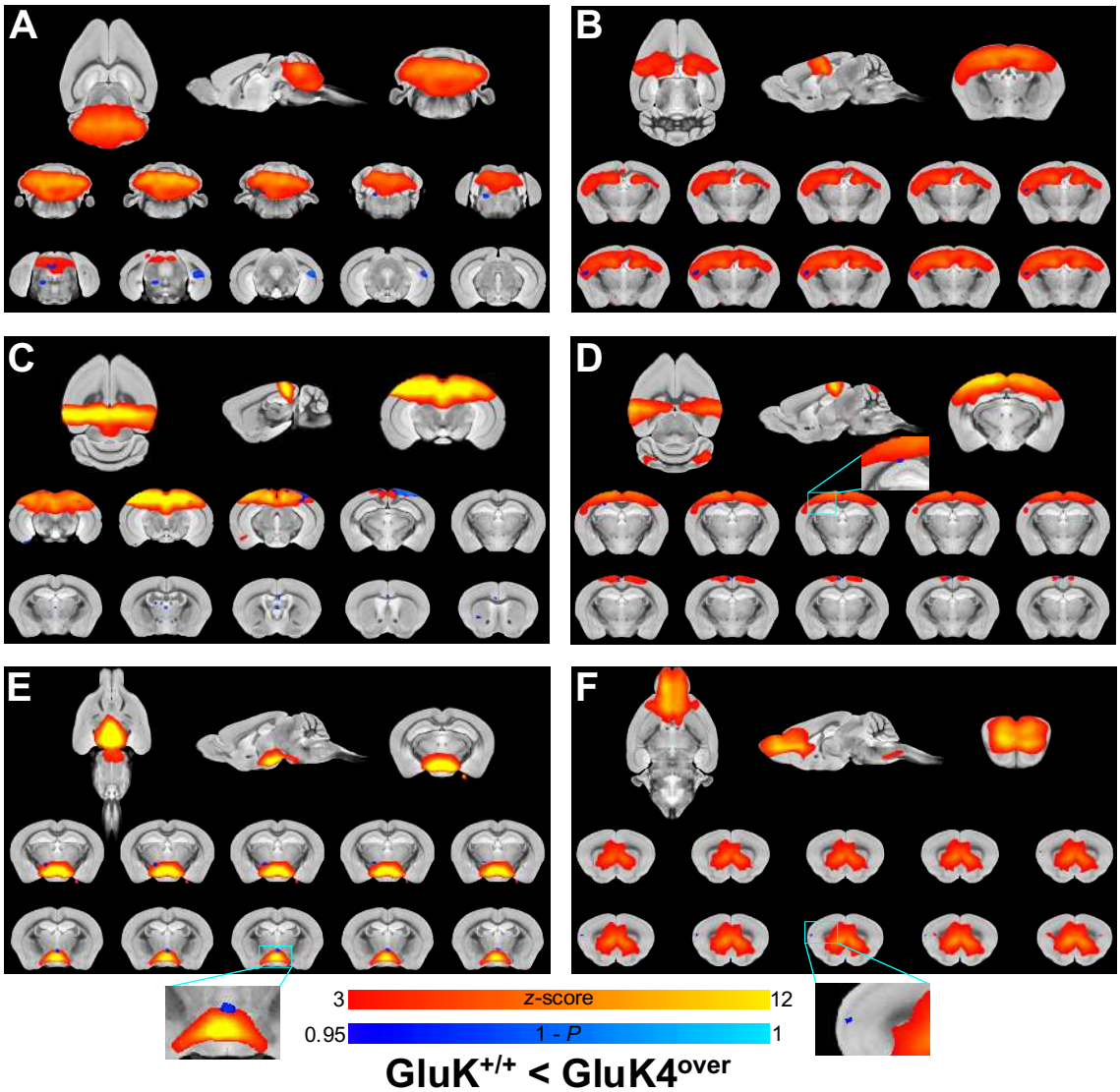

Fig. 27 | Dual Regression analysis shows increased intra-network connectivity in the GluK4^{over} animals with respect to the GluK4$^{+/+}$ counterparts (16 GluK4$^{+/+}$ vs 14 GluK4^{over}). (A, B, C, D, E, F) Comparison of various RSNs between the two genotypes overlaid on the AMBMC high-resolution template. Each panel shows the ICA network calculated from all subjects displayed as pseudo-*z*-score scaled between 3-12 on top and a statistical map of the significant differences (TFCE, FWER *P* value < 0.05) between the two groups corrected across networks (shown in blue). The *P* values are shown as 1 – *P* to facilitate visualization (an increase means more significant values). **Abbreviations:** AMBMC, Australian mouse brain mapping consortium; FWER, family-wise error rate; ICA, independent component analysis; RSNs, resting-state networks; TFCE, threshold-free cluster enhancement.

2.2.7. Correlations of RSFC with behavior

We ran a correlation analysis between the metrics previously calculated from the behavior tasks and the functional connectivity of ICA networks to find out how those networks

correlation can affect or modify the behavior. The strength of number of networks showed inflated correlation coefficient with the different metrics, however, none of these correlations survived the one-sample t-test after correcting the results for multiple comparisons across voxels and netorks. The only differences that survived after such an aggressive correction were correlations with a network that later discarded as noise (Fig. 23C). We did not take those results into considerations for obvious reasons.

Collectively, the GluK4^{over} animals appear to have faulty RSNs (Table 1). These abnormalities exist on both levels intra- and inter-networks levels. On the intra-network level, there is an increase in the strength i.e., how the networks connected to themselves. Conversely, the link between those networks appeared to be weakened in the transgenic animals.

2.3. Diffusion MRI

Microstructural abnormalities have been constantly observed in the literature in both human subjects diagnosed with ASD and in animal models (see Introduction). With this in mind, we acquired DWIs with two different b-values and fit various biophysical models in order to investigate the microstructural changes that *Grik4* overexpression might induce.

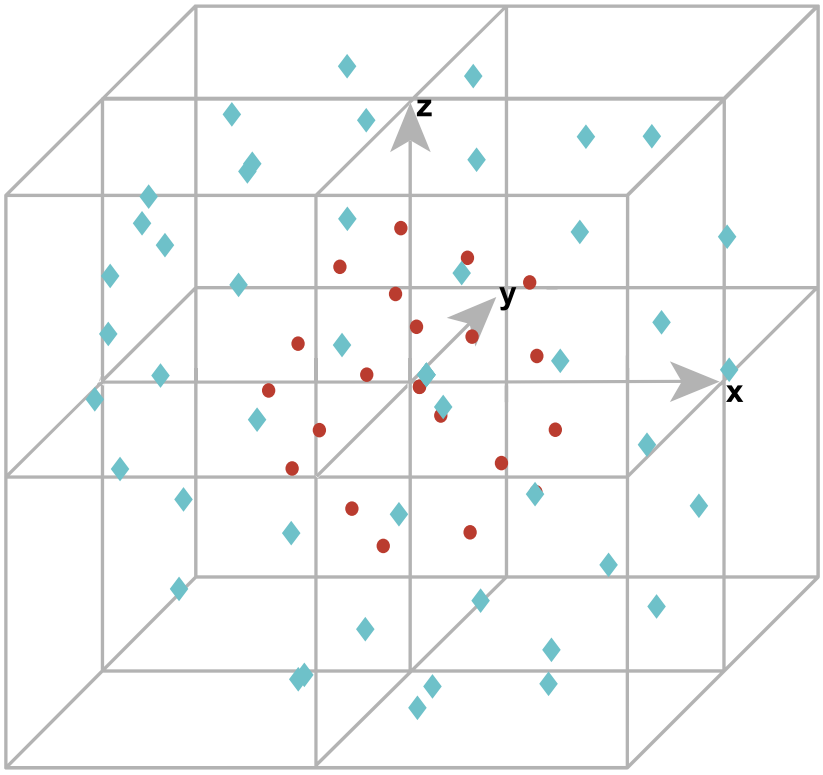

Fig. 28 | Sampling scheme of the gradient vectors used to acquire the DWIs. The vectors of both shells (1000, 2500 s/mm^2) were spatially sampled on a sphere. **Abbreviations:** DWIs, diffusion-weighted images.

2.3.1. Raw data and acquisition schemes

We acquired DWIs using a spin-echo EPI protocol with two different b-values (two shells). The first shell was acquired using a b-value of 1000 s/mm^2 and consisted of 20 DWIs with 20 unique gradient orientations (Fig. 29B) and 2 images without diffusion (2 b0 images) (Fig. 29A). The second shell, on the other hand, was acquired with a higher b-value (2500 s/mm^2), 45 DWIs across 45 unique directions (Fig. 29C), and 4 b0 images. The gradient directions in both shells were spatially sampled on a sphere (Fig. 28) for better estimation of the diffusion models.

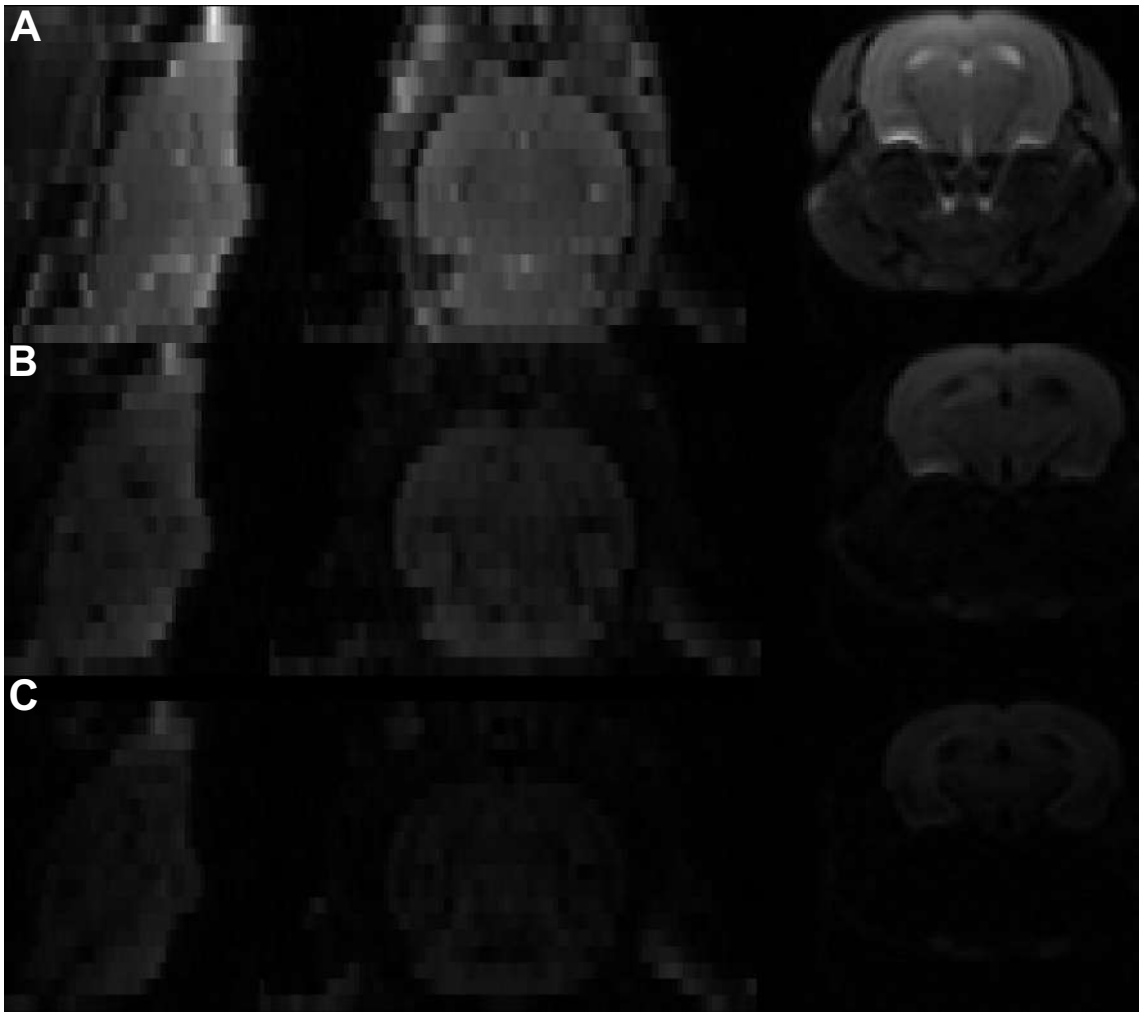

Fig. 29 | Ortho view of raw DWIs acquired using spin-echo EPI protocol from a representative animal. (A) Shows an example DWI without diffusion weighting (b0 image). **(B)** A DWI image acquired using a b-value of 1000 s/mm^2 showing higher SNR. **(C)** A DWI acquired with a b-value of 2500 s/mm^2 with apparent loss in SNR. **Abbreviations:** DWI, diffusion-weighted image; EPI, echo-planar imaging; SNR, signal-to-noise ratio.

2.3.2. Diffusion tensor imaging

The conventional tensor model (Basser et al., 1994) was fit to the DWIs acquired with the b-value of 1000 s/mm^2. The maps resulted from fitting the model (FA, MD, AD, and RD) were compared between the two genotypes and then correlated with the behavioral measures previously estimated (see Methods section). We used the TBSS (Smith et al., 2006) to map the voxel-wise differences between the two groups and later used the values from tracts to perform the linear regression with the metrics obtained from the behavior tasks.

GluK4^{over} exhibited a significant bilateral decrease in the FA values in the major WM fibers including the genu of the cc, the fornix, the forceps minor of the cc, the external capsule, the medial forebrain bundle, the fimbria, the splenium, the forceps major of the cc, and the dorsal hippocampal commissure (Fig. 30A). In the case of the rest of the maps (MD, AD, and RD), GluK4^{over} animals showed a significant increase in the values of those maps compared to the GluK4$^{+/+}$ animals, albeit, not widespread as the changes in the FA values. These increases in the MD values were quite limited and quite localized to the dorsal hippocampal commissure (Fig. 30B). The significant increase in the GluK4^{over} RD values spanned the same set of structures that witnessed the decrease in FA values including the different parts of the cc (Fig. 30C). The increases in the AD values in favor of the transgenic group were mainly in the superior colliculus (Fig. 31A). Interestingly, despite being limited, those regions displayed a strong linear correlation with the ratio of time spent in the open arms/time spent in the closed arms of the EPM. Those correlations were significant enough to survive the FWER multiple comparison correction (Fig. 31B).

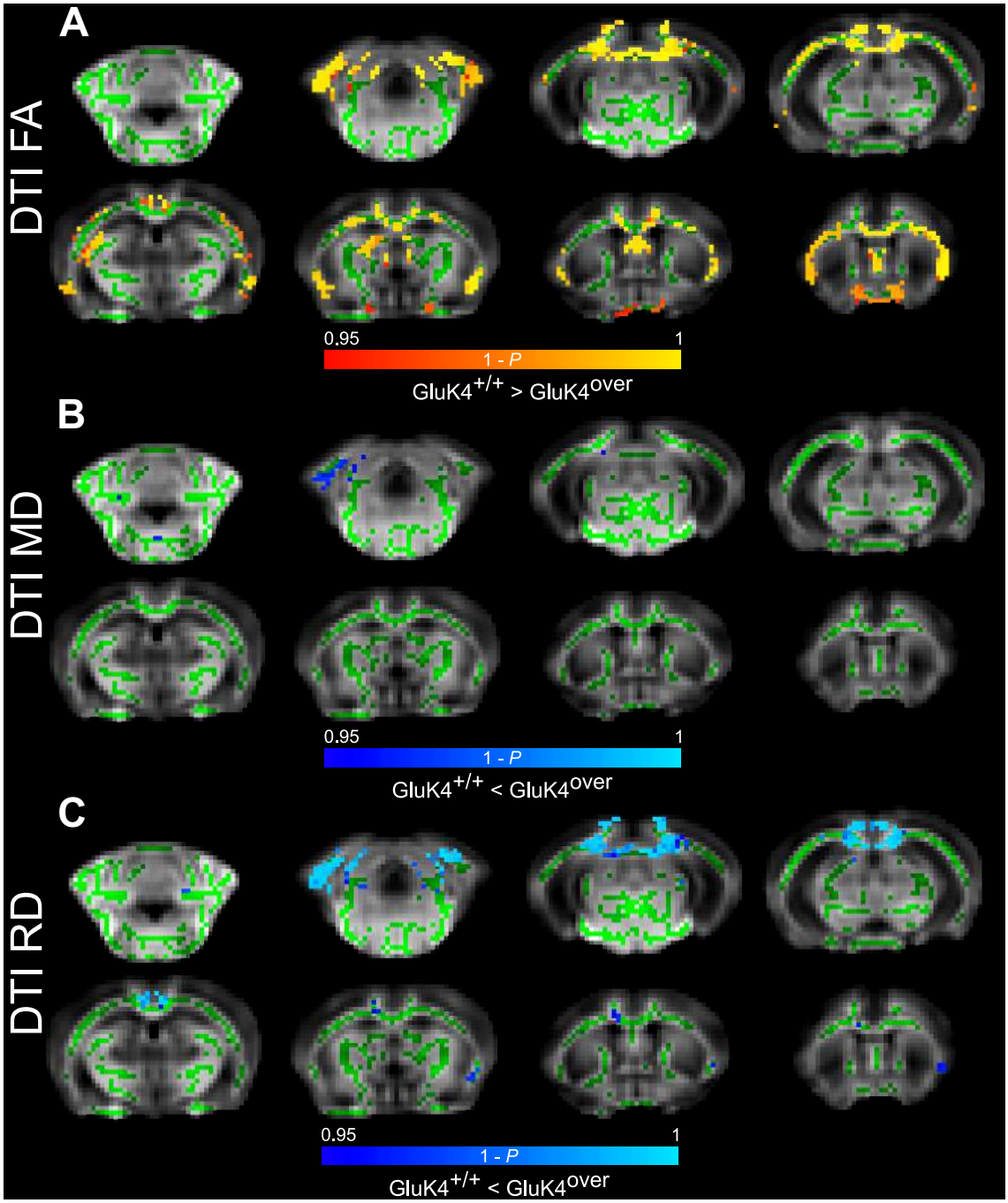

Fig. 30 | TBSS analysis shows the significant genotypic effect of *Grik4* overexpression on FA, MD, and RD maps of the tensor model ($P < 0.05$, TFCE, FWER corrected). **(A)** Shows regions where GluK4^{over} animals show a significant decrease (in red-yellow) in FA values relative to the control. **(B, C)** Regions with a significant increase (in blue) in MD **(B)** or RD **(C)** in GluK4over animals with respect to GluK4+/+ animals. The values are shown as 1- *P* (higher means more significant) to facilitate the visualization of the results. The statistical maps are overlaid on a study-based template and its WM skeleton (displayed in green). **Abbreviations:** DTI, diffusion tensor imaging; FA, fractional anisotropy; FWER, family-wise error rate; MD, mean diffusivity; RD, radial diffusivity; TBSS, tract-based spatial statistics; TFCE, threshold-free cluster enhancement.

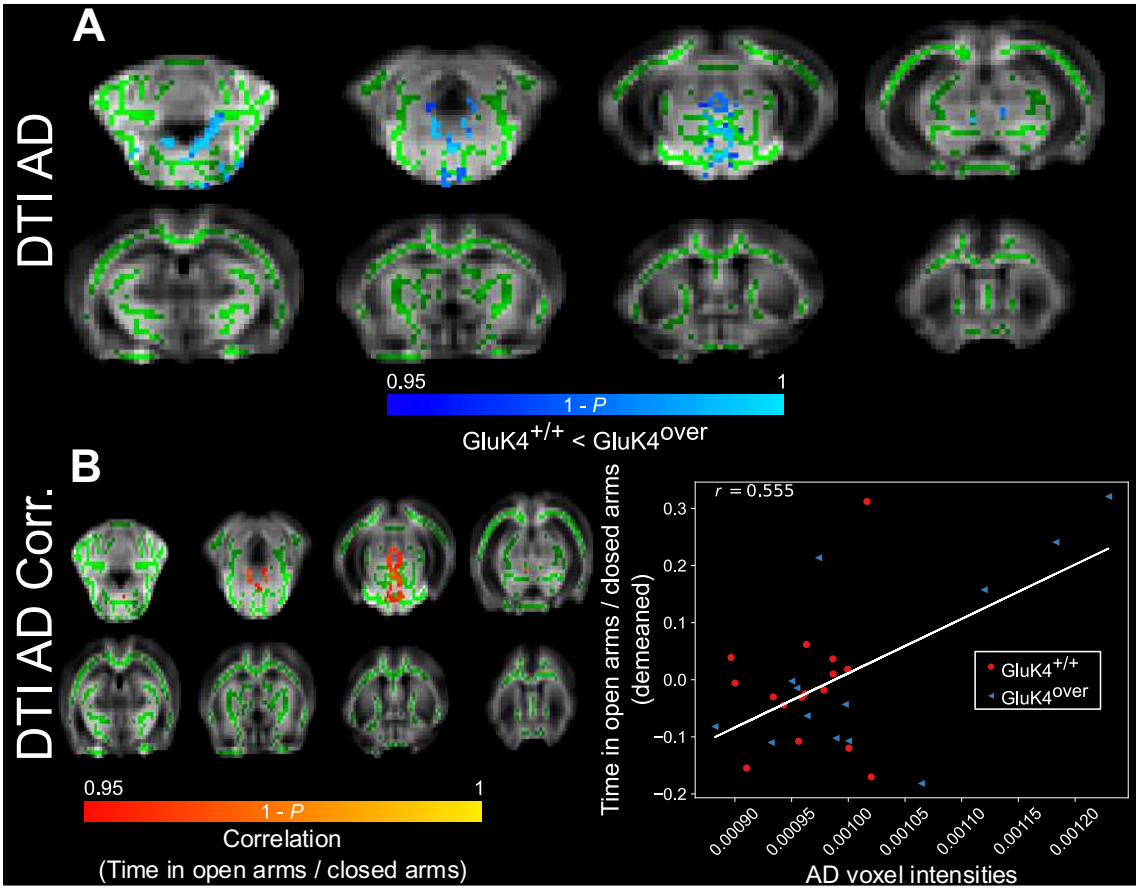

Fig. 31 | TBSS analysis of the AD values of the tensor model. (A) Shows a significant increase in the AD values in the GluK4^{over} animals in comparison with the wild-type animals. **(B)** Regions showing a significant positive correlation between the AD values and the time spent in the open arms/time spent in the closed arms of the EPM (left) and the linear regression of the voxel that shows the highest *P* value in the one-sample t-test (right). All statistical maps are shown has *P* values < 0.05 (TFCE enhanced, FWER corrected). The statistical maps are overlaid on a study-based template and its WM skeleton (displayed in green). **Abbreviations:** AD, axial diffusivity; DTI, diffusion tensor imaging; EPM, elevate plus maze; FWER, family-wise error rate; TBSS, tract-based spatial statistics; TFCE, threshold-free cluster enhancement; WM, white matter.

2.3.3. Kurtosis

After processing the first shell (1000 s/mm^2) of the diffusion data to fit the tensor model and obtain the FA, MD, RD, and AD maps, we merged the two shells together and used that merged data to fit multiple biophysical models trying to extract more information about the microstructure of the underlying tissue. We started by fitting the kurtosis model which, essentially, tries to measure the deviation from Gaussian behavior as opposed to the tensor model that is mainly concerned with the Gaussian diffusion. By fitting the kurtosis model to our multi-shell data, we obtained multiple maps that reflect different aspects of the microstructural properties. We used two different algorithms to fit the model (linear and non-linear) as an anticipation for the problems that might arise from the unusual nature of the mice data and the high noise element that might present itself as

a hurdle to accurately reach the global minimum. We did not observe a significant difference between the fitting results of the two models. We took this as an optimistic indication that both algorithms were able to reach the global minimum and hence producing similar results.

On the voxel-wise level, the TBSS analysis showed a difference between the two groups only in FA values (Fig. 32A). Akin to the FA maps of the tensor model, the GluK4^{over} animals displayed a significant decrease in the DKI FA values relative to the GluK4$^{+/+}$. The differences were mainly in the genu, the splenium, the forceps major of the cc, and the dorsal hippocampal commissure (Fig. 32A).

proved to be significant after performing the one-sample t-test and the FWER correction for multiple comparisons. We found a significant positive correlation between the FA values in the external capsule, the internal capsule, the fimbria, the splenium of the cc, the forceps major of the cc, the superior colliculus, and the dorsal hippocampal commissure (Fig. 32B). Multiple maps elicited a significant negative correlation with the distance traveled previously mentioned including the AWF, RD, MK, and AK maps (Fig. 32C, Fig. 33). Voxels of the AWF (Fig. 32C) and AK (Fig. 33C) maps located nearly in all the major WM tracts displayed such a strong negative correlation. Those tracts included the genu, the body, the splenium, the forceps minor and major of the cc, the fimbria, the fornix, the internal capsule, and the dorsal hippocampal commissure (Fig. 32C, Fig. 33C). The negative correlations with RD and MK maps were still significant, however, not widely distributed as in the case of the AWF and AK maps. The RD significant correlations were only observed in the internal capsule, the external capsule, the fimbria, and the superior colliculus (Fig. 33A). The internal capsule, the fimbria, the dorsal hippocampal commissure, and the superior colliculus in the MK maps (Fig. 33B) showed a similar negative correlation with the distance traveled in the OF behavioral experiment.

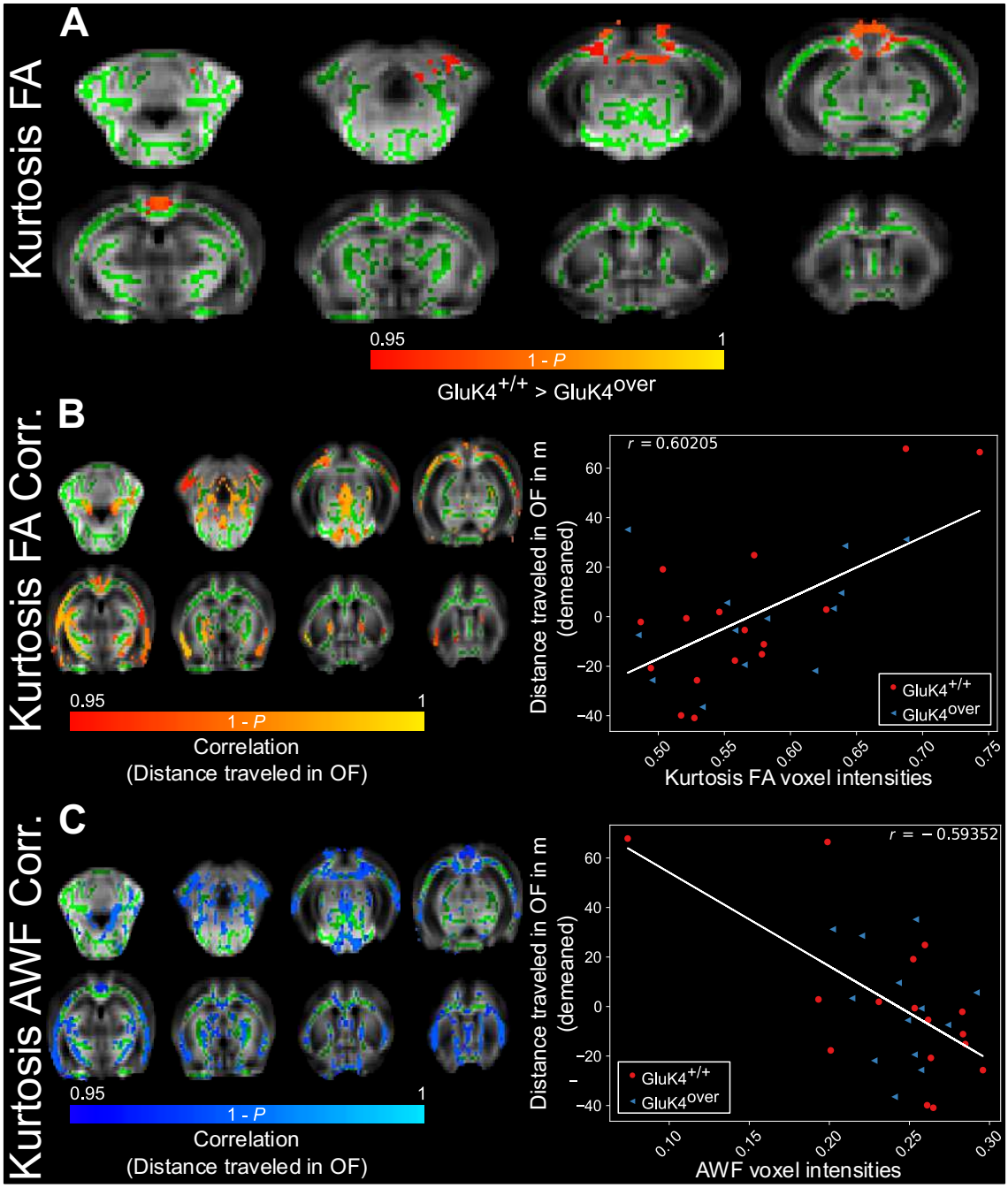

Fig. 32 | TBSS analysis of the FA and AWF values of the kurtosis model. (A) Shows a significant decrease in the FA values in the GluK4^{over} animals in comparison with the wild-type animals. **(B)** Regions showing a significant positive correlation between the FA values and the distance traveled in the OF arena in meters (left) and the linear regression of the voxel that shows the highest *P* value in the one-sample t-test (right). **(C)** Voxels where the AWF show significant anticorrelation with distance traveled in the OF arena (left) and the linear regression of the voxel that shows the highest *P* value in the one-sample t-test (right). All statistical maps are shown has *P* values < 0.05 (TFCE enhanced, FWER corrected). The statistical maps are overlaid on a study-based template and its WM skeleton (displayed in green). **Abbreviations:** AWF, axonal water fraction; FA, fractional anisotropy; FWER, family-wise error rate; OF, open field; TBSS, tract-based spatial statistics; TFCE, threshold-free cluster enhancement; WM, white matter.

On the other hand, the distance traveled in the arena of the OF test was strongly correlated to a multitude of DKI maps in both directions. We considered only those correlations that

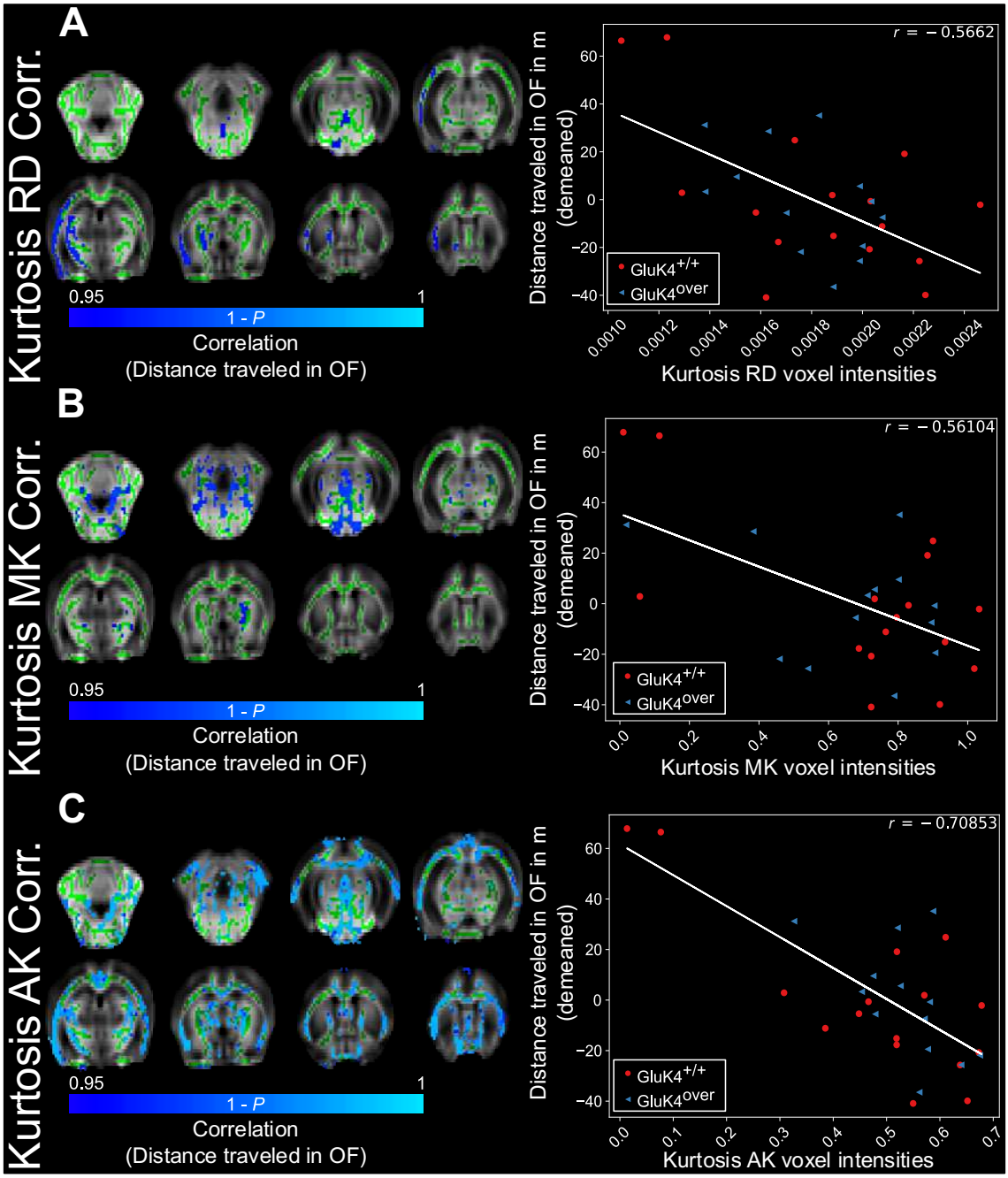

Fig. 33 | Kurtosis model maps show a significant negative correlation with the distance traveled in the OF arena in meters. (A) Regions showing anticorrelation correlation between the RD values and the distance traveled in the OF (left) and the linear regression of the voxel that shows the highest *P* value in the one-sample t-test (right). **(B)** MK maps (right) and linear regression of the highest voxel (left). **(C)** AK maps (right) and linear regression (left). All statistical maps are shown has *P* values < 0.05 (TFCE enhanced, FWER corrected). The statistical maps are overlaid on a study-based template and its WM skeleton (displayed in green). **Abbreviations:** AK, axial kurtosis; FWER, family-wise error rate; MK, mean kurtosis; OF, open field; RD, radial diffusivity; TBSS, tract-based spatial statistics; TFCE, threshold-free cluster enhancement; WM, white matter.

2.3.4. NODDI model

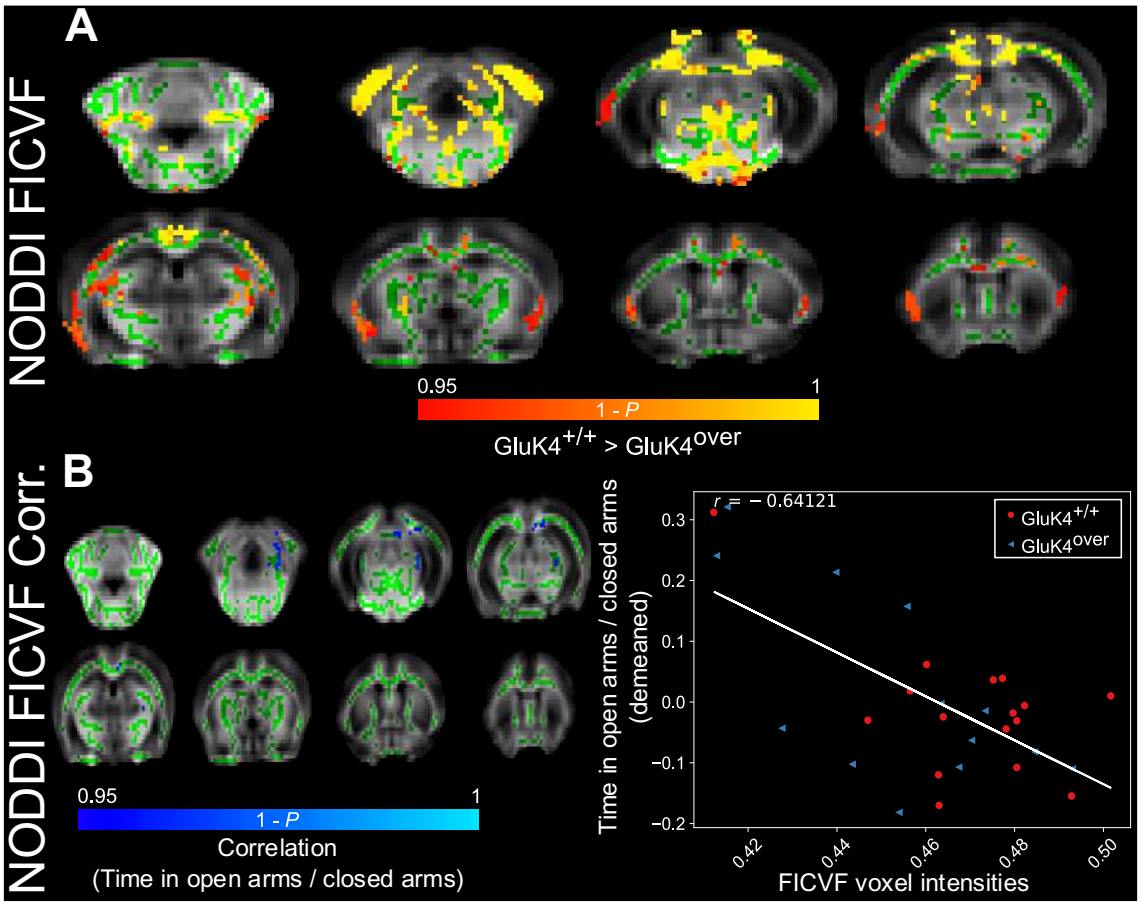

Fig. 34 | TBSS analysis of the NODDI maps. (A) Reveals a significant decrease in FICVF maps in GluK4^{over} animals with respect to the WT animals. **(B)** Shows structures with significant negative correlations with the ratio of the time spent in open arms/the time spent in the closed arms of the EPM (right) and the linear regression plot of the voxel with the highest *P* value (right). All statistical maps are shown has *P* values < 0.05 (TFCE enhanced, FWER corrected). The statistical maps are overlaid on a study-based template and its WM skeleton (displayed in green). **Abbreviations:** EPM, elevated plus maze; FICVF, intracellular volume fraction (neurite density); FWER, family-wise error rate; NODDI, neurite orientation dispersion and density imaging; OF, open field; TFCE, threshold-free cluster enhancement; TBSS, tract-based spatial statistics; WM, white matter; WT, wild-type.

The second biophysical model we fit to our data was the NODDI model (Zhang et al., 2012). NODDI model tries to probe the tissue microstructural properties by fitting a multi-compartment model to the DWIs. The fitting returns several maps reflecting different aspects of tissue microstructure including the neurite density and the orientation dispersion. Our TBSS analysis returned significant changes only in the neurite density maps (the FICVF maps). There was a significant decrease in the neurite density values in favor of the GluK4^{over} animals (Fig. 34A). Those changes were found in the genu, the body, the forceps minor and major, the splenium of the cc, the external and internal capsule, the dorsal hippocampal commissure, and the superior colliculus.

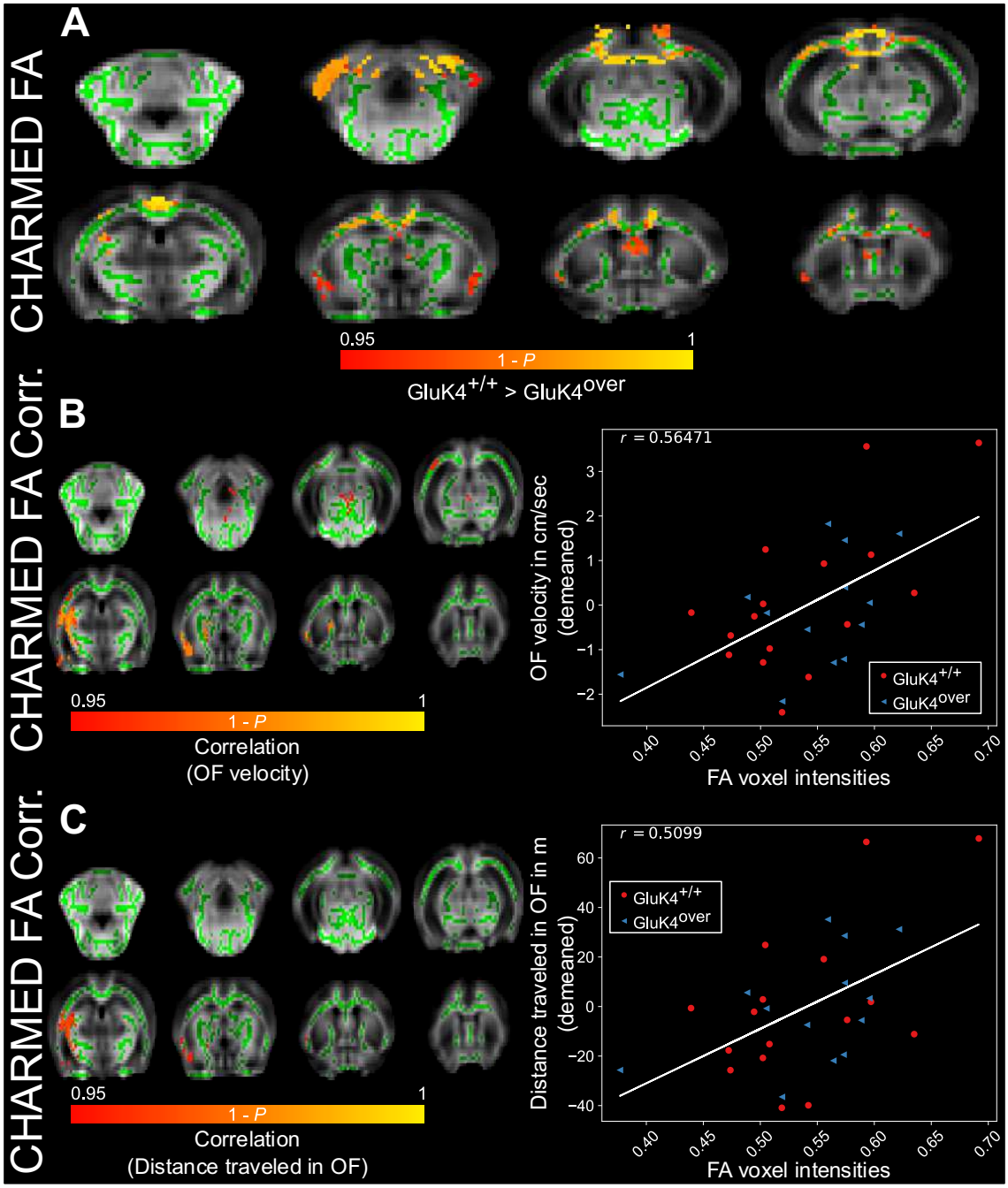

Fig. 35 | TBSS analysis of the FA maps of the CHARMED model. (A) Regions that show a significant decrease in the FA values in the GluK4^{over} animals. **(B)** Structures where FA values are significantly correlated with the velocity in the OF arena in cm/sec (left) and the linear regression plot of the voxel with the highest *P* value (right). **(C)** Structures where FA values are significantly correlated with the distance traveled in the OF arena in meters. All statistical maps are shown has *P* values < 0.05 (TFCE enhanced, FWER corrected). The statistical maps are overlaid on a study-based template and its WM skeleton (displayed in green). **Abbreviations:** CHARMED, composite hindered and restricted models of diffusion; FA, fractional anisotropy; FWER, family-wise error rate; OF, open field; TBSS, tract-based spatial statistics; TFCE, threshold-free cluster enhancement; WM, white matter.

We also observed an anticorrelation between the FICVF values and the ratio of the time spent in the open arms to the time spent in the closed arms of the EPM task (Fig. 34B). The significant correlations were limited to the splenium, the forceps major of the cc, and the dorsal hippocampal commissure (Fig. 34B). Whereas we failed to see any significant differences between the two groups in the ODI maps and moreover those maps did not display any correlations with behavioral measures that survived the multiple comparison correction.

2.3.5. CHARMED model

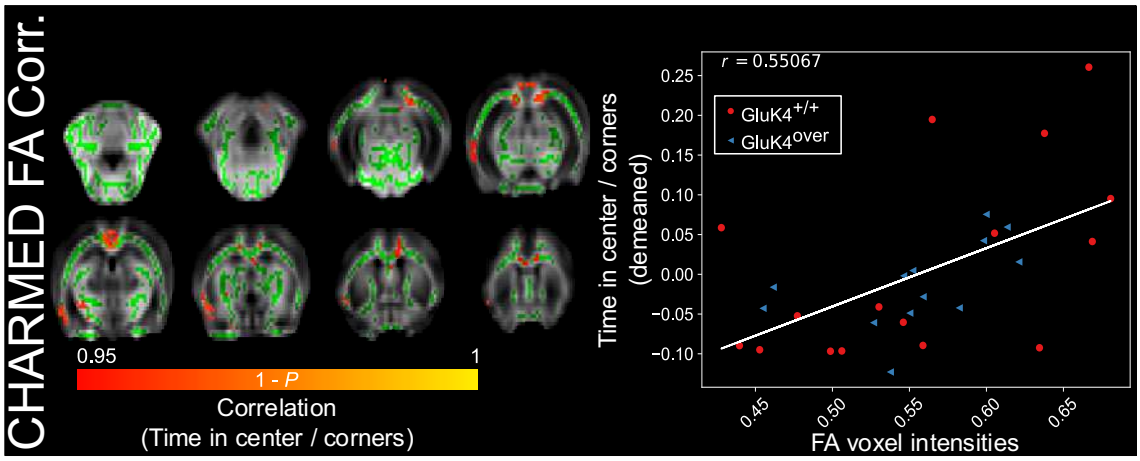

Fig. 36 | Voxel-wise analysis shows CHARMED FA values are positively correlated with the time spent in the spent / time spent the corners of the OF arena (left) and the linear regression plot of the voxel with the highest *P* value (right). All statistical maps are shown has *P* values < 0.05 (TFCE enhanced, FWER corrected). The statistical maps are overlaid on a study-based template and its WM skeleton (displayed in green). **Abbreviations:** CHARMED, composite hindered and restricted models of diffusion; FA, fractional anisotropy; FWER, family-wise error rate; OF, open field; TFCE, threshold-free cluster enhancement; WM, white matter.

The CHARMED model using a multi-compartment model (Assaf and Basser 2005) similar to the one used in the NODDI model previously discussed. The maps returned from fitting the model also give various information about different characteristics of the tissues investigated such as the IAD and FR along with the conventional FA, MD, RD, and AD maps the result from modeling the extracellular compartment as a tensor model (see above).

Akin to the DTI model, the FA values were significantly different between the two groups investigated. GluK4^{over} group suffered from a significant decrease in the FA values in the voxels spanning all the regions of the cc (the genu, body, splenium, and the forceps minor and major) in addition to the fornix, the fimbria, and the dorsal hippocampal commissure (Fig. 35A). Most of these regions showed a strong positive correlation with metrics

extracted from behavior tasks an especially the OF task, where the FA maps were found to be significantly correlated with the velocity in the arena (Fig. 35B), the distance traveled (Fig. 35C), and the ratio between the time spent in the center and the time spent in the corners (Fig. 36). The structures afflicted with such correlations varied slightly in each set of maps. For instance, while the body of the cc was found to correlate significantly with the time in center/time in corners measure (Fig. 36), that structure exhibited the same pattern neither with the velocity (Fig. 35B nor with the distance traveled (Fig. 35C) measures.

Comparing the FR maps between groups returned quite similar results to those of the FA maps; where FR values were found to be diminished in GluK4^{over} animals upon comparison with the WT counterparts (Fig. 37A). On the correlation with behavioral measures frontier, the FR values were found to be anticorrelated to both the speed and the distance traveled in the EPM arena instead of the OF one (Fig. 37B, C).

Changes in the IAD was in the same direction as the FA and FR maps (decreased in the GluK4^{over} animals), but not as widespread as the changes in those maps (Fig. 38A). Only minor changes were observed in a limited number of voxels in the external capsule, the forceps major of the cc, and the dorsal hippocampal commissure. The IAD values in the superior colliculus were found to be positively correlated with the ratio between time spent in the open arms and the time spent in the closed arms of the EPM (Fig. 38B).

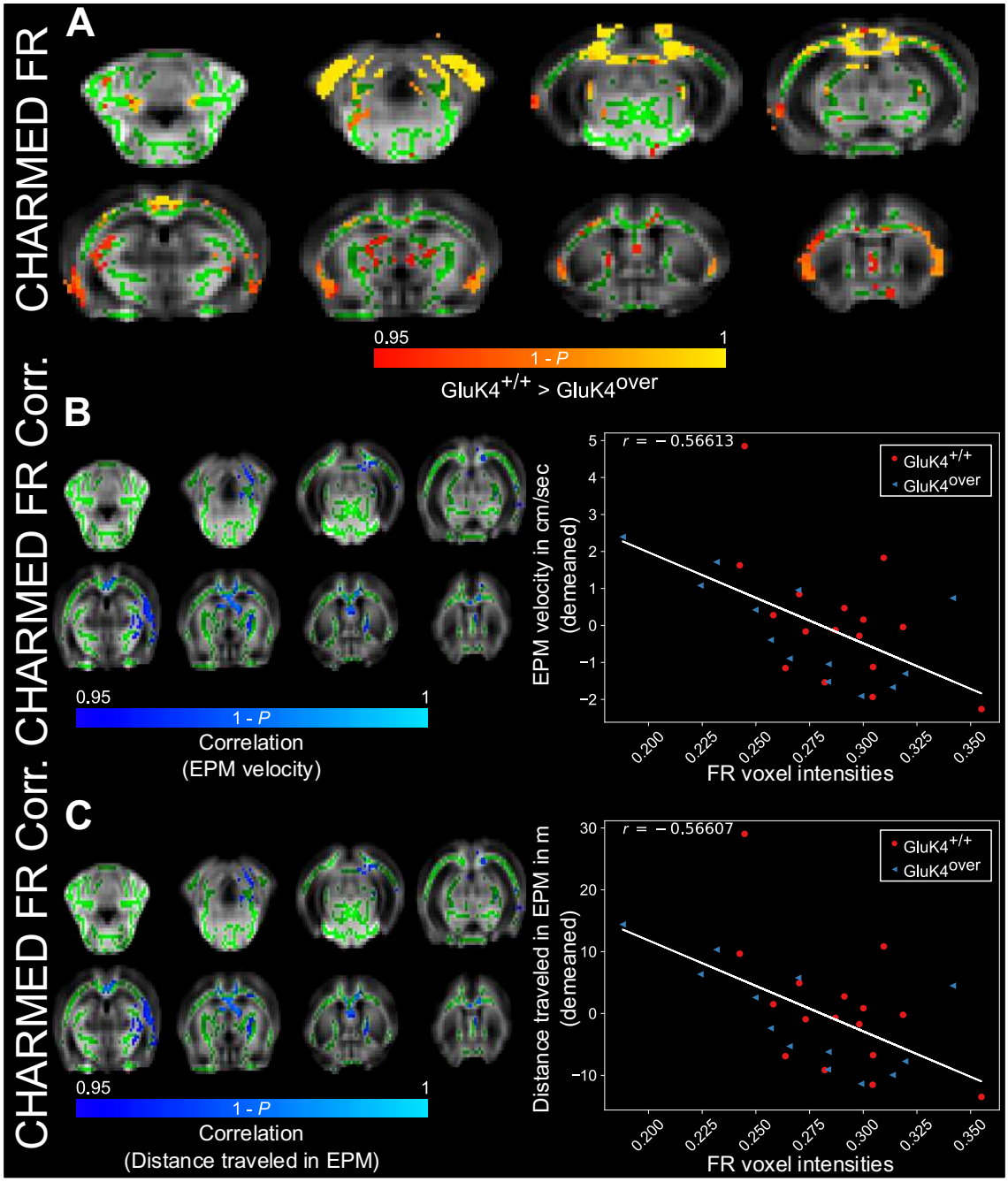

Fig. 37 | Voxel-wise analysis of the FR maps of the CHARMED model between the GluK4^{over} and GluK4$^{+/+}$ animals. (A) Regions where FR is significantly reduced in the GluK4^{over} animals when compared to control animals. **(B)** Structures with a significant negative correlation between the FR values and the velocity during performing the EPM task (left) and the linear regression plot of the voxel with the highest *P* value (right). **(C)** Structures with a significant negative correlation between the FR values and the distance traveled in the EPM arena (left) and the linear regression plot of the voxel with the highest *P* value (right). All statistical maps are shown has *P* values < 0.05 (TFCE enhanced, FWER corrected). The statistical maps are overlaid on a study-based template and its WM skeleton (displayed in green). **Abbreviations:** CHARMED, composite hindered and restricted models of diffusion; FR, restricted fraction; EPM, elevated plus maze; FWER, family-wise error rate; TFCE, threshold-free cluster enhancement; WM, white matter.

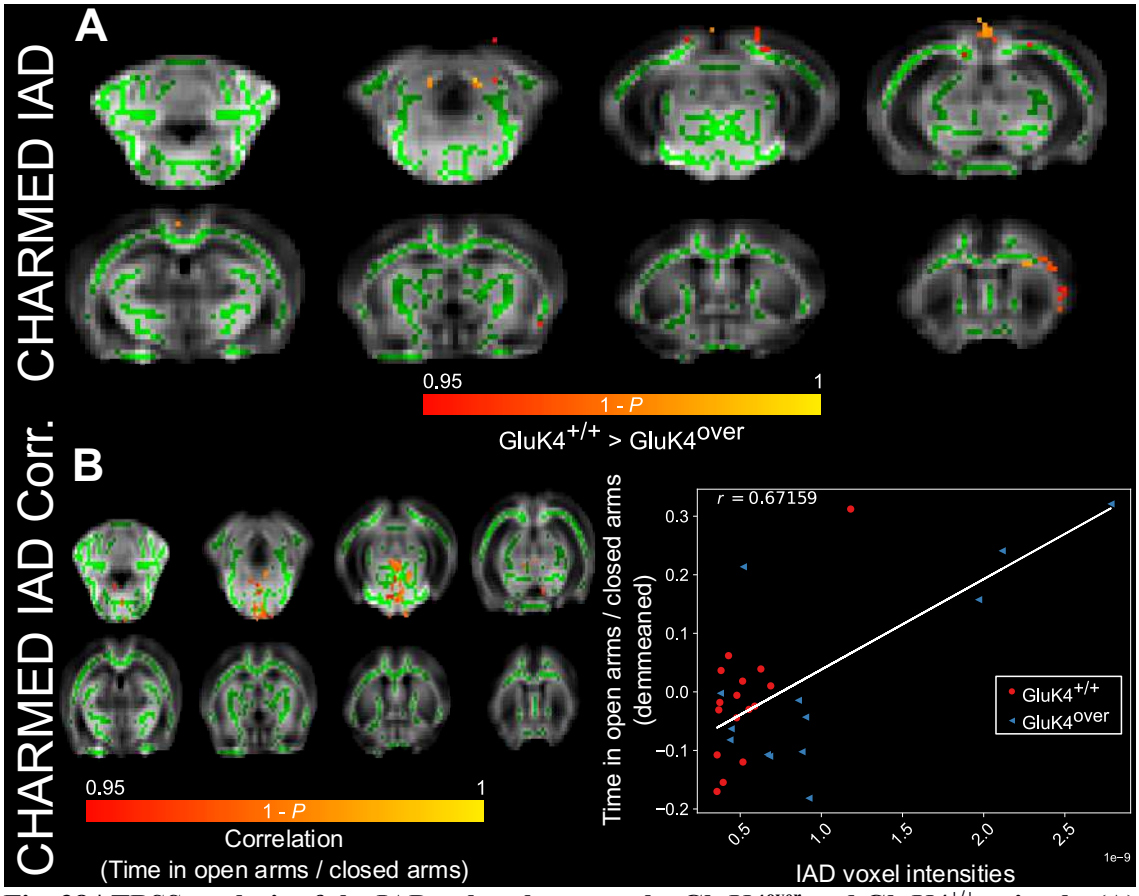

Fig. 38 | TBSS analysis of the IAD values between the GluK4^{over} and GluK4$^{+/+}$ animals. (A) Regions with decreased IAD values in the GluK4^{over} animals relative to WT. **(B)** Regions where the IAD values are correlated with the ratio of the time spent in the open arms to the time spent in the closed arms of the EPM arena (left) and the linear regression plot of the voxel with the highest *P* value (right). All statistical maps are shown has *P* values < 0.05 (TFCE enhanced, FWER corrected). The statistical maps are overlaid on a study-based template and its WM skeleton (displayed in green). **Abbreviations:** CHARMED, composite hindered and restricted models of diffusion; EPM, elevated plus maze; FWER, family-wise error rate; IAD, intra-axonal diffusivity; TBSS, tract-based spatial statistics; TFCE, threshold-free cluster enhancement; WM, white matter; WT, wild-type.

2.3.6. FBA analysis

The models we used to fit to our data whether in the simplest form such as the tensor model or more elaborate as in the case of the kurtosis, the NODDI, or the CHARMED models, typically return voxel-averaged measures. Despite the ability of some of these models such as the CHARMED to resolve the contributions of crossing fibers, theoretically at the very least, they remain unable to pin the changes to a certain fiber population within each analysis unit (i.e., the voxel). To tackle such shortcomings and in order to complement our results, we used the newly introduced FBA (Raffelt et al., 2017) as implemented in the MRtrix3 software (Tournier et al., 2019). FBA approach tries to quantify the micro and macrostructural changes in the different fiber populations within each

voxel; hence the name fixel (fiber population within a voxel) in FBA (Raffelt et al., 2015). Using that approach enabled us to get information about the fibers density and their cross-sectional differences between our two groups.

We estimated the FOD functions from the response functions obtained from the WM, the GM, and the CSF. We ascertained that each FOD was estimated correctly to reflect the contributions from the respective tissue compartment (Fig. 39). Figure 2.23 shows the three estimated FODs from a representative subject displayed in different colors and as evident from the figure, each color reflects a different tissue type. The WM FOD from all subjects were used to construct a group-based template (Fig. 40A, B). The FODs of the template were later converted to fixels (Fig. 40C) and used to run the probabilistic tractography (Fig. 40D). The metrics for the FD, FC, and FDC were derived from the fixels and were compared (see Introduction and Fig. 10 for more information) between the two groups across the tractogram (Fig. 40D).

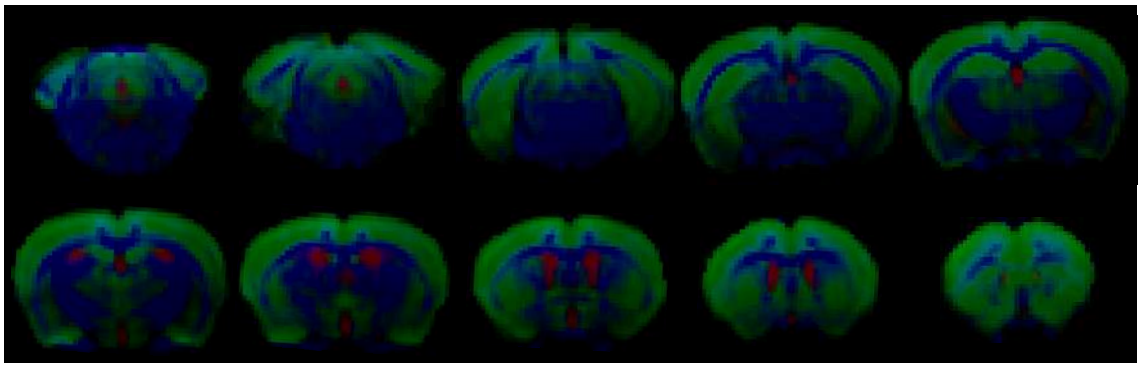

Fig. 39 | Estimation of the multi-tissue FODs. The FODs estimated from each tissue was converted to a different color (blue for WM, green for GM, and red for CSF). The figure shows how accurately the FODs are determined and not distorted by the partial volume effect between different tissue types. **Abbreviations:** CSF, cerebrospinal fluid; FOD, fiber orientation distribution; GM, gray matter; WM, white matter.

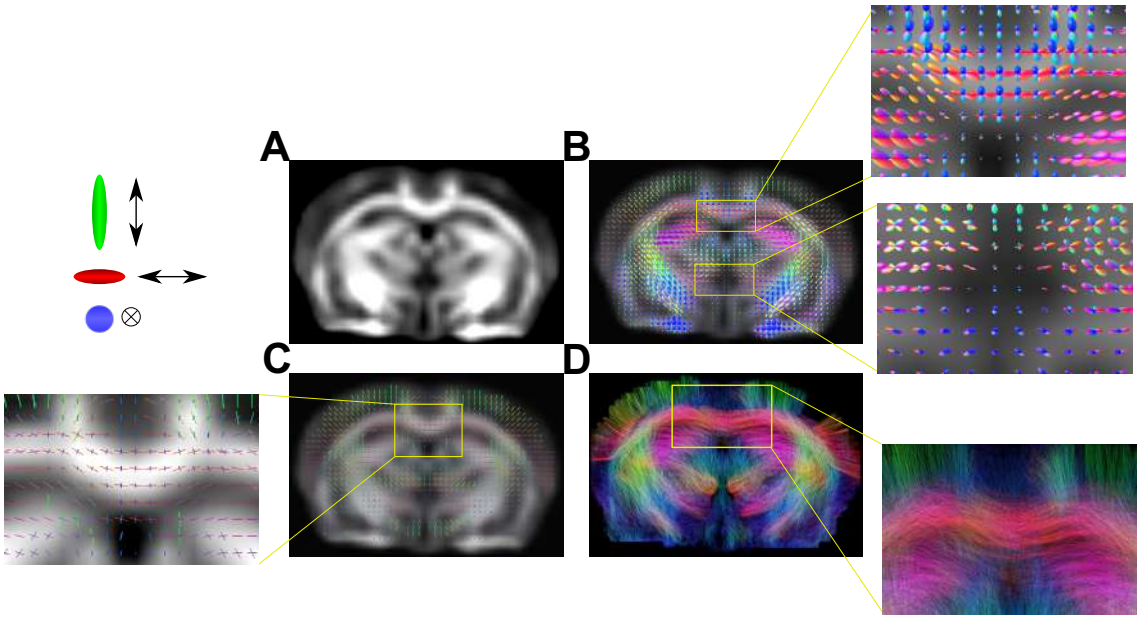

Fig. 40 | Group-based template of the WM FODs from all subjects. (A) Shows the template in grayscale with the WM appearing in white. **(B)** FODs of the group-based template with two zoomed regions in yellow boxes; part of the cc showing the probability distribution of the fibers orientation mainly going horizontally (up) and part of the GM and CSF tissues with the probability distribution of the fibers going in all directions (down). **(C)** Fixels derived from the template FODs with an enlarged region of the cc in the yellow box showing the direction of the fixels going horizontally. **(D)** Probabilistic tractogram derived from the template showing in the yellow box the direction of the fibers of the cc in red (horizontally) and in green parts of the fibers run vertically in the cortex. **Abbreviations:** cc, corpus callosum; CSF, cerebrospinal fluid; FOD, fiber orientation distribution; GM, gray matter; WM, white matter.

FBA shows a significant decrease in all three measures (FD, FC, and FDC) in the GluK4^{over} animals compared to the GluK4$^{+/+}$ animals (Fig. 41). However, the magnitude and distribution of these changes vary considerably between the three metrics. Microstructural fiber density (FD measure) decreased significantly in the GluK^{over} animals in the genu and body of the cc, the external capsule, the dorsal hippocampal commissure, and the forceps major of the cc (Fig. 41A). These changes were more widespread in the case of log (FC) where the macrostructural differences were observed the whole length of the cc in addition to the fimbria, the dorsal hippocampal commissure, and parts of the superior colliculus (Fig. 41B). The differences in the combined measure of the FD and FC (FDC) showed similar spatial spread across the previously mentioned structures (Fig. 41C).

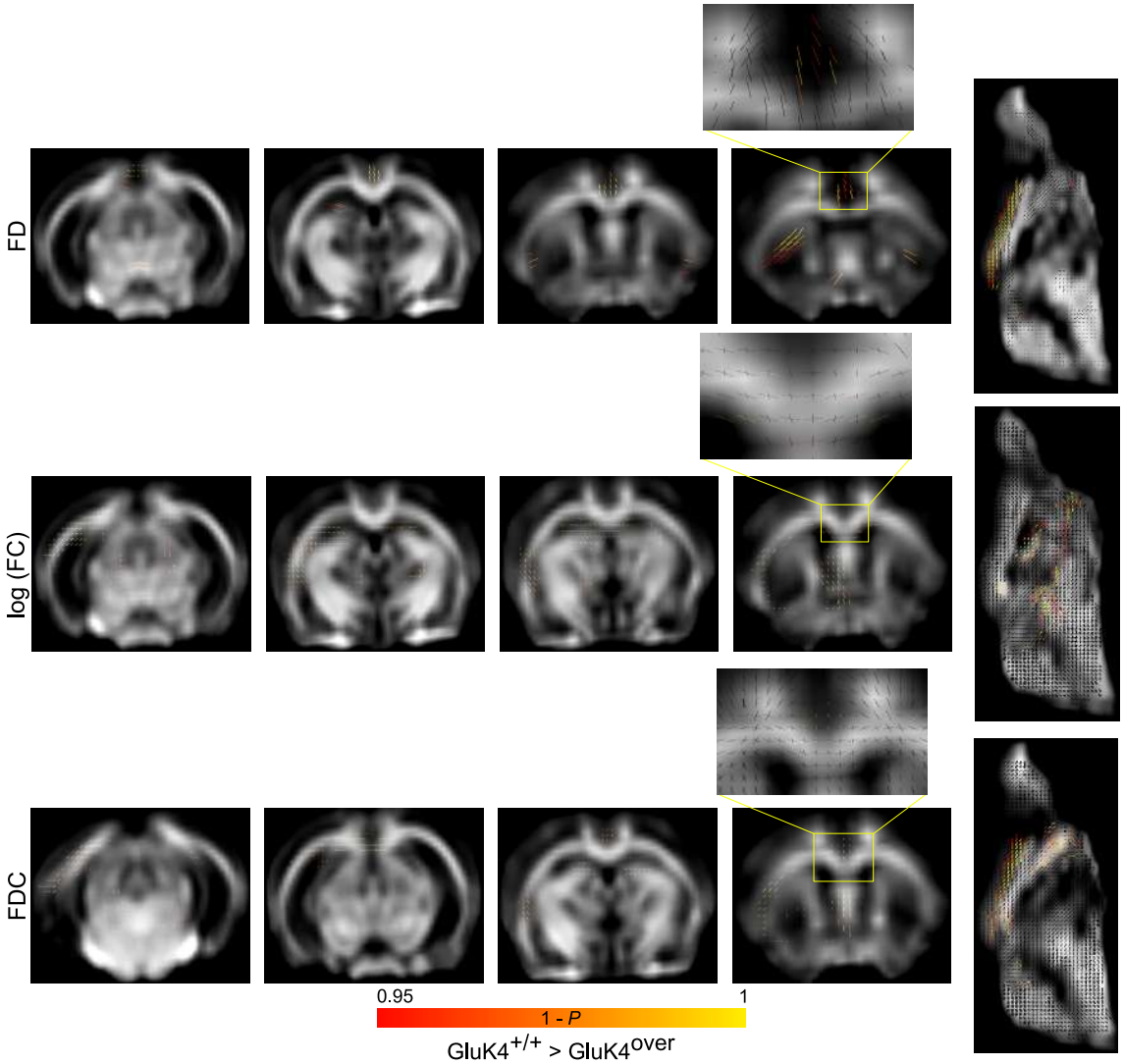

Fig. 41 | FBA analysis shows fixels with a significant decrease in the microstructural as well as in the macrostructural measures in the GluK4^{over} in comparison with the GluK4$^{+/+}$ animals. (A) Shows the differences between the two groups in the FD microstructural measure. (B) Differences in the log of the FC macrostructural measure. (C) Differences in the FDC combined measure of FD and FC. All statistical maps are shown has *P* values < 0.05 (TFCE enhanced, FWER corrected). The statistical maps are overlaid on a group-based FOD template of the WM. **Abbreviations:** FBA, fixel-based analysis; FC, fiber cross-section; FD, fiber density; FDC, combined measure of fiber density and cross-section; FOD, fiber orientation distribution; FWER, family-wise error rate; TFCE, threshold-free cluster enhancement; WM, white matter.

2.3.7. Statistics across the cc tracts

While voxel-wise analysis represented by the TBSS analysis can give us an idea about the changes between the group in a voxel-by-voxel manner, we sought after other types of analyses that can give us an idea about the average changes across whole structures such as the cc. We ran deterministic tractography on each subject and extracted the fibers that represent the whole cc (Fig. 42A, B, C). We then calculated the average values of each map previously investigated using TBSS (see above) across the tracts of the cc. The

global changes in the cc tracts reflected, to some extent, the same results we previously encountered upon using the TBSS (Fig. 30-38). There were significant decreases in the DTI FA, DTI AD, kurtosis FA, CHARMED FA, and NODDI FICVF in the GluK4^{over} animals with respect to their GluK$^{+/+}$ counterparts (Fig. 42D). There was a significant increase in the average ODI values across the cc tracts in the GluK^{over} animals that we could not observe using the voxel-wise analysis. Adversely, the voxel-wise analysis unearthed differences in the MD and RD values of the tensor model along with changes in the FR values of the CHARMED model that did not pass the significance threshold in the tract-based analysis. The changes might not be this big or not distributed uniformly across the tracts of the cc; such that to reach the same findings, we need to segment the cc to smaller tracts.

We also compared some descriptive measures of the cc tracts such as the length and number of fibers among other things. However, we could not find any significant differences between the two groups to be reported (results not shown).

The differences observed in dMRI point at fundamental changes in the microstructure of the major WM fibers. These changes were reflected in different measures calculated from various models (Table 1). We can interpret these findings in different manners. We tend to think that what we are witnessing is a loss of myelination or axonal thickness in various tracts such as the cc and the hippocampal commissure. The correlation of the dMRI parameters with the behavior further augment our conjecture.

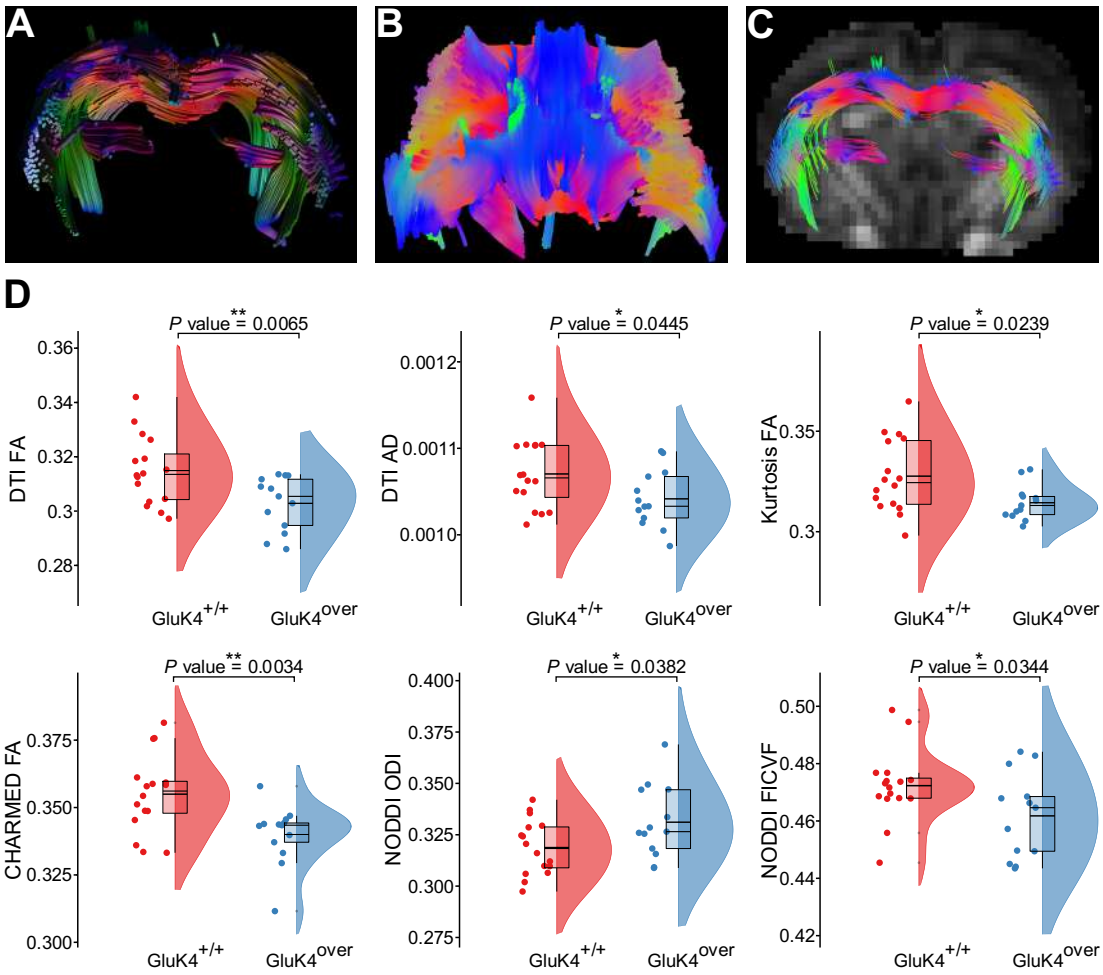

Fig 42 | tract-based statistics along the cc fibers. (A) Shows the cc fibers from a representative subject. **(B)** A different view of the cc fibers from the top. **(C)** The same cc fibers overlaid on a coronal slice of an FA map. Tracts are color-coded, red fibers run horizontally, green fibers run vertically, and blue fibers run anterior-posterior. **(D)** Raincloud plots (Allen et al., 2019) of the cc tracts measures that showed significant differences between the two groups. *$P \leq 0.05$ and **$P \leq 0.01$. **Abbreviations:** AD, axial diffusivity; CHARMED, composite hindered and restricted models of diffusion; DTI, diffusion tensor imaging; FA, fractional anisotropy; FICVF, intracellular volume fraction (neurite density); NODDI, neurite orientation dispersion and density imaging; ODI, orientation dispersion index.

2.4. Voxel-based morphometry analysis

VBM analysis presented itself as the go-to method in investigating volumetric changes in the intact brain (Ashburner and Friston 2000). While the technique can be quite straight forward in brain images acquired from humans or non-human primates, the process can be rather tricky in small animals like mice. The most arduous step is segmenting the structural 3D images into GM, WM, and CSF priors. We exploited the newly introduced TMBTA template and its priors (Barrière et al., 2020) in order to get the most faithful segmentation of the tissues. We used our subjects to construct a study-based template

(Fig. 43A), registered this template to the TMBTA template, and used the inverse transformations to bring the GM (Fig. 43B), the WM (Fig. 43C), the CSF (Fig. 43D), and the parcellation atlas (Fig. 43E) to our study-template space.

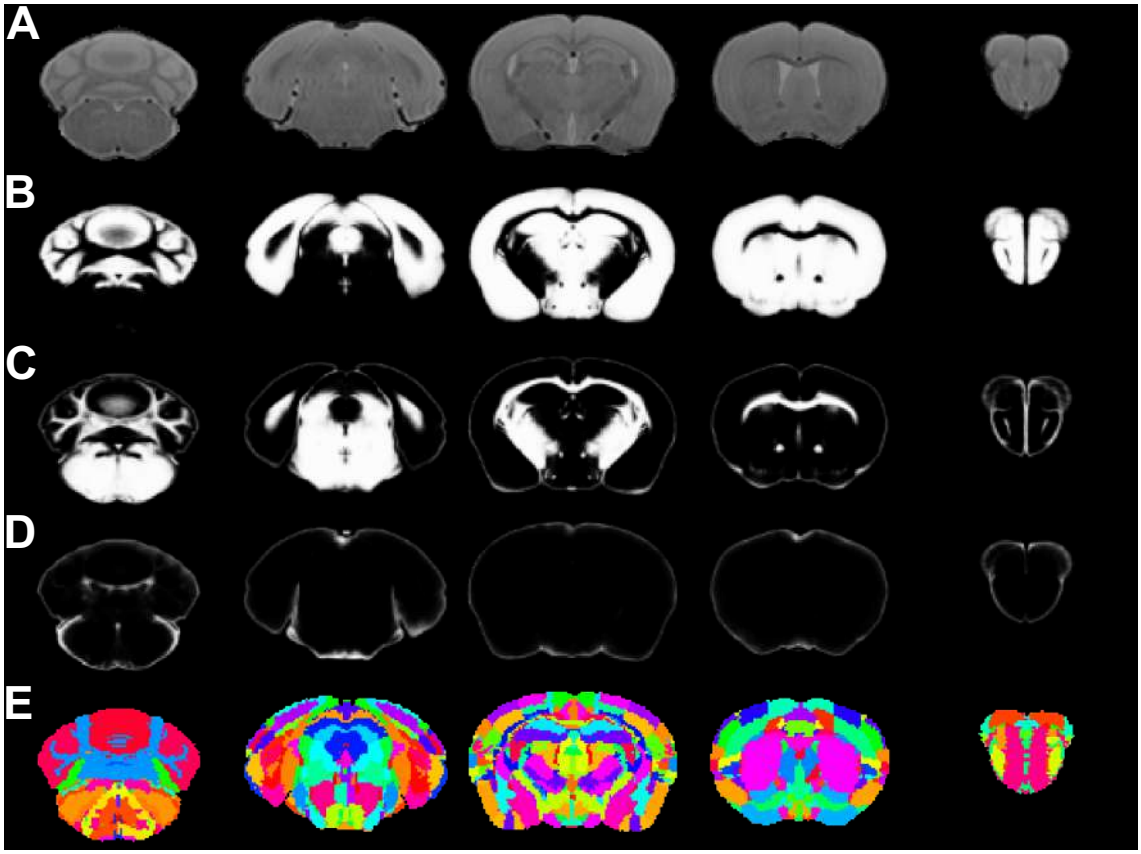

Fig. 43 | VBM study-based template and its priors and atlas calculated from all subjects. (A) Shows the template after extracting the skull. **(B)** The GM prior. **(C)** The WM prior. **(D)** The CSF prior. **(E)** The atlas parcellation. Those priors and atlas were calculated by registering the study-based template to the TMBTA high-resolution template (Barrière et al., 2020) and apply the inverse transformations to bring the priors and atlas to the in-house template. **Abbreviations:** CSF, cerebrospinal fluid; GM, gray matter; TMBTA, Turone mouse brain template and atlas; VBM, voxel-based morphometry; WM, white matter.

On the single subject's level (Fig. 44A), we removed the skull tissue (Fig. 44C), registered each subject to the study-based template (Fig. 43), and used the previously calculated priors to obtain an accurate segmentation of the GM (Fig. 44C). We proceeded to calculate the Jacobian determinants (Fig. 44D) for each subject from the non-linear warp transformations and modulated the GM priors by multiplying them by those determinants (Fig. 44E). The smoothed modulated GM images (Fig. 44F) were later used for the actual statistical analysis.

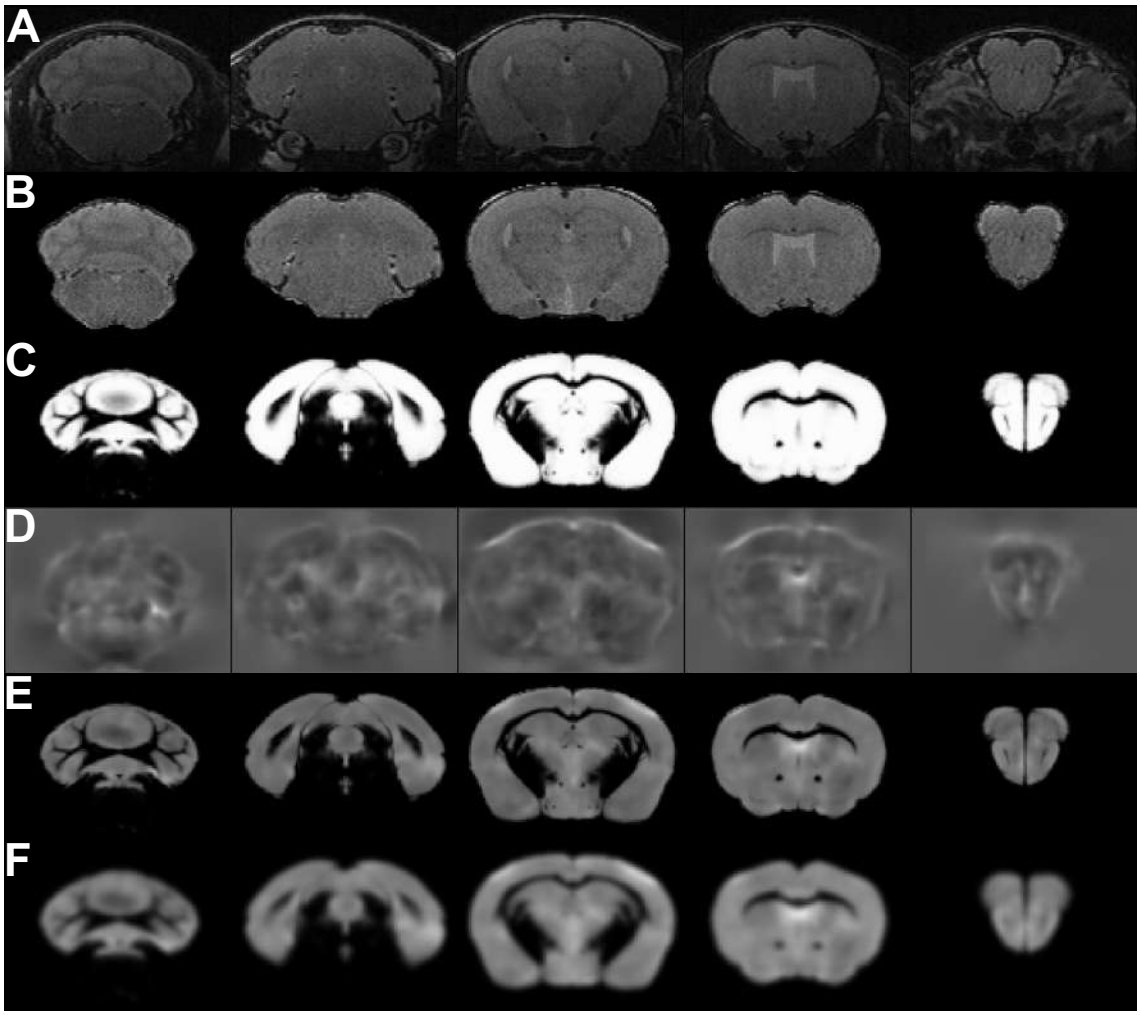

Fig. 44 | Processing of a single subject's 3D structural image. (A) Shows the raw data of the subject. **(B)** Skull removal. **(B)** The GM prior. **(D)** The Jacobian determinants calculated from the warp field of the non-linear transformations. **(E)** Modulated GM after multiplying by the Jacobian determinants. **(F)** Smoothed modulated GM image after applying the smoothing kernel. **Abbreviations:** GM, gray matter.

VBM analysis revealed multiple robust differences in both directions between the GluK4^{over} animals and the WT group (Fig. 45A). GluK4^{over} animals presented a significant shrinkage in multiple subcortical structures including the hippocampus, the striatum, the thalamus, and the cerebellum. These changes were localized in the piriform cortex, the caudate putamen, the accumbens nucleus, the septal nucleus, the bed nuclei of the stria terminalis, the globus pallidus, the hypothalamic nuclei, the thalamic nuclei, the CA1 region of the hippocampus, the dentate gyrus, the subiculum, the nucleus raphe, regions of the superior and inferior colliculus, and parts of the cerebellum (Fig. 45A). These volumetric decreases were accompanied by the expansion of several regions of the cortex in favor of the GluK4^{over} animals (Fig. 45A). The prelimbic cortex, the olfactory nucleus, the insular cortex, the orbital cortex, the primary and secondary motor cortex, the

cingulate cortex, the primary and secondary somatosensory cortex, the retrosplenial cortex, the primary and secondary visual cortex, the entorhinal cortex, and the amygdala are all structures that showed a significant volumetric increase in the GluK4^{over} group relative to the other group (Fig. 45A). The differences in both cases (shrinkage and expansion) were quite bilateral and symmetric across the midline. These results were robust enough to survive a quite drastic way of correction for multiple comparisons such as FWER correction.

We performed a ROIs analysis as well across the whole regions that exist in the TMBTA atlas parcellation (Barrière et al., 2020) with 1320 ROIs. The results of the analysis unearthed multiple structures with $P < 0.05$, however, they were not robust enough to survive the FWER multiple comparison correction across all the ROIs included in the analysis. We did not consider any results that did not survive the correction.

Aside from the volumetric differences between the two groups, we found also some structures with strong correlations with some aspects of the behavior (Fig. 45B, C). The volumes of the lateral septal nucleus and the bed nuclei of the stria terminalis appeared to be positively correlated with the ratio between the time spent in the open arms and the time spent in the closed arms of the EPM (Fig. 45B). Conversely, this ratio was found to be negatively correlated with the volumes of the restrosplenial cortex, the cingulate cortex, the prelimbic cortex (Fig. 45C). These correlations were found to be significant after performing the one-sample t-test and they survived the FWER correction for multiple comparisons.

These volumetric changes strongly suggest that the effects of the GluK4 overexpression are not fixed across the whole brain (Table 1). This extra copy of the *Grik4* gene seems to have a structure-sensitive effects, where its presence in one region can mean expansion, while in other regions can mean shrinkage.

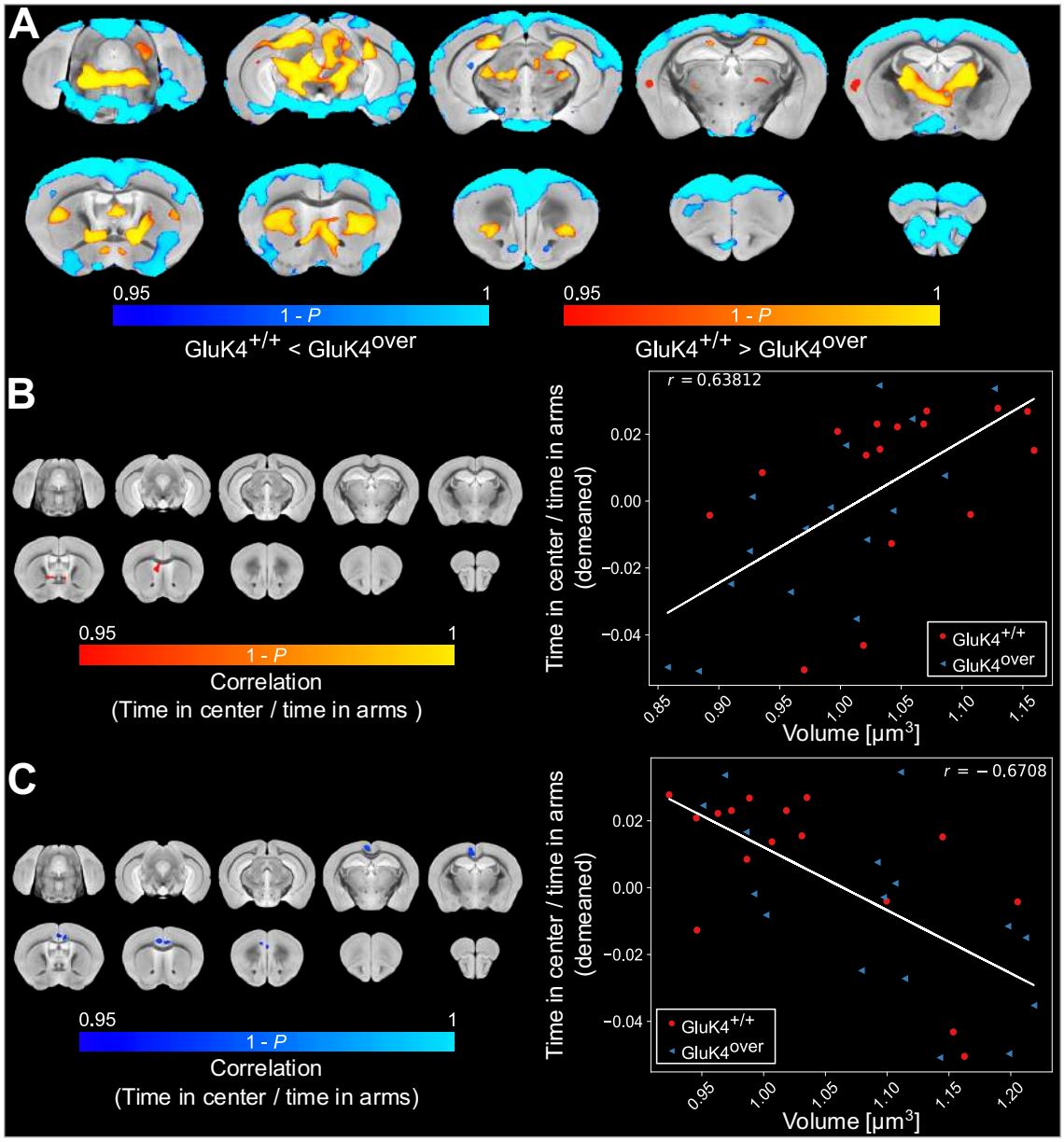

Fig. 45 | VBM analysis reveals multiple structural changes between the GluK4^{over} and GluK4$^{+/+}$ animals. (A) Voxel-wise comparison between the two groups; structures that witnessed shrinkage in GluK4^{over} animals with respect to the control group are shown in red-yellow, structures with expansion in GluK4^{over} animals are shown blue-light blue. **(B)** Structures with significant positive correlation with the time spent in open arms/time spent in closed arms of the EPM (left) and the linear regression plot of the voxel with the highest *P* value (right). **(C)** Structures with significant negative correlation with the time spent in open arms/time spent in closed arms of the EPM (left) and the linear regression plot of the voxel with the highest *P* value (right). All statistical maps ($P < 0.05$) are TFCE enhanced, FWER corrected for multiple comparisons, and overlaid on AMBMC high-resolution template. *P* values are shown as $1 - P$ (an increase means more significant). **Abbreviations:** AMBMC, the Australian mouse brain mapping consortium; EPM, elevated plus maze; FWER, family-wise error rate; TFCE, threshold-free cluster enhancement; VBM, voxel-based morphometry.

Table 1 | Summary of the multi-modal results.

Modality	Sub-modality	Affected structures (GluK4^{over} vs GluK4$^{+/+}$)
rsfMRI	Within-network strength	↑Strength: olfactory bulbs, cortex, hippocampus, cerebellum.
	Between-networks strength	↓Strength: motor cortex-hypothalamus.
dMRI	DTI	↓FA: cc/ec, fi, f, hc. ↑MD: hc. ↑RD: cc/ec, fi, f, hc. ↑AD: sc.
	Kurtosis	↓FA: cc, hc.
	NODDI	↓FICVF: cc/ec, ic, hc, sc.
	CHARMED	↓FA: cc/ec, fi, f, hc. ↓FR: cc/ec, ic, fi, f, hc. ↓IAD: cc/ec, hc.
	FBA	↓FD: cc/ec,hc. ↓FC: cc, fi, hc, sc. ↓FDC: cc/ec, fi, hc, sc.
VBM	Modulated GM	↑GM volume: cortex, Amg. ↓GM volume: hippocampus, striatum, thalamus, cerebellum.

Abbreviations: AD, axial diffusivity; Amg, amygdala; cc, corpus callosum; CHARMED, The composite hindered and restricted models of diffusion; dMRI, diffusion MRI; DTI, diffusion tensor imaging; ec, external capsule; f, fornix; FA, fractional anisotropy; FBA, fixel-based analysis; FC, fiber cross-section; FD, fiber density; FDC, combined measure of fiber density and cross-section.; fi, fimbria; FICVF, intra-cellular volume fraction (neurite density); FR, restricted fraction; GM, gray matter; hc, hippocampal commissure; IAD, intra-axonal diffusivity; ic, internal capsule; MD, mean diffusivity; NODDI, neurite orientation dispersion and density imaging; RD, radial diffusivity; rsfMRI, resting-state fMRI; sc, superior colliculus; VBM, voxel-based morphometry.

3. Stimulation of the perforant pathway and the CA3

We stimulated two different regions within the brain in order to investigate the functional ramifications of the increased dosage of the *Grik4* gene. While we used the rsfMRI to give us a window into the functional effects of the overexpression of Grik4 on the brain at rest, the stimulation experiments complemented those experiments by looking at the brain reactions upon applying external stimuli to different brain structures.

We used MRI-compatible glass electrodes with conductive threads of carbon to apply micro-electrical stimulation to the perforant pathway (Fig. 46A, C) and to the CA3 region of the hippocampus (B, D). Using electrodes to apply direct stimulation makes it feasible to target and activate deep brain structures such as the hippocampus that would not be accessible otherwise (Perez-Cervera et al., 2018). The stimulation protocols consisted of 10 cycles, 30 sec each (Canals et al., 2008); such that 4 sec of stimulation is followed by 26 sec of rest to allow the hemodynamic response to stabilize back to the base level. We used four different frequencies: 5, 10, 20, and 40 Hz.

3.1. Quality and nature of the BOLD signal

The artifacts induced by our glass electrodes were small and quite limited (Fig. 46). We covered the exposed parts of the skull with toothpaste and further covered the whole skull, above and around the electrode, with agarose gel (Fig. 46A, B). Using all of these measures, we managed to decrease the susceptibility artifacts and to acquire an excellent signal (Fig. 47). As evident from Fig. 46, both the anatomical and the EPI images have limited artifacts and minor signal dropouts (Fig. 46A-D). Limited as they were, the electrodes artifacts were visible enough to ascertain that the electrodes are positioned correctly to stimulate the desired structure. Based on those artifacts, we were able to exclude animals with extensive structural damages and animals with electrodes inserted incorrectly.

Stimulating the perforant pathway as well as the CA3 region (800 μAmp) led to an activation of the hippocampus and the dentate gyrus (Fig. 47). The activation varied relative to the structure stimulated as well as to the frequency of the stimulation. Despite the close similarity of the activation patterns between our two groups, some differences still presented themselves. We used the canonical double-gamma function to model the BOLD hemodynamic response from our data (Fig. 48). The canonical function described our data quite nicely with a small deviation pertinent to a slightly-shifted peak that might have resulted from the sampling rate (Fig. 48).

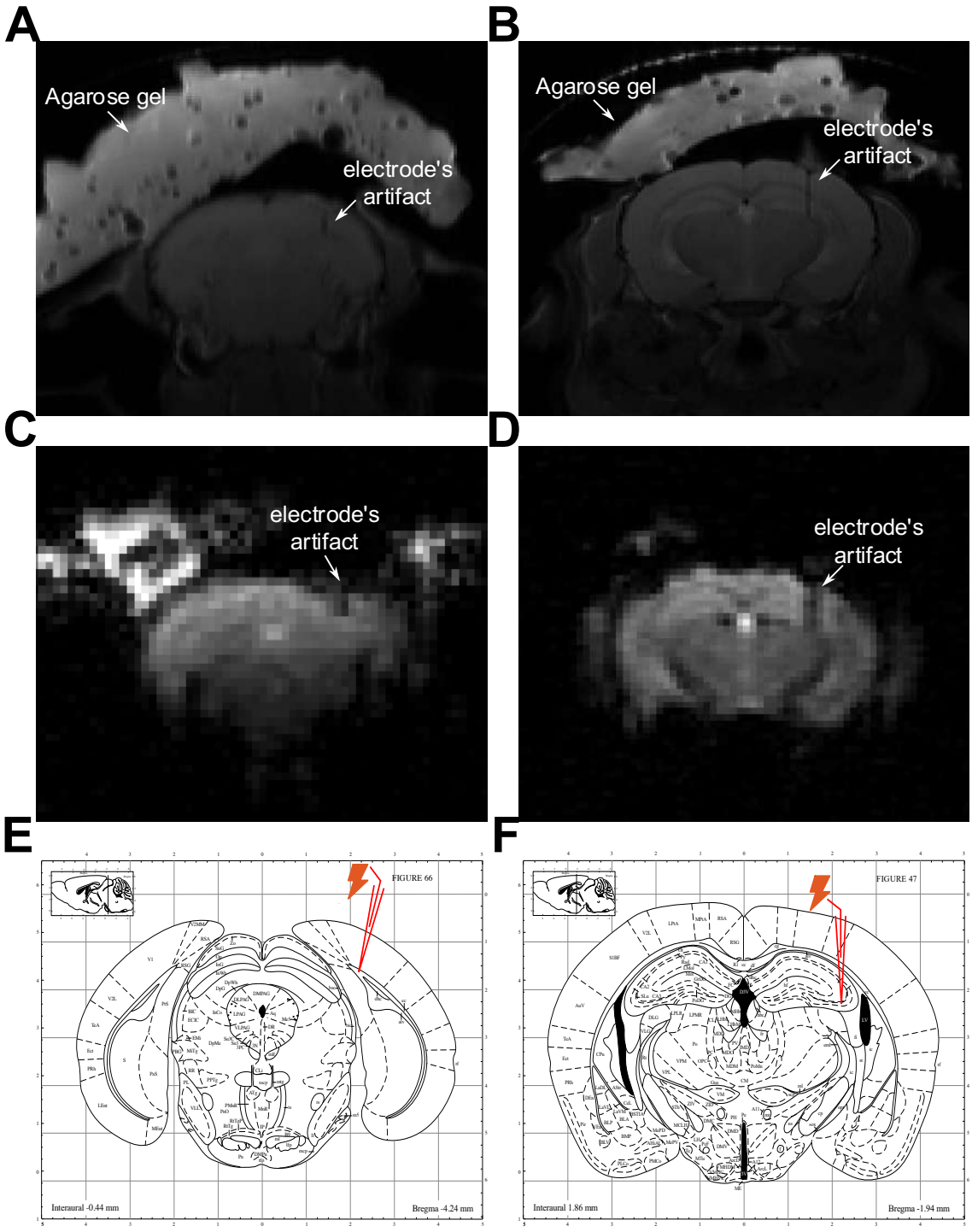

Fig. 46 | Raw anatomical and EPI images showing the placement of the electrodes. (A, B) The placement of the electrode in the anatomical image in the perforant pathway **(A)** and the CA3 region **(B). (C, D)** The location of the electrodes in the perforant pathway **(C)** and in the CA3 region **(D)** in an EPI image. **(E, F)** Planes from Paxinos' mouse atlas (Paxinos and Franklin 2004) showing the insertion location of the electrodes in the perforant pathway **(E)** and the CA3 region **(F).** The small white arrows are showing the places of the electrodes' artifacts and agarose gel used to decrease the magnetic susceptibility. **Abbreviations:** EPI, echo-planar imaging.

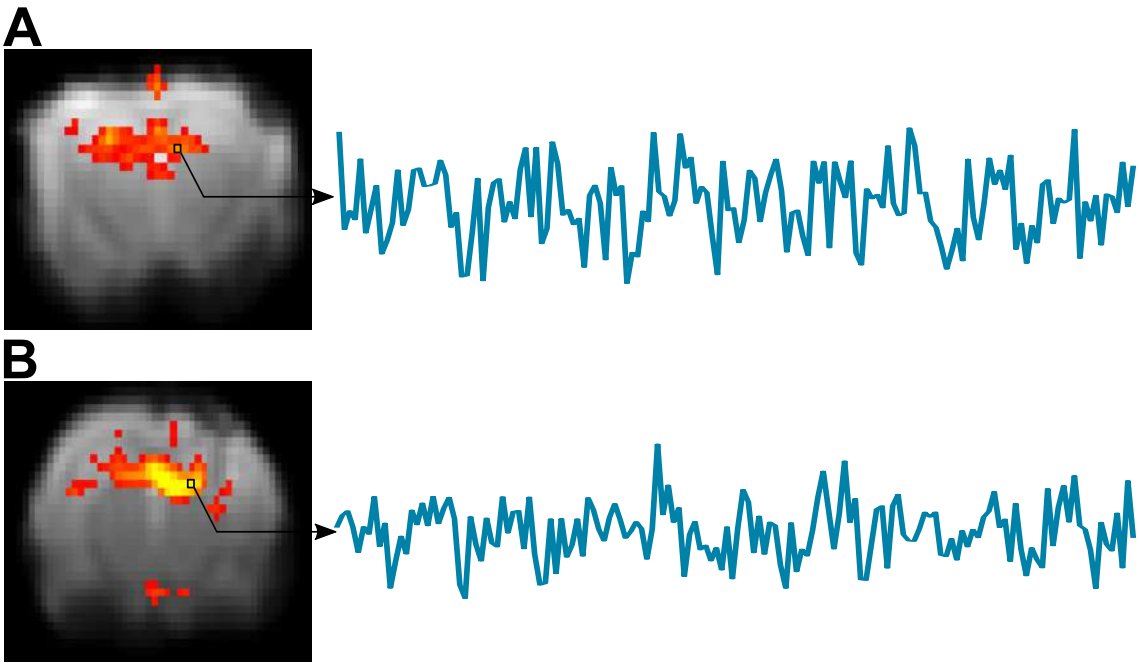

Fig. 47 | BOLD activation maps and signal time-series from a single subject. (A) Activation map from a single subject upon activating the perforant pathway (left) and the time-series from a single voxel (right). **(B)** Activation map from a single subject upon stimualting the CA3 region (left) and the single voxel time-series (right). Both activation maps are overlaid on an EPI functional image. Abbreviations: **EPI**, echo-planar imaging.

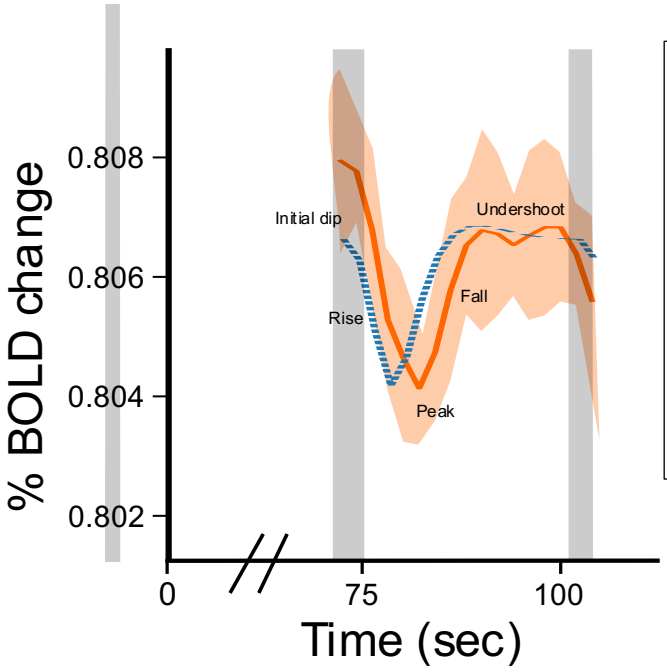

Fig. 48 | BOLD Hemodynamic response function. An example showing percentage change in the BOLD hemodynamic response averaged across multiple subjects (orange line) and the canonical double-gamma function used to model the response (dashed blue line). The orange shading represents the SEM. The is inverted to signal that response we get is a negative BOLD response. **Abbreviations:** BOLD, blood-oxygenation-level dependent; SEM, standard error of the mean.

3.2. Frequency-dependent activation and propagation upon stimulating the perforant pathway

The electrical stimulation in all the experiments using different frequencies evoked a negative BOLD response (Lauritzen et al., 2012) in all the animals tested regardless of the

genotype (Fig. 49-55). We did not detect any positive activation in any experiment which might signal to an effect of the blood vessels initiated by the urethane anesthetic used to perform the experiments. As visible from the BOLD percentage changes in Figures 49-55, the signal decreases below the base level after each epoch of stimulation.

Stimulating the perforant pathway elicited activation in the whole hippocampus regions including the CA1, CA2, CA3, and the dentate gyrus (Fig. 49-52) in a frequency-dependent manner. Applying a frequency with 5 cycles per second (5 Hz) during the 4-sec stimulation protocol did not induce any visible activation in the hippocampal or the extra-hippocampal structures in most of the subjects tested; we stopped acquiring images using the 5 Hz stimulation protocol after the first few animals in order to save time.

Applying electrical stimulation with frequencies higher than 5 Hz (i.e., 10, 20, and 40 Hz) evoked responses in almost all of our animals. The stimulation patterns varied as a function of the frequency as well as a function of the genotype. Stimulation with 10 Hz frequency in the GluK4$^{+/+}$ animals evoked a detectable BOLD response in wide regions of the dentate gyrus, the CA1, and the CA3 regions of the hippocampus ipsilaterally along with an extra-hippocampal structure such as the subiculum that was activated as well (Fig. 49A); while in the side opposite to the electrode (contralateral side), activity was detected only in limited regions of the dentate gyrus, CA1, and CA3 (Fig. 49A). As for the GluK4^{over} animals, there was a light activation detected in the dentate gyrus, the CA3 regions with no activation in the CA1 or any extra-hippocampal structure in the side ipsilateral to the electrode (Fig. 49B); in the other side of the brain, there was no activation evoked at all (49B).

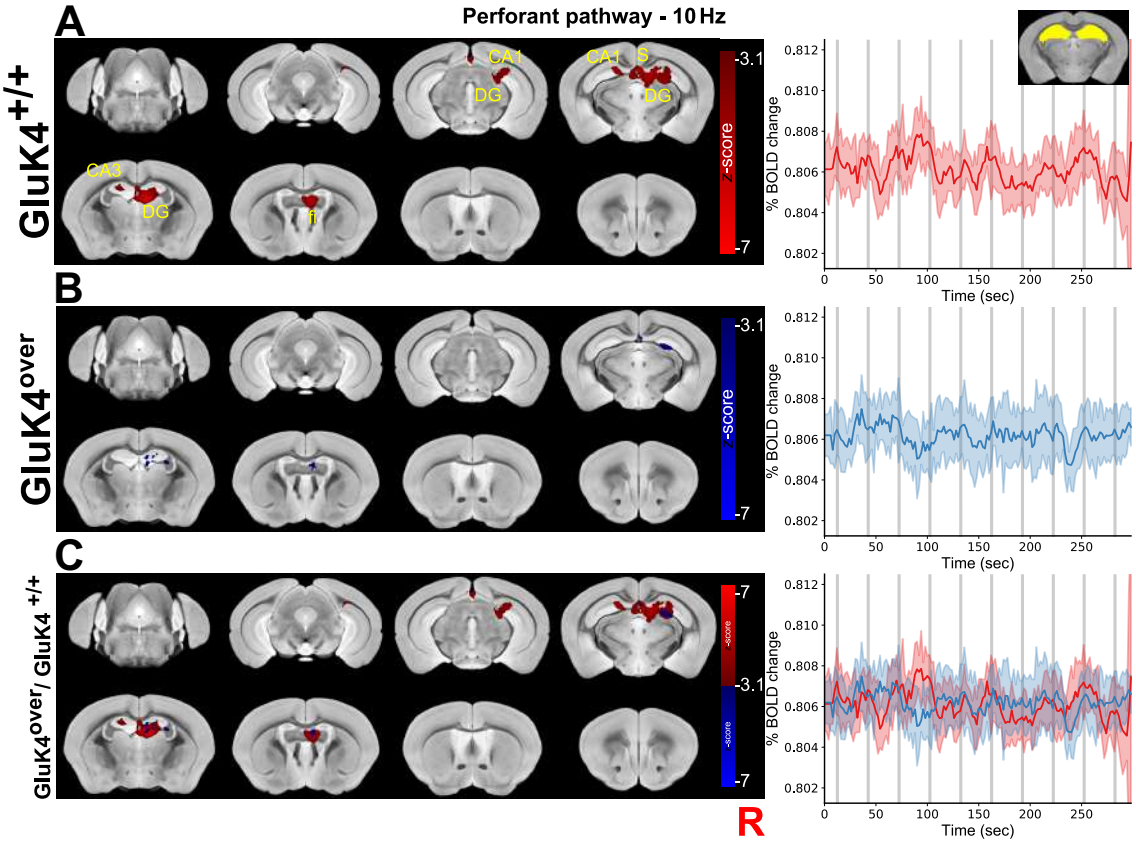

Fig. 49 | BOLD responses evoked by stimulating the perforant pathway with 10 Hz electrical stimulation. (A) Responses evoked in the GluK4$^{+/+}$ WT group (left) and the percentage change in the BOLD response averaged withing the hippocampus (right). **(B)** Responses evoked in the GluK4^{over} TG group (left) and the percentage change in the BOLD response averaged withing the hippocampus (right). **(C)** The GluK4^{over} animals' response (blue) overlaid on the response from the GluK4$^{+/+}$ animals (red) on the left side and on the right their respective BOLD percentage change in the hippocampus. The statistical maps are shown overlaid on the AMBMC high-resolution template. The uppercase R letter in the lower right side indicates the ipsilateral side of the brain. Results shown here are one-sample t-test (WT = 8; TG = 8) using cluster forming threshold ($Z > 3.1$) and corrected at $P < 0.05$ using Gaussian random field theory. The gray lines indicate the time period when the stimulation happens; the shading in each time-series depicts the SEM. **Abbreviations:** AMBMC, Australian mouse brain mapping consortium; BOLD, blood-oxygenation-level dependent; CA1, cornu ammonis-1; CA3, cornu ammonis-3; DG, dentate gyrus; fi, fimbria; R, right side; S, subiculum; SEM, standard error of the mean; TG, transgenic; WT, wild-type.

The activation induced by the 20 Hz frequency protocols was substantially bigger and more widely spread than that of the 10 Hz protocols in both groups (Fig. 50). In both groups, there was activation to the whole dentate gyrus and big parts of the CA1 and CA3 structures as well as to the subiculum and the lateral septal nucleus (Fig. 50A, B) on the ipsilateral side of the electrode. Contralaterally, the GluK4$^{+/+}$ animals showed a similar BOLD response to the ipsilateral side (Fig. 50A); where the dentate gyrus, the CA1, the CA3, and the subiculum were all activated (Fig. 50A). Conversely, the activation in the GluK4^{over} animals was very limited across the midline and only small parts of the

aforementioned structures showed responses in the hippocampus with the extra-hippocampal activation evident only in the subiculum (Fig. 50B).

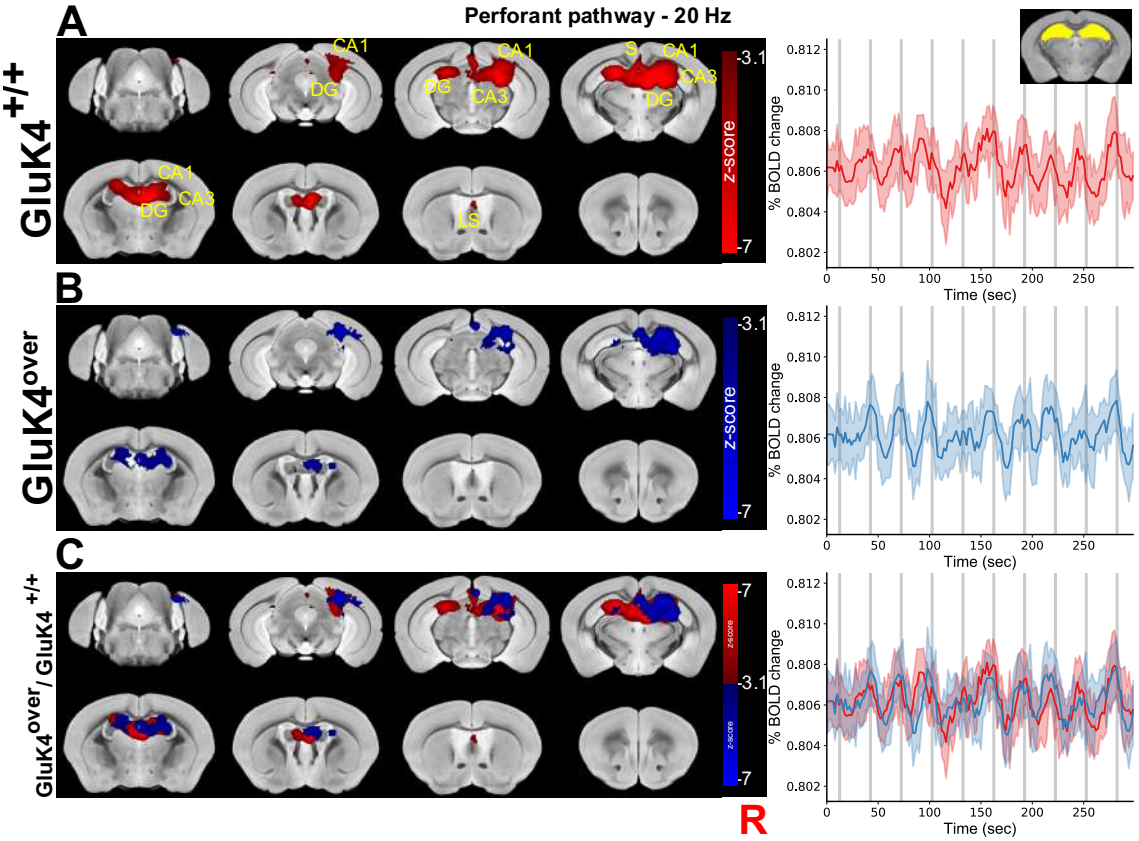

Fig. 50 | BOLD responses evoked by stimulating the perforant pathway with 20 Hz electrical stimulation. (A) Responses evoked in the GluK4$^{+/+}$ WT group (left) and the percentage change in the BOLD response averaged withing the hippocampus (right). **(B)** Responses evoked in the GluK4^{over} TG group (left) and the percentage change in the BOLD response averaged withing the hippocampus (right). **(C)** The GluK4^{over} animals' response (blue) overlaid on the response from the GluK4$^{+/+}$ animals (red) on the left side and on the right their respective BOLD percentage change in the hippocampus. The statistical maps are shown overlaid on the AMBMC high-resolution template. The uppercase R letter in the lower right side indicates the ipsilateral side of the brain. Results shown here are one-sample t-test (WT = 8; TG = 8) using cluster forming threshold ($Z > 3.1$) and corrected at $P < 0.05$ using Gaussian random field theory. The gray lines indicate the time period when the stimulation happens; the shading in each time-series indicates the SEM. **Abbreviations:** AMBMC, Australian mouse brain mapping consortium; BOLD, blood-oxygenation-level dependent; CA1, cornu ammonis-1; CA3, cornu ammonis-3; DG, dentate gyrus; LS, lateral septal nucleus; R, right side; S, subiculum; SEM, standard error of the mean; TG, transgenic; WT, wild-type.

The highest frequency used in this set of experiments was the 40 Hz frequency (Fig. 51). The BOLD response elicited from such frequency was relatively similar to the 20 Hz, however, in the case of the 40 Hz stimulation protocol, there were more extra-hippocampal structures employed in both groups (Fig. 51). The contralateral activation in the GluK4^{over} animals was very limited and almost absent (Fig. 51B); while in the control group, there was a robust activation contralaterally (Fig. 51A).

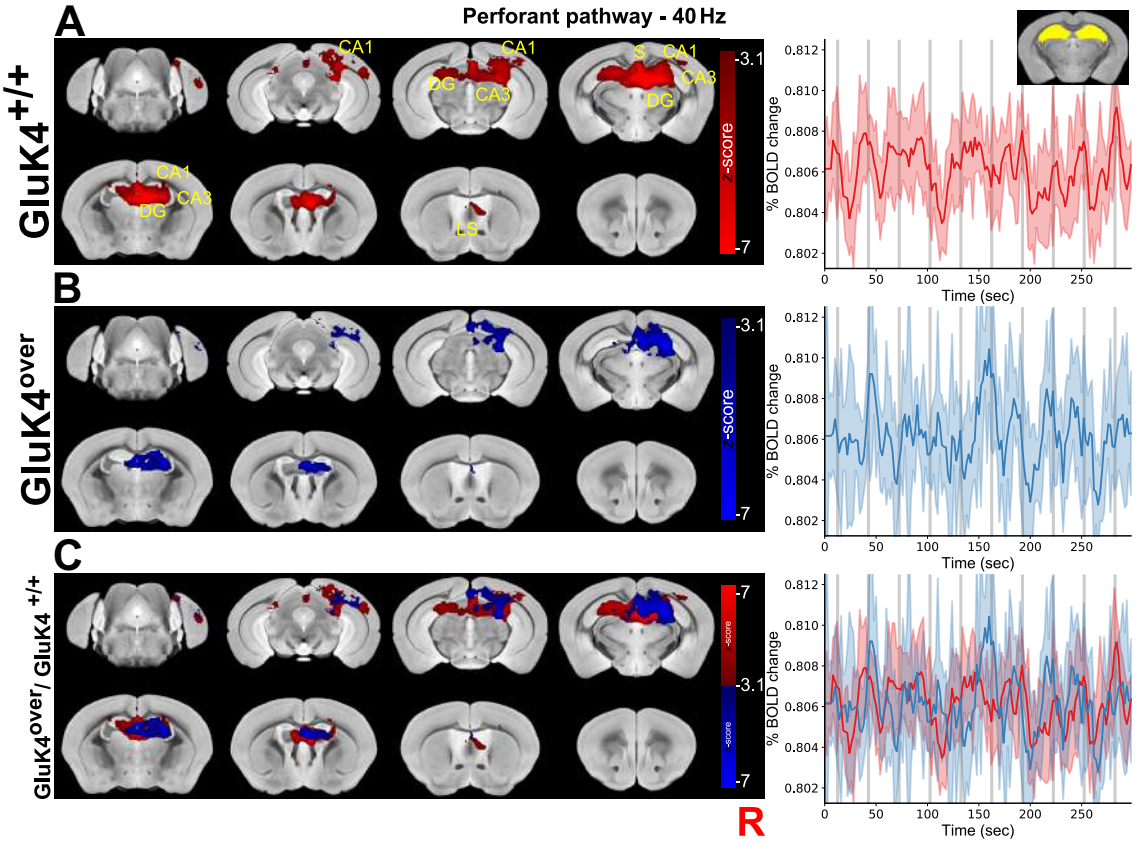

Fig. 51 | BOLD responses evoked by stimulating the perforant pathway with 40 Hz electrical stimulation. (A) Responses evoked in the GluK4$^{+/+}$ WT group (left) and the percentage change in the BOLD response averaged withing the hippocampus (right). **(B)** Responses evoked in the GluK4^{over} TG group (left) and the percentage change in the BOLD response averaged withing the hippocampus (right). **(C)** The GluK4^{over} animals' response (blue) overlaid on the response from the GluK4$^{+/+}$ animals (red) on the left side and on the right their respective BOLD percentage change in the hippocampus. The statistical maps are shown overlaid on the AMBMC high-resolution template. The uppercase R letter in the lower right side indicates the ipsilateral side of the brain. Results shown here are one-sample t-test (WT = 7; TG = 8) using cluster forming threshold ($Z > 3.1$) and corrected at $P < 0.05$ using Gaussian random field theory. The gray lines indicate the time period when the stimulation happens; the shading in each time-series indicates the SEM. **Abbreviations:** AMBMC, Australian mouse brain mapping consortium; BOLD, blood-oxygenation-level dependent; CA1, cornu ammonis-1; CA3, cornu ammonis-3; DG, dentate gyrus; LS, lateral septal nucleus; R, right side; S, subiculum; SEM, standard error of the mean; TG, transgenic; WT, wild-type.

Our voxel-wise analysis did not return any differences between the groups neither in the amplitudes nor the kinetics of the activation (Fig. 49-51). The absence of a voxel-wise difference was similar across all the frequencies.

3.3. Frequency-dependent activation and propagation upon stimulating the CA3 region

Directly stimulating the CA3 region of the hippocampus with our glass electrodes evoked bigger and more-extended figures of activation than those activation elicited upon applying the same-frequency stimulations to the perforant pathway (Fig. 52-55). Another

interesting finding was the discrepancy between the CA3 and the perforant pathway experiments regarding the signal propagation ipsilaterally and contralaterally. As mentioned above, upon stimulating the perforant pathway, there was substantial activation to the side of the electrode and limited propagation to the contralateral side and frequency and genotypic dependent manner (see above). However, in the CA3 experiments, quite the opposite was observed (see below); where the activation was ipsilaterally restricted and less bounded contralaterally.

By contrast to the perforant pathway's experiments, applying stimulations using a 5 Hz frequency protocol evoked a response in both transgenic as well as the control group (Fig. 52A, B). Despite the slow frequency, the GluK4$^{+/+}$ animals showed activation in the dentate gyrus, the CA1, the CA3 ipsilaterally and contralaterally with wider responses observed in the side opposite to the electrode (Fig. 52A); aside from the hippocampal structures, the activation extended to the subiculum, the lateral septal nucleus, and a small part of the cingulate cortex (Fig. 52A). The contralateral BOLD responses in the transgenic animals were bounded to the dentate gyrus and small parts of the CA1 and CA3 of the hippocampus; contralaterally, there was minimal or complete lack of activation to any structure in some transgenic animals (Fig. 52B).

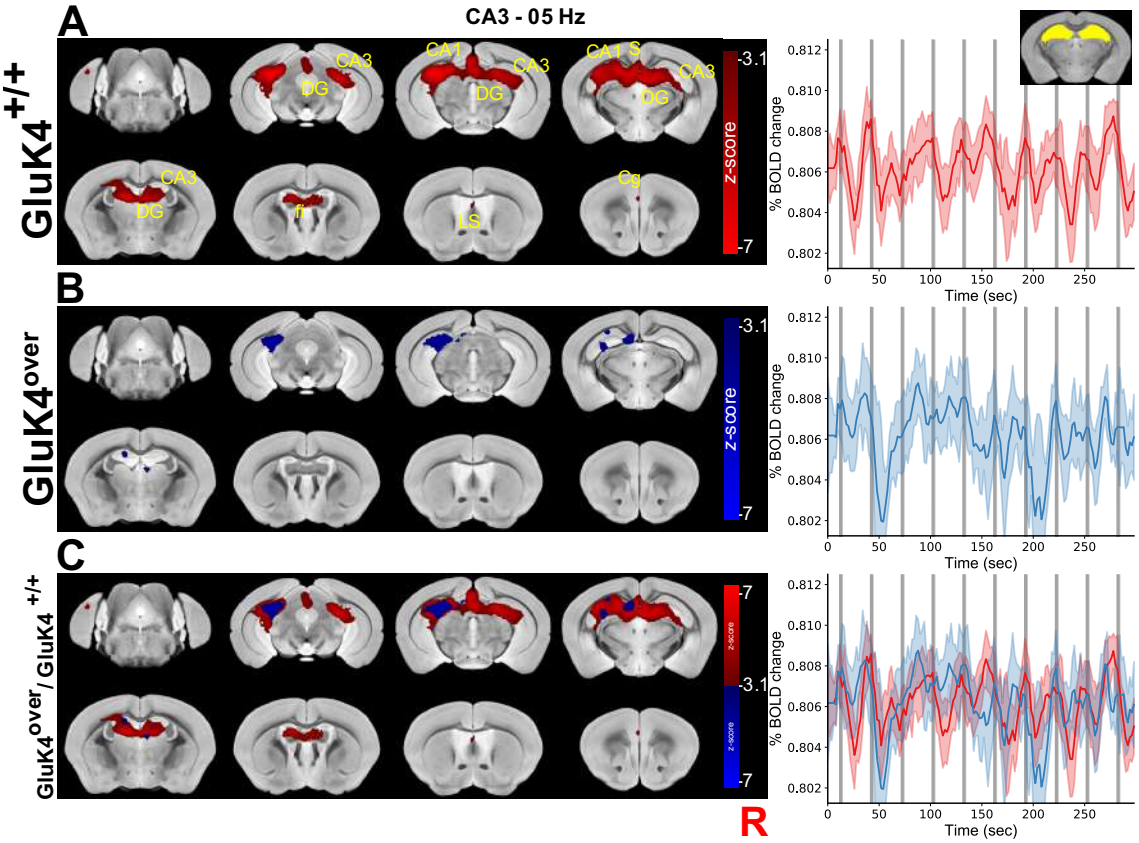

Fig. 52 | BOLD responses evoked by stimulating the CA3 region with 05 Hz electrical stimulation. (A) Responses evoked in the GluK4$^{+/+}$ WT group (left) and the percentage change in the BOLD response averaged withing the hippocampus (right). **(B)** Responses evoked in the GluK4^{over} TG group (left) and the percentage change in the BOLD response averaged withing the hippocampus (right). **(C)** The GluK4^{over} animals' response (blue) overlaid on the response from the GluK4$^{+/+}$ animals (red) on the left side and on the right their respective BOLD percentage change in the hippocampus. The statistical maps are shown overlaid on the AMBMC high-resolution template. The uppercase R letter in the lower right side indicates the ipsilateral side of the brain. Results shown here are one-sample t-test (WT = 7; TG = 8) using cluster forming threshold ($Z > 3.1$) and corrected at $P < 0.05$ using Gaussian random field theory. The gray lines indicate the time period when the stimulation happens; the shading in each time-series depicts the SEM. **Abbreviations:** AMBMC, Australian mouse brain mapping consortium; BOLD, blood-oxygenation-level dependent; CA1, cornu ammonis-1; CA3, cornu ammonis-3; Cg, cingulate cortex; DG, dentate gyrus; fi, fimbria; LS, lateral septal nucleus; R, right side; S, subiculum; SEM, standard error of the mean; TG, transgenic; WT, wild-type.

The activation with 10 Hz protocols led to quite a symmetric activation across the midline in both groups (Fig. 53). In both groups, the activation extended to all regions of the hippocampus, namely the dentate gyrus, the CA1, and the CA3. The BOLD response in GluK4^{over} animals elicited in most of the dentate gyrus and the CA3, however, in the ipsilateral side, the activation was very limited in the CA1 region (Fig. 53B). In the GluK4$^{+/+}$ group, the activation observed in the ipsilateral CA1 region was less than its contralateral counterpart (Fig. 53A). Another notable difference between the two groups was the propagation to cortical areas; where the activation in the transgenic group was mainly restricted to the hippocampal region (Fig. 53B), the activity in the control group

expanded beyond the hippocampal to the lateral septal nucleus, the cingulate cortex, and the infralimbic cortex (Fig. 53A). The subiculum was activated in both sides respective to the place of the electrode was no apparent difference group-wise (Fig. 53A, B).

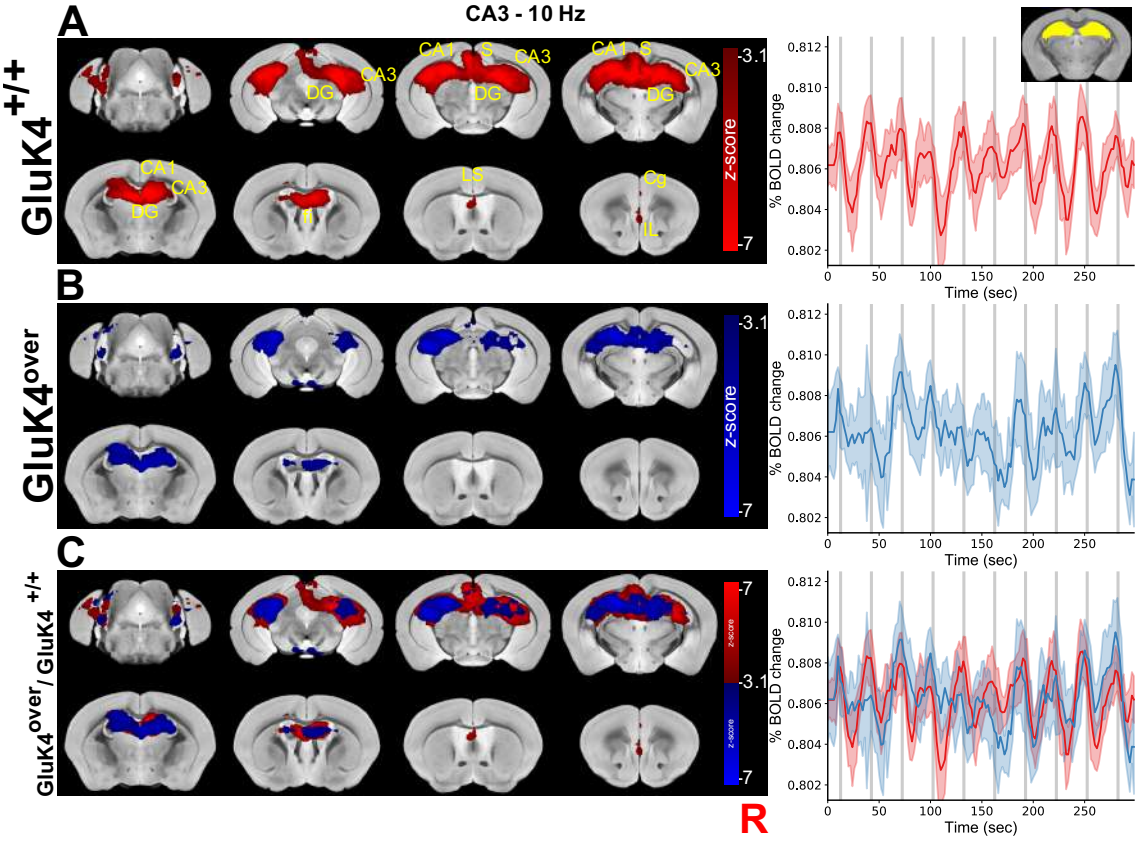

Fig. 53 | BOLD responses evoked by stimulating the CA3 region with 10 Hz electrical stimulation. (A) Responses evoked in the GluK4$^{+/+}$ WT group (left) and the percentage change in the BOLD response averaged withing the hippocampus (right). **(B)** Responses evoked in the GluK4^{over} TG group (left) and the percentage change in the BOLD response averaged withing the hippocampus (right). **(C)** The GluK4^{over} animals' response (blue) overlaid on the response from the GluK4$^{+/+}$ animals (red) on the left side and on the right their respective BOLD percentage change in the hippocampus. The statistical maps are shown overlaid on the AMBMC high-resolution template. The uppercase R letter in the lower right side indicates the ipsilateral side of the brain. Results shown here are one-sample t-test (WT = 10; TG = 9) using cluster forming threshold ($Z > 3.1$) and corrected at $P < 0.05$ using Gaussian random field theory. The gray lines indicate the time period when the stimulation happens; the shading in each time-series represents the SEM. **Abbreviations:** AMBMC, Australian mouse brain mapping consortium; BOLD, blood-oxygenation-level dependent; CA1, cornu ammonis-1; CA3, cornu ammonis-3; Cg, cingulate cortex; DG, dentate gyrus; fi, fimbria; IL, infralimbic cortex; LS, lateral septal nucleus; R, right side; S, subiculum; SEM, standard error of the mean; TG, transgenic; WT, wild-type.

Applying electrical stimulation with a 20 cycle per second (20 Hz) for four seconds elicited, by far, the biggest and the widest response of all the protocols used regardless of the genotype or the side of the electrode (Fig. 54). With such an overwhelming figure of activation, we did not observe any fundamental changes induced by overexpressing the

Grik4 gene (Fig. 54A, B). The BOLD response was ubiquitous in all the regions of the hippocampus ipsilaterally and contralaterally. The activity propagated beyond the hippocampal and hippocampal-adjacent regions to different parts of the cortex such as the motor cortex, the somatosensory cortex, the cingulate cortex (Fig. 54). The caudate putamen and some hypothalamic nuclei were included in the extra-hippocampal structures that showed BOLD response upon applying the 20 Hz stimulations.

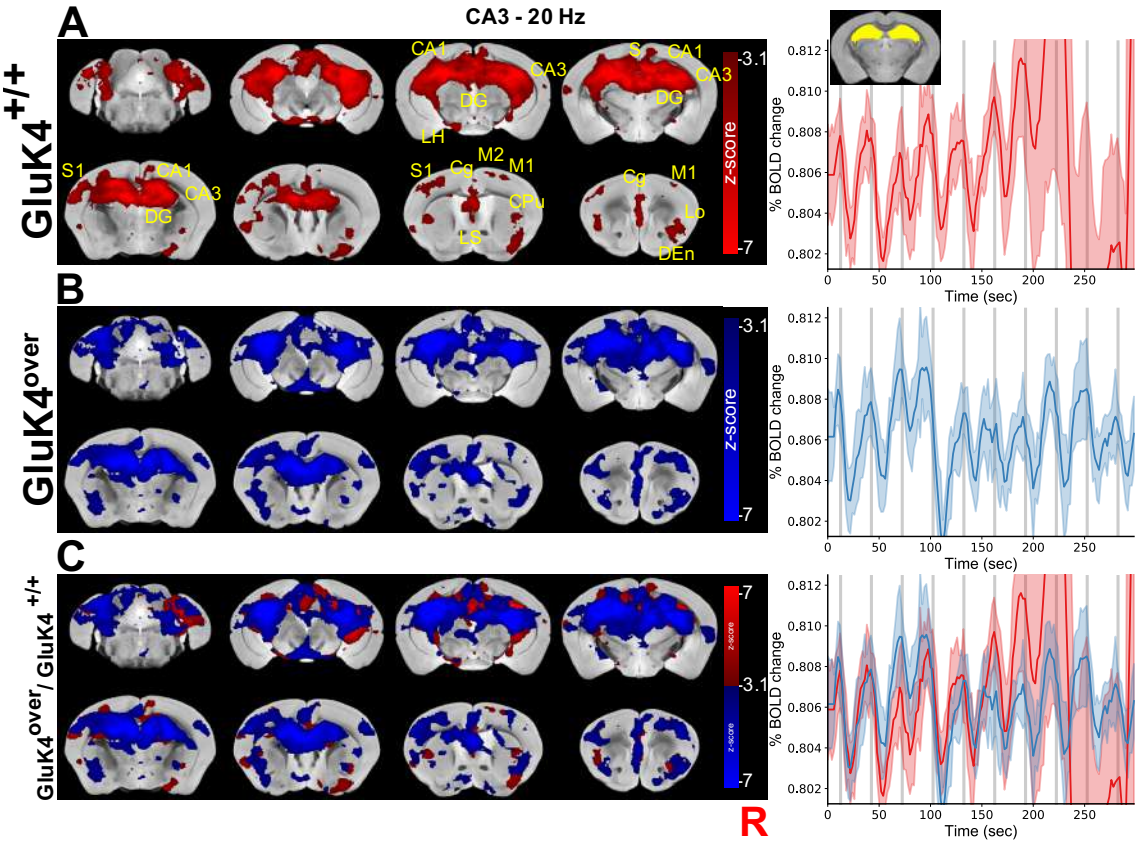

Fig. 54 | BOLD responses evoked by stimulating the CA3 region with 20 Hz electrical stimulation. (A) Responses evoked in the GluK4$^{+/+}$ WT group (left) and the percentage change in the BOLD response averaged withing the hippocampus (right). **(B)** Responses evoked in the GluK4^{over} TG group (left) and the percentage change in the BOLD response averaged withing the hippocampus (right). **(C)** The GluK4^{over} animals' response (blue) overlaid on the response from the GluK4$^{+/+}$ animals (red) on the left side and on the right their respective BOLD percentage change in the hippocampus. The statistical maps are shown overlaid on the AMBMC high-resolution template. The uppercase R letter in the lower right side indicates the ipsilateral side of the brain. Results shown here are one-sample t-test (WT = 10; TG = 9) using cluster forming threshold ($Z > 3.1$) and corrected at $P < 0.05$ using Gaussian random field theory. The gray lines indicate the time period when the stimulation happens; the shading in each time-series indicates the SEM. **Abbreviations:** AMBMC, Australian mouse brain mapping consortium; BOLD, blood-oxygenation-level dependent; CA1, cornu ammonis-1; CA3, cornu ammonis-3; Cpu, caudate putamen; DEn, dorsal endopiriform nucleus; DG, dentate gyrus; Lo, lateral orbital cortex; M1, 1º motor cortex; M2, 2º motor cortex; R, right side; S, subiculum; S1, 1º somatosensory cortex; SEM, standard error of the mean; TG, transgenic; WT, wild-type.

In what seems to follow an inverted U-shape function, the activation pattern regressed significantly with applying a higher frequency (40 Hz) akin to that induced by the 10 Hz protocol (Fig. 55). Once more, as was the case with the 10 Hz stimulation, the activity pattern was quite symmetric across the midline in both genotypes (Fig. 55A, B). However, there was a slight increase in the ipsilateral activity in the GluK4over animals such that the CA1 region of the hippocampus was completely activated (Fig. 55B). The extra-hippocampal regions that showed BOLD response was limited to small regions of the infralimbic cortex along with the lateral septal nucleus in both genotypes (Fig. 55A, B).

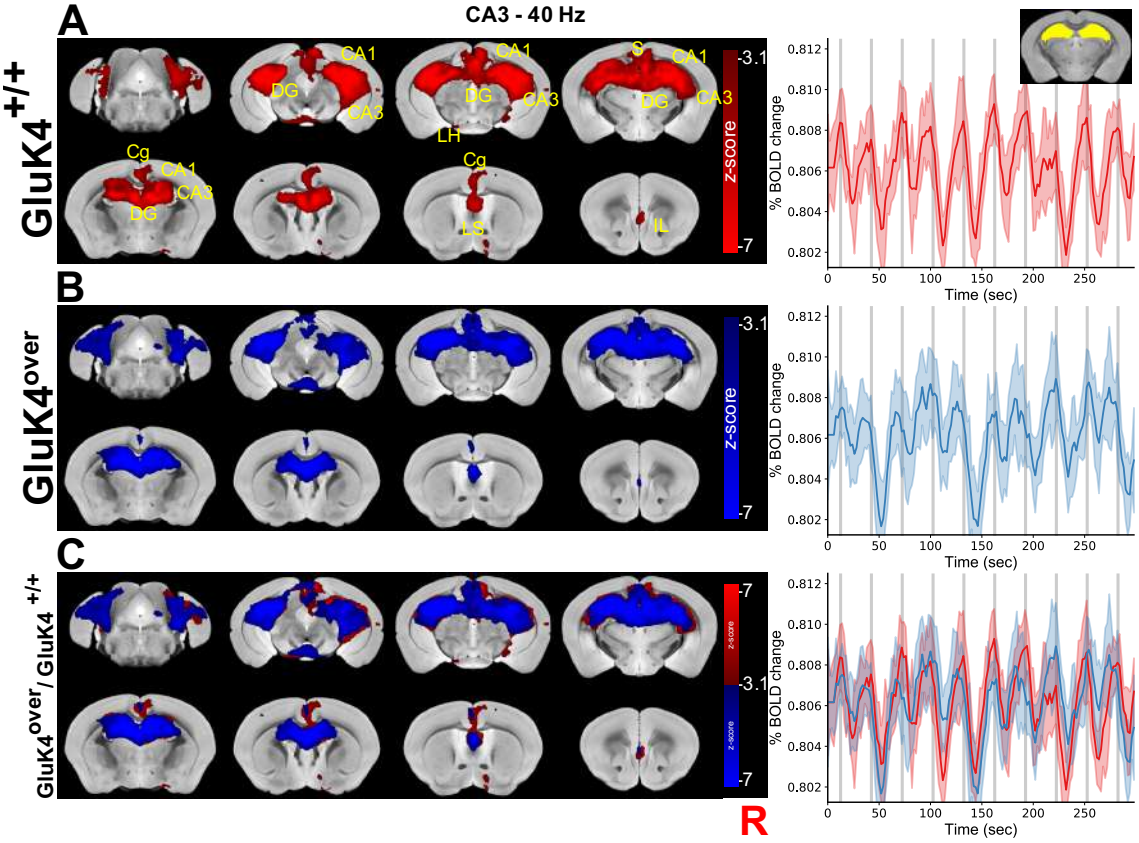

Fig. 55 | BOLD responses evoked by stimulating the CA3 region with 40 Hz electrical stimulation. (A) Responses evoked in the GluK4$^{+/+}$ WT group (left) and the percentage change in the BOLD response averaged withing the hippocampus (right). **(B)** Responses evoked in the GluK4^{over} TG group (left) and the percentage change in the BOLD response averaged withing the hippocampus (right). **(C)** The GluK4^{over} animals' response (blue) overlaid on the response from the GluK4$^{+/+}$ animals (red) on the left side and on the right their respective BOLD percentage change in the hippocampus. The statistical maps are shown overlaid on the AMBMC high-resolution template. The uppercase R letter in the lower right side indicates the ipsilateral side of the brain. Results shown here are one-sample t-test (WT = 10; TG = 9) using cluster forming threshold ($Z > 3.1$) and corrected at $P < 0.05$ using Gaussian random field theory. The gray lines indicate the time period when the stimulation happens; the shading in each time-series depicts the SEM. **Abbreviations:** AMBMC, Australian mouse brain mapping consortium; BOLD, blood-oxygenation-level dependent; CA1, cornu ammonis-1; CA3, cornu ammonis-3; Cg, cingulate cortex; DG, dentate gyrus; IL, infralimbic cortex; LS, lateral septal nucleus; R, right side; S, subiculum; SEM, standard error of the mean; TG, transgenic; WT, wild-type.

As was the case in stimulating the perforant pathway (see above), the voxel-wise analysis did not return any significant difference regarding the amplitude of the kinetics of the signal s questioned.

Taken together, those experiments show that the BOLD response elicited in the hippocampus upon applying electrical stimulation is linearly correlated to the frequency of the stimulation applied until a certain point; at which the response evoked starts to decline (inverted U-shape function). The same thing can be applied to the extra-hippocampal activity propagation; higher frequencies can expand the BOLD activity to limited regions of the cortex (Fig. 54 for example). The latter notion is specifically accurate in the case of directly stimulating the CA3 region where the activity induced by 20 Hz was observed in various regions beyond the hippocampus (Fig. 54) and such regions declined with the 40 Hz frequency (Fig. 55). We believe that stimulating the perforant pathway follows the same paradigm. Albeit, the peak frequency might be higher. Our findings from those experiments solidify the notion that frequency is a salient factor in hippocampal and extra-hippocampal activation as was observed in other reports (Moreno et al., 2016).

IV. DISCUSSION

In this study, we evaluated how an increased dosage of *Grik4* gene affects the functional networks of the mouse brain as well as its effects on the micro and macrostructure of the different brain structures. We also investigated how this is reflected in the functional communication within and between the different networks. Furthermore, we looked into multiple scenarios of how the response elicited by electrically stimulating the brain might differ as a result of overexpressing GluK4.

Our investigation led to some insights both on the functional as well as on the structural level. Interestingly, those findings were in line with other studies performed on ASD models both in mice as well as in non-human primates. The work arguably entertains different scenarios. From one side, our work highlights how disruption of a single gene encodes for a Glutamate receptor subunit can have a ripple effect that can echo through both the structural and functional organization of the brain. On the other hand, these effects were not unique neither on the functional frontier nor on the structural one. This goes in the bandwagon of different pathways can lead to similar outputs i.e., the same disorder can emerge from different origins regardless of the nature of that origin let it be a faulty gene responsible for synaptic transmission like in our case or a gene responsible for synaptic scaffolding like the case of *SHANK3*.

1. Decomposing the resting-state signal using ICA identified conserved resting-state networks

We used GE-EPI protocols to acquire 750 volumes of resting-state functional data. After standard preprocessing steps, ICA was employed to decompose the concatenated signal from all subjects into resting-state networks that were later used for Dual Regression and statistical analysis. We were able to isolate most of the commonly identified networks such as the olfactory bulb, motor cortex, somatosensory cortex, amygdala, visual cortex, dorsal hippocampus, nucleus accumbens, septum, hypothalamus, ventral hippocampus, gigantocellular reticular nucleus, and culmen lobule IV (Fig. 3.6). Also, we were able to identify multiple components that overlap with what is considered to be the mouse's DMN (Fig. 3.7). Some components, especially those of the somatosensory cortex are either incomplete or lacking from our networks. We attribute this to signal dropout in those parts of the cortex in some animals.

Those reported networks have repeatedly identified in different studies using different acquisition and analysis protocols (Jonckers et al., 2011 Mechling et al., 2014 Nasrallah et al., 2014 Sforazzini et al., 2014, Zerbi et al., 2015) and even using different anesthetics (Grandjean et al., 2014a Bukhari et al., 2017). Recently, in an across-labs study, Grandjean et al., used 17 different rest-state datasets from different labs and reported the convergence of most of these datasets to common spatially defined networks (Grandjean et al., 2020).

Those results gave a tangible testimonial on how robust and stable those networks are regardless of the acquisition protocol and more importantly on how conserved those networks are between different species (see Introduction for more details about those networks in other species). Our ability to isolate those networks, we believe, lend credence to both our acquisition protocol, quality of our data, handling of the animals, and more specifically to our preprocessing and analysis pipelines.

2. GluK4 overexpression harnesses short-range synchronizations while hinders long-range synchronization

Resting-state fMRI was used to identify multiple resting-state networks and further to determine the coherence within and between those networks. We used the group ICA resting-state networks to estimate the corresponding networks in each subject. Those subject-specific maps were then utilized to (Beckmann et al., 2005, Filippini et al., 2009) calculate a subject-wise measure of the synchroneity within each network in addition to the synchroneity strength between each pair of networks (see Methods for more details). We finally performed a group comparison to assess how the GluK4 overexpression affects those networks and the communication within and between them.

The group-wise comparisons returned multiple differences between the GluK4^{over} animals and their WT counterparts. GluK4^{over} animals showed multiple networks with increased within-network strength as demonstrated by increased synchroneity within these networks. These networks included the hippocampus, the hypothalamus, the cerebellum, the striatum, and the cortical parts of the DMN such as the cingulate, the retrosplenial, the somatosensory, and the motor cortices. Conversely, the connection strength between the motor cortex and the posterior part of the hypothalamus was hindered in the GluK4^{over}

when compared to the GluK4$^{+/+}$ animals. As we mentioned before, it was not much of a decrease in the connection strength as it was flipping the connection from a positive correlation to a negative correlation, in other words, converting the correlation between the two components to an anti-correlation.

Each RSN has a putative function and any disturbance in that network is, supposedly, going to affect the function ascribed to that network somehow (Greicius 2008). The networks afflicted with abnormalities are responsible for a wide range of cognitive and sensory stimuli perception. We could not observe any direct correlation between the fluctuations within those networks and the metrics we extracted from the behavioral tasks. That can simply mean that those networks are not affecting the behavior or the effect is done through an intermediary cascade or a non-linear correlation and that is not reflected in the metrics we used to test the correlations. We tend to believe the latter rather the former. Studies that used rsfMRI to investigate ASD in humans were significantly divided when it comes to correlation with behavior; some of those studies reported associations where others could not find this association (see Hong et al., 2020). Given this discrepancy, it is quite challenging to assign the blame for the behavioral phenotype to any single network instead, it could mean that the global pattern of connectivity, and not a single element, is the reason behind the behavioral abnormalities. On the other hand, the problem might be within the behavioral tasks themselves as such they are not refined enough to detect subtle changes in behavior and more refined tests would display the absent connection with the resting-state networks.

A more general way to describe the effects of the overexpression of GluK4 on the RSNs would be to categorize those effects as an increase in the short distance connection accompanied by a decrease in the long-distance connections. This pattern has actually been described repeatedly in characterizing ASD in human subjects (Cherkassky et al., 2006; Kennedy and Courchesne 2008, Assaf et al., 2010). This might mean that the connection between the different brain regions is disrupted to the extent that each network is unaware of the rest and is overcommunicating or “talking only to itself” (Courchesne and Pierce 2005). *In vivo* recordings seem to point in the same direction where functional connectivity in the GluK4^{over} animals appear to be higher relative to the wild-type animals (Aller et al., 2015).

Whether we call it overcommunication or increased strength, the more pressing matter is how can we interpret those findings in terms of underlying machinery? Even though the functional connectivity is essentially a statistical construct, the neuronal origin of the spontaneous BOLD fluctuations is well accepted (Laufs et al., 2003, Brookes et al., 2011). A recent study has successfully managed to record rsfMRI simultaneously with fluorescent Ca^{2+} signal (Lake et al., 2020). According to the authors, the Ca^{2+} signal recorded from excitatory neurons accounts for 30% of the BOLD spontaneous activity (Lake et al., 2020). Moreover, they found that parcellations derived from the spontaneous Ca^{2+} signal and BOLD fluctuation were quite consistent (Lake et al., 2020). Other studies have found a direct correlation between the concentration of the neurotransmitters Glutamate and GABA and the strength of the resting-state networks (Kapogiannis et al., 2013, Stagg et al., 2014). Kapogiannis et al., disclosed a positive relationship between the intrinsic local connectivity and the Glutamate/GABA ratio (Kapogiannis et al., 2013), while Stagg et al., using Dual Regression reported a negative correlation between the GABA concentration and the strength of the motor network (Stagg et al., 2014). Glutamate and GABA are considered to be the major excitatory and inhibitory neurotransmitters in the brain and are usually used as a surrogate for the excitation/inhibition balance.

The increase in local network strength or the overcommunication and the anticorrelation between networks observed in our data can be readily explained by the surfeit in the GluK4 subunit that disturbs the balance between excitation and inhibition. Comparing the expression of the exogenous *Grik4* (Aller et al., Aller et al., 2015) and the networks whose strength increased in $GluK4^{over}$ animals lends support to the previous argument, where the affected networks overlap with the structures where the overexpression of GluK4 was observed. The anticorrelation between the motor network and the hypothalamic one is nonetheless difficult to interpret. However, it is not far-fetched to assume that the between-network correlation is a proxy measure for the Glutamate/GABA ratio between those networks. We know already that the overexpression of GluK4 is not unified across all structures (Aller et al., 2015). This mismatched overexpression along with the ensued excitation/inhibition imbalance can be responsible for shifting the correlation between those structures from a positive correlation to a negative one. We also do not know whether the anticorrelation between those specific networks has a special meaning or it is more of a global pattern and only that difference was big enough to be detected

after strong statistical thresholding. Getting to the bottom of that issue requires a bigger study with a higher power.

The putative sensitivity of the functional network strength to the internal concentrations of Glutamate and GABA can have important clinical implications. The excitation/inhibition imbalance has long been invoked for various neurodevelopmental disorder and finding a biomarker sensitive to this balance can provide a great aid in the diagnosis of these disorders (Javitt et al., 2011). Our data shows not only that the functional connectivity is capable of detecting the increased excitation, but also to pinpoint this increase to the local structures where it happens.

3. GluK4^{over} changes the micro and the macrostructure of the white matter fibers

We used an SE-EPI protocol to acquire multi-shell DWIs with two different b-values. We tried to extract as much information about the underlying microstructural properties of the WM tracts as feasible. Fitting simpler models such as the DTI model were complemented by more complex models such as the CHARMED and NODDI models. Aside from those models, we sought after newly introduced approaches that use CSD to estimate more-interpretable parameters such as the fiber density and cross-section.

Group comparisons showed multiple irregularities. Irregularities such as a decrease in fractional anisotropy (FA), intracellular volume fraction (FICVF), restricted fraction (FR), and intra-axonal diffusivity (IAD) and an increase in radial discursivity (RD) and axial diffusivity (AD) values in the GluK4^{over} animal when compared with the control. Those changes were observed in most of the major WM tracts including the cc, the internal capsule, the external capsule, and the hippocampal commissure. Fixel metrics of those fibers such as the fiber density (FD), the fiber cross-section (FC), and the combined measure of both (FDC) also witnessed a significant decrease in the transgenic group relative to the wild-type group. These differences were apparent voxel-wise as well as upon averaging the values across the whole tracts of the corpus callosum/external capsule (cc/ec).

Interpreting the findings from dMRI has always been challenging. The major hurdle in front of a meaningful biological interpretation is the absence of a one-to-one

correspondence between any of the diffusion parameter and a specific aspect of the structure of the underlying tissue (Assaf et al., 2019). A change in one of the diffusion parameters such as FA can mean a change in myelin thickness, axonal diameters, axonal density, or tissue integrity (Assaf et al., 2019).

A decrease in FA values accompanied by an increase in both MD and RD values in GluK4^{over} animals technically mean that there is less diffusion parallel to the axon direction and more diffusion perpendicular to that direction. But what does this tell us about the tissue properties? RD has long been considered to be an index of myelination such that its increase has been regularly attached to a decrease in axon myelination in animal models (Song et al., 2002, Song et al., 2005, Janve et al., 2013). Using myelin basic protein (MBP) as a surrogate for myelination, Chang et al., found that MBP is robustly correlated with both FA and RD values (Chang et al., 2017). MBP was positively correlated to FA values in WM fibers, while RD was negatively correlated to only a subset of those fibers (Chang et al., 2017). It is worth mentioning also that both values were found to be negatively correlated relative to one another (De Santis et al., 2014). Our next concern was whether this is biologically plausible in our model or to put it in different words, does GluK4 have a role in myelination? Glial cells express Glutamate receptors and AMPARS and KARs are primarily expressed in oligodendrocytes (Steinhäuser and Gallo 1996). Overactivation of KARs alone or along with AMPARs was found to have a certain excitotoxic effect on the oligodendrocytes that lead to their death *in vitro* (Sánchez-Gómez and Matute 1999). So, whether exerting such effect through overactivation of AMPARs or KARs, it is quite plausible that the overexpression of GluK4 could negatively affect the axons myelination. This could mean that the tissues are not as intact as they should and that leads to more perpendicular and less parallel diffusion. We do acknowledge the precautions and warnings issued by Wheeler-Kingshott and team (Wheeler-Kingshott and Cercignani 2009) regarding the overinterpretation of the AD and RD meaning. However, we are building our speculation on biologically relevant information specific to our model in order to support the diffusion results.

Both the NODDI and the CHARMED models aim at separating the contribution of the intra- and extracellular compartments in the diffusion signal. Despite some differences inherent to each model, both models define a quantity corresponding to the axonal packing density. In our data, the FR and the FICVF form the CHARMED and the NODDI

models show a significant decrease in the transgenic animals compared to the wild-type ones. Both metrics are corresponding to the fraction of the total diffusion that is intra-axonal and these metrics are frequently described to reflect the axonal density. The similarity of the results of the two metrics gives merit to the notion that they are reflecting the same underlying quantity. FICVF decrease with dispersion index (ODI) increase are usually interpreted in neurodegenerative disorders to indicate a decreased axonal density emitting from axonal damage or degeneration along with demyelination (reviewed in Kamiya et al., 2020). We believe that the decrease in those parameters is merely reflecting that the axons are less dense due to the loss of myelin.

The tracts with significant differences in FBA analysis are mostly those that show differences in the voxel-wise analysis of the other models. However, it appears that not all the affected fibers suffer from the same anomalies. The fiber bundles of the cc/ec, for example, appear to have smaller diameters and regular density while the cingulate bundle, the fimbria, and the fornix appear to have lower density and normal cross-section (Fig. 3.25). This can also be interpreted in terms of demyelination. As expected, both types of change are reflected in the combined measure which is the closest equivalent to the results of the VBM in the gray matter i.e., there is an apparent change in the volume in most of the WM tracts regardless of the driving force behind such a change. The only aspect that is still lacking of this type of analysis, is the histological validation. There is still a shortage of article that validated the FBA results against any of the histological gold standard.

Considered together, these findings point at distinct changes in two WM populations. The first population consists of the fibers of the cc/ec and the hippocampal commissure where there is a loss of myelin and a decrease in the axonal diameters of those fibers and a second set of fibers including the cingulate bundle, the fimbria, and the fornix where they suffer also from a significant decrease in myelin, but without a change in the diameter. The FD measure cannot differentiate whether the lower density is due to lower axon count or due to axons with smaller diameters (Dhollander 2020). Bearing that in mind, we tend to explain the decrease in density in those fibers as demyelination rather than a decrease in the number of fibers on the account of failing to find a significant difference between the number of the tracts extracted from running the tractography.

The studies performed on human subjects with ASD give more traction to our interpretation. Most of these studies reported that ASD subjects exhibit a decrease in FA

accompanied by an increase in both the MD and the RD values in all the major WM tracts (Travers et al., 2012, Ameis and Catani 2015). Collectively, the postmortem studies showed that the large-diameter fibers, especially the most anterior ones, suffer from loss of myelin thickness (Zikopoulos and Barbas 2013). We believe this to be the case in our animals as well. Getting to the bottom of that issue requires a more-thorough histological investigation; examining those fibers with electron microscopy will definitely unravel more specific details than those obtained with dMRI.

Our next concern was whether these changes translate into functional abnormalities or their magnitude is not big enough to inflict harm on the functional synchronization between the different brain regions. As we discussed before, enhanced short-range connection coupled with diminished long-range connection is ubiquitous in GluK4^{over} animals. WM tracts are the major responsible for connecting and precisely synchronizing information transfer between the different brain structures (Fields 2008). The disruption in the WM fibers could explain, at least partially, this perceived lack of synchronization between the brain networks. Applying direct stimulation to the brain showed distinctively different patterns of spread. It seems that the efficiency of conveying the stimulation is diminished in the GluK4^{over} animals compared to the GluK4$^{+/+}$ animals. This pattern is more evident at lower frequencies (e.g. 5 and 10 Hz) more than at higher frequencies such as 20 or 40 Hz and upon applying the stimulation directly to a major WM pathway such as the perforant pathway. We do not have any evidence to support a claim of a problematic interhemispheric connection. Our belief is tipped in favor of explaining those findings as evidence of lower conductance in the cc fibers due to the putative decrease in myelination. While this assumption is reasonable in the perforant pathway, it does not explain why the signal moves better to the contralateral hemisphere upon stimulating the CA3 than in the ipsilateral one. This could be because of the resistance the signal faces in the axons within the hippocampus is higher than that of the hippocampal commissure fibers that connect the two hippocampi.

The kurtosis results were also quite puzzling. The comparison of the FA values obtained from fitting the kurtosis tensor to our data was quite similar to those of the DTI. However, there were no significant differences in the MD, RD, or AD values between the two groups. Fitting the kurtosis tensor requires the estimation of 21 parameters vs only 6 parameters in the case of the conventional tensor (Jensen and Helpern 2010). This can be

problematic in the presence of noise that is generated from scanning a small-sized object such as the mouse brain. However, it appears that some parameters are better estimated in some regions than in others since some tracts in a number of maps such as those in FA, RD, AWF, MK, and AK showed a significant correlation with different aspects of the behavior.

Simply put, we speculate that the WM fibers in the GluK4^{over} animals are experiencing a widespread disruption in their microstructure. Most of those fibers suffer from a decrease in diameter and/or demyelination making signal conductance suffer dramatically. Functionally, this anomaly hinders how the different brain regions communicate with each other and how the information is transferred between distant regions.

4. Overexpression of *Grik4* has an opposing, tissue-specific effect on brain morphology

Inserting an exogenous *Grik4* transgene into a WT mouse's fertilized egg led to a wide overexpression of KAR GluK4 subunit (Aller et al., 2015). This overexpression was detected in the neocortex, the hippocampus, and the striatum with different ratios of increase (Aller et al., 2015). The morphometric analysis returned a myriad of changes between the two groups, where structures such as the hippocampus, the striatum, the thalamus, and the cerebellum appeared to have decreased in size in the GluK4^{over} animals relative to the control group (Fig. 3.29). That shrinkage was found to be in contradiction to what was observed in the neocortex, where there seemed to be an overall expansion in the GluK4^{over} animals with respect to the GluK4$^{+/+}$ animals.

We are tempted to ascribe the increased dosage of the GluK4 subunit for these changes. The expression profile of the exogenous subunit appears to be localized in those structures that underwent shrinkage or expansion in the GluK4^{over} animals. However, it appears that this effect is tissue-specific such that the overexpression in a certain structure can lead to an increase in this structure's size (e.g. the neocortex), while in a different location (e.g. the hippocampus) can lead to the opposite outcome. Establishing a correlation between the percentage of change in any structure's size and the ratio of increase in GluK4 subunit expression in that structure would potentially add more weight to this argument.

We could not encounter other reports in the literature that evaluated the effects of over- or under-expression of other Glutamate subunits on the global morphology of the brain. However, we do not think of the GluK4 subunit as a one-of-a-kind or a snowflake, rather we believe that it is a crucial part of a bigger signaling pathway; any interruptions to that pathway can lead to the same outcome. However, it would be definitely intriguing to see how morphological changes might unfold as a result of abnormal expression of the different subunits of the KARs or the rest of the Glutamate receptors.

5. Tissue's micro and macrostructural properties control behavioral phenotypes

One of our aims in doing this project was to address whether the structural and functional changes as probed by MRI can explain the variability in behavior that we observed earlier (Aller et al., 2015, Arora et al., 2018). We did not perform the correlation analysis separately for each group as we believe that the relationship should be the same in both groups. This notion was confirmed by visually inspecting the linear regression plots between the various MRI parameters and the metrics extracted from the behavioral tasks (Fig. 3.15-3.22, Fig. 3.29). The points from the two groups were not clustered separately, instead they were intermixed in a random fashion. We only reported those structures whose correlations remained significant ($P < 0.05$) after correcting for multiple comparisons. We did not take into consideration those correlations which did not make the cut as there is no way to assert whether these relationships were due to real correlations or just a confound of sampling variability (see Methods section for more details about statistical corrections).

We observed various structural, but not functional connectivity, parameters from different anatomical regions that were positively or negatively correlated with some aspects of the behavior. We found that values from maps such as the AD, FA, FR, and IAD are positively correlated with measures extracted from behavioral tasks including the ratio between time spent in open arms and time spent in closed arms in the EPM arena and the distance traveled in the OF arena. While the values from other maps including the RD, AWF, MK, AK, and FICVF were negatively correlated with the aforementioned measures. In both cases, the correlations were prevalent in most voxels of the WM tracts

included in the analysis, especially the different regions of the cc (the genu, body, splenium) and the hippocampal commissure (Fig. 3.15-3.22).

We discussed earlier the value of the OF and EPM in addressing anxiety and anxiety-like behaviors. On the other hand, these maps are surrogates of different aspects of the microstructural properties such as intracellular and extracellular diffusion, axonal diameter, fiber myelination, and axonal density (see above). The markers that indicate a decrease in myelination such as the FA, RD, FICVF, FR, and AWF appear to have the most predominant effect on directing the behavior. Surprisingly enough, the kurtosis maps such as the RD, MK, AK, and AWF which did not show any difference between the two groups showed a significant correlation with behavior. This could mean that the non-Gaussian diffusion within those tracts reflects certain axonal qualities that are quite important for signal transduction. Only these properties are not different between the two groups. In our opinion, these properties come together to ensure a seamless information transfer (Fields 2008) and changes in these properties affect this transfer and hence derive the behavior out of normality.

On the macrostructural level, we found that the size of the lateral septal nucleus and the bed nuclei of the stria terminalis to be positively correlated with time spent in open arms/time spent in closed arms, while the size of some cortical structures (such as the cingulate, retrosplenial, prelimbic cortices) to be anticorrelated with that ratio (Fig. 3.29). The lateral septal nucleus is speculated to modulate fear and anxiety behavior (see Sheehan et al., 2004 for a review), this modulation is quite disputed whether it is anxiogenic or anxiolytic (see Anthony et al., 2014). The correlation between the volume of that structure and the time in open arms/time in closed arms (a clear marker of anxiety) can explain why some animals suffer from more anxiety than others. The shrinkage of such important structures, we believe, has a strong negative effect on animals' behavior and especially on fear and anxiety. Conversely, the expansion of multiple regions of the cortex was correlated with increased anxiety in our animals. These cortical regions which can be considered as a part of the mice prefrontal cortex (Laubach et al., 2018) are considered in humans as well as in rodents to be a cognitive hub. Studies have connected the prefrontal cortex and its vast connections with social behavior in rodents and humans alike in multiple studies (reviewed in Bicks et al., 2015).

Functionally speaking, there were a number of correlations with various resting-state networks. However, none of these correlations survived the multiple comparisons corrections (data not shown). Also, this might be due to the stringency of the FWER correction, we preferred to stick with the more robust findings.

All in all, we feel confident to conclude that negative alterations in microstructural properties of the WM tracts as demonstrated by dMRI and changes in macrostructural properties as probed with VBM can explain the increased anxiety phenotype that we observe in our animals. We do not know if these aberrations are the direct cause for increasing anxiety or there is another lurking variable that controls both. We speculate that the overexpression of *Grik4*, through unknown mechanisms, drives the structural changes we observe and those changes, through an intermediary mechanism, come together to change the behavioral phenotype. These results shed light on another advantage of MRI i.e., assessing the relationship between behavior and tissue properties *in vivo*.

6. GluK4^{over} animals recapitulate autism neuroimaging endophenotypes in animals and humans

Aller et al. examined the ramifications of overexpressing the GluK4 subunit on the synaptic level as well as on the behavioral level (Aller et al., 2015). We aspired in this line of work to investigate the intermediary stage between these two levels on the circuit's frontier. Much like human subjects with ASD suffer from the triad of prevalence of repetitive behavior, defective social interaction, and aberrant communication (Miles 2011), models that claim to replicate this condition in animals demonstrate abnormal behavior or autistic-like behavior such as excessive self-grooming, lack of interest in interacting with other animals, and defective ultrasonic vocalizations (see Introduction for examples on those models).

An endophenotype can be considered as a quantifiable intermediary ground between what can be perceived physically such as the behavioral phenotype and the more distal genotype that can only be elucidated through complicated tests (Gottesman and Gould 2003). Neuroimaging markers can easily fill this void and if harnessed enough, each change in one of those markers can be traced to a defective genetic function Mahajan and Mostofsky

2015. Moreover, we can detect changes in those markers ahead of the development of the behavioral phenotype giving a wider window for treatment.

The neuroimaging findings in ASD are largely heterogeneous with an apparent difficulty in replicating many studies (He et al., 2020). These disconcerting facts cast a shadow on the value and the usability of neuroimaging in investigating complex disorders such as ASD, let alone using neuroimaging as a diagnostic tool. A more progressive approach tends to recognize these disparities and attribute them to the inherent complexity of the neurodevelopmental disorders, not just ASD. Some studies have already used findings from different reports to break down the seemingly-heterogeneous neuroimaging findings into clusters with similar observations (Hong et al., 2020). This practice has led to recognizing different subtypes of ASD where markers such as functional connectivity vary widely between subtypes while remaining consistent within the same subtype (Hong et al., 2020). The same practice was extended to animal models. Ellegood and others have used structural data from 26 mice model to cluster those models into three clusters where the volumes of many regions varied by shrinkage and expansion (Ellegood et al., 2015). Closely similar work was conducted recently by Zerbi and team where, instead of structural data, they used functional connectivity data to cluster 16 ASD model into four clusters (Zerbi et al., 2020).

These results open a new horizon into looking at neuroimaging findings in neurodevelopmental disorders. While it is true that those findings do not converge into a single signature, more informant research that aims into linking genetic abnormalities with neuroimaging markers from different modalities with the behavioral phenotypes can probably help to establish signatures for different subtypes.

Despite the aforementioned disparity between clusters, a number of global patterns persisted. For example, while connectivity strength can increase or decreases depending on the ASD subtype, networks such as the somato-motor networks and the DMN appeared to be always affected (Zerbi et al., 2020). The same can be said regarding the volumetric changes where big regions of the cortex, the cerebellum, the striatum, and the hypothalamus are always affected (Ellegood et al., 2015). In spite of the absence of similar analysis regarding the dMRI results, we anticipate that the same diversity will be encountered. In the limited number of available studies that used DTI to investigate ASD in mice models, the prevalent pattern appears to be the decrease in FA and the increase in the MD values

mainly the cc fibers (Eed et al., 2020). Even though our model was not included in any of those studies, we believe that our findings would perfectly fit within one of those subtypes where a common etiology is shared such as the TREM2KO mice where an immune receptor is knocked out leading to excessive excitatory neurotransmission, decreased long-range functional connectivity, and abnormal social behavior (Filipello et al., 2018).

The elucidation of such subtypes is quite encouraging to the idea that these subtypes could be sharing an etiology such that some faulty signaling cascades could be common within the same subtype. Only by linking the genetic abnormalities with the neuroimaging markers to the behavior, a true endophenotype could emerge. Our data is a much-needed step in this direction where genetic analysis is accompanied by electrophysiology, neuroimaging, and behavioral tests. Not only were we coupling genetics with neuroimaging, but we also used all the common modalities that have the potential to be a diagnostic tool one day.

7. BOLD response is not mediated by postsynaptic glutamatergic events

Our findings from the stimulation experiments are in quite a disagreement with those from human studies. The results from our experiments unequivocally revealed a striking difference between the two groups in signal propagation (Fig. 3.33-3.39). Albeit these differences were not complemented by either a change in the amplitude or the kinetics of the BOLD signal. We know from our previous work (Aller et al., 2015, Arora et al., 2018) that the GluK4^{over} animals suffer from an imbalanced excitation/inhibition which begs the question of why this was not reflected in the BOLD response. In humans, Whalley et al. demonstrated that subjects with an indel variant in the *GRIK4* gene have higher hippocampal activation upon performing a face-processing task (Whalley et al., 2009). The indel variant grants the afflicted subjects an increase in the GLUK4 expression and an apparent protection against the bipolar disorder (Pickard et al., 2008). Our results, however, did not reflect such modulation.

This discrepancy could have ensued from the difference between the two species, an underpowered study, or a questionable statistical practice. The obvious answer would be the evolutionary gulf between the two species; to our knowledge, the traditional face-

processing task (Kanwisher et al., 1997) is infeasible in rodents for obvious reason, leaving the exact replication of these findings a long shot. The difference between the two species is quite determinant in a fundamental issue that is crucial to the BOLD contrast which is the brain energy expenditure on glutamatergic signaling. Attwell and Laughlin elegantly demonstrated that postsynaptic signaling (mostly glutamatergic) consumes up to 34% of the energy in rodents' brains, while this percentage can reach up to 74% in primates (Attwell and Laughlin 2001). If the BOLD signal is actually sensitive to energy consumption by the neurons, this might explain the difference between our findings and those reported in humans.

In the recent years, multiple reports have called into question (Button et al., 2013) the long tradition of small sample sizes in task-based fMRI studies in humans (see for example, Friston 2012 and the rebuttal Friston 2013, Ingre 2013, Lindquist et al., 2013). In Whalley's article, the sample size is quite limited (n = 18, 24) which can call into question whether the perceived difference in activation was a true effect or just a false positive one. A study with a bigger sample size might be warranted in order to still this issue.

The other statistical issue in Whalley's article was the small volume correction they employed. Performing statistical inference on ROIs in fMRI analysis with small volume correction can be problematic (see Poldrack 2007 for a review). If chosen poorly i.e., not independent from the data included in the analysis, can lead to an inflated false positive rate (see Kriegeskorte et al., 2009, Vul et al., 2009, Kriegeskorte et al., 2010, Vul and Pashler 2012 for an extended discussion about the circular analysis). We cannot confidently say that performing a whole-brain correction would change the outcome, but it would certainly a step towards settling the discrepancy.

The disagreement between our results and earlier reports could simply reflect an inherent limitation to the BOLD response; it does not reflect the postsynaptic component of the neuronal activity. How the BOLD contrast is related to the neuronal activity is a complex question with no straightforward answer (we advise the interested reader to review Huettel et al., 2014, chapter 7). We elaborated earlier (see Introduction for more) that the BOLD response was found to be coupled with the LFP response rather than the single or multiunit recording in concomitant acquisition (Logothetis et al., 2001); Logothetis and associates explained these finding such that the BOLD response reflects the integrative aspect of local processing that happens in the active area rather than the output of this

activation (Logothetis et al., 2001). We believe that this is the case in our animal, where the increase in the KARs and AMPARs mediated EPSCs (Aller et al., 2015, Arora et al., 2018) are not reflected in the BOLD response. In this scenario the differences observed in Whalley's et al. article, pending the statistical validation, is due to a phenomenon other than hyperexcitability. The notion introduced earlier (Pickard et al., 2008) that they found the indel variant has a protective value against the bipolar disorder, while the imbalance between excitation/inhibition has been always linked to a negative outcome (for instance, Dani et al., 2005, Gibson et al., 2008, Kehrer et al., 2008, Bateup et al., 2011, Wallace et al., 2012) might give some credence to that postulation. In a nutshell, we are tempted to believe that our results are not in conflict with others conducted in humans instead, they reflect different aspects of the underlying neuronal functionality and/or the inherent difference between humans and rodents.

8. Negative BOLD response under urethane anesthesia is driven by excitation, rather than, inhibition

Applying electrical microsimulation through MRI-compatible electrodes led to prevalent negative BOLD response (NBR) in the hippocampus and the extra-hippocampal regions, regardless of the point of stimulation, the frequency, or the genotype (Fig. 3.33-3.38). The robustness, the replicability of the NBR across subjects, and its correlation with the stimulation paradigm tempted us into ruling out a random noise or a motion artifact origin for the signal.

The underlying neuronal origin of the NBR is an old issue as old as the BOLD contrast itself and just as controversial. The most common interpretation of the origin of the BOLD signal involves the cerebral blood flow (CBF), the cerebral blood volume (CBV), the cerebral metabolic rate of oxygen (CMR_{O2}), the cerebral metabolic rate of glucose (CMR_{glu}), and the delicate balance between these factors (Logothetis 2008, Huettel et al., 2014, chapter 7).

The interplay of these aforementioned factors in response to neuronal activity determines whether a positive or a negative BOLD will ensue. Synaptic inhibition, an imbalance between CMR_{O2} and CBF, and vasoconstriction initiated by neurotransmitters are all events that have been linked to NBR (for an interesting review about NBR, see Lauritzen

et al., 2012). In these circumstances, vasoconstriction and increased deoxygenated hemoglobin that result from neuronal hyperpolarization are the culprit behind the sustained NBR (Devor et al., 2008, Schäfer et al., 2012). Despite the fact that most articles that reported an NBR attributed it to a decrease in synaptic activity, others have provided evidence advocating for an NBR resulted from an increase in neuronal activity (see for instance, Harel et al., 2002, Shih et al., 2009 where NBR was attached to increased spiking activity).

Even though a lot of investigations that tackled the NBR phenomenon were performed on animals, the effect of anesthetics (when used) was the focus of little-to-no attention. We used urethane at a moderate dosage (1.3 g/kg) to induce anesthesia before performing the surgery to implant the electrodes. Urethane is known for its long-lasting effect and its minimal effect on the cardiovascular, the respiratory systems, and neurotransmission (Hara and Harris 2002). However, some reports have indicated that, at certain concentrations, urethane has the potential to depress the contractability of the vascular smooth muscles (Maggi and Meli 1986). In an interesting article, Liu et al. found that that most of the positive BOLD response they observed under isoflurane and medetomidine, was rendered negative upon using urethane as anesthetics (Liu et al., 2012); the authors interpreted these findings as a mixture of urethane's effect on the blood flow as well as the multichannel blocking effects (Liu et al., 2012). Other groups, however, reported positive BOLD response and no NBR using also urethane as an anesthetic (Canals et al., 2008, Moreno et al., 2016). The effect of urethane concentration and the species of the animals used can be safely neglected since all of the previous studies used quite similar concentrations of urethane in the same model animals (rats).

The data acquired under urethane is even scarcer in mice. In two different studies, eliciting BOLD responses by sensory stimulation returned only positive activation under four different anesthetics including urethane (Schroeter et al., 2014, Schlegel et al., 2015). Jego and team reported positive BOLD responses upon stimulating the hippocampus using a similar paradigm to ours (Jego et al., 2014); only medetomidine was used to induce sleep. These results that apparently are contradictory can be interpreted either as the NBR is a "capricious phenomenon" as indicated by Lauritzen and others (Lauritzen et al., 2012) (it depends on the structure affected) or as a reflection of the breaking down of

neurovascular coupling due to anesthesia (Sharp et al., 2015). There is no evidence that those two scenarios are mutually exclusives.

We believe, at least, in our case the breaking down of the neurovascular coupling due to anesthesia is responsible for the NBR. Huang et al. stated that the BOLD response is likely to be a contribution of two factors working together or one of them acting separately; those factors are the blood oxygenation and vessel radius (Huang et al., 1996). Under urethane anesthesia, the blood vessels are dilated and quite unresponsive and hence only one factor is controlling the signal which is the blood oxygenation. Upon activation, there is plenty of blood to provide oxygen to the active neurons, their activity leads to the accumulation of deoxygenated blood that is not perfused away courtesy of the unresponsive blood vessel. Since the BOLD response is actually only sensitive to the paramagnetic deoxygenated blood, the accumulation of this type of blood causes the negative response even though the neurons are being activated. This effect is probably more evident in our mice as an implication of the surgeries. A definitive evidence is still lacking to prove or negate this conjecture. It would be really interesting to perform a somatosensory stimulation paradigm in awake mice and observe how the signal changes on the contralateral and the ipsilateral sides upon injecting the animal with urethane.

9. Limitations and future directions

In this body of investigation, we tried to probe the structural and functional substrates of overexpressing GluK4 KAR subunit. Our research showed a wide variety of abnormalities on both frontiers. However, the work suffered from various shortcomings that should be noticed and rectified in similar future endeavors.

We restricted our experiments to mice males for various biological and technical reasons. One of our preliminary goals was to isolate the effects of increasing the dose of *Grik4* gene and with this in mind, we were trying to eliminate all the variability between the two groups under investigation including background, environment, age, weight, and gender. On the other hand, our mice females exhibited a significant difference in body weight and subsequently in the dosage of anesthesia required to put them to sleep. Those two factors had the potential to confound our results so we took the decision of restricting

the work to males only. Increasing the total number of animals in future experiments might help those differences to converge.

Another important issue was the cross-sectional nature of the work. Better insights and deeper understanding of how synaptic transmission can translate into structural and functional abnormalities could be obtained by observing the animals at different time points. Given the non-invasive nature of the MRI, the same number of animals would be used. This is particularly important also because all the synaptic transmission experiments were conducted on young animals (p17 for example). It would be interesting to see how structural and functional MRI results develop over different ages.

We did all of our functional scans under anesthesia. Anesthesia is quite important in such experiments in order to limit the head movement of the animal in the scanning bed. As has been shown extensively in the literature, anesthesia does have a deleterious effect on the BOLD signal and the resting-state networks. Conducting the experiments on awake animals might be a step forward in establishing a relationship between activities on cellular and network levels. Furthermore, it will help to settle the issue of the NBR.

Even though OF and EPM provides a good proxy for the anxiety, they are not refined enough and can reflect multiple things. Acquiring more refined behavioral tests with social nature and assessing their correlation with the functional and structural imaging will add a huge value to those modules. We discussed earlier how the correlation between resting-state networks and behavior is lacking and how this might be due to the nature of the behavioral tasks.

Concurrent recording of BOLD response side by side with single unit recording could confirm or negate our hypothesis about the activation that drives negative BOLD response. Another way to approach this question would be to use GABA-transaminase inhibitors and see if this causes elevation or demotion of the response. An elevation would falsify our hypothesis and proves that the activity was, after all, driven by neuronal deactivation.

V. CONCLUSIONS

Conclusions

We analyzed the implications of the increased dosage of *Grik4* gene in the brain using multi-parametric MRI to unearth changes on the functional and structural levels that might stem from such expression. The results indicate various alterations on both levels, in addition to the correlations between some of those changes and the behavioral tasks the animal performed prior to the scanning sessions. In light of those findings, we feel confident to conclude that the overexpression of GluK4 subunit, and probably many more, can widely affect the brain networks and induce many developmental changes that are associated with alteration in the behavior. On the other hand, the MRI technique with its various modalities proved not only to be able to detect theses anomalies, but also to accurately pinpoint them to structures where they occur.

Conclusiones

Analizamos las implicaciones del aumento de la dosis del gen *Grik4* en el cerebro mediante resonancia magnética multiparamétrica para descubrir cambios en los niveles funcionales y estructurales que podrían derivarse de dicha expresión. Los resultados indican varias alteraciones en ambos niveles, además de las correlaciones entre algunos de esos cambios y las tareas de comportamiento que el animal realizaba antes de las sesiones de exploración. A la luz de esos hallazgos, nos sentimos confiados para concluir que la sobreexpresión de la subunidad GluK4, y probablemente muchas más, pueden afectar ampliamente las redes cerebrales e inducir muchos cambios en el desarrollo asociados con la alteración del comportamiento. Por otro lado, la técnica de resonancia magnética con sus diversas modalidades demostró no solo poder detectar estas anomalías, sino también señalarlas con precisión a las estructuras donde ocurren.

VI. ANNEX: AUTHOR'S PUBLISHED SCIENTIFIC CONTRIBUTION

This article appears published after peer review in Journal of Neuroscience Methods 343: 108814. 2020 (https://doi.org/10.1016/j.jneumeth.2020.108814)

Diffusion-weighted MRI in neurodegenerative and psychiatric animal models: experimental strategies and main outcomes

Amr Eed[1], Antonio Cerdán Cerdá[1], Juan Lerma[1], Silvia De Santis[1,2]
[1]Instituto de Neurociencias, CSIC/UMH, San Juan de Alicante, Alicante, Spain.
[2]CUBRIC, School of Psychology, Cardiff University, Cardiff, UK
Corresponding: Silvia De Santis, dsilvia@umh.es

Abstract - Preclinical MRI approaches constitute a key tool to study a wide variety of neurological and psychiatric illnesses, allowing a more direct investigation of the disorder substrate and, at the same time, the possibility of back-translating such findings to human subjects. However, the lack of consensus on the optimal experimental scheme used to acquire the data has led to relatively high heterogeneity in the choice of protocols, which can potentially impact the comparison between results obtained by different groups, even using the same animal model. This is especially true for diffusion-weighted MRI data, where certain experimental choices can impact not only on the accuracy and precision of the extracted biomarkers, but also on their biological meaning. With this in mind, we extensively examined preclinical imaging studies that used diffusion-weighted MRI to investigate neurodegenerative, neurodevelopmental and psychiatric disorders in rodent models. In this review, we discuss the main findings for each preclinical model, with a special focus on the analysis and comparison of the different acquisition strategies used across studies and their impact on the heterogeneity of the findings.

Introduction

Magnetic resonance imaging (MRI), a technique widely used in the clinical practice as a diagnostic tool, has revealed a fundamental importance as a powerful, non-invasive analysis tool also in animal studies and, more specifically, in preclinical pharmaceutical research. The development of high field scanners (e.g. 7T) has significantly improved the spatial resolution, granting access to the investigation of small animals like rodents. Indeed, in recent years, knock-out or transgenic mice, where specific genes have been removed or altered, have been widely used in fundamental research. The combination of these models with this powerful imaging technique can shed light onto how genetic alterations derived into pathologies. Because of its non-invasiveness, MRI allows repeated observations on the same subject as well as longitudinal studies and is being increasingly used in rodent models of brain diseases.

The landscape of MRI can widely be divided into two major areas: structural and functional. Structural MRI is mainly concerned with conveying information about the underlying tissue properties, while patterns of brain activity can be measured and compared using functional contrasts. Structural contrasts such as T_1 and T_2 are suited for mapping brain anatomy and hence are widely used in clinical investigation to extract key information such as cortical thickness and the volume of different anatomical structures. Conversely, functional contrasts are meant to catch the brain in action. Sensitizing the machine to events such as blood oxygenation or blood flow is the basis for blood oxygenation level-dependent and cerebral blood flow functional MRI.

Diffusion weighted MRI (dw-MRI) belongs to the structural domain (see Huettel et al., 2014 for a review about the different contrasts), but it stands out due its ability to extract information about the microstructural properties (as in the range of microns) of the tissue in contrast with millimeters level other structural modalities work on.

Amongst the different contrasts available, dw-MRI is widely used to study the brain and brain-related pathologies. This review examines the experimental procedures used to infer structural differences in murine neurodegenerative, neurodevelopment and psychiatric models versus wild type animals. The manuscript is structured as follows. First, we briefly explain the fundaments of dw-MRI and introduce the different parameters that define the acquisition scheme. We then describe the most popular model used to fit the diffusion signal, the diffusion tensor imaging (DTI), along with some of the most used advanced models. After introducing the state-of-the-art of preclinical

modelling, we highlight the relevant aspects that hamper the results homogeneity and, ultimately, the transference to the clinic. The body of this article consists of an overview of the different experimental strains and preparations, dw-MRI acquisition parameters, biophysical models, and main results that where reported so far using dw-MRI to characterize the most common pathologies of the central nervous system.

Diffusion-weighted MRI: theory, experimental scheme, and biophysical models

Dw-MRI contrast is sensitive to the random displacement of water molecules, which in biological tissues is constantly hindered by the presence of barriers in the form of cell membranes and other organelles inside the cell. By probing the path water molecules follow while diffusing, important characteristics of the underlying microstructure can be measured (see Jones 2010, Emsell et al., 2016).

Sensitizing the MRI signal to diffusion usually requires a diffusion-sensitized acquisition sequence; the pulsed gradient spin echo (PGSE) is the most common (Stejskal and Tanner 1965). The measured signal is an exponential decay defined as follows:

$$S = S_0 \cdot e^{-bD} \quad (1.1)$$

Where:

$$b = \gamma^2 G^2 \delta^2 \left(\Delta - \frac{\delta}{3}\right) \quad (1.2)$$

S_0 represents the signal in absence of diffusion weighting, S is the signal, D is the diffusion coefficient of the water molecules, γ is the gyromagnetic ratio, G is the strength of the gradient applied, δ is gradient duration, and Δ is the time difference between the two gradient pulses. The diffusion time Δ describes the amount of time the water molecules are allowed to displace before acquiring the signal. The PGSE sequence is illustrated in Fig. 1. A typical diffusion experiment will encompass several diffusion-weighted images along different noncollinear, non-coplanar unique directions

along with one or more images acquired without gradient, serving as a reference. The amount of diffusion weighting applied is quantified by the b-value (Le Bihan and Breton 1985).

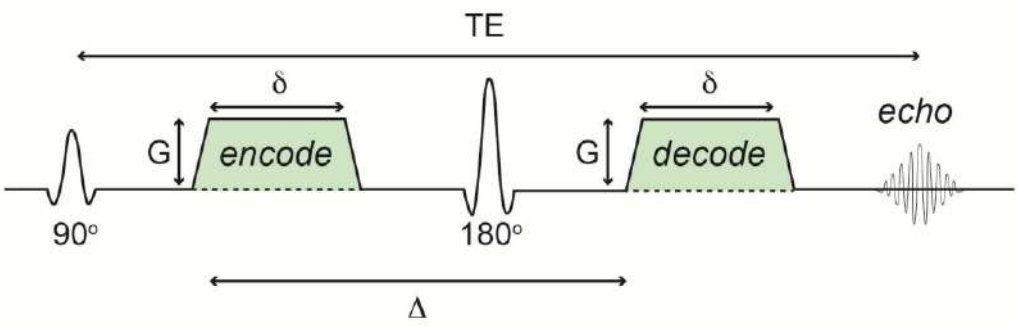

Figure 1: Pulsed gradient spin echo (PGSE) sequence. The basic PGSE sequence consists of two radio-frequency pulses, an excitation pulse (90°), a refocusing pulse (180°), and two gradient pulses (green trapezoids). G represent the strength, and δ the duration of the gradient. The diffusion time, Δ, is the time from the start of the first gradient pulse to the start of the second gradient pulse. TE is the echo time.

Since its inception by Basser et al., in 1994, diffusion tensor imaging (DTI) has gained wide acceptance as the go-to method of modelling the diffusion signal as a consequence of its simplicity, robustness, and the reasonable acquisition parameters (Basser et al., 1994). DTI uses a 3 × 3 apparent diffusion tensor to represent diffusion in 3D space (see Kingsley 2006). Multiple measures can be calculated from the diffusion tensor; the most frequently used are fractional anisotropy (FA), mean diffusivity (MD), axial diffusivity (L1), and radial diffusivity (RD) (Basser 1995).

Despite its popularity, DTI suffers from a number of limitations, the main one being that it assumes that the diffusion follows a Gaussian distribution, while the signal can also come from intracellular water molecules where restrictions generate a deviation from Gaussian behaviour (Curran et al., 2016). Numerous advanced models have been developed over the years to mend the pitfalls of the DTI model. Diffusion kurtosis imaging (DKI) quantifies the degree to which the diffusing water molecules displacement probability deviates from the Gaussian distribution, which gives a more realistic view of the diffusion in tissues like the gray matter where the non-Gaussian diffusion is ubiquitous. The same PGSE is usually used in DKI, however, it requires

higher b-values along with a larger number of gradient orientations, as the calculations are more complex than those of DTI (Jensen et al., 2005, Lu et al., 2006, Jensen et al., 2011, reviewed in Jensen and Helpern 2010).

Other approaches aim at modelling the signal as a multi-compartment model separating the contributions of the intra from extracellular compartments (see Alexander et al., 2019 for a review). The composite hindered and restricted model of diffusion (CHARMED), for instance, assumes two models of diffusion: an intra-axonal restricted diffusion, and a hindered diffusion happening elsewhere. A notable strength of such a model is that it can, to a certain degree, resolve the issue of crossing-fibers within the same voxel. A simpler approach such as neurite orientation dispersion and density imaging (NODDI) models instead the dispersion around a single fiber direction (Zhang et al., 2012).

These models have definitely enriched the insights we gain from dw-MRI by providing a more realistic view of the diffusion process more than the usual DTI. However, they require a multi-shell acquisition and higher b-values that might lead to higher noise (Alexander et al., 2019).

Animal models and dw-MRI

The recent developments in molecular biology and genome editing techniques have echoed through all fields and MRI was no exception. The ability to recapitulate human disorders using animal models opened a big window for a closer look into these diseases using the rich varieties of MRI modalities. Due to the physical gap between humans and small animals like rodents, scanning small animals require special set-ups to accommodate the smaller size. Custom coils and higher field strengths are needed in order to produce a useful resolution and an improved SNR. Other things such as anesthesia, mechanisms for head fixation to limit motion artifacts and maintaining the animal's core temperature and respiration rate also often require special attention and maintenance.

A major roadblock in the face of moving dw-MRI more into the clinic is the lack of solid validation of the pathological correlates of the changes frequently elucidated by imaging. Histological samples obtained posthumously from patients are rarely available and hard to get. Using animal models comes in handy in such cases, where the post-MRI histological examination is becoming mainstream. Using immunohistochemical

techniques, things such as axons demyelination, β-amyloid accumulation, and changes in cell morphology can be investigated, quantified, and further linked to the dw-MRI findings, establishing a framework to understand the meaning of the variations in the imaging contrast (Oguz et al., 2012). These advantages do not come without a cost. Due to the evolutionary gulf between humans and rodents, these models cannot recapitulate all the aspects of a given disorder; instead, they can be thought of as a representation of a certain aspect of the disease and hence caution should always be employed when interpreting or extrapolating such findings to human studies (Jones 2010). In addition, correlating histological and imaging findings has its own shortcomings, like the difficulty of matching images between the two modalities (Horowitz et al., 2015).

Another important issue to take into account when looking at preclinical dw-MRI results and their translatability to humans, is the lack of a homogeneous strategy for designing the experimental protocol. While some parameters mostly impact on the SNR, others affect the range of diffusion on which the study is focusing. Specifically, changing the diffusion time Δ might shift the sensitivity of the analysis from mostly extracellular water to restricted water. Similarly, a high b-value will give more information about compartment undergoing slower diffusion compared to lower b-values (Assaf et al., 2008). In addition, both high Δ and high b-values will translate into a lower SNR, potentially affecting the sensitivity to changes (Hagmann et al., 2006). Also the choice of the biophysical model used to analyze the data impacts on the results, where more advanced models can increase both sensitivity and specificity to changes compared to DTI (De Santis et al., 2017). Finally, the number of unique orientations determines the accuracy and the precision of the obtained parameters and generally, a number below 20-30 is considered suboptimal (Jones and Basser 2004).

To assess the homogeneity of the results and the employed experimental protocol across studies, we searched the PubMed website for preclinical studies using dw-MRI to investigate neurodegenerative or neurodevelopmental disorders and employing rodents. Entrez tool from the Biopython library was used to scrape the website (git repository: https://github.com/amrka/pubmed_scrape_dw-MRI_preclinical). A combination of terms was used in the search including, "diffusion tensor imaging AND mice", “diffusion tensor imaging AND rats", "diffusion tensor imaging AND ferrets", "diffusion MRI AND mice", "diffusion MRI AND rats", and "diffusion MRI AND ferrets". The unique hits were refined manually in order to remove irrelevant articles. We only included results reported by the authors which reached statistical significance,

regardless of the analysis or the statistical methods used. A summary of the disease, the model used, acquisition parameters, and the most relevant results can be found in Tables 1-2, and the main experimental parameters are plotted for the different diseases investigated in Figure 2.

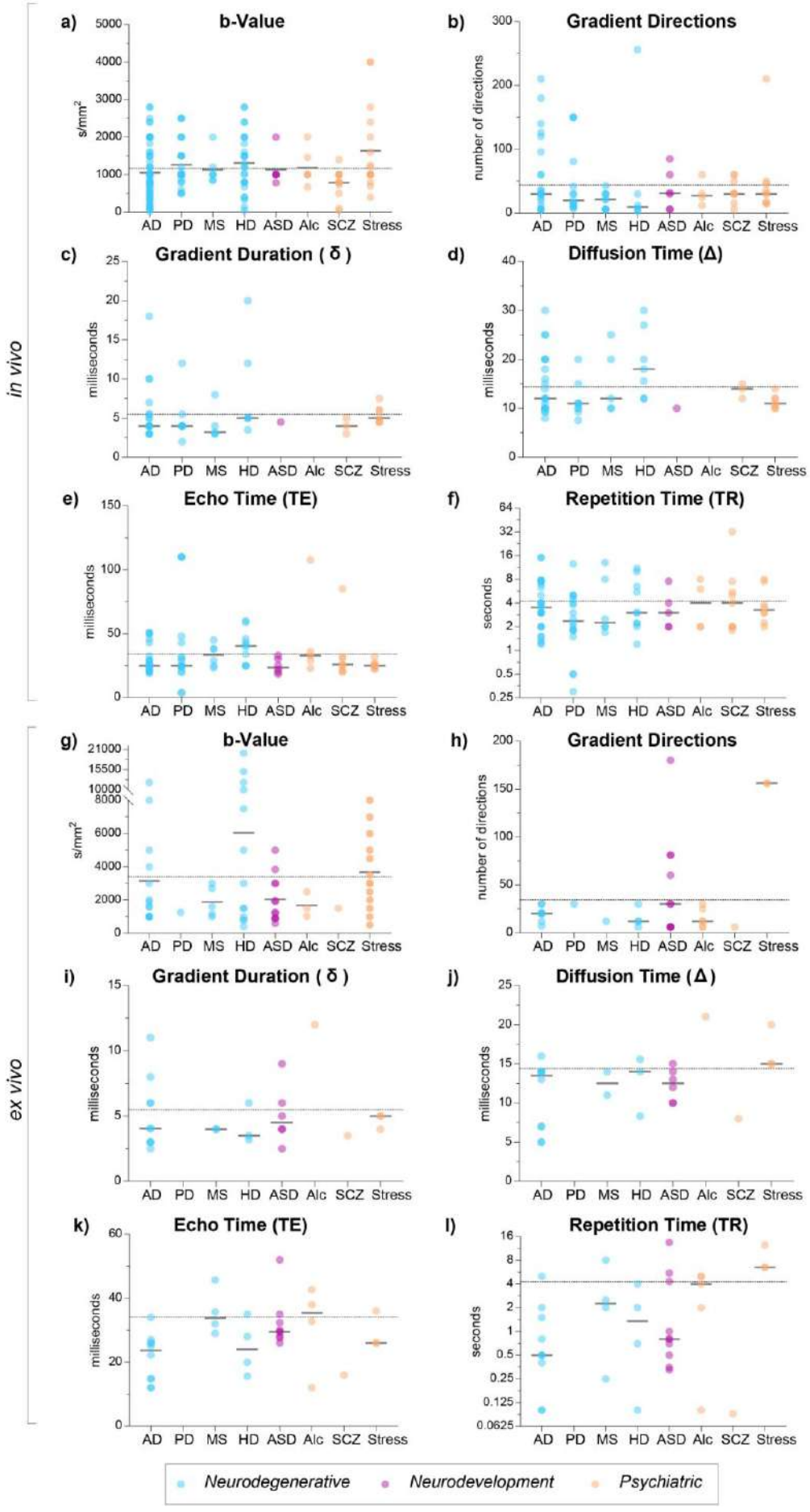
in vivo
ex vivo
a) b-Value
s/mm²
b) Gradient Directions
number of directions
c) Gradient Duration (δ)
milliseconds
d) Diffusion Time (Δ)
milliseconds
e) Echo Time (TE)
milliseconds
f) Repetition Time (TR)
seconds
g) b-Value
s/mm²
h) Gradient Directions
number of directions
i) Gradient Duration (δ)
milliseconds
j) Diffusion Time (Δ)
milliseconds
k) Echo Time (TE)
milliseconds
l) Repetition Time (TR)
seconds
AD PD MS HD ASD Alc SCZ Stress
Neurodegenerative
Neurodevelopment
Psychiatric

Figure 2. Dw-MRI parameters used in Neurodegenerative (blue), Neurodevelopment (purple) and Psychiatric (orange) preclinical models *in vivo* **(a-f)** and *ex vivo* **(g-l)**. Each plot represent one dw-MRI parameter: **(a,g)** b-Value; **(b,h)** number of noncollinear, non-coplanar gradient directions; **(c,i)** gradient duration, δ; **(d,j)** diffusion time, Δ; **(e,k)** echo time, TE; **(f,l)** repetition time, TR. The dashed line represents the mean parameter value calculated across all included articles. The narrow continuous line represents mean in specific neuropathology. Dots represent the corresponding parameter values used in each article. Abbreviations: AD=Alzheimer's disease; PD=Parkinson's disease; MS=Multiple sclerosis; HD=Huntington's disease; ASD=Autism spectrum disorder; Alc=Alcoholism; SCZ=Schizophrenia.

Neurodegenerative diseases

Diseases such as Alzheimer's, Parkinson's, Huntington's, and multiple sclerosis together represent the most prevalent neurodegenerative disorders, with a total burden of 23% of the disability-adjusted life years, which is expected to further grow by 2030 (World Health Organization). The deposition of misfolded Amyloid-β (Aβ) plaques between nerve cells and tau neurofibrillary tangles inside the neurons are the most prominent hallmarks of Alzheimer's disease (AD); such aggregation starts a cascade of events, involving inflammation, neuronal and synaptic degeneration, and formation of tau neurofibrillary tangles, that eventually leads to cognitive deterioration (Small and Duff 2008). AD has been linked to mutations in genes responsible for the formation and cleavage of Amyloid-β such as amyloid precursor protein (*APP*), γ-secretase proteins presenilin 1 (*PSEN1*), and presenilin 2 (*PSEN2*) (Small and Duff 2008). Other genetic risk factors such as *APOE* and *TREM2* genes have been linked to sporadic and early-onset forms of AD (Scheltens et al., 2016).

Being unique to humans, finding an effective animal model that recapitulates the entire biology of AD remains elusive; genetically modified mice engineered to overexpress APP are an important tool, but replicate only one aspect of the disorder (Drummond and Wisniewski 2017). The majority of the articles examined for this review used APP/PSEN1 mouse model with APP gene carrying the Swedish double mutation (KM670/671NL) and PSEN1 with one type of mutations such as L166p (Vanhoutte et al., 2013) or ΔE9 (Qin et al., 2013). A preponderance of studies using

models with APP harboring the Swedish double mutations (Tg2576) with no PSEN1 mutations was still observed (Harms et al., 2006). Both kinds of models give rise to amyloid deposition in various brain structures but differ in the time course of such deposition. Other models incorporate other mutations aiming to better replicate the disorder by allowing the formation of tau-neurofibrillary tangles such as the triple transgenic (3xTg) model (Snow et al., 2017). Not surprisingly, the mouse was the animal of choice occupying the biggest chunk of the literature with a few articles settling for using rats instead (Munoz-Moreno et al., 2018, Anckaerts et al., 2019). Owing to the rodents' small-sized brains, a strong magnetic field is mandatory. Field strengths between 4.7 T to 11.7 T were employed in all the studies.

FA, MD, L1, and RD are the most commonly reported scalar measures whether in region of interest (ROI), voxel-based (VBA) type of analysis, or both. Results showed a good agreement between studies regardless of the model used, the acquisition parameters, or the type of the analysis. Most studies reported a decrease in FA accompanied by an increase in MD in white matter structures such as the corpus callosum, fornix, internal capsule, and external capsule as well as in gray matter tissues including the hippocampus, large parts of the cortex, and the thalamus (Fig. 3a) (Shu et al., 2013, Qin et al., 2013). Using the same model and similar acquisition parameters with slightly younger animals, Zerbi and coworkers showed a voxel-wise increase in MD in the fimbria and the hippocampus, but lower MD in the body of the corpus callosum, the fornix, and the cerebral peduncle (Zerbi et al., 2013). This discrepancy cannot be explained by different amyloid deposition patterns. Interestingly, Zerbi et al. used a b-value of 1000 s/mm^2, while Qin and Shu et al. chose a b-value of 800 s/mm^2. This slight difference can translate into a better SNR, but also a different sensitivity to hindered versus restricted compartments. A staggering amount of human studies seems to be in accordance with the former results (see for example Stahl et al., 2007, Zhang et al., 2007, Agosta et al., 2011, Shu et al., 2011). Post-mortem literature reported alterations in the microstructure in various brain tissues, including loss of myelin, cellular death, and neurodegeneration. Such alterations affect the structural integrity and can be the cause behind the decrease in FA values and the increase in MD, respectively. Intriguingly, the results from applying advanced models seem to corroborate these findings. Using DKI, some studies have reported an increase in all three of DKI metrics (axial kurtosis (AK), mean kurtosis (MK), and radial kurtosis (RK)) in parts of the cortex, whilst they did not report any change in those metrics in the hippocampus or any

of the white matter main tracts (Vanhoutte et al., 2013, Praet et al., 2018). One interpretation might be that DKI is sensitive to certain aspects of the underlying abnormalities that DTI metrics are impartial to. Using NODDI on an animal model of tau pathology, a strong correlation between the tau burden in the cortex and hippocampus and the neural density in these structures has been found (Colgan et al., 2016). Such correlations might hint at a sensitivity of NODDI metrics towards tau-related pathology, however, the results are quite limited by the small sample size.

RD and L1 are fairly reported alongside FA and MD with no general consensus on the direction of the changes in the different structures. A longitudinal study showed a decrease in RD values at 12 months, then reported an increase in these values at 16 and 18 months (Sun et al., 2005). However, as elegantly demonstrated by Wheeler-Kingshott et al., the lax usage of the L1 and RD should be discouraged especially in regions such as the gray matter where crossing fibers are ubiquitous (Wheeler-Kingshott and Cercignani 2009).

A progressive loss of dopaminergic neurons in the substantia negra (SN) and together with the deposition of a misfolded protein called α-synuclein intracellularly, forming the Lewy bodies, constitutes the cardinal hallmarks of Parkinson's disease (PD) (Poewe et al., 2017). Unlike AD, the majority of PD incidents are idiopathic with a marginal number of cases that can be attributed to heritable factors or exposure to environmental toxins (Nalls et al., 2014, Ascherio and Schwarzschild 2016). Creating an effective animal model of PD that embodies the disorder's pathophysiology remains elusive (Beal 2010) with most of the studies settling for the traditional toxin-treated models. Toxins such as 6-hydroxydopamine (6-OHDA), rotenone, and 1-methyl-4-phenyl-1,2,3,6-tetrahydropyridine (MPTP) were unilaterally injected either directly in the SN itself (see, for example, Liu et al., 2017), the striatum (Perlbarg et al., 2018), or the medial forebrain bundle in a few studies (Monnot et al., 2017). Interestingly, PD studies witnessed a surge in using rats, rather than mice, as the animal of choice, probably to facilitate performing the surgeries of the intracranial injection. A few studies used transgenic mice or rats harboring mutations that were linked to the familial form of PD in humans, such as TNWT-61 transgenic mice that overexpress α-synuclein (Khairnar et al., 2015, Khairnar et al., 2016, Khairnar et al., 2017), or rat models featuring a knock-out of *PINK1*, as it has been implicated in cases of familial early-onset parkinsonism (Ferris et al., 2018). Despite the recapitulation of some of the hallmarks of PD, these models lack the neurodegeneration of the dopaminergic neurons,

limiting their potential to symptomatic research. Perhaps the most interesting animal model would be the one known as the MitoPark mouse, which faithfully mimics most of the hallmarks of PD including the progressive neurodegeneration; however, the fact that it is not built on a human genetic mutation limits its potential (Beal 2010).

Unfortunately, due to the variation in the substance injected, doses, and site of injection, comparing the results between different studies is quite challenging (Table 1). The SN as the structure associated the most with PD, showed different values of DTI scalar metrics across different studies (Fig. 3b). Using models of both 6-OHDA and rotenone, Liu et al. reported an immediate FA decrease in the SN, followed by an increase six weeks after the injection in comparison with the sham controls (Liu et al., 2018a), while a persistent decrease after one and six weeks was also reported (Fang et al., 2018). This decrease in FA was also observed in the MitoPark animals (Cong et al., 2016).

A number of studies used DKI to investigate TNWT-61 animal model at different stages. Many structures showed an increase in all three kurtosis measures (MK, AK, RK). The changes in the SN, ipsilaterally to the injection, start as early as six months of age, while they can appear by three months in regions such as the striatum (Khairnar et al., 2015, Khairnar et al., 2016, Khairnar et al., 2017). These findings might favor the DKI metrics as more sensitive measures than the DTI ones that could have the potential to serve as an early diagnostic tool.

Huntington's disease (HD) emerges from a mutation in the *HTT* gene that encodes for a protein of unknown function called Huntingtin. The mutated form of Huntingtin protein tends to have a toxic effect on neurons, especially the striatum's medium spiny neurons. This toxicity is usually manifested as motor as well as cognitive and behavioral symptoms (Bates et al., 2015). The understanding of the molecular background of HD is very well reflected in the rodent models used to study the illness. All the models have an *HTT* gene featuring a different number of CAG repeats, the very same repeats associated with the disease in humans (Blockx et al., 2012a, Teo et al., 2016, Gatto et al., 2019). The use of transgenic rat model (TgHD) was quite common in giving this model an edge due to the brain size and the possible enhanced SNR (Table 1). The homogeneity of the molecular background of the models was also evident in terms of the results. Even though there was a wide gap in the ages of the animals used, the results seemed to be in accordance with each other. The values of FA in all the articles that reported a significant change in the corpus callosum or its various sub-

components were found to be decreased with the respect to the control animals (Chyi and Chang 1999, Xiang et al., 2011, Garcia-Miralles et al., 2016, Teo et al., 2016, Gatto et al., 2019), while this was reversed in some of the gray matter structures such as the striatum (Fig. 3c) (Blockx et al., 2012b, Antonsen et al., 2013). Using a simple acquisition protocol of only one shell of 800 s/mm^2 and 6 directions, Blockx et al. failed to unearth any differences (Blockx et al., 2011), whilst using a multi-shell acquisition of severn shells, they reported numerous significant in changes (Blockx et al., 2012a, Blockx et al., 2012b).

Multiple sclerosis (MS) is a severe disease which causes demyelination and axonal damage, both focally and globally (Filippi et al., 2018). Due to the poorly understood etiology, the available animal models poorly recapitulate the disorder such that the demyelination in those models is induced while the MS has a spontaneous onset (Rice 2012). The most popular model is what is called experimental autoimmune encephalomyelitis (EAE) where the animals are immunized with a myelin antigen to harness the immunity to attack its own myelin (Rice 2012). The other available models feature toxic demyelination, where the animals are is that toxic to the oligodendrocytes such as cuprizone.

The literature reviewed used exclusively the EAE (Nishioka et al., 2017, Crombe et al., 2018) or the cuprizone model (CPZ) (Song et al., 2005, Atkinson et al., 2019), while one article experimented with a mixed model of both worlds (Boretius et al., 2012). As expected, a diminished FA was observed in the corpus callosum and, more importantly, in the optic nerve and the optic tracts (Fig. 3d) (Sun et al., 2007, Nishioka et al., 2017, Nishioka et al., 2019) recapitulating an important feature of MS in humans where patients suffer from visual deficits (Table 1). A significant difference in the MD values between MS models and their corresponding control was reported only twice (Crombe et al., 2018, Atkinson et al., 2019). Both studies used reasonable acquisition protcols consist of two shells and a sufficient number of directions. Factors such as different diffusion time and spatial resolution might be in play in such adverserial results. Diffusion times of 12 ms with a resolution of 82 × 81 × 203 μm^3 (Crombe et al., 2018), 10 ms with resolution of 156 × 156 × 1000 μm^3 (Atkinson et al., 2019) have been reported. Despite the gain in SNR, the lower resolution used in this latter study makes the partial volume effect a real concern here.

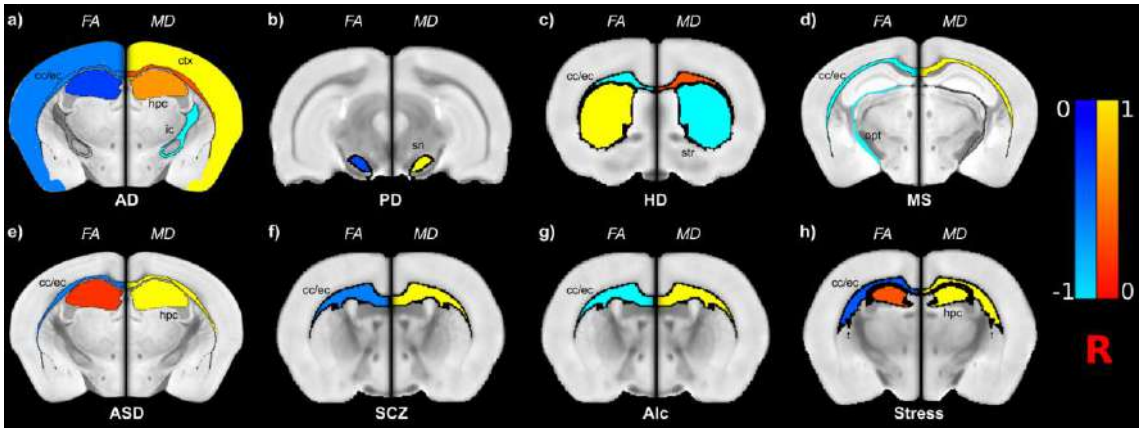

Figure 3. Visual representation of the number of studies reporting increase (in red) and/or decrease (in blue) in FA and MD in neurodegenerative (a-d) and neurodevelopmental and mood disorders (e-h) in the most affected structures. Results are overlaid on a high-resolution template of a mouse brain (a, d, e) or a rat brain (b, c, f, g, h) depending on which animal model is used more frequently in each disease. Results are calculated as ((# of studies reporting an FA or an MD increase - # of studies reporting an FA or an MD decrease) / total # of studies). FA results are displayed on the left hemispheres and MD results are displayed on the right hemispheres. We used the AMBMC MRI mouse brain template and atlas (Richards et al., 2011, Ullmann et al., 2013, Ullmann et al., 2014, Janke and Ullmann 2015) and the SIGMA MRI rat brain template and atlas (Barrière et al., 2019). **Abbreviations:** FA, fractional anisotropy; AD, Alzheimer's disease; Alc, Alcoholism; ASD, Autism spectrum disorder; cc/ec, corpus callosum/external capsule; ctx, different parts of the cortex; HD, Huntington's disease; hpc, hippocampus; ic, internal capsule; MD, mean diffusivity; MS, multiple sclerosis; opt, optic tract; PD, Parkinson's disease; R, right; SCZ, schizophrenia; sn, substantia nigra; str, striatum.

Neurodevelopmental and psychiatric disorders

While preclinical models of neurodegenerative disorders have a long tradition in biomedical research, more recently imaging techniques have been applied also to look at subtle changes in psychiatric and neurodevlopmental animal models. Autism spectrum disorders (ASD) describe a myriad of heterogeneous neurodevelopmental disorders characterized by ill-forms of communication with others, the pervasiveness of repetitive behaviors, and social disinterest (Miles 2011). A growing body of evidence

defined the genetic component, rather than the environmental, to be the major cause behind ASD. Genome-wide association studies (GWAS) studies have identified a number of genes associated with a high risk of developing ASD such as *ANK2*, *ARID1B*, *CACNA2D3*, *FOXP1*, *GRIK4*, and *GRIN2B* (Iossifov et al., 2014). Such mutations inspired the development of animal models trying to recapitulate the essence of ASD. However, interpreting such results must be put in the context of the uniqueness of the disorder to humans.

Due to the heterogeneity that comes with ASD, our search highlighted the usage of various models aiming at recapitulating different mutations, with a limited number of articles using the same model. Such a limitation made it challenging to compare the models to each other. However, some global patterns were observed (Table 2). The majority of the articles reported a decrease in FA in WM structures such as the corpus callosum, the external capsule, the fornix, and the anterior commissure (for instance, Ellegood et al., 2011, Dodero et al., 2013, Zerbi et al., 2019) as well as some other GM tissues such as the hippocampus, the cerebellum, and the thalamus (Fig. 3e) (Ellegood et al., 2011). This decrease was accompanied in some cases with an increase in RD or other scalar metrics. The opposite change in FA and RD, albeit to a lower extent, was also reported. In his longitudinal study, for instance, Kumar et al. reported a trend of increasing FA values in the corpus callosum that peaked at P70 where compared to a cross-sectional control, was significantly different (Kumar et al., 2012). This could hint at a change in the model throughout its lifetime reminiscent of the ASD in humans as briefed earlier. Such a discrepancy can emanate from a multitude of factors, not least of all the very nature of ASD rather than the models themselves, or can be attributed to poor acquisition protocols, where most of the literature reported the use of only 6 directions which, potentially, can lead to a poor tensor estimation (Ellegood et al., 2011, Kumar et al., 2012, Kumar et al., 2014, Kumar et al., 2018, Pervolaraki et al., 2019). Another prominent drawback in the literature analyzed is the dominant use of male animals in most of the studies (Kumar et al., 2012, Zerbi et al., 2019).

Aside from the direction of the change in FA and RD, these articles seem to agree on a change in the microstructure of the white matter tracts running between different brain structures, giving support to the tantalizing hypothesis that ASD is a connectivity problem where long-range connectivity is diminished in favor of increased local connectivity (Belmonte et al., 2004, Courchesne and Pierce 2005, Rippon et al., 2007, Rane et al., 2015).

Another interesting facet of the ASD literature included is the uprising trend of scanning the brains post-fixation (*ex vivo*) rather than in vivo. Despite the lack of definitive proof that one approach is superior to the other, the process of fixation does affect some properties of the tissue and can lead to significant shrinkage in the axons (Horowitz Horowitz et al., 2015) casting some doubts on the findings of such studies.

Akin to ASD, Schizophrenia (SCZ) is a multifarious disorder with presentations that differ from case to case. SCZ appears to be the product of complex intercalation between a multitude of genetic and environmental risk factors. GWAS studies identified plenty of genes to be associated with an increased risk of developing SCZ including those implicated in various vital functions such as immunity, synaptic function, and development. Various pieces of evidence point at the complicity of a faulty dopaminergic and glutamatergic neurotransmission in the genesis of the positive and the negative symptoms of SCZ, respectively (Kahn et al., 2015, Owen et al., 2016, Marder and Cannon 2019).

Administration of agents such as amphetamine or phencyclidine, that interfere with the dopaminergic or the glutamatergic pathways, was the classical way of generating animals recapitulating some of the SCZ aspects (Katsnelson 2014). In the current literature, animals treated with N-methyl-d-aspartate receptor (NMDAR) antagonists agents such as MK801 (dizocilpine) (Wu et al., 2016) or prenatally exposed to compounds such as methylazoxymethanol acetate (MAM) (Chin et al., 2011) or endotoxins such as polyinosinic:polycytidylic acid (poly I:C) (Missault et al., 2019, Di Biase et al., 2020) were used as SCZ animal models. Other transgenic models that lack essential genes such as Gclm knock-out (Gclm KO) (Corcoba et al., 2015) or express a faulty protein were also used such as *EGR3* rat model (Ma et al., 2015).

The results depicted a general pattern of diminished FA and increased RD values in all the tissues examined including the corpus callosum (Fig. 3f), the fornix, and the cingulum (Table 2). The non-conflicting results are probably emitting from the limited number of the studies conducted rather than reflecting a solid underlying dysfunction in the microstructure, since every model is mostly affected in a different manner. In addition, it should be noticed that the experimental setup chosen is quite homogeneous across the different studies, as evident from Figure 1.

Due to its global impact as a major risk factor for a wide variety of illnesses and ultimately for premature death, the consumption of alcohol and its correlation with

health problem has been for long a subject of meticulous scrutiny (Rehm et al., 2003, Ezzati et al., 2006). The deleterious effect the alcohol has on the brain tissue is very well established, and changes in the WM microstructure are widely studied employing dw-MRI.

All the studies were performed on rats, except for one study that used ferrets (Tang et al., 2018). Different studies employed different protocols to deliver various doses of alcohol, some of which were aiming at inducing chronic alcohol consumption (Vetreno et al., 2016, Luo et al., 2017), while the others were mimicking the binge drinking cases (Pfefferbaum et al., 2015). As was the case in ASD, all the studies aside from one (Tang et al., 2018) incorporated only male rats in their investigation.

As per the studies investigated, alcohol seems to affect GM tissues such as the cerebellum, the neocortex, the thalamus, and the somatosensory cortex. Some studies also found significant differences in the WM tracts including the corpus callosum and the fornix (Pfefferbaum et al., 2015, De Santis et al., 2019). The changes in the corpus callosum and the fornix seem to follow the same direction with a decrease in the FA and L1 values and an increase in the values of MD and RD (Fig. 3g and Table 2). Unlike in WM, a decrease, rather than an increase, was reported for MD values in GM tissues when alcohol esposed animals were compared to their respective control (Vetreno et al., 2016, Chen et al., 2017), although the studies used two different alcohol delivery approaches (chronic versus acute) and different experimental strategies. Although in the case of the later study, the decrease in the MD values was not progressive as the values after 2 hours of administration slightly towered over the 30 minutes after administration values before it decreased again (Chen et al., 2017).

Chen and others, using DKI in a longitudinal study, showed an initial decrease in the MK metric in the frontal lobe 30 minutes after acute administration of alcohol, followed by a significant increase two and six hours after compared to the naive control and the 30 minutes post-consumption time point (Chen et al., 2017). Besides giving credence to the sensitivity of DKI to minor changes, these results could mean that alcohol has an acute early-stage effect (Sippel 1974, Tabakoff et al., 1976) followed by a long-lasting effect (Crews et al., 2006, Crews and Nixon 2009, Kane and Drew 2016). Interestingly, in another longitudinal study, De Santis et al. reported changes in the corpus callosum and the fornix that progressed even after 6 weeks of abstinence (De Santis et al., 2019).

Stress is essentially a coping response to threats that might challenge the individual's existence and can provide an adaptation mechanism to changes that might occur in the subject's homeostasis. Chronic exposure to stress during different life stages can lead to several social abnormalities and aberrant interactions, as well as to developing depression and different forms of aggression (Lupien et al., 2009, Roozendaal et al., 2009, Sandi and Haller 2015). Rodents studies of stress seem to follow the same paradigm of using mainstream animals such as C57 mice (Grandjean et al., 2016, Liu et al., 2018b) or stress-hyper-reactive animals such as Wister Kyoto (WKY) rats (Zalsman et al., 2015, Zalsman et al., 2017). The animals were then exposed to different types of stressors for various amounts of time to mimic the state of chronic stress exposure. The stressors can vary between putting the rodent with an aggressor, wetting cage, elevated platform, or restraining. Some protocols include using more than one stressor (Hemanth Kumar et al., 2014). The animals are typically screened to test their resilience to stress experienced earlier and then categorized into anhedonic susceptible animals and resilient animals. Results indicate that indeed chronic stress can have a physical toll on the brain's microstructure. Numerous structures that are implicated in the stress response such as the hippocampus (Fig. 3h), the amygdala, and the hypothalamus were found to be affected in these studies. However, the paradigms used to induce stress varied widely between studies in addition to a wide discrepancy in the acquisition parameters which might explain the apparent contradictions. A vivid example would be the DKI results reported in some of the studies included (Delgado y Palacios et al., 2011, Khan et al., 2016, Khan et al., 2018a, Khan et al., 2018b). Despite using the same stress-inducing protocols, the findings varied substantially (Table 2). A noteworthy issue is the use of two values with only 9 directions to estimate the kurtosis tensor (Khan et al., 2018a), while the minimum requirments are 15 directions per b-value (Jensen and Helpern 2010).

Conclusions

Dw-MRI is a powerful tool to investigate microstructural abnormalities in the intact brain. Tapping the potential of such technique in preclinical investigation has the potential to boost our understanding of a multitude of disorders. However, using dw-MRI is a delicate process and requires strong knowledge of proper acquisition

parameters; in this review, we highlighted several cases in which the observed heterogeneity of the results can be at least partially explained by the experimental choice, rather than by true biological variability in the model. Future work is needed to reach a consensus on the optimal experimental scheme to be used; however, a few points can be highlighted. We encourage, whenever possible, the use of a stronger magnetic field (7-11T or higher for mice and at least 4.7T or higher for rats). If one is interested in information coming from the extracellular space, a conventional DTI sequence with b=1000 s/mm^2 and a minimum of 30 directions, as used in the majority of the studies included in this review, is recommended. For pathologies in which axonal involvement is expected, we suggest increasing the b-value range and the diffusion time to explore higher b-values and access more advanced dw-MRI models, keeping in mind that the reduction in the SNR needs to be compensated with more directions and/or more repetitions. Lastly, whenever possible, an isotropic resolution should be the first choice followed by an in-plane isotropic acquisition.

Acknowledgments: SDS was supported by the European Research Council through a Marie Skłodowska-Curie Individual Fellowship (Grant #749506) and by the Generalitat Valenciana through a Subvencion a la Excelencia de Juniors Investigadores (SEJI/2019/038). AE was supported by La Caixa-Severo Ochoa predoctoral fellowship from Obra Social La Caixa. All authors also acknowledge financial support from the Spanish State Research Agency through the Severo Ochoa Program for Centres of Excellence in R&D (SEV- 2017-0723).

Author contributions: SDS: conceptualization, supervision, visualization, writing, reviewing and editing. AE: literature search, writing, reviewing, visualization, and editing. ACC: literature search, visualization, reviewing, and editing. JL: reviewing and editing.

Conflicts of interests: The authors declare no conflicts of interests.

Table 1. Summary of the neurodegenerative studies included in the review.

Article	Disorder	Animal	Model name	Control sample size	Model sample size	Field strength	No shells	Max B-value(s/mm2)	No. directions	In vivo or ex vivo	Results in model compared to WT ↓ or ↑
Badea et al., 2016	AD	Mice	CVN-AD	8	9	9.4T	1	1595	12	Ex vivo	VBA: ↓FA; ROIs: ↓FA, ↓AD, ↑RD, ↑ADC
Thiessen et al., 2010	AD	Mice	TgCRND8	4	7	7T	8	1345	64	In vivo	ROIs: No differences
Mueggler et al., 2004	AD	Mice	APP23	5-6	8-10	7T	5	2000	N/A	In vivo	ROIs: ↓ADC
Munoz-Moreno et al., 2018	AD	Rats	TgF344-AD	9	9	7T	1	1000	60	In vivo	ROIs: ↓FA-W, ↑FD-W
Snow et al., 2017	AD	Mice	3xTg	8	7	7T	1	1000	6	In vivo	ROIs: ↓FA, ↓AD
Shu et al., 2013	AD	Mice	APP/PS1	9	9	7T	1	800	N/A	In vivo	VBA: ↑FA, ↑AD, ↑MD, ↑RD; ROIs: ↑FA, ↑AD, ↑MD, ↑RD
Qin et al., 2013	AD	Mice	APP/PS1	9	9	7T	1	800	30	In vivo	VBA: ↑FA, ↑AD, ↑MD, ↑RD; ROIs: ↑FA, ↑AD, ↑MD, ↑RD: cortex
Muller et al., 2013	AD	Mice	Tg2576	5	7	11.7T	1	1000	30	In vivo	VBA: ↑FA, ↓FA, ↓AD, ↓MD, ↓RD; ROIs: ↓FA
Praet et al., 2018	AD	Mice	APP/PS1	20	19	7T	7	2800	140	In vivo	VBA: ↓FA, ↑RD, ↑AK; ROIs: ↓FA, ↑RD, ↑AD, ↓AD, ↑MD, ↑AK, ↑MK, ↑RK
Harms et al., 2006	AD	Mice	APPsw (Tg2576)	9-10	9-10	7T	1	1890	20	Ex vivo	ROIs: ↓RA
Sun et al., 2005	AD	Mice	APPsw (Tg2576)	8	8	4.7T	1	764	6	In vivo	ROIs: ↑RD, ↓Tr, ↓AD, ↓RD, ↓RA
Kastyak-Ibrahim et al.,	AD	Mice	3xTg	3-4	8	7T	1	1034	307	In vivo ex vivo	ROIs (In vivo): No differences; ROIs (Ex

2013.											vivo): No differences
Song et al., 2004	AD	Mice	PDAPP	8-20	10-11	4.7T	1	764	6	In vivo	ROIs: ↓RA, ↑Tr, ↑RD, ↑AD
Shen et al., 2018	AD	Mice	APP/PS1	12	12	7T	1	1000	30	In vivo	ROIS: No differences
Colgan et al., 2016	AD	Mice	rTg4510	5	5	9.4T	2	2000	50	In vivo	ROIs: ↑IsoVF, ↓IsoVF, ↑NDI, ↓NDI↑MD↑FA↓FA, ↑ODI, ↓ODI
Vanhoutte et al., 2013	AD	Mice	APP/PS1	5	5	9.4T	7	2800	210	In vivo	ROIs: ↑rMK, ↑rRK, ↑rAK
Zerbi et al., 2014	AD	Mice	apoE4 apoE-KO	9-10	8-10	11.7T	1	1000	30	In vivo	VBA (apoE4): ↑MD, ↓FA; ROIs (apoE4): ↑MD, ↑AD; VBA (apoE-KO): ↑MD, ↓FA ROIs (apoE4-KO): No differences
Grandjean et al., 2014	AD	Mice	arcAβ	7-10	8-11	9.4T	1	690	36	In vivo	VBA: ↓FA; ROIs: ↓FA
Grandjean et al., 2016b	AD	Mice	arcAβ E22ΔAβ PSAPP	11-12	9-12	9.4T	1	1000	36	In vivo	VBA (arcAβ): No differences; ROIs (arcAβ); ↑FA, ↑AD,↓RD VBA (E22ΔAβ): No differences; ROIs (E22ΔAβ): No differences VBA (PSAPP): No differences; ROIs (PSAPP): ↓FA
Zerbi et al., 2013	AD	Mice	APP/PS1	15	9	11.7T	1	1000	30	In vivo	VBA: ↓FA, ↑FA, ↓MD, ↑MD, ↓AD, ↑AD, ↓RD, ↑RD; ROIs: ↓FA, ↓MD, ↑MD, ↓AD, ↑AD, ↑RD
Anckaerts et	AD	Rats	TgF344-AD	10	11	7T	1	800	60	In vivo	VBA: ↓FA, ↑FA, ↓MD,

al., 2019											↑MD, ↓AD, ↑AD, ↓RD, ↑RD; ROIs: ↓FA
Khairnar et al., 2015	PD	Mice	TNWT-61	7	7	9.4T	5	2500	150	In vivo	VBA (TBSS): ↑MK, ↑AK, ↑RK, ↓MD, ↓RD; ROIs: ↑AK, ↑RK, ↓RD, ↓MD, ↓AD, ↓RD
Khairnar et al., 2017	PD	Mice	TNWT-61	15	15	9.4T	5	2500	150	In vivo	VBA (TBSS): ↑MK, ↑AK, ↓AD; ROIs: ↑MK, ↑AK, ↑RK, ↓RD, ↑FA
Khairnar et al., 2016	PD	Mice	TNWT-61	12	9	9.4T	5	2500	150	In vivo	VBA (TBSS): ↑MK, ↑AK, ↑FA, ↓AD, ↓RD; ROIs: ↑MK, ↑AK, ↑RK, ↓MD, ↓AD, ↓RD
Arab et al., 2019	PD	Mice	METH	5-6	9-11	9.4T	5	2500	150	In vivo	VBA (TBSS): ↑FA, ↑RK, ↓MD, ↓AD, ↓RD; ROIs: ↓MK, ↓RK, ↑AD, ↑RD, ↑MK, ↓MD, ↓RD, ↑FA
Cong et al., 2016	PD	Mice	MitoPark	9	6	7T	1	1200	30	In vivo	ROIs: ↓ADC, ↓FA
Perlbarg et al., 2018	PD	Rats	6-OHDA	5	10	11.7T	1	1500	81	In vivo	ROIs: ↑FA, ↑MD, ↑AD
Ferris et al., 2018	PD	Rats	PINK1	15	15	7T	1	1000	10	In vivo	ROIs: No differences
Cai et al., 2019	PD	Rats	PINK1	10	10	7T	1	1000	10	In vivo	ROIs: ↓ADC, ↓AD, ↓RD, ↓FA
Liu et al., 2018a	PD	Rats	Rotenone 6-OHDA	6	12	3T	1	1000	15	In vivo	ROIs (Rotenone): ↓FA; ROIs (6-OHDA): ↓FA, ↑FA
Boska et al., 2007	PD	Mice	MPTP	5	5	7T	1	800	12	In vivo	ROIs: ↓FA, ↑MD, ↑AD, ↑RD
Liu et al.,	PD	Rats	Rotenone	6	12	3T	1	1000	15	In vivo	ROIs: ↓FA, ↑MD

2017											
Soria et al., 2011	PD	Rats	6-OHDA inj	4	8	7T	1	1000	30	In vivo	ROIs: ↓FA, ↓AD, ↑RD
Van Camp et al., 2009	PD	Rats	6-OHDA	4	5	7T	1	800	7	In vivo	ROIs: No differences; VBA: ↑FA; VBA-guided ROIs: ↑FA, ↓L1
Monnot et al., 2017	PD	Rats	6-OHDA	4	4	9.4T	1	1250	30	Ex vivo	VBA: ↓FA, ↑RD; ROIs: No differences
Fang et al., 2018	PD	Rats	6-OHDA	8	8	3T	1	1000	15	In vivo	ROIs: ↓FA
Blockx et al., 2012a	HD	Rats	TgHD	5-6	6	9.4T	7	2800	107	In vivo	ROIs: ↓FA, ↓MD, ↓AD, ↓RD, ↑FA, ↑MD, ↑AD, ↑RD, ↑MK, ↑AK, ↑RK, ↑KA
Blockx et al., 2012b	HD	Rats	TgHD	7	7	9.4T	7	2800	105	In vivo	ROIs: ↑FA, ↑MD, ↑AD, ↑RD, ↑KA, ↑RK
Gatto et al., 2019	HD	Mice	R6/2	3	3	17.6T	1	1500	12	Ex vivo	ROIs: ↓FA, ↑MD, ↑AD, ↑RD
Garcia-Miralles et al., 2016	HD	Mice	YAC128	7	8	7T	1	1500	30	In vivo	VBA: ↓FA; ROIs: ↓FA
Teo et al., 2016	HD	Mice Rats	YAC128 BACHD	8-13	8-14	7T	1	1500 1000	30 256	In vivo	VBA (YAC128): ↓FA; ROIs (YAC128): ↓FA; ROIs (BACHD): ↓FA
Xiang et al., 2011	HD	Mice	R6/2	3	3	11.7T	1	1500	6	Ex vivo	ROIs: ↓FA
Gatto et al., 2015	HD	Mice	YFP, R6/2	3	3	9.4T	1	1000	12	Ex vivo	ROIs: ↓FA
Antonsen et al., 2013	HD	Rats	TgHD	4	5	7T	1	800	12	Ex vivo	VBA: ↑FA, ↓MD, ↓AD, ↓RD, ↑RD; ROIs: ↑FA, ↓MD, ↓AD, ↓RD
Blockx et al., 2011	HD	Rats	TgHD	10	10	9.4T	1	800	6	In vivo	ROIs: No differences

Nishioka et al., 2017	MS	Mice	EAE	5	5	11.7T	1	850	21	In vivo	ROIs: ↓FA, ↑RD
Atkinson et al., 2019	MS	Mice	CPZ	5-6	6-8	7T 9.4T	1	1000 3000	30 30	In vivo ex vivo	ROIs (in vivo): ↓FA, ↑RD; VBA (TBSS): in vivo: ↓FA, ↑MD, ↑RD, ↑L1; ROIs (ex vivo): ↓FA
Crombe et al., 2018	MS	Mice	EAE	15	16	4.7T	2	2700	65	In vivo	ROIs: ↓MD, ↓AD
Sun et al., 2007	MS	Mice	EAE	16	16	4.7T	1	847	6	In vivo	ROIs: ↓AD, ↑RD
Planche et al., 2017	MS	Mice	EAE 2	12	12	4.7T	1	2000	30	In vivo	ROIs: ↓FA, ↑AD
Nishioka et al., 2019	MS	Mice	EAE	8	4-7	11.7T	1	850	21	In vivo	ROIs: ↓Tr, ↓FA, ↓AD, ↑RD
Boretius et al., 2012	MS	Mice	CPZ CPZ + EAE	5	5	9.4T	1	1000	12	In vivo	ROIs: ↓FA, ↓AD, ↑RD
Song et al., 2005	MS	Mice	CPZ	8	6-12	4.7T	1	1600	6	Ex vivo	ROIs: ↓RA, ↑RD, ↑Tr

Abbreviations: ↑, increase; ↓, decrease; ADC, apparent diffusion coefficient; AK, axial kurtosis; FA, fractional anisotropy; FA-W, weighted fractional anisotropy; FD-W, weighted fiber density; HD, Huntington's disease; IsoVF, isotropic volume fraction; KA, kurtosis anisotropy; KO, Knock-out; L1, axial diffusivity; MD, mean diffusivity; MK, mean kurtosis; MS, multiple sclerosis; N/A, not aplicable; NDI, neurite density; ODI, orientation dispersion index; PD, Parkinson's disease; RA, relative anisotropy; rAK, relative axial kurtosis; RD, radial diffusivity; RK, radial kurtosis; rMK, relative mean kurtosis; ROI, region of interest; rRK, relative radial kurtosis; T, tesla; TBSS, tract-based spatial statistics; Tr, trace; VBA, voxel-based analysis; WT, wild type. Sample sizes are displayed as (minimum-maximum) in cases where there are different age groups or multiple models in the same study.

Table 2. Summary of neurodevelopmental/psychiatric disorders included in the review.

Article	Disorder	Animal	Model name	Control sample size	Model sample size	Field strength	No shells	Max B-value(s/mm2)	No. directions	In vivo or ex vivo	Results in model compared to WT ↓ or ↑
Liska et al., 2017	ASD	Mice	Cntnap2$^{-/-}$	13	10	7T	1	3000	81	Ex vivo	Tractography: No differences
Zerbi et al., 2019	ASD	Mice	Fmr1$^{-/y}$	23	26	7T	2	2000	180	Ex vivo	ROIs: ↓FA, ↑RD
Wilkes et al., 2019	ASD	Mice	C58/J	10	17	17,6	2	3000	60	Ex vivo	ROIs: ↓FA, ↓AD
Kumar et al., 2012	ASD	Mice	BALB/cJ	11-12	27-28	9.4T	1	786.73	6	In vivo	ROIs (cross-sectional): ↓FA, ↑FA, ↑MD; ROIs (longitudinal): ↑FA
Ellegood et al., 2013	ASD	Mice	BTBR T+tf/J (BTBR)	12	12	7T	1	1917	30	Ex vivo	VBA: ↓FA, ↑FA; ROIs: ↓FA
Kumar et al., 2014	ASD	Mice	NL-3	7-9	5-10	9.4T	1	902	6	Ex vivo	ROIs: No differences
Ellegood et al., 2011	ASD	Mice	NL-3	8	8	7T	1	1956	6	Ex vivo	VBA: ↓FA, ↑RD; ROIs: No differences
Dodero et al., 2013	ASD	Mice	BTBR T+tf/J (BTBR)	9	9	7T	1	1262	81	Ex vivo	VBA (TBSS): ↓FA; ROIs: ↓FA
Haberl et al., 2015	ASD	Mice	Fmr1$^{-/y}$	12	7	11.7T	1	1000	30	In vivo	ROIs: ↓FA
Kumar et al., 2018	ASD	Mice	16p11.2 hemideletion (del/+)	12	9	9.4T	1	902	6	Ex vivo	VBA (TBSS): ↓FA, ↓FA
Pervolaraki et al., 2019	ASD	Mice	Nrxn2α KO	6	6	9.4T	1	1200	6	Ex vivo	ROIs: ↑FA, ↓FA, ↑AD, ↓RD, ↓ADC

Missault et al., 2019	SCZ	Rats	Poly I:C	11	10-15	7T	1	800	60	In vivo	VBA: No differences
Zhang et al., 2019	SCZ	Mice	ErbB4-KO (ErbB4-/-)	27	23	7T	1	800	30	In vivo	VBA: ↓FA
Corcoba et al., 2015	SCZ	Mice	Gclm KO	16	15	14.1T	1	1000	6	In vivo	ROIs: ↓FA, ↑RD
Ma et al., 2015	SCZ	Rats	EGR3	6	6	3T	1	1000	32	In vivo	ROIs: No differences; Fiber tracts: No differences
Chin et al., 2011	SCZ	Rats	MAM	7	4	7T	1	730	30	In vivo	ROIs: ↓FA
Di Biase et al., 2020	SCZ	Rats	Poly I:C	8	9	7T	1	1400	50	In vivo	VBA (TBSS): ↑F_W
Gimenez et al., 2017	SCZ	Mice	MAP6-KO	8	8	7T	1	1500	6	Ex vivo	No differences in transversal ADC
Wu et al., 2016	SCZ	Rats	MK801	11	12	7T	1	800	60	In vivo	VBA: ↓FA; ROIs: ↓FA, ↑MD, ↑AD, ↑RD
Vetreno et al., 2016	Alc	Rats	Intragastric	7	7	9.4T	1	N/A	12	Ex vivo	ROIs: ↑FA, ↓MD, ↓AD
Luo et al., 2017	Alc	Rats	Intragastric	10	10	7T	1	1031.7	6	In vivo	ROIs: ↓FA
Chen et al., 2017	Alc	Rats	Intragastric	5	10	7T	2	2000	60	In vivo	ROIs: ↓MK, ↑MK, ↓FA, ↑FA, ↓MD, ↑MD
Pfefferbaum et al., 2015	Alc	Rats	Intragastric	9	10	3T	1	1464	6	In vivo	VBA (TBSS): ↓FA
De Santis et al., 2019	Alc	Rats	Marchigian Sardinian	9	9-18	7T	1	1000	30	In vivo	VBA (TBSS) (1mo consumption): ↓FA, ↑MD, ↓L1, ↑RD; Fiber tracts (1 mo consumption): ↓FA, ↑MD, ↑RD; VBA (TBSS): (2 wks): ↓FA,

											↓L1; VBA (TBSS) (6 wks abistenance): ↓FA, ↓L1, ↑RD
Tang et al., 2018	Alc	Ferrets	Intraperitoneal	6	6	7T	2	4000	128	Ex vivo	ROIs: ↑FA, ↓MK, ↓AK, ↓RK
Liu et al., 2018b	Stress	Mice	CSDS	7	7-10	7T	1	1000	30	In vivo	ROIs: ↓FA, ↑MD, ↑RD
Grandjean et al., 2016a	Stress	Mice	CPS	27	26	9.4T	1	1000	36	In vivo	VBA: No differences; ROIs: ↑FA
Zalsman et al., 2017	Stress	Rats	WKY	20	20	7T	1	1000	15	In vivo	VBA: ↓FA, ↑FA, ↑MD, ↑AD, ↓AD, ↑RD Fiber tracts: ↓FA, ↑MD, ↑AD, ↑RD
Zalsman et al., 2015	Stress	Rats	WKY	22	19	7T	1	1000	15	In vivo	VBA: ↑ADC, ↓FA, ↑FA
Hemanth Kumar et al., 2014	Stress	Rats	CMS	10	10	7T	1	700	46	In vivo	ROIs: ↓FA, ↑FA, ↑MD, ↓MD, ↑AD, ↑RD
Khan et al., 2018a	Stress	Rats	CMS	8	8	9.4T	2	2500	18	In vivo	ROIs: ↑FA, ↑AD, ↑AK, ↑RK
van der Marel et al., 2013	Depression	Rats	5-HTT$^{-/-}$	11	14	4.7T	1	1250	50	In vivo	VBA (TBSS): No differences; ROIs: ↓FA: genu cc
Delgado y Palacios et al., 2011	Stress	Rats	CMS	7	7	9.4T	7	2800	210	In vivo	ROIs: ↓MK, ↓RK
Khan et al., 2016 Khan et al., 2018b	Stress	Rats	CMS	8	8	9.4	14	8000	156	Ex vivo	ROIs: ↑NDI, ↓MD, ↓$D_{eff,}$ ↓D_L

Abbreviations: ↑, increase; ↓, decrease; Deff, extracellular diffusivity; ADC, apparent diffusion coefficient; AK, axial kurtosis; Alc, Alcoholism; ASD, autism spectrum disorder; DL, intraneurite diffusivity; FA, fractional anisotropy; FA-W, weighted fractional anisotropy; FD-W, weighted fiber density; Fw, extracellular water fraction;

KO, Knock-out; L1, axial diffusivity; MD, mean diffusivity; MK, mean kurtosis; mo, month; N/A, not aplicable; NDI, neurite density; RD, radial diffusivity; RK, radial kurtosis; ROI, region of interest; SCZ, schizophrenia; T, tesla; TBSS, tract-based spatial statistics; Tr, trace; VBA, xoxel-based analysis; wk, week; WT, wild type Poly I:C, polyinosinic:polycytidylic Acid; MAM, methylazoxymethanol acetate; WKY, Wistar-Kyoto strain; CMS, chronic mild stress; CPS, chronic psychosocial stress; CSDS, chronic social defeat; MK801, dizocilpine. Sample sizes are displayed as (minimum-maximum) in cases where there are different age groups or multiple models in the same study.

Bibliography:

Agosta, F., M. Pievani, S. Sala, C. Geroldi, S. Galluzzi, G. B. Frisoni and M. Filippi (2011). "White matter damage in Alzheimer disease and its relationship to gray matter atrophy." Radiology **258**(3): 853-863. doi: 10.1148/radiol.10101284

Alexander, D. C., T. B. Dyrby, M. Nilsson and H. Zhang (2019). "Imaging brain microstructure with diffusion MRI: practicality and applications." NMR Biomed **32**(4): e3841. doi: 10.1002/nbm.3841

Anckaerts, C., I. Blockx, P. Summer, J. Michael, J. Hamaide, C. Kreutzer, H. Boutin, S. Couillard-Despres, M. Verhoye and A. Van der Linden (2019). "Early functional connectivity deficits and progressive microstructural alterations in the TgF344-AD rat model of Alzheimer's Disease: A longitudinal MRI study." Neurobiol Dis **124**: 93-107. doi: 10.1016/j.nbd.2018.11.010

Antonsen, B. T., Y. Jiang, J. Veraart, H. Qu, H. P. Nguyen, J. Sijbers, S. von Horsten, G. A. Johnson and T. B. Leergaard (2013). "Altered diffusion tensor imaging measurements in aged transgenic Huntington disease rats." Brain Struct Funct **218**(3): 767-778. doi: 10.1007/s00429-012-0427-0

Ascherio, A. and M. A. Schwarzschild (2016). "The epidemiology of Parkinson's disease: risk factors and prevention." The Lancet. Neurology **15**(12): 1257-1272. doi: 10.1016/S1474-4422(16)30230-7

Assaf, Y., T. Blumenfeld-Katzir, Y. Yovel and P. J. Basser (2008). "AxCaliber: a method for measuring axon diameter distribution from diffusion MRI." Magn Reson Med **59**(6): 1347-1354. doi: 10.1002/mrm.21577

Atkinson, K. C., J. B. Lee, J. P. C. Hasselmann, S. H. Kim, A. Drew, J. Soto, J. A. Katzenellenbogen, N. G. Harris, A. Obenaus and S. K. Tiwari-Woodruff (2019). "Diffusion tensor imaging identifies aspects of therapeutic estrogen receptor beta ligand-induced remyelination in a mouse model of multiple sclerosis." Neurobiol Dis **130**: 104501. doi: 10.1016/j.nbd.2019.104501

Barrière, D. A., R. Magalhães, A. Novais, P. Marques, E. Selingue, F. Geffroy, F. Marques, J. Cerqueira, J. C. Sousa, F. Boumezbeur, M. Bottlaender, T. M. Jay, A. Cachia, N. Sousa and S. Mériaux (2019). "The SIGMA rat brain templates and atlases for multimodal MRI data analysis and visualization." Nature Communications **10**(1): 5699. doi: 10.1038/s41467-019-13575-7

Basser, P. J. (1995). "Inferring microstructural features and the physiological state of tissues from diffusion-weighted images." NMR Biomed **8**(7-8): 333-344.

Basser, P. J., J. Mattiello and D. Lebihan (1994). "Estimation of the Effective Self-Diffusion Tensor from the NMR Spin Echo." Journal of Magnetic Resonance, Series B **103**(3): 247-254. doi: https://doi.org/10.1006/jmrb.1994.1037

Bates, G. P., R. Dorsey, J. F. Gusella, M. R. Hayden, C. Kay, B. R. Leavitt, M. Nance, C. A. Ross, R. I. Scahill, R. Wetzel, E. J. Wild and S. J. Tabrizi (2015). "Huntington disease." Nature reviews. Disease primers **1**: 15005-15005. doi: 10.1038/nrdp.2015.5

Beal, M. F. (2010). "Parkinson's disease: a model dilemma." Nature **466**(7310): S8-S10. doi: 10.1038/466S8a

Belmonte, M. K., G. Allen, A. Beckel-Mitchener, L. M. Boulanger, R. A. Carper and S. J. Webb (2004). "Autism and abnormal development of brain connectivity." J Neurosci **24**(42): 9228-9231. doi: 10.1523/JNEUROSCI.3340-04.2004

Blockx, I., G. De Groof, M. Verhoye, J. Van Audekerke, K. Raber, D. Poot, J. Sijbers, A. P. Osmand, S. Von Horsten and A. Van der Linden (2012a). "Microstructural changes observed with DKI in a transgenic Huntington rat model: evidence for abnormal neurodevelopment." Neuroimage **59**(2): 957-967. doi: 10.1016/j.neuroimage.2011.08.062

Blockx, I., N. Van Camp, M. Verhoye, R. Boisgard, A. Dubois, B. Jego, E. Jonckers, K. Raber, K. Siquier, B. Kuhnast, F. Dolle, H. P. Nguyen, S. Von Horsten, B. Tavitian and A. Van der Linden (2011). "Genotype specific age related changes in a transgenic rat model of Huntington's disease." Neuroimage **58**(4): 1006-1016. doi: 10.1016/j.neuroimage.2011.07.007

Blockx, I., M. Verhoye, J. Van Audekerke, I. Bergwerf, J. X. Kane, Y. P. R. Delgado, J. Veraart, B. Jeurissen, K. Raber, S. von Horsten, P. Ponsaerts, J. Sijbers, T. B. Leergaard and A. Van der Linden (2012b). "Identification and characterization of Huntington related pathology: an in vivo DKI imaging study." Neuroimage **63**(2): 653-662. doi: 10.1016/j.neuroimage.2012.06.032

Boretius, S., A. Escher, T. Dallenga, C. Wrzos, R. Tammer, W. Bruck, S. Nessler, J. Frahm and C. Stadelmann (2012). "Assessment of lesion pathology in a new animal model of MS by multiparametric MRI and DTI." Neuroimage **59**(3): 2678-2688. doi: 10.1016/j.neuroimage.2011.08.051

Chen, X. R., J. Y. Zeng, Z. W. Shen, L. M. Kong and W. B. Zheng (2017). "Diffusion Kurtosis Imaging Detects Microstructural Changes in the Brain after Acute Alcohol Intoxication in Rats." Biomed Res Int **2017**: 4757025. doi: 10.1155/2017/4757025

Chin, C. L., P. Curzon, A. J. Schwartz, E. M. O'Connor, L. E. Rueter, G. B. Fox, M. Day and A. M. Basso (2011). "Structural abnormalities revealed by magnetic resonance

imaging in rats prenatally exposed to methylazoxymethanol acetate parallel cerebral pathology in schizophrenia." Synapse **65**(5): 393-403. doi: 10.1002/syn.20857

Chyi, T. and C. Chang (1999). "Temporal evolution of 3-nitropropionic acid-induced neurodegeneration in the rat brain by T2-weighted, diffusion-weighted, and perfusion magnetic resonance imaging." Neuroscience **92**(3): 1035-1041. doi: 10.1016/s0306-4522(99)00076-7

Colgan, N., B. Siow, J. M. O'Callaghan, I. F. Harrison, J. A. Wells, H. E. Holmes, O. Ismail, S. Richardson, D. C. Alexander, E. C. Collins, E. M. Fisher, R. Johnson, A. J. Schwarz, Z. Ahmed, M. J. O'Neill, T. K. Murray, H. Zhang and M. F. Lythgoe (2016). "Application of neurite orientation dispersion and density imaging (NODDI) to a tau pathology model of Alzheimer's disease." Neuroimage **125**: 739-744. doi: 10.1016/j.neuroimage.2015.10.043

Cong, L., E. R. Muir, C. Chen, Y. Qian, J. Liu, K. C. Biju, R. A. Clark, S. Li and T. Q. Duong (2016). "Multimodal MRI Evaluation of the MitoPark Mouse Model of Parkinson's Disease." PLoS One **11**(3): e0151884. doi: 10.1371/journal.pone.0151884

Corcoba, A., P. Steullet, J. M. Duarte, Y. Van de Looij, A. Monin, M. Cuenod, R. Gruetter and K. Q. Do (2015). "Glutathione Deficit Affects the Integrity and Function of the Fimbria/Fornix and Anterior Commissure in Mice: Relevance for Schizophrenia." Int J Neuropsychopharmacol **19**(3): pyv110. doi: 10.1093/ijnp/pyv110

Courchesne, E. and K. Pierce (2005). "Why the frontal cortex in autism might be talking only to itself: local over-connectivity but long-distance disconnection." Curr Opin Neurobiol **15**(2): 225-230. doi: 10.1016/j.conb.2005.03.001

Crews, F., K. Nixon, D. Kim, J. Joseph, B. Shukitt-Hale, L. Qin and J. Zou (2006). "BHT blocks NF-kappaB activation and ethanol-induced brain damage." Alcohol Clin Exp Res **30**(11): 1938-1949. doi: 10.1111/j.1530-0277.2006.00239.x

Crews, F. T. and K. Nixon (2009). "Mechanisms of neurodegeneration and regeneration in alcoholism." Alcohol Alcohol **44**(2): 115-127. doi: 10.1093/alcalc/agn079

Crombe, A., V. Planche, G. Raffard, J. Bourel, N. Dubourdieu, A. Panatier, H. Fukutomi, V. Dousset, S. Oliet, B. Hiba and T. Tourdias (2018). "Deciphering the microstructure of hippocampal subfields with in vivo DTI and NODDI: Applications to experimental multiple sclerosis." Neuroimage **172**: 357-368. doi: 10.1016/j.neuroimage.2018.01.061

Curran, K. M., L. Emsell and A. Leemans (2016). Quantitative DTI Measures. Diffusion Tensor Imaging: A Practical Handbook. W. Van Hecke, L. Emsell and S. Sunaert. New York, NY, Springer New York**:** 65-87.

De Santis, S., P. Bach, L. Perez-Cervera, A. Cosa-Linan, G. Weil, S. Vollstadt-Klein, D. Hermann, F. Kiefer, P. Kirsch, R. Ciccocioppo, W. H. Sommer and S. Canals (2019). "Microstructural White Matter Alterations in Men With Alcohol Use Disorder and Rats With Excessive Alcohol Consumption During Early Abstinence." JAMA Psychiatry **76**(7): 749-758. doi: 10.1001/jamapsychiatry.2019.0318

De Santis, S., T. Granberg, R. Ouellette, C. A. Treaba, F. Qiuyun, E. Herranz, C. Mainero and N. Toschi (2017). "Early axonal damage in normal appearing white matter in multiple sclerosis: Novel insights from multi-shell diffusion MRI." Conf Proc IEEE Eng Med Biol Soc **2017**: 3024-3027. doi: 10.1109/EMBC.2017.8037494

Delgado y Palacios, R., A. Campo, K. Henningsen, M. Verhoye, D. Poot, J. Dijkstra, J. Van Audekerke, H. Benveniste, J. Sijbers, O. Wiborg and A. Van der Linden (2011). "Magnetic resonance imaging and spectroscopy reveal differential hippocampal changes in anhedonic and resilient subtypes of the chronic mild stress rat model." Biol Psychiatry **70**(5): 449-457. doi: 10.1016/j.biopsych.2011.05.014

Di Biase, M. A., G. Katabi, Y. Piontkewitz, S. Cetin-Karayumak, I. Weiner and O. Pasternak (2020). "Increased extracellular free-water in adult male rats following in utero exposure to maternal immune activation." Brain Behav Immun **83**: 283-287. doi: 10.1016/j.bbi.2019.09.010

Dodero, L., M. Damiano, A. Galbusera, A. Bifone, S. A. Tsaftsaris, M. L. Scattoni and A. Gozzi (2013). "Neuroimaging Evidence of Major Morpho-Anatomical and Functional Abnormalities in the BTBR T+TF/J Mouse Model of Autism." PLOS ONE **8**(10): e76655. doi: 10.1371/journal.pone.0076655

Drummond, E. and T. Wisniewski (2017). "Alzheimer's disease: experimental models and reality." Acta Neuropathol **133**(2): 155-175. doi: 10.1007/s00401-016-1662-x

Ellegood, J., J. P. Lerch and R. M. Henkelman (2011). "Brain abnormalities in a Neuroligin3 R451C knockin mouse model associated with autism." Autism Res **4**(5): 368-376. doi: 10.1002/aur.215

Emsell, L., W. Van Hecke and J.-D. Tournier (2016). Introduction to Diffusion Tensor Imaging. Diffusion Tensor Imaging: A Practical Handbook. W. Van Hecke, L. Emsell and S. Sunaert. New York, NY, Springer New York**:** 7-19.

Ezzati, M., S. V. Hoorn, A. D. Lopez, G. Danaei, A. Rodgers, C. D. Mathers and C. J. L. Murray (2006). Comparative Quantification of Mortality and Burden of Disease Attributable to Selected Risk Factors. Global Burden of Disease and Risk Factors. A. D. Lopez, C. D. Mathers, M. Ezzati, D. T. Jamison and C. J. L. Murray. Washington (DC).

Fang, Y., T. Zheng, L. Liu, D. Gao, Q. Shi, Y. Dong and D. Du (2018). "Role of the combination of FA and T2* parameters as a new diagnostic method in therapeutic evaluation of parkinson's disease." J Magn Reson Imaging **48**(1): 84-93. doi: 10.1002/jmri.25900

Ferris, C. F., T. R. Morrison, S. Iriah, S. Malmberg, P. Kulkarni, J. C. Hartner and M. Trivedi (2018). "Evidence of Neurobiological Changes in the Presymptomatic PINK1 Knockout Rat." J Parkinsons Dis **8**(2): 281-301. doi: 10.3233/jpd-171273

Filippi, M., A. Bar-Or, F. Piehl, P. Preziosa, A. Solari, S. Vukusic and M. A. Rocca (2018). "Multiple sclerosis." Nature reviews. Disease primers **4**(1): 43-43. doi: 10.1038/s41572-018-0041-4

Garcia-Miralles, M., X. Hong, L. J. Tan, N. S. Caron, Y. Huang, X. V. To, R. Y. Lin, S. Franciosi, S. Papapetropoulos, L. Hayardeny, M. R. Hayden, K. H. Chuang and M. A. Pouladi (2016). "Laquinimod rescues striatal, cortical and white matter pathology and results in modest behavioural improvements in the YAC128 model of Huntington disease." Sci Rep **6**: 31652. doi: 10.1038/srep31652

Gatto, R. G., A. Q. Ye, L. Colon-Perez, T. H. Mareci, A. Lysakowski, S. D. Price, S. T. Brady, M. Karaman, G. Morfini and R. L. Magin (2019). "Detection of axonal degeneration in a mouse model of Huntington's disease: comparison between diffusion tensor imaging and anomalous diffusion metrics." Magma **32**(4): 461-471. doi: 10.1007/s10334-019-00742-6

Grandjean, J., D. Azzinnari, A. Seuwen, H. Sigrist, E. Seifritz, C. R. Pryce and M. Rudin (2016). "Chronic psychosocial stress in mice leads to changes in brain functional connectivity and metabolite levels comparable to human depression." Neuroimage **142**: 544-552. doi: 10.1016/j.neuroimage.2016.08.013

Hagmann, P., L. Jonasson, P. Maeder, J. P. Thiran, V. J. Wedeen and R. Meuli (2006). "Understanding diffusion MR imaging techniques: from scalar diffusion-weighted imaging to diffusion tensor imaging and beyond." Radiographics **26 Suppl 1**: S205-223. doi: 10.1148/rg.26si065510

Harms, M. P., J. J. Kotyk and K. M. Merchant (2006). "Evaluation of white matter integrity in ex vivo brains of amyloid plaque-bearing APPsw transgenic mice using magnetic resonance diffusion tensor imaging." Exp Neurol **199**(2): 408-415. doi: 10.1016/j.expneurol.2006.01.002

Hemanth Kumar, B. S., S. K. Mishra, R. Trivedi, S. Singh, P. Rana and S. Khushu (2014). "Demyelinating evidences in CMS rat model of depression: a DTI study at 7 T." Neuroscience **275**: 12-21. doi: 10.1016/j.neuroscience.2014.05.037

Horowitz, A., D. Barazany, I. Tavor, G. Yovel and Y. Assaf (2015). "Response to the comments on the paper by Horowitz et al. (2014)." Brain structure & function **220**(3): 1791-1792. doi: 10.1007/s00429-015-1031-x

Huettel, S. A., A. W. Song and G. McCarthy (2014). Functional Magnetic Resonance Imaging, Sinauer.

Iossifov, I., B. J. O'Roak, S. J. Sanders, M. Ronemus, N. Krumm, D. Levy, H. A. Stessman, K. T. Witherspoon, L. Vives, K. E. Patterson, J. D. Smith, B. Paeper, D. A. Nickerson, J. Dea, S. Dong, L. E. Gonzalez, J. D. Mandell, S. M. Mane, M. T. Murtha, C. A. Sullivan, M. F. Walker, Z. Waqar, L. Wei, A. J. Willsey, B. Yamrom, Y.-h. Lee, E. Grabowska, E. Dalkic, Z. Wang, S. Marks, P. Andrews, A. Leotta, J. Kendall, I. Hakker, J. Rosenbaum, B. Ma, L. Rodgers, J. Troge, G. Narzisi, S. Yoon, M. C. Schatz, K. Ye, W. R. McCombie, J. Shendure, E. E. Eichler, M. W. State and M. Wigler (2014). "The contribution of de novo coding mutations to autism spectrum disorder." Nature **515**: 216. doi: 10.1038/nature13908
https://www.nature.com/articles/nature13908 - supplementary-information

Janke, A. L. and J. F. Ullmann (2015). "Robust methods to create ex vivo minimum deformation atlases for brain mapping." Methods **73**: 18-26. doi: 10.1016/j.ymeth.2015.01.005

Jensen, J. H., M. F. Falangola, C. Hu, A. Tabesh, O. Rapalino, C. Lo and J. A. Helpern (2011). "Preliminary observations of increased diffusional kurtosis in human brain following recent cerebral infarction." NMR Biomed **24**(5): 452-457. doi: 10.1002/nbm.1610

Jensen, J. H. and J. A. Helpern (2010). "MRI quantification of non-Gaussian water diffusion by kurtosis analysis." NMR in biomedicine **23**(7): 698-710. doi: 10.1002/nbm.1518

Jensen, J. H., J. A. Helpern, A. Ramani, H. Lu and K. Kaczynski (2005). "Diffusional kurtosis imaging: the quantification of non-gaussian water diffusion by means of magnetic resonance imaging." Magn Reson Med **53**(6): 1432-1440. doi: 10.1002/mrm.20508

Jones, D. K. (2010). Diffusion MRI, Oxford University Press.

Jones, D. K. and P. J. Basser (2004). ""Squashing peanuts and smashing pumpkins": how noise distorts diffusion-weighted MR data." Magnetic resonance in medicine **52**(5): 979-993. doi: 10.1002/mrm.20283

Kahn, R. S., I. E. Sommer, R. M. Murray, A. Meyer-Lindenberg, D. R. Weinberger, T. D. Cannon, M. O'Donovan, C. U. Correll, J. M. Kane, J. van Os and T. R. Insel (2015).

"Schizophrenia." Nature reviews. Disease primers **1**: 15067-15067. doi: 10.1038/nrdp.2015.67

Kane, C. J. and P. D. Drew (2016). "Inflammatory responses to alcohol in the CNS: nuclear receptors as potential therapeutics for alcohol-induced neuropathologies." J Leukoc Biol **100**(5): 951-959. doi: 10.1189/jlb.3MR0416-171R

Katsnelson, A. (2014). "Drug development: The modelling challenge." Nature **508**(7494): S8-S9. doi: 10.1038/508S8a

Khairnar, A., P. Latta, E. Drazanova, J. Ruda-Kucerova, N. Szabo, A. Arab, B. Hutter-Paier, D. Havas, M. Windisch, A. Sulcova, Z. Starcuk, Jr. and I. Rektorova (2015). "Diffusion Kurtosis Imaging Detects Microstructural Alterations in Brain of alpha-Synuclein Overexpressing Transgenic Mouse Model of Parkinson's Disease: A Pilot Study." Neurotox Res **28**(4): 281-289. doi: 10.1007/s12640-015-9537-9

Khairnar, A., J. Ruda-Kucerova, E. Drazanova, N. Szabo, P. Latta, A. Arab, B. Hutter-Paier, D. Havas, M. Windisch, A. Sulcova, Z. Starcuk, Jr., A. Kiraly and I. Rektorova (2016). "Late-stage alpha-synuclein accumulation in TNWT-61 mouse model of Parkinson's disease detected by diffusion kurtosis imaging." J Neurochem **136**(6): 1259-1269. doi: 10.1111/jnc.13500

Khairnar, A., J. Ruda-Kucerova, N. Szabo, E. Drazanova, A. Arab, B. Hutter-Paier, J. Neddens, P. Latta, Z. Starcuk, Jr. and I. Rektorova (2017). "Early and progressive microstructural brain changes in mice overexpressing human alpha-Synuclein detected by diffusion kurtosis imaging." Brain Behav Immun **61**: 197-208. doi: 10.1016/j.bbi.2016.11.027

Khan, A. R., A. Chuhutin, O. Wiborg, C. D. Kroenke, J. R. Nyengaard, B. Hansen and S. N. Jespersen (2016). "Biophysical modeling of high field diffusion MRI demonstrates micro-structural aberration in chronic mild stress rat brain." Neuroimage **142**: 421-430. doi: 10.1016/j.neuroimage.2016.07.001

Khan, A. R., B. Hansen, O. Wiborg, C. D. Kroenke and S. N. Jespersen (2018a). "Diffusion MRI and MR spectroscopy reveal microstructural and metabolic brain alterations in chronic mild stress exposed rats: A CMS recovery study." Neuroimage **167**: 342-353. doi: 10.1016/j.neuroimage.2017.11.053

Khan, A. R., C. D. Kroenke, O. Wiborg, A. Chuhutin, J. R. Nyengaard, B. Hansen and S. N. Jespersen (2018b). "Differential microstructural alterations in rat cerebral cortex in a model of chronic mild stress depression." PLoS One **13**(2): e0192329. doi: 10.1371/journal.pone.0192329

Kingsley, P. B. (2006). "Introduction to diffusion tensor imaging mathematics: Part I. Tensors, rotations, and eigenvectors." Concepts in Magnetic Resonance Part A **28A**(2): 101-122. doi: 10.1002/cmr.a.20048

Kumar, M., J. T. Duda, W. T. Hwang, C. Kenworthy, R. Ittyerah, S. Pickup, E. S. Brodkin, J. C. Gee, T. Abel and H. Poptani (2014). "High resolution magnetic resonance imaging for characterization of the neuroligin-3 knock-in mouse model associated with autism spectrum disorder." PLoS One **9**(10): e109872. doi: 10.1371/journal.pone.0109872

Kumar, M., S. Kim, S. Pickup, R. Chen, A. H. Fairless, R. Ittyerah, T. Abel, E. S. Brodkin and H. Poptani (2012). "Longitudinal in-vivo diffusion tensor imaging for assessing brain developmental changes in BALB/cJ mice, a model of reduced sociability relevant to autism." Brain Res **1455**: 56-67. doi: 10.1016/j.brainres.2012.03.041

Kumar, V. J., N. M. Grissom, S. E. McKee, H. Schoch, N. Bowman, R. Havekes, M. Kumar, S. Pickup, H. Poptani, T. M. Reyes, M. Hawrylycz, T. Abel and T. Nickl-Jockschat (2018). "Linking spatial gene expression patterns to sex-specific brain structural changes on a mouse model of 16p11.2 hemideletion." Transl Psychiatry **8**(1): 109. doi: 10.1038/s41398-018-0157-z

Le Bihan, D. and E. Breton (1985). "Imagerie de diffusion in-vivo par résonance magnétique nucléaire." Comptes-Rendus de l'Académie des Sciences **93**(5): 27-34.

Liu, L. X., D. Du, Z. Q. Wang, Y. Fang, T. Zheng, Y. C. Dong, Q. L. Shi, M. Zhao, F. Xiao and J. Du (2018a). "Differences in brain pathological changes between rotenone and 6-hydroxydopamine Parkinson's disease models." Neural Regen Res **13**(7): 1276-1280. doi: 10.4103/1673-5374.235076

Liu, L. X., D. Du, T. Zheng, Y. Fang, Y. S. Chen, H. L. Yi, Q. Y. He, D. W. Gao and Q. L. Shi (2017). "Detecting dopaminergic neuronal degeneration using diffusion tensor imaging in a rotenone-induced rat model of Parkinson's disease: fractional anisotropy and mean diffusivity values." Neural Regen Res **12**(9): 1485-1491. doi: 10.4103/1673-5374.213559

Liu, X., J. Yuan, Y. Guang, X. Wang and Z. Feng (2018b). "Longitudinal in vivo Diffusion Tensor Imaging Detects Differential Microstructural Alterations in the Hippocampus of Chronic Social Defeat Stress-Susceptible and Resilient Mice." Front Neurosci **12**: 613. doi: 10.3389/fnins.2018.00613

Lu, H., J. H. Jensen, A. Ramani and J. A. Helpern (2006). "Three-dimensional characterization of non-gaussian water diffusion in humans using diffusion kurtosis imaging." NMR Biomed **19**(2): 236-247. doi: 10.1002/nbm.1020

Luo, J., Z. Shen, G. Chen, D. Wang and X. Yu (2017). "Pontine Changes in Metabolites and Axonal Fibres of Rats Following Four-week Alcohol Exposure: In Vivo Diffusion Tensor Imaging and 1h-magnetic Resonance Spectroscopy Study at 7.0 T." Alcohol Alcohol **52**(2): 145-150. doi: 10.1093/alcalc/agw087

Lupien, S. J., B. S. McEwen, M. R. Gunnar and C. Heim (2009). "Effects of stress throughout the lifespan on the brain, behaviour and cognition." Nat Rev Neurosci **10**(6): 434-445. doi: 10.1038/nrn2639

Ma, E., T. Song, H. Zhang, J. Lu, L. Wang, Q. Zhao, R. Guo, M. Li, G. Ma, G. Lu and K. Li (2015). "The reduction of volume and fiber bundle connections in the hippocampus of EGR3 transgenic schizophrenia rats." Neuropsychiatr Dis Treat **11**: 1625-1638. doi: 10.2147/ndt.S81440

Marder, S. R. and T. D. Cannon (2019). "Schizophrenia." The New England journal of medicine **381**(18): 1753-1761. doi: 10.1056/NEJMra1808803

Miles, J. H. (2011). "Autism spectrum disorders—A genetics review." Genetics In Medicine **13**: 278. doi: 10.1097/GIM.0b013e3181ff67ba

Missault, S., C. Anckaerts, S. Ahmadoun, I. Blockx, M. Barbier, K. Bielen, D. Shah, S. Kumar-Singh, W. H. De Vos, A. Van der Linden, S. Dedeurwaerdere and M. Verhoye (2019). "Hypersynchronicity in the default mode-like network in a neurodevelopmental animal model with relevance for schizophrenia." Behav Brain Res **364**: 303-316. doi: 10.1016/j.bbr.2019.02.040

Monnot, C., X. Zhang, S. Nikkhou-Aski, P. Damberg and P. Svenningsson (2017). "Asymmetric dopaminergic degeneration and levodopa alter functional corticostriatal connectivity bilaterally in experimental parkinsonism." Exp Neurol **292**: 11-20. doi: 10.1016/j.expneurol.2017.02.014

Munoz-Moreno, E., R. Tudela, X. Lopez-Gil and G. Soria (2018). "Early brain connectivity alterations and cognitive impairment in a rat model of Alzheimer's disease." Alzheimers Res Ther **10**(1): 16. doi: 10.1186/s13195-018-0346-2

Nalls, M. A., N. Pankratz, C. M. Lill, C. B. Do, D. G. Hernandez, M. Saad, A. L. DeStefano, E. Kara, J. Bras, M. Sharma, C. Schulte, M. F. Keller, S. Arepalli, C. Letson, C. Edsall, H. Stefansson, X. Liu, H. Pliner, J. H. Lee, R. Cheng, C. International Parkinson's Disease Genomics, G. I. Parkinson's Study Group Parkinson's Research: The Organized, andMe, GenePd, C. NeuroGenetics Research, G. Hussman Institute of Human, I. Ashkenazi Jewish Dataset, H. Cohorts for, E. Aging Research in Genetic, C. North American Brain Expression, C. United Kingdom Brain Expression, C. Greek Parkinson's Disease, G. Alzheimer Genetic Analysis, M. A. Ikram, J. P. A. Ioannidis, G. M. Hadjigeorgiou, J. C. Bis, M. Martinez, J. S. Perlmutter, A. Goate, K. Marder, B.

Fiske, M. Sutherland, G. Xiromerisiou, R. H. Myers, L. N. Clark, K. Stefansson, J. A. Hardy, P. Heutink, H. Chen, N. W. Wood, H. Houlden, H. Payami, A. Brice, W. K. Scott, T. Gasser, L. Bertram, N. Eriksson, T. Foroud and A. B. Singleton (2014). "Large-scale meta-analysis of genome-wide association data identifies six new risk loci for Parkinson's disease." Nature genetics **46**(9): 989-993. doi: 10.1038/ng.3043

Nishioka, C., H. F. Liang, B. Barsamian and S. W. Sun (2019). "Sequential phases of RGC axonal and somatic injury in EAE mice examined using DTI and OCT." Mult Scler Relat Disord **27**: 315-323. doi: 10.1016/j.msard.2018.11.010

Nishioka, C., H. F. Liang, C. F. Chung and S. W. Sun (2017). "Disease stage-dependent relationship between diffusion tensor imaging and electrophysiology of the visual system in a murine model of multiple sclerosis." Neuroradiology **59**(12): 1241-1250. doi: 10.1007/s00234-017-1904-1

Oguz, I., M. S. McMurray, M. Styner and J. M. Johns (2012). "The translational role of diffusion tensor image analysis in animal models of developmental pathologies." Dev Neurosci **34**(1): 5-19. doi: 10.1159/000336825

Owen, M. J., A. Sawa and P. B. Mortensen (2016). "Schizophrenia." Lancet (London, England) **388**(10039): 86-97. doi: 10.1016/S0140-6736(15)01121-6

Perlbarg, V., J. Lambert, B. Butler, M. Felfli, R. Valabregue, A. L. Privat, S. Lehericy and A. Petiet (2018). "Alterations of the nigrostriatal pathway in a 6-OHDA rat model of Parkinson's disease evaluated with multimodal MRI." PLoS One **13**(9): e0202597. doi: 10.1371/journal.pone.0202597

Pervolaraki, E., A. L. Tyson, F. Pibiri, S. L. Poulter, A. C. Reichelt, R. J. Rodgers, S. J. Clapcote, C. Lever, L. C. Andreae and J. Dachtler (2019). "The within-subject application of diffusion tensor MRI and CLARITY reveals brain structural changes in Nrxn2 deletion mice." Mol Autism **10**: 8. doi: 10.1186/s13229-019-0261-9

Pfefferbaum, A., N. M. Zahr, D. Mayer, T. Rohlfing and E. V. Sullivan (2015). "Dynamic responses of selective brain white matter fiber tracts to binge alcohol and recovery in the rat." PLoS One **10**(4): e0124885. doi: 10.1371/journal.pone.0124885

Poewe, W., K. Seppi, C. M. Tanner, G. M. Halliday, P. Brundin, J. Volkmann, A.-E. Schrag and A. E. Lang (2017). "Parkinson disease." Nature reviews. Disease primers **3**: 17013-17013. doi: 10.1038/nrdp.2017.13

Praet, J., N. V. Manyakov, L. Muchene, Z. Mai, V. Terzopoulos, S. de Backer, A. Torremans, P. J. Guns, T. Van De Casteele, A. Bottelbergs, B. Van Broeck, J. Sijbers, D. Smeets, Z. Shkedy, L. Bijnens, D. J. Pemberton, M. E. Schmidt, A. Van der Linden and M. Verhoye (2018). "Diffusion kurtosis imaging allows the early detection and

longitudinal follow-up of amyloid-beta-induced pathology." Alzheimers Res Ther **10**(1): 1. doi: 10.1186/s13195-017-0329-8

Qin, Y. Y., M. W. Li, S. Zhang, Y. Zhang, L. Y. Zhao, H. Lei, K. Oishi and W. Z. Zhu (2013). "In vivo quantitative whole-brain diffusion tensor imaging analysis of APP/PS1 transgenic mice using voxel-based and atlas-based methods." Neuroradiology **55**(8): 1027-1038. doi: 10.1007/s00234-013-1195-0

Rane, P., D. Cochran, S. M. Hodge, C. Haselgrove, D. N. Kennedy and J. A. Frazier (2015). "Connectivity in Autism: A Review of MRI Connectivity Studies." Harv Rev Psychiatry **23**(4): 223-244. doi: 10.1097/HRP.0000000000000072

Rehm, J., R. Room, K. Graham, M. Monteiro, G. Gmel and C. T. Sempos (2003). "The relationship of average volume of alcohol consumption and patterns of drinking to burden of disease: an overview." Addiction **98**(9): 1209-1228. doi: 10.1046/j.1360-0443.2003.00467.x

Rice, J. (2012). "Animal models: Not close enough." Nature **484**(7393): S9-S9. doi: 10.1038/nature11102

Richards, K., C. Watson, R. F. Buckley, N. D. Kurniawan, Z. Yang, M. D. Keller, R. Beare, P. F. Bartlett, G. F. Egan, G. J. Galloway, G. Paxinos, S. Petrou and D. C. Reutens (2011). "Segmentation of the mouse hippocampal formation in magnetic resonance images." Neuroimage **58**(3): 732-740. doi: 10.1016/j.neuroimage.2011.06.025

Rippon, G., J. Brock, C. Brown and J. Boucher (2007). "Disordered connectivity in the autistic brain: challenges for the "new psychophysiology"." Int J Psychophysiol **63**(2): 164-172. doi: 10.1016/j.ijpsycho.2006.03.012

Roozendaal, B., B. S. McEwen and S. Chattarji (2009). "Stress, memory and the amygdala." Nat Rev Neurosci **10**(6): 423-433. doi: 10.1038/nrn2651

Sandi, C. and J. Haller (2015). "Stress and the social brain: behavioural effects and neurobiological mechanisms." Nat Rev Neurosci **16**(5): 290-304. doi: 10.1038/nrn3918

Scheltens, P., K. Blennow, M. M. B. Breteler, B. de Strooper, G. B. Frisoni, S. Salloway and W. M. Van der Flier (2016). "Alzheimer's disease." Lancet (London, England) **388**(10043): 505-517. doi: 10.1016/S0140-6736(15)01124-1

Shu, N., Z. Wang, Z. Qi, K. Li and Y. He (2011). "Multiple diffusion indices reveals white matter degeneration in Alzheimer's disease and mild cognitive impairment: a

tract-based spatial statistics study." J Alzheimers Dis **26 Suppl 3**: 275-285. doi: 10.3233/JAD-2011-0024

Shu, X., Y. Y. Qin, S. Zhang, J. J. Jiang, Y. Zhang, L. Y. Zhao, D. Shan and W. Z. Zhu (2013). "Voxel-based diffusion tensor imaging of an APP/PS1 mouse model of Alzheimer's disease." Mol Neurobiol **48**(1): 78-83. doi: 10.1007/s12035-013-8418-6

Sippel, H. W. (1974). "The acetaldehyde content in rat brain during ethanol metabolism." J Neurochem **23**(2): 451-452. doi: 10.1111/j.1471-4159.1974.tb04380.x

Small, S. A. and K. Duff (2008). "Linking Abeta and tau in late-onset Alzheimer's disease: a dual pathway hypothesis." Neuron **60**(4): 534-542. doi: 10.1016/j.neuron.2008.11.007

Snow, W. M., R. Dale, Z. O'Brien-Moran, R. Buist, D. Peirson, M. Martin and B. C. Albensi (2017). "In Vivo Detection of Gray Matter Neuropathology in the 3xTg Mouse Model of Alzheimer's Disease with Diffusion Tensor Imaging." J Alzheimers Dis **58**(3): 841-853. doi: 10.3233/jad-170136

Song, S. K., J. Yoshino, T. Q. Le, S. J. Lin, S. W. Sun, A. H. Cross and R. C. Armstrong (2005). "Demyelination increases radial diffusivity in corpus callosum of mouse brain." Neuroimage **26**(1): 132-140. doi: 10.1016/j.neuroimage.2005.01.028

Stahl, R., O. Dietrich, S. J. Teipel, H. Hampel, M. F. Reiser and S. O. Schoenberg (2007). "White matter damage in Alzheimer disease and mild cognitive impairment: assessment with diffusion-tensor MR imaging and parallel imaging techniques." Radiology **243**(2): 483-492. doi: 10.1148/radiol.2432051714

Stejskal, E. O. and J. E. Tanner (1965). "Spin Diffusion Measurements: Spin Echoes in the Presence of a Time- Dependent Field Gradient." The Journal of Chemical Physics **42**(1): 288-292. doi: 10.1063/1.1695690

Sun, S. W., H. F. Liang, R. E. Schmidt, A. H. Cross and S. K. Song (2007). "Selective vulnerability of cerebral white matter in a murine model of multiple sclerosis detected using diffusion tensor imaging." Neurobiol Dis **28**(1): 30-38. doi: 10.1016/j.nbd.2007.06.011

Sun, S. W., S. K. Song, M. P. Harms, S. J. Lin, D. M. Holtzman, K. M. Merchant and J. J. Kotyk (2005). "Detection of age-dependent brain injury in a mouse model of brain amyloidosis associated with Alzheimer's disease using magnetic resonance diffusion tensor imaging." Exp Neurol **191**(1): 77-85. doi: 10.1016/j.expneurol.2004.09.006

Tabakoff, B., R. A. Anderson and R. F. Ritzmann (1976). "Brain acetaldehyde after ethanol administration." Biochem Pharmacol **25**(11): 1305-1309. doi: 10.1016/0006-2952(76)90094-0

Tang, S., S. Xu, R. P. Gullapalli and A. E. Medina (2018). "Effects of Early Alcohol Exposure on Functional Organization and Microstructure of a Visual-Tactile Integrative Circuit." Alcohol Clin Exp Res **42**(4): 727-734. doi: 10.1111/acer.13611

Teo, R. T., X. Hong, L. Yu-Taeger, Y. Huang, L. J. Tan, Y. Xie, X. V. To, L. Guo, R. Rajendran, A. Novati, C. Calaminus, O. Riess, M. R. Hayden, H. P. Nguyen, K. H. Chuang and M. A. Pouladi (2016). "Structural and molecular myelination deficits occur prior to neuronal loss in the YAC128 and BACHD models of Huntington disease." Hum Mol Genet **25**(13): 2621-2632. doi: 10.1093/hmg/ddw122

Ullmann, J. F., C. Watson, A. L. Janke, N. D. Kurniawan, G. Paxinos and D. C. Reutens (2014). "An MRI atlas of the mouse basal ganglia." Brain Struct Funct **219**(4): 1343-1353. doi: 10.1007/s00429-013-0572-0

Ullmann, J. F., C. Watson, A. L. Janke, N. D. Kurniawan and D. C. Reutens (2013). "A segmentation protocol and MRI atlas of the C57BL/6J mouse neocortex." Neuroimage **78**: 196-203. doi: 10.1016/j.neuroimage.2013.04.008

Vanhoutte, G., S. Pereson, Y. P. R. Delgado, P. J. Guns, B. Asselbergh, J. Veraart, J. Sijbers, M. Verhoye, C. Van Broeckhoven and A. Van der Linden (2013). "Diffusion kurtosis imaging to detect amyloidosis in an APP/PS1 mouse model for Alzheimer's disease." Magn Reson Med **69**(4): 1115-1121. doi: 10.1002/mrm.24680

Vetreno, R. P., R. Yaxley, B. Paniagua and F. T. Crews (2016). "Diffusion tensor imaging reveals adolescent binge ethanol-induced brain structural integrity alterations in adult rats that correlate with behavioral dysfunction." Addict Biol **21**(4): 939-953. doi: 10.1111/adb.12232

Wheeler-Kingshott, C. A. M. and M. Cercignani (2009). "About "axial" and "radial" diffusivities." Magnetic resonance in medicine **61**(5): 1255-1260. doi: 10.1002/mrm.21965

Wilkes, B. J., C. Bass, H. Korah, M. Febo and M. H. Lewis (2019). "Volumetric magnetic resonance and diffusion tensor imaging of C58/J mice: neural correlates of repetitive behavior." Brain Imaging Behav. doi: 10.1007/s11682-019-00158-9

Wu, H., X. Wang, Y. Gao, F. Lin, T. Song, Y. Zou, L. Xu and H. Lei (2016). "NMDA receptor antagonism by repetitive MK801 administration induces schizophrenia-like structural changes in the rat brain as revealed by voxel-based morphometry and

diffusion tensor imaging." Neuroscience **322**: 221-233. doi: 10.1016/j.neuroscience.2016.02.043

Xiang, Z., M. Valenza, L. Cui, V. Leoni, H. K. Jeong, E. Brilli, J. Zhang, Q. Peng, W. Duan, S. A. Reeves, E. Cattaneo and D. Krainc (2011). "Peroxisome-proliferator-activated receptor gamma coactivator 1 alpha contributes to dysmyelination in experimental models of Huntington's disease." J Neurosci **31**(26): 9544-9553. doi: 10.1523/jneurosci.1291-11.2011

Zalsman, G., A. Gutman, L. Shbiro, R. Rosenan, J. J. Mann and A. Weller (2015). "Genetic vulnerability, timing of short-term stress and mood regulation: A rodent diffusion tensor imaging study." Eur Neuropsychopharmacol **25**(11): 2075-2085. doi: 10.1016/j.euroneuro.2015.08.006

Zalsman, G., A. Weller, L. Shbiro, R. Barzilay, A. Gutman, A. Weizman, J. J. Mann, J. Wasserman and D. Wasserman (2017). "Fibre tract analysis using diffusion tensor imaging reveals aberrant connectivity in a rat model of depression." World J Biol Psychiatry **18**(8): 615-623. doi: 10.1080/15622975.2016.1190866

Zerbi, V., M. Kleinnijenhuis, X. Fang, D. Jansen, A. Veltien, J. Van Asten, N. Timmer, P. J. Dederen, A. J. Kiliaan and A. Heerschap (2013). "Gray and white matter degeneration revealed by diffusion in an Alzheimer mouse model." Neurobiol Aging **34**(5): 1440-1450. doi: 10.1016/j.neurobiolaging.2012.11.017

Zerbi, V., M. Markicevic, F. Gasparini, A. Schroeter, M. Rudin and N. Wenderoth (2019). "Inhibiting mGluR5 activity by AFQ056/Mavoglurant rescues circuit-specific functional connectivity in Fmr1 knockout mice." Neuroimage **191**: 392-402. doi: 10.1016/j.neuroimage.2019.02.051

Zhang, H., T. Schneider, C. A. Wheeler-Kingshott and D. C. Alexander (2012). "NODDI: practical in vivo neurite orientation dispersion and density imaging of the human brain." Neuroimage **61**(4): 1000-1016. doi: 10.1016/j.neuroimage.2012.03.072

Zhang, Y., N. Schuff, G. H. Jahng, W. Bayne, S. Mori, L. Schad, S. Mueller, A. T. Du, J. H. Kramer, K. Yaffe, H. Chui, W. J. Jagust, B. L. Miller and M. W. Weiner (2007). "Diffusion tensor imaging of cingulum fibers in mild cognitive impairment and Alzheimer disease." Neurology **68**(1): 13-19. doi: 10.1212/01.wnl.0000250326.77323.01

VII. BIBLIOGRPAHY

Abrahams, B. S. and D. H. Geschwind (2008). "Advances in autism genetics: on the threshold of a new neurobiology." Nature Reviews Genetics **9**: 341.

Alexander, D. C., T. B. Dyrby, M. Nilsson and H. Zhang (2019). "Imaging brain microstructure with diffusion MRI: practicality and applications." NMR Biomed **32**(4): e3841.

Allen, M., D. Poggiali, K. Whitaker, T. R. Marshall and R. A. Kievit (2019). "Raincloud plots: a multi-platform tool for robust data visualization." Wellcome open research **4**: 63-63.

Aller, M. I., V. Pecoraro, A. V. Paternain, S. Canals and J. Lerma (2015). "Increased Dosage of High-Affinity Kainate Receptor Gene grik4 Alters Synaptic Transmission and Reproduces Autism Spectrum Disorders Features." J Neurosci **35**(40): 13619-13628.

Ameis, S. H. and M. Catani (2015). "Altered white matter connectivity as a neural substrate for social impairment in Autism Spectrum Disorder." Cortex **62**: 158-181.

Anthony, Todd E., N. Dee, A. Bernard, W. Lerchner, N. Heintz and David J. Anderson (2014). "Control of Stress-Induced Persistent Anxiety by an Extra-Amygdala Septohypothalamic Circuit." Cell **156**(3): 522-536.

Araki, K., H. Meguro, E. Kushiya, C. Takayama, Y. Inoue and M. Mishina (1993). "Selective Expression of the Glutamate Receptor Channel δ2 Subunit in Cerebellar Purkinje Cells." Biochemical and Biophysical Research Communications **197**(3): 1267-1276.

Arfanakis, K., D. Cordes, V. M. Haughton, C. H. Moritz, M. A. Quigley and M. E. Meyerand (2000). "Combining independent component analysis and correlation analysis to probe interregional connectivity in fMRI task activation datasets." Magn Reson Imaging **18**(8): 921-930.

Arora, V., V. Pecoraro, M. I. Aller, C. Roman, A. V. Paternain and J. Lerma (2018). "Increased Grik4 Gene Dosage Causes Imbalanced Circuit Output and Human Disease-Related Behaviors." Cell Rep **23**(13): 3827-3838.

Ashburner, J. and K. J. Friston (2000). "Voxel-based morphometry--the methods." Neuroimage **11**(6 Pt 1): 805-821.

Ashburner, J. and K. J. Friston (2001). "Why voxel-based morphometry should be used." Neuroimage **14**(6): 1238-1243.

Asperger, H. (1944). "Die „Autistischen Psychopathen" im Kindesalter." Archiv für Psychiatrie und Nervenkrankheiten **117**(1): 76-136.

Assaf, M., K. Jagannathan, V. D. Calhoun, L. Miller, M. C. Stevens, R. Sahl, . . . G. D. Pearlson (2010). "Abnormal functional connectivity of default mode sub-networks in autism spectrum disorder patients." Neuroimage **53**(1): 247-256.

Assaf, Y. and P. J. Basser (2005). "Composite hindered and restricted model of diffusion (CHARMED) MR imaging of the human brain." Neuroimage **27**(1): 48-58.

Assaf, Y., R. Z. Freidlin, G. K. Rohde and P. J. Basser (2004). "New modeling and experimental framework to characterize hindered and restricted water diffusion in brain white matter." Magn Reson Med **52**(5): 965-978.

Assaf, Y., H. Johansen-Berg and M. Thiebaut de Schotten (2019). "The role of diffusion MRI in neuroscience." NMR in Biomedicine **32**(4): e3762.

Attwell, D. and S. B. Laughlin (2001). "An Energy Budget for Signaling in the Grey Matter of the Brain." Journal of Cerebral Blood Flow & Metabolism **21**(10): 1133-1145.

Avants, B. B., N. J. Tustison, G. Song, P. A. Cook, A. Klein and J. C. Gee (2011). "A reproducible evaluation of ANTs similarity metric performance in brain image registration." Neuroimage **54**(3): 2033-2044.

Bai, D., B. H. K. Yip, G. C. Windham, A. Sourander, R. Francis, R. Yoffe, . . . S. Sandin (2019). "Association of Genetic and Environmental Factors With Autism in a 5-Country Cohort." JAMA Psychiatry **76**(10): 1035-1043.

Barrière, D. A., A. Ella, F. Szeremeta, H. Adriaensen, W. Même, E. Chaillou, . . . M. Keller (2020). "Brain orchestration of pregnancy and maternal behavior in mice." 2020.2005.2023.112045.

Basser, P. J. (1995). "Inferring microstructural features and the physiological state of tissues from diffusion-weighted images." NMR Biomed **8**(7-8): 333-344.

Basser, P. J., J. Mattiello and D. Lebihan (1994). "Estimation of the Effective Self-Diffusion Tensor from the NMR Spin Echo." Journal of Magnetic Resonance, Series B **103**(3): 247-254.

Basser, P. J., S. Pajevic, C. Pierpaoli, J. Duda and A. Aldroubi (2000). "In vivo fiber tractography using DT-MRI data." Magn Reson Med **44**(4): 625-632.

Bateup, H. S., K. T. Takasaki, J. L. Saulnier, C. L. Denefrio and B. L. Sabatini (2011). "Loss of Tsc1 In Vivo Impairs Hippocampal mGluR-LTD and Increases Excitatory Synaptic Function." The Journal of Neuroscience **31**(24): 8862.

Beckmann, C. F., M. DeLuca, J. T. Devlin and S. M. Smith (2005). "Investigations into resting-state connectivity using independent component analysis." Philos Trans R Soc Lond B Biol Sci **360**(1457): 1001-1013.

Beckmann, C. F. and S. M. Smith (2004). "Probabilistic independent component analysis for functional magnetic resonance imaging." IEEE Trans Med Imaging **23**(2): 137-152.

Bedford, S. A., M. T. M. Park, G. A. Devenyi, S. Tullo, J. Germann, R. Patel, . . . M. M. Chakravarty (2019). "Large-scale analyses of the relationship between sex, age and intelligence quotient heterogeneity and cortical morphometry in autism spectrum disorder." Mol Psychiatry.

Belachew, S. and V. Gallo (2004). "Synaptic and extrasynaptic neurotransmitter receptors in glial precursors' quest for identity." Glia **48**(3): 185-196.

Benes, F. M., M. S. Todtenkopf and P. Kostoulakos (2001). "GluR5,6,7 subunit immunoreactivity on apical pyramidal cell dendrites in hippocampus of schizophrenics and manic depressives." Hippocampus **11**(5): 482-491.

Berker, E. A., A. H. Berker and A. Smith (1986). "Translation of Broca's 1865 report. Localization of speech in the third left frontal convolution." Arch Neurol **43**(10): 1065-1072.

Berman, J. I., M. S. Berger, S. W. Chung, S. S. Nagarajan and R. G. Henry (2007a). "Accuracy of diffusion tensor magnetic resonance imaging tractography assessed using intraoperative subcortical stimulation mapping and magnetic source imaging." J Neurosurg **107**(3): 488-494.

Berman, R. F., I. N. Pessah, P. R. Mouton, D. Mav and J. Harry (2007b). "Low-Level Neonatal Thimerosal Exposure: Further Evaluation of Altered Neurotoxic Potential in SJL Mice." Toxicological Sciences **101**(2): 294-309.

Berry-Kravis, E., V. Des Portes, R. Hagerman, S. Jacquemont, P. Charles, J. Visootsak, . . . F. von Raison (2016). "Mavoglurant in fragile X syndrome: Results of two randomized, double-blind, placebo-controlled trials." Science Translational Medicine **8**(321): 321ra325.

Bertero, A., A. Liska, M. Pagani, R. Parolisi, M. E. Masferrer, M. Gritti, . . . A. Gozzi (2018). "Autism-associated 16p11.2 microdeletion impairs prefrontal functional connectivity in mouse and human." Brain **141**(7): 2055-2065.

Bettler, B., J. Boulter, I. Hermans-Borgmeyer, A. O'Shea-Greenfield, E. S. Deneris, C. Moll, . . . S. Heinemann (1990). "Cloning of a novel glutamate receptor subunit, GluR5: Expression in the nervous system during development." Neuron **5**(5): 583-595.

Bicks, L. K., H. Koike, S. Akbarian and H. Morishita (2015). "Prefrontal Cortex and Social Cognition in Mouse and Man." **6**(1805).

Binder, J. R., J. A. Frost, T. A. Hammeke, P. S. Bellgowan, S. M. Rao and R. W. Cox (1999). "Conceptual processing during the conscious resting state. A functional MRI study." J Cogn Neurosci **11**(1): 80-95.

Biswal, B., A. G. Hudetz, F. Z. Yetkin, V. M. Haughton and J. S. Hyde (1997a). "Hypercapnia reversibly suppresses low-frequency fluctuations in the human motor cortex during rest using echo-planar MRI." J Cereb Blood Flow Metab **17**(3): 301-308.

Biswal, B., F. Z. Yetkin, V. M. Haughton and J. S. Hyde (1995). "Functional connectivity in the motor cortex of resting human brain using echo-planar MRI." Magn Reson Med **34**(4): 537-541.

Biswal, B. B. (2012). "Resting state fMRI: A personal history." NeuroImage **62**(2): 938-944.

Biswal, B. B., J. Van Kylen and J. S. Hyde (1997b). "Simultaneous assessment of flow and BOLD signals in resting-state functional connectivity maps." NMR Biomed **10**(4-5): 165-170.

Blazquez Freches, G., C. Chavarrias and N. Shemesh (2018). "BOLD-fMRI in the mouse auditory pathway." NeuroImage **165**: 265-277.

Blumenfeld-Katzir, T., O. Pasternak, M. Dagan and Y. Assaf (2011). "Diffusion MRI of structural brain plasticity induced by a learning and memory task." PloS one **6**(6): e20678-e20678.

Borsook, D. and L. Becerra (2011). "CNS animal fMRI in pain and analgesia." Neuroscience & Biobehavioral Reviews **35**(5): 1125-1143.

Bozdagi, O., T. Sakurai, D. Papapetrou, X. Wang, D. L. Dickstein, N. Takahashi, . . . J. D. Buxbaum (2010). "Haploinsufficiency of the autism-associated Shank3 gene leads to deficits in synaptic function, social interaction, and social communication." Molecular Autism **1**(1): 15.

Brady, S., G. Siegel, R. W. Albers and D. Price (2012). Basic Neurochemistry: Principles of Molecular, Cellular, and Medical Neurobiology, Elsevier Science.

Breasted, J. H. (2013). The Edwin Smith Surgical Papyrus, V1: Hieroglyphic Transliteration, Translation and Commentary, Literary Licensing, LLC.

Brookes, M. J., M. Woolrich, H. Luckhoo, D. Price, J. R. Hale, M. C. Stephenson, . . . P. G. Morris (2011). "Investigating the electrophysiological basis of resting state networks using magnetoencephalography." Proceedings of the National Academy of Sciences **108**(40): 16783.

Brown, R. (1828). "XXVII. A brief account of microscopical observations made in the months of June, July and August 1827, on the particles contained in the pollen of plants; and on the general existence of active molecules in organic and inorganic bodies." The Philosophical Magazine **4**(21): 161-173.

Buckner, R. L. (2012). "The serendipitous discovery of the brain's default network." Neuroimage **62**(2): 1137-1145.

Buckner, R. L., J. R. Andrews-Hanna and D. L. Schacter (2008). "The Brain's Default Network." Annals of the New York Academy of Sciences **1124**(1): 1-38.

Buckner, R. L. and L. M. DiNicola (2019). "The brain's default network: updated anatomy, physiology and evolving insights." Nature Reviews Neuroscience **20**(10): 593-608.

Bukhari, Q., A. Schroeter, D. M. Cole and M. Rudin (2017). "Resting State fMRI in Mice Reveals Anesthesia Specific Signatures of Brain Functional Networks and Their Interactions." **11**(5).

Bureau, I., S. Bischoff, S. F. Heinemann and C. Mulle (1999). "Kainate Receptor-Mediated Responses in the CA1 Field of Wild-Type and GluR6-Deficient Mice." **19**(2): 653-663.

Burnashev, N. and P. Szepetowski (2015). "NMDA receptor subunit mutations in neurodevelopmental disorders." Current Opinion in Pharmacology **20**: 73-82.

Button, K. S., J. P. A. Ioannidis, C. Mokrysz, B. A. Nosek, J. Flint, E. S. J. Robinson and M. R. Munafò (2013). "Power failure: why small sample size undermines the reliability of neuroscience." Nature Reviews Neuroscience **14**(5): 365-376.

Buxton, R. B., E. C. Wong and L. R. Frank (1998). "Dynamics of blood flow and oxygenation changes during brain activation: the balloon model." Magn Reson Med **39**(6): 855-864.

Canals, S., M. Beyerlein, H. Merkle and N. K. Logothetis (2009). "Functional MRI evidence for LTP-induced neural network reorganization." Curr Biol **19**(5): 398-403.

Canals, S., M. Beyerlein, Y. Murayama and N. K. Logothetis (2008). "Electric stimulation fMRI of the perforant pathway to the rat hippocampus." Magn Reson Imaging **26**(7): 978-986.

Carlisi, C. O., L. J. Norman, S. S. Lukito, J. Radua, D. Mataix-Cols and K. Rubia (2017). "Comparative Multimodal Meta-analysis of Structural and Functional Brain Abnormalities in Autism Spectrum Disorder and Obsessive-Compulsive Disorder." Biol Psychiatry **82**(2): 83-102.

Castillo, P. E., R. C. Malenka and R. A. Nicoll (1997). "Kainate receptors mediate a slow postsynaptic current in hippocampal CA3 neurons." Nature **388**(6638): 182-186.

Catani, M., R. J. Howard, S. Pajevic and D. K. Jones (2002). "Virtual in vivo interactive dissection of white matter fasciculi in the human brain." Neuroimage **17**(1): 77-94.

Catches, J. S., J. Xu and A. Contractor (2012). "Genetic ablation of the GluK4 kainate receptor subunit causes anxiolytic and antidepressant-like behavior in mice." Behavioural Brain Research **228**(2): 406-414.

Chang, E. H., M. Argyelan, M. Aggarwal, T.-S. S. Chandon, K. H. Karlsgodt, S. Mori and A. K. Malhotra (2017). "The role of myelination in measures of white matter integrity: Combination of diffusion tensor imaging and two-photon microscopy of CLARITY intact brains." NeuroImage **147**: 253-261.

Chang, L. C., D. K. Jones and C. Pierpaoli (2005). "RESTORE: robust estimation of tensors by outlier rejection." Magn Reson Med **53**(5): 1088-1095.

Chaste, P. and M. Leboyer (2012). "Autism risk factors: genes, environment, and gene-environment interactions." Dialogues in clinical neuroscience **14**(3): 281-292.

Chen, R., Y. Jiao and E. H. Herskovits (2011). "Structural MRI in autism spectrum disorder." Pediatr Res **69**(5 Pt 2): 63r-68r.

Chen, X., C. Tong, Z. Han, K. Zhang, B. Bo, Y. Feng and Z. Liang (2020). "Sensory evoked fMRI paradigms in awake mice." NeuroImage **204**: 116242.

Cherkassky, V. L., R. K. Kana, T. A. Keller and M. A. Just (2006). "Functional connectivity in a baseline resting-state network in autism." Neuroreport **17**(16): 1687-1690.

Chung, H. W., M. C. Chou and C. Y. Chen (2011). "Principles and limitations of computational algorithms in clinical diffusion tensor MR tractography." AJNR Am J Neuroradiol **32**(1): 3-13.

Clarke, V. R., B. A. Ballyk, K. H. Hoo, A. Mandelzys, A. Pellizzari, C. P. Bath, . . . D. Bleakman (1997). "A hippocampal GluR5 kainate receptor regulating inhibitory synaptic transmission." Nature **389**(6651): 599-603.

Cong, L., E. R. Muir, C. Chen, Y. Qian, J. Liu, K. C. Biju, . . . T. Q. Duong (2016). "Multimodal MRI Evaluation of the MitoPark Mouse Model of Parkinson's Disease." PLoS One **11**(3): e0151884.

Conn, P. J. and J. P. Pin (1997). "Pharmacology and functions of metabotropic glutamate receptors." Annu Rev Pharmacol Toxicol **37**: 205-237.

Contractor, A., C. Mulle and G. T. Swanson (2011). "Kainate receptors coming of age: milestones of two decades of research." Trends Neurosci **34**(3): 154-163.

Conturo, T. E., N. F. Lori, T. S. Cull, E. Akbudak, A. Z. Snyder, J. S. Shimony, . . . M. E. Raichle (1999). "Tracking neuronal fiber pathways in the living human brain." Proceedings of the National Academy of Sciences of the United States of America **96**(18): 10422-10427.

Corbett, B. A., V. Carmean, S. Ravizza, C. Wendelken, M. L. Henry, C. Carter and S. M. Rivera (2009). "A functional and structural study of emotion and face processing in children with autism." Psychiatry Res **173**(3): 196-205.

Cossart, R., R. Tyzio, C. Dinocourt, M. Esclapez, J. C. Hirsch, Y. Ben-Ari and C. Bernard (2001). "Presynaptic Kainate Receptors that Enhance the Release of GABA on CA1 Hippocampal Interneurons." Neuron **29**(2): 497-508.

Costabile, J. D., E. Alaswad, S. D'Souza, J. A. Thompson and D. R. Ormond (2019). "Current Applications of Diffusion Tensor Imaging and Tractography in Intracranial Tumor Resection." **9**(426).

Courchesne, E. and K. Pierce (2005). "Why the frontal cortex in autism might be talking only to itself: local over-connectivity but long-distance disconnection." Current Opinion in Neurobiology **15**(2): 225-230.

Cox, R. W. (1996). "AFNI: software for analysis and visualization of functional magnetic resonance neuroimages." Comput Biomed Res **29**(3): 162-173.

Crawley, J. N. (2008). "Behavioral Phenotyping Strategies for Mutant Mice." Neuron **57**(6): 809-818.

Crombe, A., V. Planche, G. Raffard, J. Bourel, N. Dubourdieu, A. Panatier, . . . T. Tourdias (2018). "Deciphering the microstructure of hippocampal subfields with in vivo DTI and NODDI: Applications to experimental multiple sclerosis." Neuroimage **172**: 357-368.

Curran, K. M., L. Emsell and A. Leemans (2016). Quantitative DTI Measures. Diffusion Tensor Imaging: A Practical Handbook. W. Van Hecke, L. Emsell and S. Sunaert. New York, NY, Springer New York**:** 65-87.

D'Esposito, M., L. Y. Deouell and A. Gazzaley (2003). "Alterations in the BOLD fMRI signal with ageing and disease: a challenge for neuroimaging." Nature Reviews Neuroscience **4**(11): 863-872.

D'Esposito, M., E. Zarahn, G. K. Aguirre and B. Rypma (1999). "The Effect of Normal Aging on the Coupling of Neural Activity to the Bold Hemodynamic Response." NeuroImage **10**(1): 6-14.

Dani, V. S., Q. Chang, A. Maffei, G. G. Turrigiano, R. Jaenisch and S. B. Nelson (2005). "Reduced cortical activity due to a shift in the balance between excitation and inhibition in a mouse model of Rett syndrome." Proceedings of the National Academy of Sciences of the United States of America **102**(35): 12560-12565.

Dauguet, J., S. Peled, V. Berezovskii, T. Delzescaux, S. K. Warfield, R. Born and C. F. Westin (2007). "Comparison of fiber tracts derived from in-vivo DTI tractography with 3D histological neural tract tracer reconstruction on a macaque brain." Neuroimage **37**(2): 530-538.

Davenport, H. W. (1991). "Early history of the concept of chemical transmission of the nerve impulse." The Physiologist **34**(4): 129, 178-190.

Davies, R. R., V. L. Scahill, A. Graham, G. B. Williams, K. S. Graham and J. R. Hodges (2009). "Development of an MRI rating scale for multiple brain regions: comparison with volumetrics and with voxel-based morphometry." Neuroradiology **51**(8): 491-503.

De Luca, M., C. F. Beckmann, N. De Stefano, P. M. Matthews and S. M. Smith (2006). "fMRI resting state networks define distinct modes of long-distance interactions in the human brain." Neuroimage **29**(4): 1359-1367.

De Rubeis, S., X. He, A. P. Goldberg, C. S. Poultney, K. Samocha, A. Ercument Cicek, . . . J. D. Buxbaum (2014). "Synaptic, transcriptional and chromatin genes disrupted in autism." Nature **515**: 209.

De Santis, S., P. Bach, L. Perez-Cervera, A. Cosa-Linan, G. Weil, S. Vollstadt-Klein, . . . S. Canals (2019). "Microstructural White Matter Alterations in Men With Alcohol Use Disorder and Rats With Excessive Alcohol Consumption During Early Abstinence." JAMA Psychiatry **76**(7): 749-758.

De Santis, S., M. Drakesmith, S. Bells, Y. Assaf and D. K. Jones (2014). "Why diffusion tensor MRI does well only some of the time: variance and covariance of white matter tissue microstructure attributes in the living human brain." Neuroimage **89**(100): 35-44.

Deisseroth, K. (2011). "Optogenetics." Nature Methods **8**(1): 26-29.

Delettre, C., A. Messe, L. A. Dell, O. Foubet, K. Heuer, B. Larrat, . . . C. C. Hilgetag (2019). "Comparison between diffusion MRI tractography and histological tract-tracing of cortico-cortical structural connectivity in the ferret brain." Netw Neurosci **3**(4): 1038-1050.

Devor, A., E. M. C. Hillman, P. Tian, C. Waeber, I. C. Teng, L. Ruvinskaya, . . . D. A. Boas (2008). "Stimulus-Induced Changes in Blood Flow and 2-Deoxyglucose Uptake Dissociate in Ipsilateral Somatosensory Cortex." The Journal of Neuroscience **28**(53): 14347.

Devor, A., P. Tian, N. Nishimura, I. C. Teng, E. M. C. Hillman, S. N. Narayanan, . . . A. M. Dale (2007). "Suppressed Neuronal Activity and Concurrent Arteriolar Vasoconstriction May Explain Negative Blood Oxygenation Level-Dependent Signal." The Journal of Neuroscience **27**(16): 4452.

Dhollander, T., Clemente, A., Singh, M., Boonstra, F., Civier, O., D., J. F. D., … Caeyenberghs, K. (2020). "Fixel-based Analysis of Diffusion MRI: Methods, Applications, Challenges and Opportunities." OSF Preprints.

Dingledine, R., K. Borges, D. Bowie and S. F. Traynelis (1999). "The Glutamate Receptor Ion Channels." Pharmacological Reviews **51**(1): 7.

Dodero, L., M. Damiano, A. Galbusera, A. Bifone, S. A. Tsaftsaris, M. L. Scattoni and A. Gozzi (2013). "Neuroimaging Evidence of Major Morpho-Anatomical and Functional Abnormalities in the BTBR T+TF/J Mouse Model of Autism." PLOS ONE **8**(10): e76655.

Dracheva, S., W. Byne, B. Chin and V. Haroutunian (2008). "Ionotropic glutamate receptor mRNA expression in the human thalamus: absence of change in schizophrenia." Brain Res **1214**: 23-34.

Eed, A., A. Cerdán Cerdá, J. Lerma and S. De Santis (2020). "Diffusion-weighted MRI in neurodegenerative and psychiatric animal models: Experimental strategies and main outcomes." Journal of Neuroscience Methods **343**: 108814.

Egebjerg, J., B. Bettler, I. Hermans-Borgmeyer and S. Heinemann (1991). "Cloning of a cDNA for a glutamate receptor subunit activated by kainate but not AMPA." Nature **351**(6329): 745-748.

Einstein, A. (1905). "On the Movement of Small Particles Suspended in a Stationary Liquid Demanded by the Molecular-Kinetic Theory of Heat." Theory of Brownian Movement.

Einstein, A. (1956). Investigations on the Theory of the Brownian Movement, Dover Publications.

Eklund, A., T. E. Nichols and H. Knutsson (2016). "Cluster failure: Why fMRI inferences for spatial extent have inflated false-positive rates." Proc Natl Acad Sci U S A **113**(28): 7900-7905.

Ellegood, J., E. Anagnostou, B. A. Babineau, J. N. Crawley, L. Lin, M. Genestine, . . . J. P. Lerch (2015). "Clustering autism: using neuroanatomical differences in 26 mouse models to gain insight into the heterogeneity." Mol Psychiatry **20**(1): 118-125.

Ellegood, J., J. P. Lerch and R. M. Henkelman (2011). "Brain abnormalities in a Neuroligin3 R451C knockin mouse model associated with autism." Autism Res **4**(5): 368-376.

Elliott, T. R. (1905). "The action of adrenalin." The Journal of Physiology **32**(5-6): 401-467.

Ellison-Wright, I. and E. Bullmore (2009). "Meta-analysis of diffusion tensor imaging studies in schizophrenia." Schizophr Res **108**(1-3): 3-10.

Elsabbagh, M., G. Divan, Y. J. Koh, Y. S. Kim, S. Kauchali, C. Marcín, . . . E. Fombonne (2012). "Global prevalence of autism and other pervasive developmental disorders." Autism Res **5**(3): 160-179.

Emsell, L., C. Chaddock, N. Forde, W. Van Hecke, G. J. Barker, A. Leemans, . . . C. McDonald (2014). "White matter microstructural abnormalities in families multiply affected with bipolar I disorder: a diffusion tensor tractography study." Psychol Med **44**(10): 2139-2150.

Emsell, L., C. Langan, W. Van Hecke, G. J. Barker, A. Leemans, S. Sunaert, . . . C. McDonald (2013a). "White matter differences in euthymic bipolar I disorder: a combined magnetic resonance imaging and diffusion tensor imaging voxel-based study." Bipolar Disord **15**(4): 365-376.

Emsell, L., A. Leemans, C. Langan, W. Van Hecke, G. J. Barker, P. McCarthy, . . . C. McDonald (2013b). "Limbic and callosal white matter changes in euthymic bipolar I disorder: an advanced diffusion magnetic resonance imaging tractography study." Biol Psychiatry **73**(2): 194-201.

Enager, P., H. Piilgaard, N. Offenhauser, A. Kocharyan, P. Fernandes, E. Hamel and M. Lauritzen (2009). "Pathway-specific variations in neurovascular and neurometabolic coupling in rat primary somatosensory cortex." Journal of Cerebral Blood Flow and Metabolism **29**(5): 976-986.

Erreger, K., P. E. Chen, D. J. A. Wyllie and S. F. Traynelis (2004). "Glutamate Receptor Gating." **16**(3): 187-224.

Errico, F., V. D'Argenio, F. Sforazzini, F. Iasevoli, M. Squillace, G. Guerri, . . . A. Usiello (2015). "A role for D-aspartate oxidase in schizophrenia and in schizophrenia-related symptoms induced by phencyclidine in mice." Translational Psychiatry **5**(2): e512-e512.

Fick, A. (1855). "Ueber Diffusion." Annalen der Physik **170**(1): 59-86.

Fields, R. D. (2008). "White matter in learning, cognition and psychiatric disorders." Trends in Neurosciences **31**(7): 361-370.

Filipello, F., R. Morini, I. Corradini, V. Zerbi, A. Canzi, B. Michalski, . . . M. Matteoli (2018). "The Microglial Innate Immune Receptor TREM2 Is Required for Synapse Elimination and Normal Brain Connectivity." Immunity **48**(5): 979-991.e978.

Filippini, N., B. J. MacIntosh, M. G. Hough, G. M. Goodwin, G. B. Frisoni, S. M. Smith, . . . C. E. Mackay (2009). "Distinct patterns of brain activity in young carriers of the APOE-ε4 allele." Proceedings of the National Academy of Sciences **106**(17): 7209.

Finger, S. (2004). Minds Behind the Brain: A History of the Pioneers and Their Discoveries, Oxford University Press, USA.

Fisahn, A. (2005). "Kainate receptors and rhythmic activity in neuronal networks: hippocampal gamma oscillations as a tool." J Physiol **562**(Pt 1): 65-72.

Fombonne, E. (2001). "Is There an Epidemic of Autism?" Pediatrics **107**(2): 411.

Fornito, A., A. Zalesky, C. Pantelis and E. T. Bullmore (2012). "Schizophrenia, neuroimaging and connectomics." Neuroimage **62**(4): 2296-2314.

Fox, M. D. and M. E. Raichle (2007). "Spontaneous fluctuations in brain activity observed with functional magnetic resonance imaging." Nature Reviews Neuroscience **8**(9): 700-711.

Fox, P. T. (2012). "The coupling controversy." NeuroImage **62**(2): 594-601.

Fox, P. T. and M. E. Raichle (1986). "Focal physiological uncoupling of cerebral blood flow and oxidative metabolism during somatosensory stimulation in human subjects." Proceedings of the National Academy of Sciences **83**(4): 1140.

Friston, K. (2012). "Ten ironic rules for non-statistical reviewers." NeuroImage **61**(4): 1300-1310.

Friston, K. (2013). "Sample size and the fallacies of classical inference." NeuroImage **81**: 503-504.

Friston, K. J., A. P. Holmes, K. J. Worsley, J. P. Poline, C. D. Frith and R. S. J. Frackowiak (1994). "Statistical parametric maps in functional imaging: A general linear approach." Human Brain Mapping **2**(4): 189-210.

Gallo, V., L. M. Upson, W. P. Hayes, L. Vyklicky, C. A. Winters and A. Buonanno (1992). "Molecular cloning and development analysis of a new glutamate receptor subunit isoform in cerebellum." The Journal of Neuroscience **12**(3): 1010.

Garcia, J. O., A. Ashourvan, S. F. Muldoon, J. M. Vettel and D. S. Bassett (2018). "Applications of community detection techniques to brain graphs: Algorithmic considerations and implications for neural function." Proceedings of the IEEE. Institute of Electrical and Electronics Engineers **106**(5): 846-867.

Garyfallidis, E., M. Brett, B. Amirbekian, A. Rokem, S. van der Walt, M. Descoteaux, . . . C. Dipy (2014). "Dipy, a library for the analysis of diffusion MRI data." Front Neuroinform **8**: 8.

Geiger, J. R. P., J. Lübke, A. Roth, M. Frotscher and P. Jonas (1997). "Submillisecond AMPA Receptor-Mediated Signaling at a Principal Neuron–Interneuron Synapse." Neuron **18**(6): 1009-1023.

Gereau, R. W. and G. Swanson (2008). The Glutamate Receptors, Humana Press.

Gernsbacher, M. A., M. Dawson and H. H. Goldsmith (2005). "Three Reasons Not to Believe in an Autism Epidemic." Current directions in psychological science **14**(2): 55-58.

Geschwind, D. H. and M. W. State (2015). "Gene hunting in autism spectrum disorder: on the path to precision medicine." The Lancet Neurology **14**(11): 1109-1120.

Gibson, J. R., A. F. Bartley, S. A. Hays and K. M. Huber (2008). "Imbalance of Neocortical Excitation and Inhibition and Altered UP States Reflect Network Hyperexcitability in the Mouse Model of Fragile X Syndrome." Journal of Neurophysiology **100**(5): 2615-2626.

Giuliani, N. R., V. D. Calhoun, G. D. Pearlson, A. Francis and R. W. Buchanan (2005). "Voxel-based morphometry versus region of interest: a comparison of two methods for analyzing gray matter differences in schizophrenia." Schizophr Res **74**(2-3): 135-147.

Goense, J., H. Merkle and N. K. Logothetis (2012). "High-resolution fMRI reveals laminar differences in neurovascular coupling between positive and negative BOLD responses." Neuron **76**(3): 629-639.

Good, C. D., I. S. Johnsrude, J. Ashburner, R. N. Henson, K. J. Friston and R. S. Frackowiak (2001). "A voxel-based morphometric study of ageing in 465 normal adult human brains." Neuroimage **14**(1 Pt 1): 21-36.

Good, C. D., R. I. Scahill, N. C. Fox, J. Ashburner, K. J. Friston, D. Chan, . . . R. S. J. Frackowiak (2002). "Automatic Differentiation of Anatomical Patterns in the Human Brain: Validation with Studies of Degenerative Dementias." NeuroImage **17**(1): 29-46.

Gorgolewski, K., C. D. Burns, C. Madison, D. Clark, Y. O. Halchenko, M. L. Waskom and S. S. Ghosh (2011). "Nipype: a flexible, lightweight and extensible neuroimaging data processing framework in python." Front Neuroinform **5**: 13.

Gottesman, I. I. and T. D. Gould (2003). "The Endophenotype Concept in Psychiatry: Etymology and Strategic Intentions." American Journal of Psychiatry **160**(4): 636-645.

Gozzi, A. and A. J. Schwarz (2016). "Large-scale functional connectivity networks in the rodent brain." Neuroimage **127**: 496-509.

Grabrucker, A. M., M. J. Schmeisser, M. Schoen and T. M. Boeckers (2011). "Postsynaptic ProSAP/Shank scaffolds in the cross-hair of synaptopathies." Trends in Cell Biology **21**(10): 594-603.

Grandjean, J., C. Canella, C. Anckaerts, G. Ayrancı, S. Bougacha, T. Bienert, . . . A. Gozzi (2020). "Common functional networks in the mouse brain revealed by multi-centre resting-state fMRI analysis." NeuroImage **205**: 116278.

Grandjean, J., A. Schroeter, I. Batata and M. Rudin (2014a). "Optimization of anesthesia protocol for resting-state fMRI in mice based on differential effects of anesthetics on functional connectivity patterns." Neuroimage **102 Pt 2**: 838-847.

Grandjean, J., A. Schroeter, P. He, M. Tanadini, R. Keist, D. Krstic, . . . M. Rudin (2014b). "Early Alterations in Functional Connectivity and White Matter Structure in a Transgenic Mouse Model of Cerebral Amyloidosis." The Journal of Neuroscience **34**(41): 13780.

Greger, I. H., J. F. Watson and S. G. Cull-Candy (2017). "Structural and Functional Architecture of AMPA-Type Glutamate Receptors and Their Auxiliary Proteins." Neuron **94**(4): 713-730.

Greicius, M. (2008). "Resting-state functional connectivity in neuropsychiatric disorders." Current Opinion in Neurology **21**(4).

Greicius, M. D., V. Kiviniemi, O. Tervonen, V. Vainionpaa, S. Alahuhta, A. L. Reiss and V. Menon (2008). "Persistent default-mode network connectivity during light sedation." Hum Brain Mapp **29**(7): 839-847.

Greicius, M. D., B. Krasnow, A. L. Reiss and V. Menon (2003). "Functional connectivity in the resting brain: A network analysis of the default mode hypothesis." Proceedings of the National Academy of Sciences **100**(1): 253.

Griffanti, L., G. Douaud, J. Bijsterbosch, S. Evangelisti, F. Alfaro-Almagro, M. F. Glasser, . . . S. M. Smith (2017). "Hand classification of fMRI ICA noise components." Neuroimage **154**: 188-205.

Grill-Spector, K., N. Knouf and N. Kanwisher (2004). "The fusiform face area subserves face perception, not generic within-category identification." Nat Neurosci **7**(5): 555-562.

Griswold, A. J., D. Ma, H. N. Cukier, L. D. Nations, M. A. Schmidt, R.-H. Chung, . . . M. A. Pericak-Vance (2012). "Evaluation of copy number variations reveals novel candidate genes in autism spectrum disorder-associated pathways." Human Molecular Genetics **21**(15): 3513-3523.

Haar, S., S. Berman, M. Behrmann and I. Dinstein (2016). "Anatomical Abnormalities in Autism?" Cereb Cortex **26**(4): 1440-1452.

Hall, G. B., K. A. Doyle, J. Goldberg, D. West and P. Szatmari (2010). "Amygdala engagement in response to subthreshold presentations of anxious face stimuli in adults with autism spectrum disorders: preliminary insights." PLoS One **5**(5): e10804.

Handwerker, D. A., J. M. Ollinger and M. D'Esposito (2004). "Variation of BOLD hemodynamic responses across subjects and brain regions and their effects on statistical analyses." NeuroImage **21**(4): 1639-1651.

Hansen, K. B., K. K. Ogden, H. Yuan and S. F. Traynelis (2014). "Distinct functional and pharmacological properties of Triheteromeric GluN1/GluN2A/GluN2B NMDA receptors." Neuron **81**(5): 1084-1096.

Hansen, K. B., F. Yi, R. E. Perszyk, H. Furukawa, L. P. Wollmuth, A. J. Gibb and S. F. Traynelis (2018). "Structure, function, and allosteric modulation of NMDA receptors." The Journal of General Physiology **150**(8): 1081.

Hansen, K. B., F. Yi, R. E. Perszyk, F. S. Menniti and S. F. Traynelis (2017). NMDA Receptors in the Central Nervous System. NMDA Receptors: Methods and Protocols. N. Burnashev and P. Szepetowski. New York, NY, Springer New York**:** 1-80.

Hara, K. and R. A. Harris (2002). "The anesthetic mechanism of urethane: the effects on neurotransmitter-gated ion channels." Anesth Analg **94**(2): 313-318, table of contents.

Harel, N., S.-P. Lee, T. Nagaoka, D.-S. Kim and S.-G. Kim (2002). "Origin of Negative Blood Oxygenation Level—Dependent fMRI Signals." Journal of Cerebral Blood Flow & Metabolism **22**(8): 908-917.

Harms, R. L., F. J. Fritz, A. Tobisch, R. Goebel and A. Roebroeck (2017). "Robust and fast nonlinear optimization of diffusion MRI microstructure models." Neuroimage **155**: 82-96.

Hassel, B. and R. Dingledine (2012). Chapter 17 - Glutamate and Glutamate Receptors. Basic Neurochemistry (Eighth Edition). S. T. Brady, G. J. Siegel, R. W. Albers and D. L. Price. New York, Academic Press**:** 342-366.

Hatton, C. J. and P. Paoletti (2005). "Modulation of triheteromeric NMDA receptors by N-terminal domain ligands." Neuron **46**(2): 261-274.

He, Y., L. Byrge and D. P. Kennedy (2020). "Nonreplication of functional connectivity differences in autism spectrum disorder across multiple sites and denoising strategies." Human Brain Mapping **41**(5): 1334-1350.

Health, N. I. o. M. (2018). "Autism Spectrum Disorder." Retrieved June 18th, 2019, from https://www.nimh.nih.gov/health/topics/autism-spectrum-disorders-asd/index.shtml.

Hestrin, S., R. A. Nicoll, D. J. Perkel and P. Sah (1990). "Analysis of excitatory synaptic action in pyramidal cells using whole-cell recording from rat hippocampal slices." J Physiol **422**: 203-225.

Hofstetter, S., I. Tavor, S. Tzur Moryosef and Y. Assaf (2013). "Short-Term Learning Induces White Matter Plasticity in the Fornix." The Journal of Neuroscience **33**(31): 12844.

Hong, S.-J., J. T. Vogelstein, A. Gozzi, B. C. Bernhardt, B. T. T. Yeo, M. P. Milham and A. Di Martino (2020). "Toward Neurosubtypes in Autism." Biological Psychiatry **88**(1): 111-128.

Huang, W., I. Plyka, H. Li, E. M. Eisenstein, N. D. Volkow and C. S. Springer (1996). "Magnetic resonance imaging (MRI) detection of the murine brain response to light: temporal differentiation and negative functional MRI changes." Proceedings of the National Academy of Sciences **93**(12): 6037.

Huettel, S. A., A. W. Song and G. McCarthy (2014). Functional Magnetic Resonance Imaging, Sinauer.

Huettner, J. E. (1990). "Glutamate receptor channels in rat DRG neurons: activation by kainate and quisqualate and blockade of desensitization by Con A." Neuron **5**(3): 255-266.

Humphreys, K., U. Hasson, G. Avidan, N. Minshew and M. Behrmann (2008). "Cortical patterns of category-selective activation for faces, places and objects in adults with autism." Autism Res **1**(1): 52-63.

Hussain, N. K., G. H. Diering, J. Sole, V. Anggono and R. L. Huganir (2014). "Sorting Nexin 27 regulates basal and activity-dependent trafficking of AMPARs." Proceedings of the National Academy of Sciences of the United States of America **111**(32): 11840-11845.

Hyder, F., K. L. Behar, M. A. Martin, A. M. Blamire and R. G. Shulman (1994). "Dynamic magnetic resonance imaging of the rat brain during forepaw stimulation." J Cereb Blood Flow Metab **14**(4): 649-655.

Iacobucci, G. J. and G. K. Popescu (2017). "NMDA receptors: linking physiological output to biophysical operation." Nature Reviews Neuroscience **18**(4): 236-249.

Ingre, M. (2013). "Why small low-powered studies are worse than large high-powered studies and how to protect against "trivial" findings in research: comment on Friston (2012)." Neuroimage **81**: 496-498.

Iossifov, I., B. J. O'Roak, S. J. Sanders, M. Ronemus, N. Krumm, D. Levy, . . . M. Wigler (2014). "The contribution of de novo coding mutations to autism spectrum disorder." Nature **515**: 216.

James, S. J., S. Rose, S. Melnyk, S. Jernigan, S. Blossom, O. Pavliv and D. W. Gaylor (2009). "Cellular and mitochondrial glutathione redox imbalance in lymphoblastoid cells

derived from children with autism." FASEB journal : official publication of the Federation of American Societies for Experimental Biology **23**(8): 2374-2383.

Janve, V. A., Z. Zu, S. Y. Yao, K. Li, F. L. Zhang, K. J. Wilson, . . . D. F. Gochberg (2013). "The radial diffusivity and magnetization transfer pool size ratio are sensitive markers for demyelination in a rat model of type III multiple sclerosis (MS) lesions." Neuroimage **74**: 298-305.

Javitt, D. C., D. Schoepp, P. W. Kalivas, N. D. Volkow, C. Zarate, K. Merchant, . . . C.-M. Lee (2011). "Translating glutamate: from pathophysiology to treatment." Science translational medicine **3**(102): 102mr102-102mr102.

Jbabdi, S. and H. Johansen-Berg (2011). "Tractography: where do we go from here?" Brain Connect **1**(3): 169-183.

Jeffrey-Gauthier, R., J. P. Guillemot and M. Piche (2013). "Neurovascular coupling during nociceptive processing in the primary somatosensory cortex of the rat." Pain **154**(8): 1434-1441.

Jego, P., J. Pacheco-Torres, A. Araque and S. Canals (2014). "Functional MRI in mice lacking IP3-dependent calcium signaling in astrocytes." J Cereb Blood Flow Metab **34**(10): 1599-1603.

Jenkinson, M., P. Bannister, M. Brady and S. Smith (2002). "Improved optimization for the robust and accurate linear registration and motion correction of brain images." Neuroimage **17**(2): 825-841.

Jenkinson, M., C. F. Beckmann, T. E. Behrens, M. W. Woolrich and S. M. Smith (2012). "Fsl." Neuroimage **62**(2): 782-790.

Jensen, J. H. and J. A. Helpern (2010). "MRI quantification of non-Gaussian water diffusion by kurtosis analysis." NMR in biomedicine **23**(7): 698-710.

Jensen, J. H., J. A. Helpern, A. Ramani, H. Lu and K. Kaczynski (2005). "Diffusional kurtosis imaging: the quantification of non-gaussian water diffusion by means of magnetic resonance imaging." Magn Reson Med **53**(6): 1432-1440.

Jonas, P. and N. Burnashev (1995). "Molecular mechanisms controlling calcium entry through AMPA-type glutamate receptor channels." Neuron **15**(5): 987-990.

Jonckers, E., D. Shah, J. Hamaide, M. Verhoye and A. Van der Linden (2015). "The power of using functional fMRI on small rodents to study brain pharmacology and disease." **6**(231).

Jonckers, E., J. Van Audekerke, G. De Visscher, A. Van der Linden and M. Verhoye (2011). "Functional connectivity fMRI of the rodent brain: comparison of functional connectivity networks in rat and mouse." PLoS One **6**(4): e18876.

Jonckers, E., A. Van der Linden and M. Verhoye (2013). "Functional magnetic resonance imaging in rodents: an unique tool to study in vivo pharmacologic neuromodulation." Current Opinion in Pharmacology **13**(5): 813-820.

Jones, D. K. (2010). Diffusion MRI, Oxford University Press.

Jones, D. K., T. R. Knosche and R. Turner (2013). "White matter integrity, fiber count, and other fallacies: the do's and don'ts of diffusion MRI." Neuroimage **73**: 239-254.

Jones, D. K., A. Simmons, S. C. Williams and M. A. Horsfield (1999). "Non-invasive assessment of axonal fiber connectivity in the human brain via diffusion tensor MRI." Magn Reson Med **42**(1): 37-41.

Kakegawa, W., Y. Miyoshi, K. Hamase, S. Matsuda, K. Matsuda, K. Kohda, . . . M. Yuzaki (2011). "D-Serine regulates cerebellar LTD and motor coordination through the δ2 glutamate receptor." Nature Neuroscience **14**: 603.

Kamada, K., T. Todo, T. Ota, K. Ino, Y. Masutani, S. Aoki, . . . N. Saito (2009). "The motor-evoked potential threshold evaluated by tractography and electrical stimulation." J Neurosurg **111**(4): 785-795.

Kamiya, K., M. Hori and S. Aoki (2020). "NODDI in clinical research." Journal of Neuroscience Methods **346**: 108908.

Kandel, E., J. Schwartz, T. Jessell, S. Siegelbaum and A. J Hudspeth (2013). Principles of Neural Science, Fifth Edition.

Kanner, L. (1943). "Autistic disturbances of affective contact." Nervous Child **2**: 217-250.

Kanwisher, N., J. McDermott and M. M. Chun (1997). "The Fusiform Face Area: A Module in Human Extrastriate Cortex Specialized for Face Perception." The Journal of Neuroscience **17**(11): 4302.

Kapogiannis, D., D. A. Reiter, A. A. Willette and M. P. Mattson (2013). "Posteromedial cortex glutamate and GABA predict intrinsic functional connectivity of the default mode network." Neuroimage **64**: 112-119.

Karas, G. B., P. Scheltens, S. A. Rombouts, P. J. Visser, R. A. van Schijndel, N. C. Fox and F. Barkhof (2004). "Global and local gray matter loss in mild cognitive impairment and Alzheimer's disease." Neuroimage **23**(2): 708-716.

Katsnelson, A. (2018). "Modeling autism." Lab Animal **47**: 41.

Kehrer, C., N. Maziashvili, T. Dugladze and T. Gloveli (2008). "Altered excitatory-inhibitory balance in the NMDA-hypofunction model of schizophrenia." **1**(6).

Keilholz, S. D. (2014). "The neural basis of time-varying resting-state functional connectivity." Brain Connect **4**(10): 769-779.

Keinanen, K., W. Wisden, B. Sommer, P. Werner, A. Herb, T. A. Verdoorn, . . . P. H. Seeburg (1990). "A family of AMPA-selective glutamate receptors." Science **249**(4968): 556.

Kennedy, D. P. and E. Courchesne (2008). "The intrinsic functional organization of the brain is altered in autism." NeuroImage **39**(4): 1877-1885.

Kingsley, P. B. (2006). "Introduction to diffusion tensor imaging mathematics: Part II. Anisotropy, diffusion-weighting factors, and gradient encoding schemes." Concepts in Magnetic Resonance Part A **28A**(2): 123-154.

Klein, A., J. Andersson, B. A. Ardekani, J. Ashburner, B. Avants, M. C. Chiang, . . . R. V. Parsey (2009). "Evaluation of 14 nonlinear deformation algorithms applied to human brain MRI registration." Neuroimage **46**(3): 786-802.

Knight, H. M., R. Walker, R. James, D. J. Porteous, W. J. Muir, D. H. R. Blackwood and B. S. Pickard (2012). "GRIK4/KA1 protein expression in human brain and correlation with bipolar disorder risk variant status." American Journal of Medical Genetics Part B: Neuropsychiatric Genetics **159B**(1): 21-29.

Kocharyan, A., P. Fernandes, X.-K. Tong, E. Vaucher and E. Hamel (2007). "Specific Subtypes of Cortical GABA Interneurons Contribute to the Neurovascular Coupling Response to Basal Forebrain Stimulation." Journal of Cerebral Blood Flow & Metabolism **28**(2): 221-231.

Kriegeskorte, N., M. A. Lindquist, T. E. Nichols, R. A. Poldrack and E. Vul (2010). "Everything You Never Wanted to Know about Circular Analysis, but Were Afraid to Ask." **30**(9): 1551-1557.

Kriegeskorte, N., W. K. Simmons, P. S. Bellgowan and C. I. Baker (2009). "Circular analysis in systems neuroscience: the dangers of double dipping." Nat Neurosci **12**(5): 535-540.

Kyriakopoulos, M. and S. Frangou (2009). "Recent diffusion tensor imaging findings in early stages of schizophrenia." Curr Opin Psychiatry **22**(2): 168-176.

Lake, E. M. R., X. Ge, X. Shen, P. Herman, F. Hyder, J. A. Cardin, . . . R. T. Constable (2020). "Simultaneous cortex-wide fluorescence Ca2+ imaging and whole-brain fMRI." Nature Methods.

Lalonde, R. and C. Strazielle (2008). "Relations between open-field, elevated plus-maze, and emergence tests as displayed by C57/BL6J and BALB/c mice." J Neurosci Methods **171**(1): 48-52.

Langley, J. N. (1901). "Observations on the physiological action of extracts of the supra-renal bodies." The Journal of physiology **27**(3): 237-256.

Lau, C. G. and R. S. Zukin (2007). "NMDA receptor trafficking in synaptic plasticity and neuropsychiatric disorders." Nat Rev Neurosci **8**(6): 413-426.

Laubach, M., L. M. Amarante, K. Swanson and S. R. White (2018). "What, If Anything, Is Rodent Prefrontal Cortex?" eNeuro **5**(5): ENEURO.0315-0318.2018.

Laufs, H. (2008). "Endogenous brain oscillations and related networks detected by surface EEG-combined fMRI." Human Brain Mapping **29**(7): 762-769.

Laufs, H., K. Krakow, P. Sterzer, E. Eger, A. Beyerle, A. Salek-Haddadi and A. Kleinschmidt (2003). "Electroencephalographic signatures of attentional and cognitive default modes in spontaneous brain activity fluctuations at rest." Proceedings of the National Academy of Sciences **100**(19): 11053.

Lauritzen, M. (2005). "Reading vascular changes in brain imaging: is dendritic calcium the key?" Nat Rev Neurosci **6**(1): 77-85.

Lauritzen, M., C. Mathiesen, K. Schaefer and K. J. Thomsen (2012). "Neuronal inhibition and excitation, and the dichotomic control of brain hemodynamic and oxygen responses." Neuroimage **62**(2): 1040-1050.

Lazar, M., D. M. Weinstein, J. S. Tsuruda, K. M. Hasan, K. Arfanakis, M. E. Meyerand, . . . A. L. Alexander (2003). "White matter tractography using diffusion tensor deflection." Hum Brain Mapp **18**(4): 306-321.

Le Bihan, D. and E. Breton (1985). "Imagerie de diffusion in-vivo par résonance magnétique nucléaire." **93**(5): 27-34.

Le Bihan, D., E. Breton, D. Lallemand, P. Grenier, E. Cabanis and M. Laval-Jeantet (1986). "MR imaging of intravoxel incoherent motions: application to diffusion and perfusion in neurologic disorders." Radiology **161**(2): 401-407.

Le Bihan, D. and H. Johansen-Berg (2012). "Diffusion MRI at 25: exploring brain tissue structure and function." Neuroimage **61**(2): 324-341.

Leblond, C. S., C. Nava, A. Polge, J. Gauthier, G. Huguet, S. Lumbroso, . . . T. Bourgeron (2014). "Meta-analysis of SHANK Mutations in Autism Spectrum Disorders: A Gradient of Severity in Cognitive Impairments." PLOS Genetics **10**(9): e1004580.

Lee, J. H., R. Durand, V. Gradinaru, F. Zhang, I. Goshen, D. S. Kim, . . . K. Deisseroth (2010). "Global and local fMRI signals driven by neurons defined optogenetically by type and wiring." Nature **465**(7299): 788-792.

Leemans, A., B. Jeurissen, J. Sijbers and D. Jones (2009). ExploreDTI: a graphical toolbox for processing, analyzing, and visualizing diffusion MR data. Proc Intl Soc Mag Reson Med.

Leithner, C. and G. Royl (2014). "The oxygen paradox of neurovascular coupling." J Cereb Blood Flow Metab **34**(1): 19-29.

Leithner, C., G. Royl, N. Offenhauser, M. Füchtemeier, M. Kohl-Bareis, A. Villringer, . . . U. Lindauer (2009). "Pharmacological Uncoupling of Activation Induced Increases in CBF and CMRO2." Journal of Cerebral Blood Flow & Metabolism **30**(2): 311-322.

Lerma, J. (1997). "Kainate reveals its targets." Neuron **19**(6): 1155-1158.

Lerma, J. (2003). "Roles and rules of kainate receptors in synaptic transmission." Nature Reviews Neuroscience **4**(6): 481-495.

Lerma, J. (2011). "Net(o) excitement for kainate receptors." Nature Neuroscience **14**(7): 808-810.

Lerma, J. and J. M. Marques (2013). "Kainate receptors in health and disease." Neuron **80**(2): 292-311.

Lerma, J., A. V. Paternain, J. R. Naranjo and B. Mellstrom (1993). "Functional kainate-selective glutamate receptors in cultured hippocampal neurons." Proc Natl Acad Sci U S A **90**(24): 11688-11692.

Lerma, J., A. V. Paternain, A. Rodriguez-Moreno and J. C. Lopez-Garcia (2001). "Molecular physiology of kainate receptors." Physiol Rev **81**(3): 971-998.

Lerma, J., R. S. Zukin and M. V. Bennett (1990). "Glycine decreases desensitization of N-methyl-D-aspartate (NMDA) receptors expressed in Xenopus oocytes and is required for NMDA responses." Proceedings of the National Academy of Sciences **87**(6): 2354.

Lester, R. A., J. D. Clements, G. L. Westbrook and C. E. Jahr (1990). "Channel kinetics determine the time course of NMDA receptor-mediated synaptic currents." Nature **346**(6284): 565-567.

Lester, R. A. and C. E. Jahr (1992). "NMDA channel behavior depends on agonist affinity." J Neurosci **12**(2): 635-643.

Li, S. J., B. Biswal, Z. Li, R. Risinger, C. Rainey, J. K. Cho, . . . E. A. Stein (2000). "Cocaine administration decreases functional connectivity in human primary visual and motor cortex as detected by functional MRI." Magn Reson Med **43**(1): 45-51.

Liao, Y., X. Huang, Q. Wu, C. Yang, W. Kuang, M. Du, . . . Q. Gong (2013). "Is depression a disconnection syndrome? Meta-analysis of diffusion tensor imaging studies in patients with MDD." J Psychiatry Neurosci **38**(1): 49-56.

Lindquist, M. A., B. Caffo and C. Crainiceanu (2013). "Ironing out the statistical wrinkles in "ten ironic rules"." Neuroimage **81**: 499-502.

Liska, A., A. Bertero, R. Gomolka, M. Sabbioni, A. Galbusera, N. Barsotti, . . . A. Gozzi (2017). "Homozygous Loss of Autism-Risk Gene CNTNAP2 Results in Reduced Local and Long-Range Prefrontal Functional Connectivity." Cerebral Cortex **28**(4): 1141-1153.

Liu, X., R. Li, Z. Yang, A. G. Hudetz and S. J. Li (2012). "Differential effect of isoflurane, medetomidine, and urethane on BOLD responses to acute levo-tetrahydropalmatine in the rat." Magn Reson Med **68**(2): 552-559.

Loewi, O. (1935). "The Ferrier Lecture: On Problems Connected with the Principle of Humoral Transmission of Nervous Impulses." Proceedings of the Royal Society of London. Series B, Biological Sciences **118**(809): 299-316.

Logothetis, N. (2010). "Neurovascular uncoupling: Much ado about nothing." **2**(2).

Logothetis, N. K. (2008). "What we can do and what we cannot do with fMRI." Nature **453**(7197): 869-878.

Logothetis, N. K., J. Pauls, M. Augath, T. Trinath and A. Oeltermann (2001). "Neurophysiological investigation of the basis of the fMRI signal." Nature **412**(6843): 150-157.

Lomeli, H., R. Sprengel, D. J. Laurie, G. Köhr, A. Herb, P. H. Seeburg and W. Wisden (1993). "The rat delta-1 and delta-2 subunits extend the excitatory amino acid receptor family." FEBS Letters **315**(3): 318-322.

Lowe, M. J., M. Dzemidzic, J. T. Lurito, V. P. Mathews and M. D. Phillips (2000). "Correlations in low-frequency BOLD fluctuations reflect cortico-cortical connections." Neuroimage **12**(5): 582-587.

Lowe, M. J., B. J. Mock and J. A. Sorenson (1998). "Functional connectivity in single and multislice echoplanar imaging using resting-state fluctuations." Neuroimage **7**(2): 119-132.

Lowe, M. J. J. M. R. M. i. P., Biology and Medicine (2010). "A historical perspective on the evolution of resting-state functional connectivity with MRI." **23**(5): 279-288.

Lowry, E. R., A. Kruyer, E. H. Norris, C. R. Cederroth and S. Strickland (2013). "The GluK4 kainate receptor subunit regulates memory, mood, and excitotoxic neurodegeneration." Neuroscience **235**: 215-225.

Lu, H., J. H. Jensen, A. Ramani and J. A. Helpern (2006). "Three-dimensional characterization of non-gaussian water diffusion in humans using diffusion kurtosis imaging." NMR Biomed **19**(2): 236-247.

Lu, H., S. Patel, F. Luo, S. J. Li, C. J. Hillard, B. D. Ward and J. S. Hyde (2004). "Spatial correlations of laminar BOLD and CBV responses to rat whisker stimulation with neuronal activity localized by Fos expression." Magn Reson Med **52**(5): 1060-1068.

Lu, H., Q. Zou, H. Gu, M. E. Raichle, E. A. Stein and Y. Yang (2012). "Rat brains also have a default mode network." Proceedings of the National Academy of Sciences **109**(10): 3979.

Lu, W., Y. Shi, A. C. Jackson, K. Bjorgan, M. J. During, R. Sprengel, . . . R. A. Nicoll (2009). "Subunit Composition of Synaptic AMPA Receptors Revealed by a Single-Cell Genetic Approach." Neuron **62**(2): 254-268.

Mack, S., E. R. Kandel, T. M. Jessell, J. H. Schwartz, S. A. Siegelbaum and A. J. Hudspeth (2013). Principles of Neural Science, Fifth Edition, McGraw-Hill Education.

Maggi, C. A. and A. Meli (1986). "Suitability of urethane anesthesia for physiopharmacological investigations in various systems. Part 2: Cardiovascular system." Experientia **42**(3): 292-297.

Maguire, E. A., D. G. Gadian, I. S. Johnsrude, C. D. Good, J. Ashburner, R. S. Frackowiak and C. D. Frith (2000). "Navigation-related structural change in the hippocampi of taxi drivers." Proc Natl Acad Sci U S A **97**(8): 4398-4403.

Mahajan, R. and S. H. Mostofsky (2015). "Neuroimaging endophenotypes in autism spectrum disorder." CNS spectrums **20**(4): 412-426.

Malhotra, D. and J. Sebat (2012). "CNVs: Harbingers of a Rare Variant Revolution in Psychiatric Genetics." Cell **148**(6): 1223-1241.

Mantini, D., M. G. Perrucci, C. Del Gratta, G. L. Romani and M. Corbetta (2007). "Electrophysiological signatures of resting state networks in the human brain." Proc Natl Acad Sci U S A **104**(32): 13170-13175.

Marques, J. M., R. J. Rodrigues, S. Valbuena, J. L. Rozas, S. Selak, P. Marin, . . . J. Lerma (2013). "CRMP2 Tethers Kainate Receptor Activity to Cytoskeleton Dynamics during Neuronal Maturation." **33**(46): 18298-18310.

Martin, C. (2014). "Contributions and complexities from the use of in vivo animal models to improve understanding of human neuroimaging signals." **8**(211).

Martin, S. J., P. D. Grimwood and R. G. M. Morris (2000). "Synaptic Plasticity and Memory: An Evaluation of the Hypothesis." Annual Review of Neuroscience **23**(1): 649-711.

Mathis, A., P. Mamidanna, K. M. Cury, T. Abe, V. N. Murthy, M. W. Mathis and M. Bethge (2018). "DeepLabCut: markerless pose estimation of user-defined body parts with deep learning." Nat Neurosci **21**(9): 1281-1289.

Matsuda, K., E. Miura, T. Miyazaki, W. Kakegawa, K. Emi, S. Narumi, . . . M. Yuzaki (2010). "Cbln1 Is a Ligand for an Orphan Glutamate Receptor δ2, a Bidirectional Synapse Organizer." **328**(5976): 363-368.

Mayer, M. L., G. L. Westbrook and P. B. Guthrie (1984). "Voltage-dependent block by Mg2+ of NMDA responses in spinal cord neurones." Nature **309**(5965): 261-263.

McFarlane, H. G., G. K. Kusek, M. Yang, J. L. Phoenix, V. J. Bolivar and J. N. Crawley (2008). "Autism-like behavioral phenotypes in BTBR T+tf/J mice." Genes, Brain and Behavior **7**(2): 152-163.

Mechelli, A., C. J. Price, K. J. Friston and J. Ashburner (2005). "Voxel-Based Morphometry of the Human Brain: Methods and Applications." Current Medical Imaging Reviews **1**(2): 105-113.

Mechling, A. E., N. S. Hübner, H. L. Lee, J. Hennig, D. von Elverfeldt and L. A. Harsan (2014). "Fine-grained mapping of mouse brain functional connectivity with resting-state fMRI." Neuroimage **96**: 203-215.

Melyan, Z., H. V. Wheal and B. Lancaster (2002). "Metabotropic-Mediated Kainate Receptor Regulation of IsAHP and Excitability in Pyramidal Cells." Neuron **34**(1): 107-114.

Merboldt, K.-D., W. Hanicke and J. Frahm (1985). "Self-diffusion NMR imaging using stimulated echoes." Journal of Magnetic Resonance (1969) **64**(3): 479-486.

Michetti, C., A. Caruso, M. Pagani, M. Sabbioni, L. Medrihan, G. David, . . . M. L. Scattoni (2017). "The Knockout of Synapsin II in Mice Impairs Social Behavior and Functional Connectivity Generating an ASD-like Phenotype." Cerebral Cortex **27**(10): 5014-5023.

Miles, J. H. (2011). "Autism spectrum disorders—A genetics review." Genetics In Medicine **13**: 278.

Monaco, A. P. and A. J. Bailey (2001). "The search for susceptibility genes." The Lancet **358**: S3.

Moreno, A., R. G. M. Morris and S. Canals (2016). "Frequency-Dependent Gating of Hippocampal-Neocortical Interactions." Cereb Cortex **26**(5): 2105-2114.

Moretto, E., L. Murru, G. Martano, J. Sassone and M. Passafaro (2018). "Glutamatergic synapses in neurodevelopmental disorders." Progress in Neuro-Psychopharmacology and Biological Psychiatry **84**: 328-342.

Mori, S., B. J. Crain, V. P. Chacko and P. C. van Zijl (1999). "Three-dimensional tracking of axonal projections in the brain by magnetic resonance imaging." Ann Neurol **45**(2): 265-269.

Mori, S. and J. D. Tournier (2013). Introduction to Diffusion Tensor Imaging: And Higher Order Models, Elsevier Science.

Mori, S. and J. Zhang (2006). "Principles of diffusion tensor imaging and its applications to basic neuroscience research." Neuron **51**(5): 527-539.

Moy, S. S., J. J. Nadler, N. B. Young, A. Perez, L. P. Holloway, R. P. Barbaro, . . . J. N. Crawley (2007). "Mouse behavioral tasks relevant to autism: Phenotypes of 10 inbred strains." Behavioural Brain Research **176**(1): 4-20.

Nasrallah, F. A., H. C. Tay and K. H. Chuang (2014). "Detection of functional connectivity in the resting mouse brain." Neuroimage **86**: 417-424.

Nickerson, L. D., S. M. Smith, D. Öngür and C. F. Beckmann (2017). "Using Dual Regression to Investigate Network Shape and Amplitude in Functional Connectivity Analyses." Front Neurosci **11**: 115.

Niranjan, A., I. N. Christie, S. G. Solomon, J. A. Wells and M. F. Lythgoe (2016). "fMRI mapping of the visual system in the mouse brain with interleaved snapshot GE-EPI." Neuroimage **139**: 337-345.

Niswender, C. M. and P. J. Conn (2010). "Metabotropic glutamate receptors: physiology, pharmacology, and disease." Annu Rev Pharmacol Toxicol **50**: 295-322.

Nowak, L., P. Bregestovski, P. Ascher, A. Herbet and A. Prochiantz (1984). "Magnesium gates glutamate-activated channels in mouse central neurones." Nature **307**(5950): 462-465.

Ogawa, S. (2012). "Finding the BOLD effect in brain images." NeuroImage **62**(2): 608-609.

Ogawa, S., T. M. Lee, A. R. Kay and D. W. Tank (1990a). "Brain magnetic resonance imaging with contrast dependent on blood oxygenation." Proc Natl Acad Sci U S A **87**(24): 9868-9872.

Ogawa, S., T. M. Lee, A. S. Nayak and P. Glynn (1990b). "Oxygenation-sensitive contrast in magnetic resonance image of rodent brain at high magnetic fields." Magn Reson Med **14**(1): 68-78.

Ogawa, S., T. M. Lee, R. Stepnoski, W. Chen, X. H. Zhu and K. Ugurbil (2000). "An approach to probe some neural systems interaction by functional MRI at neural time scale down to milliseconds." Proc Natl Acad Sci U S A **97**(20): 11026-11031.

Ogawa, S., D. W. Tank, R. Menon, J. M. Ellermann, S. G. Kim, H. Merkle and K. Ugurbil (1992). "Intrinsic signal changes accompanying sensory stimulation: functional brain mapping with magnetic resonance imaging." Proceedings of the National Academy of Sciences **89**(13): 5951.

Ohue, S., S. Kohno, A. Inoue, D. Yamashita, H. Harada, Y. Kumon, . . . T. Ohnishi (2011). "Accuracy of Diffusion Tensor Magnetic Resonance Imaging-Based Tractography for Surgery of Gliomas Near the Pyramidal Tract: A Significant Correlation Between Subcortical Electrical Stimulation and Postoperative Tractography." Neurosurgery **70**(2): 283-294.

Oliver, G. and E. A. Schäfer (1895). "The Physiological Effects of Extracts of the Suprarenal Capsules." The Journal of Physiology **18**(3): 230-276.

Paddock, S., G. Laje, D. Charney, A. J. Rush, A. F. Wilson, A. J. M. Sorant, . . . F. J. McMahon (2007). "Association of GRIK4 With Outcome of Antidepressant Treatment in the STAR*D Cohort." American Journal of Psychiatry **164**(8): 1181-1188.

Pagani, M., A. Bertero, A. Liska, A. Galbusera, M. Sabbioni, N. Barsotti, . . . A. Gozzi (2019). "Deletion of Autism Risk Gene Shank3 Disrupts Prefrontal Connectivity." The Journal of Neuroscience **39**(27): 5299.

Pajevic, S. and C. Pierpaoli (1999). "Color schemes to represent the orientation of anisotropic tissues from diffusion tensor data: application to white matter fiber tract mapping in the human brain." Magn Reson Med **42**(3): 526-540.

Pan, W. J., J. C. Billings, J. K. Grooms, S. Shakil and S. D. Keilholz (2015). "Considerations for resting state functional MRI and functional connectivity studies in rodents." Front Neurosci **9**: 269.

Paoletti, P., C. Bellone and Q. Zhou (2013). "NMDA receptor subunit diversity: impact on receptor properties, synaptic plasticity and disease." Nature Reviews Neuroscience **14**(6): 383-400.

Parker, G. J., K. E. Stephan, G. J. Barker, J. B. Rowe, D. G. MacManus, C. A. Wheeler-Kingshott, . . . R. Turner (2002). "Initial demonstration of in vivo tracing of axonal projections in the macaque brain and comparison with the human brain using diffusion tensor imaging and fast marching tractography." Neuroimage **15**(4): 797-809.

Paternain, A. V., M. Morales and J. Lerma (1995). "Selective antagonism of AMPA receptors unmasks kainate receptor-mediated responses in hippocampal neurons." Neuron **14**(1): 185-189.

Pauling, L. and C. D. Coryell (1936). "The Magnetic Properties and Structure of Hemoglobin, Oxyhemoglobin and Carbonmonoxyhemoglobin." Proceedings of the National Academy of Sciences of the United States of America **22**(4): 210-216.

Pawela, C. P., B. B. Biswal, Y. R. Cho, D. S. Kao, R. Li, S. R. Jones, . . . J. S. Hyde (2008). "Resting-state functional connectivity of the rat brain." Magnetic Resonance in Medicine **59**(5): 1021-1029.

Paxinos, G. and K. B. J. Franklin (2004). The Mouse Brain in Stereotaxic Coordinates, Elsevier Academic Press.

Peça, J., C. Feliciano, J. T. Ting, W. Wang, M. F. Wells, T. N. Venkatraman, . . . G. Feng (2011). "Shank3 mutant mice display autistic-like behaviours and striatal dysfunction." Nature **472**: 437.

Pelphrey, K. A., J. P. Morris, G. McCarthy and K. S. Labar (2007). "Perception of dynamic changes in facial affect and identity in autism." Soc Cogn Affect Neurosci **2**(2): 140-149.

Perez-Cervera, L., J. M. Carames, L. M. Fernandez-Molla, A. Moreno, B. Fernandez, E. Perez-Montoyo, . . . J. Pacheco-Torres (2018). "Mapping Functional Connectivity in the Rodent Brain Using Electric-Stimulation fMRI." Methods Mol Biol **1718**: 117-134.

Pergher, V., P. Demaerel, O. Soenen, C. Saarela, J. Tournoy, B. Schoenmakers, . . . M. M. Van Hulle (2019). "Identifying brain changes related to cognitive aging using VBM and visual rating scales." NeuroImage: Clinical **22**: 101697.

Peterson, D. J., M. Ryan, S. L. Rimrodt, L. E. Cutting, M. B. Denckla, W. E. Kaufmann and E. M. Mahone (2011). "Increased regional fractional anisotropy in highly screened attention-deficit hyperactivity disorder (ADHD)." J Child Neurol **26**(10): 1296-1302.

Pickard, B. S., H. M. Knight, R. S. Hamilton, D. C. Soares, R. Walker, J. K. Boyd, . . . W. J. Muir (2008). "A common variant in the 3'UTR of the GRIK4 glutamate receptor gene affects transcript abundance and protects against bipolar disorder." Proc Natl Acad Sci U S A **105**(39): 14940-14945.

Pickard, B. S., M. P. Malloy, A. Christoforou, P. A. Thomson, K. L. Evans, S. W. Morris, . . . W. J. Muir (2006). "Cytogenetic and genetic evidence supports a role for the kainate-type glutamate receptor gene, GRIK4, in schizophrenia and bipolar disorder." Molecular Psychiatry **11**(9): 847-857.

Pierce, K., F. Haist, F. Sedaghat and E. Courchesne (2004). "The brain response to personally familiar faces in autism: findings of fusiform activity and beyond." Brain **127**(Pt 12): 2703-2716.

Pierce, K., R. A. Muller, J. Ambrose, G. Allen and E. Courchesne (2001). "Face processing occurs outside the fusiform 'face area' in autism: evidence from functional MRI." Brain **124**(Pt 10): 2059-2073.

Pierce, K. and E. Redcay (2008). "Fusiform function in children with an autism spectrum disorder is a matter of "who"." Biol Psychiatry **64**(7): 552-560.

Pin, J.-P., T. Galvez and L. Prézeau (2003). "Evolution, structure, and activation mechanism of family 3/C G-protein-coupled receptors." Pharmacology & Therapeutics **98**(3): 325-354.

Poldrack, R. A. (2007). "Region of interest analysis for fMRI." Soc Cogn Affect Neurosci **2**(1): 67-70.

Popa, D., A. T. Popescu and D. Paré (2009). "Contrasting Activity Profile of Two Distributed Cortical Networks as a Function of Attentional Demands." The Journal of Neuroscience **29**(4): 1191.

Price, S., D. Paviour, R. Scahill, J. Stevens, M. Rossor, A. Lees and N. Fox (2004). "Voxel-based morphometry detects patterns of atrophy that help differentiate progressive supranuclear palsy and Parkinson's disease." Neuroimage **23**(2): 663-669.

Raffelt, D. A., R. E. Smith, G. R. Ridgway, J. D. Tournier, D. N. Vaughan, S. Rose, . . . A. Connelly (2015). "Connectivity-based fixel enhancement: Whole-brain statistical analysis of diffusion MRI measures in the presence of crossing fibres." Neuroimage **117**: 40-55.

Raffelt, D. A., J. D. Tournier, R. E. Smith, D. N. Vaughan, G. Jackson, G. R. Ridgway and A. Connelly (2017). "Investigating white matter fibre density and morphology using fixel-based analysis." Neuroimage **144**(Pt A): 58-73.

Raichle, M. E. (2015). "The Brain's Default Mode Network." Annual Review of Neuroscience **38**(1): 433-447.

Raichle, M. E., A. M. MacLeod, A. Z. Snyder, W. J. Powers, D. A. Gusnard and G. L. Shulman (2001). "A default mode of brain function." Proceedings of the National Academy of Sciences **98**(2): 676.

Ramón y Cajal, S. (1909). Histologie du système nerveux de l'homme & des vertébrés. Paris :, Maloine.

Rancillac, A., J. Rossier, M. Guille, X.-K. Tong, H. Geoffroy, C. Amatore, . . . B. Cauli (2006). "Glutamatergic Control of Microvascular Tone by Distinct GABA Neurons in the Cerebellum." The Journal of Neuroscience **26**(26): 6997.

Reed, M. D., K. E. Price, J. Archbold, A. Moffa and M. Febo (2013). "Predator odor-evoked BOLD activation in the awake rat: Modulation by oxytocin and V1a vasopressin receptor antagonists." Brain Research **1494**: 70-83.

Represa, A., E. Tremblay and Y. Ben-Ari (1987). "Kainate binding sites in the hippocampal mossy fibers: localization and plasticity." Neuroscience **20**(3): 739-748.

Rodrigues, R. J. and J. Lerma (2012). "Metabotropic signaling by kainate receptors." Wiley Interdisciplinary Reviews: Membrane Transport and Signaling **1**(4): 399-410.

Rodríguez-Moreno, A., O. Herreras and J. Lerma (1997). "Kainate Receptors Presynaptically Downregulate GABAergic Inhibition in the Rat Hippocampus." Neuron **19**(4): 893-901.

Rodriguez-Moreno, A. and J. Lerma (1998). "Kainate receptor modulation of GABA release involves a metabotropic function." Neuron **20**(6): 1211-1218.

Rowe, M., B. Siow, D. C. Alexander, U. Ferizi and S. Richardson (2016). Concepts of Diffusion in MRI. Diffusion Tensor Imaging: A Practical Handbook. W. Van Hecke, L. Emsell and S. Sunaert. New York, NY, Springer New York**:** 23-35.

Roy, C. S. and C. S. Sherrington (1890). "On the Regulation of the Blood-supply of the Brain." The Journal of physiology **11**(1-2): 85-158.117.

Ruigrok, A. N. V., G. Salimi-Khorshidi, M.-C. Lai, S. Baron-Cohen, M. V. Lombardo, R. J. Tait and J. Suckling (2014). "A meta-analysis of sex differences in human brain structure." Neuroscience and biobehavioral reviews **39**(100): 34-50.

Sah, P., S. Hestrin and R. A. Nicoll (1990). "Properties of excitatory postsynaptic currents recorded in vitro from rat hippocampal interneurones." J Physiol **430**: 605-616.

Sánchez-Gómez, M. V. and C. Matute (1999). "AMPA and Kainate Receptors Each Mediate Excitotoxicity in Oligodendroglial Cultures." Neurobiology of Disease **6**(6): 475-485.

Sarrazin, S., C. Poupon, J. Linke, M. Wessa, M. Phillips, M. Delavest, . . . J. Houenou (2014). "A multicenter tractography study of deep white matter tracts in bipolar I disorder: psychotic features and interhemispheric disconnectivity." JAMA Psychiatry **71**(4): 388-396.

Scarr, E., M. Beneyto, J. H. Meador-Woodruff and B. Dean (2005). "Cortical glutamatergic markers in schizophrenia." Neuropsychopharmacology **30**(8): 1521-1531.

Scattoni, M. L., S. U. Gandhy, L. Ricceri and J. N. Crawley (2008). "Unusual Repertoire of Vocalizations in the BTBR T+tf/J Mouse Model of Autism." PLOS ONE **3**(8): e3067.

Schafer, J. R., I. Kida, D. L. Rothman, F. Hyder and F. Xu (2005). "Adaptation in the rodent olfactory bulb measured by fMRI." Magn Reson Med **54**(2): 443-448.

Schafer, J. R., I. Kida, F. Xu, D. L. Rothman and F. Hyder (2006). "Reproducibility of odor maps by fMRI in rodents." NeuroImage **31**(3): 1238-1246.

Schäfer, K., F. Blankenburg, R. Kupers, J. M. Grüner, I. Law, M. Lauritzen and H. B. W. Larsson (2012). "Negative BOLD signal changes in ipsilateral primary somatosensory cortex are associated with perfusion decreases and behavioral evidence for functional inhibition." NeuroImage **59**(4): 3119-3127.

Scheeringa, R., K. M. Petersson, A. Kleinschmidt, O. Jensen and M. C. M. Bastiaansen (2012). "EEG α power modulation of fMRI resting-state connectivity." Brain connectivity **2**(5): 254-264.

Schizophrenia Working Group of the Psychiatric Genomics, C. (2014). "Biological insights from 108 schizophrenia-associated genetic loci." Nature **511**(7510): 421-427.

Schlegel, F., A. Schroeter and M. Rudin (2015). "The hemodynamic response to somatosensory stimulation in mice depends on the anesthetic used: Implications on analysis of mouse fMRI data." Neuroimage **116**: 40-49.

Scholvinck, M. L., D. A. Leopold, M. J. Brookes and P. H. Khader (2013). "The contribution of electrophysiology to functional connectivity mapping." Neuroimage **80**: 297-306.

Schroeder, J. C., D. Reim, T. M. Boeckers and M. J. Schmeisser (2017). Genetic Animal Models for Autism Spectrum Disorder. Social Behavior from Rodents to Humans: Neural Foundations and Clinical Implications. M. Wöhr and S. Krach. Cham, Springer International Publishing**:** 311-324.

Schroeter, A., F. Schlegel, A. Seuwen, J. Grandjean and M. Rudin (2014). "Specificity of stimulus-evoked fMRI responses in the mouse: The influence of systemic physiological changes associated with innocuous stimulation under four different anesthetics." NeuroImage **94**: 372-384.

Sforazzini, F., A. Bertero, L. Dodero, G. David, A. Galbusera, M. L. Scattoni, . . . A. Gozzi (2016). "Altered functional connectivity networks in acallosal and socially impaired BTBR mice." Brain Struct Funct **221**(2): 941-954.

Sforazzini, F., A. J. Schwarz, A. Galbusera, A. Bifone and A. Gozzi (2014). "Distributed BOLD and CBV-weighted resting-state networks in the mouse brain." Neuroimage **87**: 403-415.

Shah, D., E. Jonckers, J. Praet, G. Vanhoutte, R. Delgado y Palacios, C. Bigot, . . . A. Van der Linden (2013). "Resting State fMRI Reveals Diminished Functional Connectivity in a Mouse Model of Amyloidosis." PLOS ONE **8**(12): e84241.

Sharp, P. S., K. Shaw, L. Boorman, S. Harris, A. J. Kennerley, M. Azzouz and J. Berwick (2015). "Comparison of stimulus-evoked cerebral hemodynamics in the awake mouse and under a novel anesthetic regime." Sci Rep **5**: 12621.

Sheehan, T. P., R. A. Chambers and D. S. Russell (2004). "Regulation of affect by the lateral septum: implications for neuropsychiatry." Brain Research Reviews **46**(1): 71-117.

Shepherd, J. D. and R. L. Huganir (2007). "The Cell Biology of Synaptic Plasticity: AMPA Receptor Trafficking." Annual Review of Cell and Developmental Biology **23**(1): 613-643.

Shih, Y.-Y. I., C.-C. V. Chen, B.-C. Shyu, Z.-J. Lin, Y.-C. Chiang, F.-S. Jaw, . . . C. Chang (2009). "A New Scenario for Negative Functional Magnetic Resonance Imaging Signals: Endogenous Neurotransmission." The Journal of Neuroscience **29**(10): 3036.

Shih, Y. Y., Y. Y. Chen, H. Y. Lai, Y. C. Kao, B. C. Shyu and T. Q. Duong (2013). "Ultra high-resolution fMRI and electrophysiology of the rat primary somatosensory cortex." Neuroimage **73**: 113-120.

Shyu, B. C., C. Y. Lin, J. J. Sun, S. Sylantyev and C. Chang (2004). "A method for direct thalamic stimulation in fMRI studies using a glass-coated carbon fiber electrode." J Neurosci Methods **137**(1): 123-131.

Silverman, J. L., S. S. Tolu, C. L. Barkan and J. N. Crawley (2010a). "Repetitive self-grooming behavior in the BTBR mouse model of autism is blocked by the mGluR5 antagonist MPEP." Neuropsychopharmacology : official publication of the American College of Neuropsychopharmacology **35**(4): 976-989.

Silverman, J. L., M. Yang, C. Lord and J. N. Crawley (2010b). "Behavioural phenotyping assays for mouse models of autism." Nature Reviews Neuroscience **11**: 490.

Sirotin, Y. B. and A. Das (2009). "Anticipatory haemodynamic signals in sensory cortex not predicted by local neuronal activity." Nature **457**(7228): 475-479.

Sloviter, R. S. and B. P. Damiano (1981). "On the relationship between kainic acid-induced epileptiform activity and hippocampal neuronal damage." Neuropharmacology **20**(11): 1003-1011.

Smith, S. E. P., J. Li, K. Garbett, K. Mirnics and P. H. Patterson (2007). "Maternal immune activation alters fetal brain development through interleukin-6." The Journal of neuroscience : the official journal of the Society for Neuroscience **27**(40): 10695-10702.

Smith, S. M., P. T. Fox, K. L. Miller, D. C. Glahn, P. M. Fox, C. E. Mackay, . . . C. F. Beckmann (2009). "Correspondence of the brain's functional architecture during activation and rest." Proc Natl Acad Sci U S A **106**(31): 13040-13045.

Smith, S. M., M. Jenkinson, H. Johansen-Berg, D. Rueckert, T. E. Nichols, C. E. Mackay, . . . T. E. Behrens (2006). "Tract-based spatial statistics: voxelwise analysis of multi-subject diffusion data." Neuroimage **31**(4): 1487-1505.

Smith, S. M., K. L. Miller, G. Salimi-Khorshidi, M. Webster, C. F. Beckmann, T. E. Nichols, . . . M. W. Woolrich (2011). "Network modelling methods for FMRI." NeuroImage **54**(2): 875-891.

Smucny, J., K. P. Wylie and J. R. Tregellas (2014). "Functional magnetic resonance imaging of intrinsic brain networks for translational drug discovery." Trends in Pharmacological Sciences **35**(8): 397-403.

Sobolevsky, A. I., M. P. Rosconi and E. Gouaux (2009). "X-ray structure, symmetry and mechanism of an AMPA-subtype glutamate receptor." Nature **462**: 745.

Song, S. K., S. W. Sun, M. J. Ramsbottom, C. Chang, J. Russell and A. H. Cross (2002). "Dysmyelination revealed through MRI as increased radial (but unchanged axial) diffusion of water." Neuroimage **17**(3): 1429-1436.

Song, S. K., J. Yoshino, T. Q. Le, S. J. Lin, S. W. Sun, A. H. Cross and R. C. Armstrong (2005). "Demyelination increases radial diffusivity in corpus callosum of mouse brain." Neuroimage **26**(1): 132-140.

Soto, D., X. Altafaj, C. Sindreu and A. Bayés (2014). "Glutamate receptor mutations in psychiatric and neurodevelopmental disorders." Communicative & integrative biology **7**(1): e27887-e27887.

Squillace, M., L. Dodero, M. Federici, S. Migliarini, F. Errico, F. Napolitano, . . . A. Gozzi (2014). "Dysfunctional dopaminergic neurotransmission in asocial BTBR mice." Translational Psychiatry **4**(8): e427-e427.

Stafford, J. M., B. R. Jarrett, O. Miranda-Dominguez, B. D. Mills, N. Cain, S. Mihalas, . . . D. A. Fair (2014). "Large-scale topology and the default mode network in the mouse connectome." Proceedings of the National Academy of Sciences **111**(52): 18745.

Stagg, C. J., V. Bachtiar, U. Amadi, C. A. Gudberg, A. S. Ilie, C. Sampaio-Baptista, . . . H. Johansen-Berg (2014). "Local GABA concentration is related to network-level resting functional connectivity." eLife **3**: e01465.

Stein, T., C. Moritz, M. Quigley, D. Cordes, V. Haughton and E. Meyerand (2000). "Functional connectivity in the thalamus and hippocampus studied with functional MR imaging." AJNR Am J Neuroradiol **21**(8): 1397-1401.

Steinhäuser, C. and V. Gallo (1996). "News on glutamate receptors in glial cells." Trends Neurosci **19**(8): 339-345.

Stejskal, E. O. and J. E. Tanner (1965). "Spin Diffusion Measurements: Spin Echoes in the Presence of a Time-Dependent Field Gradient." The Journal of Chemical Physics **42**(1): 288-292.

Sterling, L., G. Dawson, S. Webb, M. Murias, J. Munson, H. Panagiotides and E. Aylward (2008). "The role of face familiarity in eye tracking of faces by individuals with autism spectrum disorders." J Autism Dev Disord **38**(9): 1666-1675.

Stieltjes, B., W. E. Kaufmann, P. C. van Zijl, K. Fredericksen, G. D. Pearlson, M. Solaiyappan and S. Mori (2001). "Diffusion tensor imaging and axonal tracking in the human brainstem." Neuroimage **14**(3): 723-735.

Straub, C., D. L. Hunt, M. Yamasaki, K. S. Kim, M. Watanabe, P. E. Castillo and S. Tomita (2011). "Distinct functions of kainate receptors in the brain are determined by the auxiliary subunit Neto1." Nat Neurosci **14**(7): 866-873.

Tashiro, A., A. Dunaevsky, R. Blazeski, C. A. Mason and R. Yuste (2003). "Bidirectional Regulation of Hippocampal Mossy Fiber Filopodial Motility by Kainate Receptors: A Two-Step Model of Synaptogenesis." Neuron **38**(5): 773-784.

Tax, C. M., W. M. Otte, M. A. Viergever, R. M. Dijkhuizen and A. Leemans (2015). "REKINDLE: robust extraction of kurtosis INDices with linear estimation." Magn Reson Med **73**(2): 794-808.

Taylor, D. G. and M. C. Bushell (1985). "The spatial mapping of translational diffusion coefficients by the NMR imaging technique." Physics in Medicine and Biology **30**(4): 345-349.

Thirion, B., G. Varoquaux, E. Dohmatob and J.-B. Poline (2014). "Which fMRI clustering gives good brain parcellations?" **8**(167).

Thulborn, K. R. (2012). "My starting point: The discovery of an NMR method for measuring blood oxygenation using the transverse relaxation time of blood water." NeuroImage **62**(2): 589-593.

Thulborn, K. R., J. C. Waterton, P. M. Matthews and G. K. Radda (1982). "Oxygenation dependence of the transverse relaxation time of water protons in whole blood at high field." Biochim Biophys Acta **714**(2): 265-270.

Tournier, J. D., S. Mori and A. Leemans (2011). "Diffusion tensor imaging and beyond." Magn Reson Med **65**(6): 1532-1556.

Tournier, J. D., R. Smith, D. Raffelt, R. Tabbara, T. Dhollander, M. Pietsch, . . . A. Connelly (2019). "MRtrix3: A fast, flexible and open software framework for medical image processing and visualisation." Neuroimage **202**: 116137.

Travers, B. G., N. Adluru, C. Ennis, P. M. Tromp do, D. Destiche, S. Doran, . . . A. L. Alexander (2012). "Diffusion tensor imaging in autism spectrum disorder: a review." Autism Res **5**(5): 289-313.

Traynelis, S. F., L. P. Wollmuth, C. J. McBain, F. S. Menniti, K. M. Vance, K. K. Ogden, . . . R. Dingledine (2010). "Glutamate Receptor Ion Channels: Structure, Regulation, and Function." Pharmacological Reviews **62**(3): 405.

Trussell, L. O., S. Zhang and I. M. Raman (1993). "Desensitization of AMPA receptors upon multiquantal neurotransmitter release." Neuron **10**(6): 1185-1196.

Tsai, G. and J. T. Coyle (2002). "Glutamatergic mechanisms in schizophrenia." Annual review of pharmacology and toxicology **42**: 165-179.

Uemura, T., S.-J. Lee, M. Yasumura, T. Takeuchi, T. Yoshida, M. Ra, . . . M. Mishina (2010). "Trans-Synaptic Interaction of GluRδ2 and Neurexin through Cbln1 Mediates Synapse Formation in the Cerebellum." Cell **141**(6): 1068-1079.

Valbuena, S., Á. García, W. Mazier, A. V. Paternain and J. Lerma (2019). "Unbalanced dendritic inhibition of CA1 neurons drives spatial-memory deficits in the Ts2Cje Down syndrome model." Nature Communications **10**(1): 4991.

Valbuena, S. and J. Lerma (2016). "Non-canonical Signaling, the Hidden Life of Ligand-Gated Ion Channels." Neuron **92**(2): 316-329.

Van Camp, N., R. R. Peeters and A. Van der Linden (2005). "A comparison between blood oxygenation level-dependent and cerebral blood volume contrast in the rat cerebral and cerebellar somatosensoric cortex during electrical paw stimulation." J Magn Reson Imaging **22**(4): 483-491.

Van Camp, N., M. Verhoye, C. I. De Zeeuw and A. Van der Linden (2006). "Light stimulus frequency dependence of activity in the rat visual system as studied with high-resolution BOLD fMRI." J Neurophysiol **95**(5): 3164-3170.

Van Den Berge, N., D. L. Albaugh, A. Salzwedel, C. Vanhove, R. Van Holen, W. Gao, . . . Y.-Y. I. Shih (2017). "Functional circuit mapping of striatal output nuclei using simultaneous deep brain stimulation and fMRI." NeuroImage **146**: 1050-1061.

van Ewijk, H., D. J. Heslenfeld, M. P. Zwiers, J. K. Buitelaar and J. Oosterlaan (2012). "Diffusion tensor imaging in attention deficit/hyperactivity disorder: a systematic review and meta-analysis." Neurosci Biobehav Rev **36**(4): 1093-1106.

Van Hecke, W., L. Emsell and S. Sunaert (2015). Diffusion Tensor Imaging: A Practical Handbook, Springer New York.

van Rooij, D., E. Anagnostou, C. Arango, G. Auzias, M. Behrmann, G. F. Busatto, . . . J. K. Buitelaar (2018). "Cortical and Subcortical Brain Morphometry Differences Between Patients With Autism Spectrum Disorder and Healthy Individuals Across the Lifespan: Results From the ENIGMA ASD Working Group." Am J Psychiatry **175**(4): 359-369.

Vanhoutte, G., S. Pereson, Y. P. R. Delgado, P. J. Guns, B. Asselbergh, J. Veraart, . . . A. Van der Linden (2013). "Diffusion kurtosis imaging to detect amyloidosis in an APP/PS1 mouse model for Alzheimer's disease." Magn Reson Med **69**(4): 1115-1121.

Vederine, F. E., M. Wessa, M. Leboyer and J. Houenou (2011). "A meta-analysis of whole-brain diffusion tensor imaging studies in bipolar disorder." Prog Neuropsychopharmacol Biol Psychiatry **35**(8): 1820-1826.

Via, E., J. Radua, N. Cardoner, F. Happe and D. Mataix-Cols (2011). "Meta-analysis of gray matter abnormalities in autism spectrum disorder: should Asperger disorder be subsumed under a broader umbrella of autistic spectrum disorder?" Arch Gen Psychiatry **68**(4): 409-418.

Vignes, M., V. R. Clarke, M. J. Parry, D. Bleakman, D. Lodge, P. L. Ornstein and G. L. Collingridge (1998). "The GluR5 subtype of kainate receptor regulates excitatory synaptic transmission in areas CA1 and CA3 of the rat hippocampus." Neuropharmacology **37**(10-11): 1269-1277.

Vignes, M. and G. L. Collingridge (1997). "The synaptic activation of kainate receptors." Nature **388**(6638): 179-182.

Vincent, J. L., G. H. Patel, M. D. Fox, A. Z. Snyder, J. T. Baker, D. C. Van Essen, . . . M. E. Raichle (2007). "Intrinsic functional architecture in the anaesthetized monkey brain." Nature **447**(7140): 83-86.

Volk, L., S.-L. Chiu, K. Sharma and R. L. Huganir (2015). "Glutamate synapses in human cognitive disorders." Annual review of neuroscience **38**: 127-149.

Vul, E., C. Harris, P. Winkielman and H. Pashler (2009). "Puzzlingly High Correlations in fMRI Studies of Emotion, Personality, and Social Cognition." Perspect Psychol Sci **4**(3): 274-290.

Vul, E. and H. Pashler (2012). "Voodoo and circularity errors." NeuroImage **62**(2): 945-948.

Wahlsten, D., P. Metten and J. C. Crabbe (2003). "Survey of 21 inbred mouse strains in two laboratories reveals that BTBR T/+ tf/tf has severely reduced hippocampal commissure and absent corpus callosum." Brain Research **971**(1): 47-54.

Wallace, Michael L., Alain C. Burette, Richard J. Weinberg and Benjamin D. Philpot (2012). "Maternal Loss of Ube3a Produces an Excitatory/Inhibitory Imbalance through Neuron Type-Specific Synaptic Defects." Neuron **74**(5): 793-800.

Wang, X., A. L. Bey, B. M. Katz, A. Badea, N. Kim, L. K. David, . . . Y.-h. Jiang (2016). "Altered mGluR5-Homer scaffolds and corticostriatal connectivity in a Shank3 complete knockout model of autism." Nature Communications **7**: 11459.

Wang, X., Y. Zhao, X. Zhang, H. Badie, Y. Zhou, Y. Mu, . . . H. Xu (2013). "Loss of sorting nexin 27 contributes to excitatory synaptic dysfunction by modulating glutamate receptor recycling in Down's syndrome." Nature medicine **19**(4): 473-480.

Werling, D. M., J. K. Lowe, R. Luo, R. M. Cantor and D. H. Geschwind (2014). "Replication of linkage at chromosome 20p13 and identification of suggestive sex-differential risk loci for autism spectrum disorder." Molecular Autism **5**(1): 13.

Werner, E. and G. Dawson (2005). "Validation of the Phenomenon of Autistic Regression Using Home Videotapes." JAMA Psychiatry **62**(8): 889-895.

Whalley, H. C., B. S. Pickard, A. M. McIntosh, R. Zuliani, E. C. Johnstone, D. H. R. Blackwood, . . . J. Hall (2009). "A GRIK4 variant conferring protection against bipolar disorder modulates hippocampal function." Molecular Psychiatry **14**: 467.

Wheeler-Kingshott, C. A. M. and M. Cercignani (2009). "About "axial" and "radial" diffusivities." Magnetic resonance in medicine **61**(5): 1255-1260.

Whitwell, J. L. (2009). "Voxel-based morphometry: an automated technique for assessing structural changes in the brain." J Neurosci **29**(31): 9661-9664.

Winkler, A. M., M. A. Webster, J. C. Brooks, I. Tracey, S. M. Smith and T. E. Nichols (2016). "Non-parametric combination and related permutation tests for neuroimaging." Hum Brain Mapp **37**(4): 1486-1511.

Wisden, W. and P. H. Seeburg (1993). "Mammalian ionotropic glutamate receptors." Curr Opin Neurobiol **3**(3): 291-298.

Wöhr, M., F. I. Roullet and J. N. Crawley (2011). "Reduced scent marking and ultrasonic vocalizations in the BTBR T+tf/J mouse model of autism." Genes, Brain and Behavior **10**(1): 35-43.

Wright, I. C., P. K. McGuire, J. B. Poline, J. M. Travere, R. M. Murray, C. D. Frith, . . . K. J. Friston (1995). "A voxel-based method for the statistical analysis of gray and white matter density applied to schizophrenia." Neuroimage **2**(4): 244-252.

Wu, H., X. Wang, Y. Gao, F. Lin, T. Song, Y. Zou, . . . H. Lei (2016). "NMDA receptor antagonism by repetitive MK801 administration induces schizophrenia-like structural changes in the rat brain as revealed by voxel-based morphometry and diffusion tensor imaging." Neuroscience **322**: 221-233.

Xiang, Z., M. Valenza, L. Cui, V. Leoni, H. K. Jeong, E. Brilli, . . . D. Krainc (2011). "Peroxisome-proliferator-activated receptor gamma coactivator 1 alpha contributes to dysmyelination in experimental models of Huntington's disease." J Neurosci **31**(26): 9544-9553.

Xiong, J., L. M. Parsons, J. H. Gao and P. T. Fox (1999). "Interregional connectivity to primary motor cortex revealed using MRI resting state images." Hum Brain Mapp **8**(2-3): 151-156.

Yamazaki, M., K. Araki, A. Shibata and M. Mishina (1992). "Molecular cloning of a cDNA encoding a novel member of the mouse glutamate receptor channel family." Biochem Biophys Res Commun **183**(2): 886-892.

Yang, M., M. Scattoni, V. Zhodzishsky, T. Chen, H. Caldwell, W. Young, . . . J. Crawley (2007). "Social approach behaviors are similar on conventional versus reverse lighting cycles, and in replications across cohorts, in BTBR T+ tf/J, C57BL/6J, and vasopressin receptor 1B mutant mice." Frontiers in Behavioral Neuroscience **1**: 1.

Yang, X., F. Hyder and R. G. Shulman (1996). "Activation of single whisker barrel in rat brain localized by functional magnetic resonance imaging." Proc Natl Acad Sci U S A **93**(1): 475-478.

Yasumura, M., T. Yoshida, S.-J. Lee, T. Uemura, J.-Y. Joo and M. Mishina (2012). "Glutamate receptor δ1 induces preferentially inhibitory presynaptic differentiation of cortical neurons by interacting with neurexins through cerebellin precursor protein subtypes." Journal of Neurochemistry **121**(5): 705-716.

Yushkevich, P. A., J. Piven, H. C. Hazlett, R. G. Smith, S. Ho, J. C. Gee and G. Gerig (2006). "User-guided 3D active contour segmentation of anatomical structures: significantly improved efficiency and reliability." Neuroimage **31**(3): 1116-1128.

Zerbi, V., J. Grandjean, M. Rudin and N. Wenderoth (2015). "Mapping the mouse brain with rs-fMRI: An optimized pipeline for functional network identification." Neuroimage **123**: 11-21.

Zerbi, V., M. Pagani, M. Markicevic, M. Matteoli, D. Pozzi, M. Fagiolini, . . . N. Wenderoth (2020). "Brain mapping across 16 autism mouse models reveals a spectrum of functional connectivity subtypes." bioRxiv: 2020.2010.2015.340588.

Zerbi, V., M. Wiesmann, T. L. Emmerzaal, D. Jansen, M. Van Beek, M. P. C. Mutsaers, . . . A. J. Kiliaan (2014). "Resting-State Functional Connectivity Changes in Aging apoE4 and apoE-KO Mice." The Journal of Neuroscience **34**(42): 13963.

Zhang, H., T. Schneider, C. A. Wheeler-Kingshott and D. C. Alexander (2012). "NODDI: practical in vivo neurite orientation dispersion and density imaging of the human brain." Neuroimage **61**(4): 1000-1016.

Zhang, W., F. St-Gelais, C. P. Grabner, J. C. Trinidad, A. Sumioka, M. Morimoto-Tomita, . . . S. Tomita (2009). "A transmembrane accessory subunit that modulates kainate-type glutamate receptors." Neuron **61**(3): 385-396.

Zhou, Y., J. Sharma, Q. Ke, R. Landman, J. Yuan, H. Chen, . . . S. Yang (2019). "Atypical behaviour and connectivity in SHANK3-mutant macaques." Nature **570**(7761): 326-331.

Zikopoulos, B. and H. Barbas (2013). "Altered neural connectivity in excitatory and inhibitory cortical circuits in autism." **7**(609).